IAEA-TECDOC-1069

Characterization of ceramics and semiconductors using nuclear techniques

Final report of a co-ordinated research project

INTERNATIONAL ATOMIC ENERGY AGENCY IAEA

L

The originating Section of this publication in the IAEA was:

Industrial Applications and Chemistry Section
International Atomic Energy Agency
Wagramer Strasse 5
P.O. Box 100
A-1400 Vienna, Austria

CHARACTERIZATION OF CERAMICS AND
SEMICONDUCTORS USING NUCLEAR TECHNIQUES
IAEA, VIENNA, 1999
IAEA-TECDOC-1069
ISSN 1011–4289

Printed by the IAEA in Austria
March 1999

FOREWORD

The last few years have witnessed important advances in the development and applications of nuclear techniques in the characterization of new inorganic materials of technological importance. Recent advances in the understanding of materials and their behaviour have created means to modify known materials to meet new technological requirements and to design and synthesize new materials with desirable properties. High performance improvements have been achieved in semiconductors. New processes are yielding improved multifunctional ceramics. The application of nuclear and nuclear related techniques has contributed much to the understanding, characterization and modification of materials.

With the aim of promoting research and facilitating more extensive application of nuclear techniques for material development, the IAEA established in 1994 a Co-ordinated Research Project (CRP) on Characterization of Ceramics and Semiconductors using Nuclear Techniques. The first Research Co-ordination Meeting (RCM) was held in Sacavém (Portugal) in March 1994, and the second RCM was held in Leuven (Belgium) in October 1995. This publication includes results obtained from research undertaken until completion of all contracts and agreements under this CRP in 1997.

Important information on characterization of inorganic materials of technological importance by nuclear techniques has been gained during the development of this CRP. The development of techniques and instrumentation was also an important objective. Several techniques were developed further, such as small angle neutron diffraction, X ray and electron diffraction, Mössbauer spectroscopy, microwave irradiation and Raman spectroscopy.

This publication reviews and summarizes recent developments on characterization of ceramics and semiconductors using nuclear techniques. It includes an assessment of the current status and trends in nuclear techniques in the characterization of inorganic materials of technological importance, such as advanced ceramics and semiconductors. The TECDOC presents new achievements on ceramic superconductor behaviour under neutron induced defects, optimization of structure of mineral gels, low temperature preparation of fine particles of ferrites, crystal luminescence of ceramic composites with improved plastic properties, thin film defects and detoxification of asbestos. The investigation of chemical composition, phase transitions and magnetic properties of ferrites by Mössbauer spectroscopy is largely developed.

The IAEA wishes to thank all the scientists who contributed to the progress of this CRP. The IAEA officer responsible for this publication was J. Thereska of the Division of Physical and Chemical Sciences.

EDITORIAL NOTE

In preparing this publication for press, staff of the IAEA have made up the pages from the original manuscript(s). The views expressed do not necessarily reflect those of the IAEA, the governments of the nominating Member States or the nominating organizations.

Throughout the text names of Member States are retained as they were when the text was compiled.

The use of particular designations of countries or territories does not imply any judgement by the publisher, the IAEA, as to the legal status of such countries or territories, of their authorities and institutions or of the delimitation of their boundaries.

The mention of names of specific companies or products (whether or not indicated as registered) does not imply any intention to infringe proprietary rights, nor should it be construed as an endorsement or recommendation on the part of the IAEA.

CONTENTS

SUMMARY OF THE CO-ORDINATED RESEARCH PROJECT

Introduction

The shift from the traditional technologies typical of developing countries to the high technology based industries typical of developed countries is markedly dependent on the development of advanced materials or improvement in the properties of existing materials. Improved materials not only affect economic demands but environmental issues as well. Products made from high durability materials have a longer life cycle, producing less waste and affecting lower overall energy investment. Similar advantages are gained when using miniaturized systems. Engines made from temperature resistant materials provide better burning efficiency, thereby decreasing both fuel output and gas formation. Parasitic heat production will decrease and efficiency increase when electricity can be transferred by superconductors.

Energy is a current concern. There is a recognized need to find new, economical sources of energy and use the present resources more efficiently. Materials will undoubtedly play a significant role in these developments. For example, the direct conversion of solar into electrical energy has been demonstrated. However, the cost of the materials for the construction of solar cells is still high. Therefore researchers are going in the direction of the development of less costly but efficient materials.

Advanced ceramics have already found important applications in many technologies. Semiconductors have made possible the advent of integrated circuits that have totally revolutionized the electronics and computer industries, not to mention our everyday life, over the past two decades. Advanced ceramics and semiconductors are the subject of numerous investigations from different standpoints in many academic institutions and industries all over the world.

There are many materials which have found application in high technologies. Ceramics play a very important role in these applications due to their specific properties, and also in many cases due to their availability, low cost and environmental compatibility. Advanced ceramics can be classified as structural ceramics, where the mechanical function is important, and functional ceramics. In the case of functional ceramics, special properties such as electrical, magnetic, catalytic, thermal, etc., are of interest for their applications. These materials are expected to become an increasing significant component of so-called intelligent systems (sensors, actuators, power sources, computers, etc.). In the field of electro-ceramics (electrical function), high-temperature superconductors are expected to have a prominent role in many applications. Of high potential are ionic conductors such as oxygen, proton, sodium and lithium conductors (e.g. ZrO_2 (Y_2O_3), $SrCeO_3$ (Yb_2O_3), b type-Al_2O_3 (Na_2O), LiI:g type-Al_2O_3). They can be used as solid electrolytes for batteries, fuel cells, chemical sensors and electrochemical pumps. Ceramic semiconductors such as $BaTiO_3$, $SrTiO_3$, SnO_2, TiO_2, $PbZrO_3$ have found applications as capacitor materials, chemical sensors and actuators. Mixed conducting materials combine both ionic and electronic conductivity, enabling neutral components to permeate, dissolve or remove them. This is an important factor for advanced electrodes and the electrochemical storage of $H_2(NbH_x)$ or $Li(TiS_2)$ as a cathode in lithium batteries.

Ferrites are also very important materials in high technologies. These materials are characterized by specific electrical and magnetic properties. They have an appreciably higher

electrical resistance and lower saturation magnetization in relation to silicon steels or permalloys. This reduces eddy-current losses and makes ferrite suitable for making cores (toroids) which have application in the production of special transformers, coils and chokes. Ferrites have also found applications in magnetic recording media, memory devices and magneto-optical displays. Ceramics based on rare earth iron garnets are used as waveguides in the very high frequencies region. When these ferrite ceramics are used, the stability of frequency is much better than when metal wave guides are used, due to the better dilation-temperature properties of garnet ceramics. Ferrites can also be used as catalysts for specific chemical reactions.

Thermal functions are important for appropriate substrate materials such as aluminium nitrate (AlN) or diamond films exhibiting high thermal conductivity that are nevertheless electrical insulators. Glass-ceramics are examples of composite materials with low thermal treatment.

In the future, the very important materials will be those which exhibit multifunctional properties (for example, the optimization of mechanical properties with thermal and chemical resistivity). Multifunctionality of the properties of advanced materials can also be achieved in composite materials (for example, organic/inorganic components). Finally, the functional properties of advanced materials can be changed by reducing the dimension of particles (powders) or thickness (films). In this case, the active role of the surface is much more important than that of the bulk of the material.

Many physical and chemical methods are used today for the characterization of advanced materials and monitoring the physico-chemical stages during their synthesis. Nuclear methods have proved very fruitful in the investigation of advanced ceramics and semiconductors.

Mössbauer spectroscopy is traditionally used in the study of various oxide ceramics and metal alloys. This method can be used in investigating the phase composition of materials, clustering, valence state and the coordination of metal cations. It can be also used in the investigation of the interface of the oxide film/metal substrate. Mössbauer spectroscopy is especially useful in the determination of cation distribution in magnetic oxides. Recently, Mössbauer spectroscopy has been extensively used in monitoring mechanochemical effects in advanced ceramics.

Neutron-based techniques have also found important applications in material science. These techniques can be used to investigate the structural properties of advanced ceramics and also to modify the properties of the material by inducing structural defects. Neutron radiography, neutron diffraction, neutron small angle and very small angle scattering are examples of neutron-based techniques. The irradiation of materials can be performed using fast or thermal neutrons.

Neutron radiography is one of the most typical applications of small reactors and was a first step for material-oriented neutron work. This technique was mainly applied in solving various metallurgical problems, e.g. in the investigation of the diffusion of hydrogen in ceramics or metal alloys and the corresponding after effects. Sensitivities for hydrogen detector to the order, 1%, for oxygen to the order of 3%, and for metallic composites to 5% are feasible.

Neutron diffraction has been successfully used in determining crystal structures. This technique can be applied to large samples due to the high penetrating power of neutrons, thus eliminating most systematic errors, while neutrons are scattered equally well among oxygen, nitrogen and other light atomic constituents of ceramics. Determination of the crystal structure of the high temperature superconductor, ($YBa_2Cu_2O_{7-d}$), is perhaps the best known example of the success of neutrons compared to X ray diffraction (the problem of the exact location of heavy metal and oxygen atoms). Neutron diffraction has also found applications in other mixed metal oxides, zeolites, etc.

Small angle neutron scattering (SANS) is very useful in the investigation of the microstructure of advanced ceramics on nano-scale. Basically, this technique requires a well colimated beam of roughly monochromatic neutrons around the transmitted beam axis. The restriction of small angles eliminates Bragg scattering from individual atoms which occurs at larger angles. This technique is sensitive to large inhomogeneities and cracks which are serious problems in the tailoring of advanced ceramics. It is especially useful in the investigation of the microporosity of nanosized materials.

The properties of advanced ceramics, e.g. semiconductors, can be influenced by neutron irradiation. In many cases the critical current density, which for presently available high-temperature superconductors is a weak point, can be increased by more than one order of magnitude after neutron irradiation.

Positron annihilation lifetime (PAL) spectroscopy has been successfully used in the determination of free volume holes in porous materials as protective coatings, silica gels and polymers. This technique is based on the fact that ortho-positronium "atom" (σ-Ps), a bound state of the positron and the electron, is preferentially localized in the free-volume holes, where σ-Ps lifetime is relevant to the hole size. The calculations take into account that σ-Ps formation probability is proportional to the concentration of holes.

In view of the growing interest in materials science and technology in developing countries, as expressed during the Workshop on the Characterization of New Materials held in Beijing in August 1990, and by the participants of the International Conference on Advanced Materials held in Strasbourg in May 1991, and with a view to increasing the utilization of nuclear techniques in the development and processing of new materials, it was proposed to undertake a detailed review of this subject.

A Consultants Meeting on Nuclear Techniques in the Development of Advanced Ceramic Technologies was held in Vienna in October 1991 with the following objectives:

- To assess the best possibilities of introducing into practice the modern nuclear techniques for materials research and development in developing countries.

- To evaluate access to a wide variety of equipment on an international scale; exposure of material scientists in the developing countries to hands-on use of highly sophisticated equipment and apprecation of new technologies.

- To evaluate the need for a Co-ordinated Research Project (CRP) on "Characterization of Ceramics and Semi-conductors using Nuclear Techniques". Subsequently, a CRP on this subject was established in which 19 investigators from 19 Member States participated.

The first Research Co-ordination Meeting (RCM) of the CRP held in Sacavém (Portugal) in March 1994, had the following goals:

- Application of nuclear techniques in the investigation of inclusions-pores, point defects-clusters, neutron-induced defects and impurities and defects in semiconductors.

- Development of methods and instrumentation; and

- Strengthening of the cooperation among the participating scientists.

At the second RCM of the CRP held in Leuven (Belgium) in October 1995, the main achievements, obtained during the realization of this program, were reviewed. Also, at this meeting Mössbauer spectroscopic investigations of ferrite ceramics, asbestos, iron oxide precipitates and the effects of ball-milling of various materials were presented.

Main achievements of the CRP

- Mössbauer spectroscopy has contributed to research in physics, chemistry, metallurgy, mineralogy and biochemistry. This spectroscopy is an excellent tool for studying the chemical composition, phase transitions and magnetic properties of ferrites. These applications of Mössbauer spectroscopy are not only important from an academic standpoint but are also of great importance for researchers and engineers involved in the chemical production of ferrite ceramics. The Mössbauer spectroscopy was applied in the investigation of Fe-bearing oxide phases which form during the preparation of ferrite ceramics. Special attention was paid to the early stages of the ferritization of rare earth's. These investigations were also a contribution to the search for low temperature precursors which may significantly decrease the temperature of the synthesis of ferrite ceramics and films. Ni^{2+}, Nd^{3+}, Sm^{3+}, Gd^{3+}, Eu^{3+} and Er^{3+} were used as model cations in the investigations of the formation of ferrite ceramics and their characterization by Mössbauer spectroscopy. Stoichiometric $NiFe_2O_4$ was obtained by the thermal decomposition of mixed nitrates of Ni^{2+} and Fe^{3+} of the molar ratio $NiO:Fe_2O_3$ = 1:1. The nature of Fe-bearing oxide phases present at low temperatures was investigated by Mössbauer spectroscopy. Nickel ferrite powder was subjected to ball-milling. On the basis of Mössbauer spectra, it was concluded that the ball-milling of $NiFe_2O_4$ has a greater influence on the degree of inversion than on the other structural properties of this spinel. Mössbauer spectroscopy, FT-IR and visible and near infrared diffuse reflectance spectra provide conclusive evidence that the ferritization of Ni^{2+} ions in the mixed hydroxide suspensions is possible even at 25°C. The formation of Fe-bearing oxide phases, formed in the systems Nd_2O_3-Fe_2O_3, Sm_2O_3-Fe_2O_3 and Gd_2O_3-Fe_2O_3 was monitored by Mössbauer spectroscopy. The presence of an amorphous fraction in the samples $(1-x)Fe_2O_3 + xEu_2O_3$, $0<x<1$, prepared by chemical coprecipitation, was detected by XRD even at the relatively high temperature of the sample preparation (600°C). Similar results were obtained for analogous samples in the system Er_2O_3-Fe_2O_3, where the samples heated up to 650°C were amorphous for XRD. Mössbauer spectroscopic investigations proved that these amorphous fractions actually contained very small and/or poor crystalline Fe-bearing oxide particles.

- Asbestos, one of the oldest minerals used by humans, is today banned for many applications due to its toxicity. In this document, the origin of the toxicity of some types of asbestos after they are inhaled by humans is discussed. A method for the drastic reduction

of the toxicity of asbestos, based on the microwave irradiation of asbestos, is proposed. The modifications in the bulk material included a change, $Fe^{2+} \rightarrow Fe^{3+}$, principally at the M1 site. The oxidation of Fe^{2+} was manifested by a reduced probability for the fibers to be airborne and the second in a reduction of the peroxidation ability.

- Mössbauer spectroscopy was used to investigate the reduction of magnetite by Al and Mg during mechanical alloying. Fe-bearing oxide phases, formed during the preparation of precipitated iron based catalysts, were also characterized by Mössbauer spectroscopy. The nature and yield of these oxide phases were strongly dependent on the precipitation chemistry.

- For many years, it has been known that some compounds (natural and synthetic) markedly change their chemical, physical and structural properties during mechanical treatment (*ball-milling*). *With time, this area of investigation became a separate discipline in* chemistry, often referred to as mechanochemistry. Ball-milling of various minerals is a common step in their utilization, and for this reason it is important to know the changes occurring in the mineral during this process. The effects of the ball-milling of chalcopyrite were monitored using Mössbauer spectroscopy and XRD. Tests were performed with chalcopyrite mixed with iron and zinc, with and without surfactant. The effects of surfactants were manifested in eliminating the oxidation and clustering of the fine particles. The antiferromagnetic chalcopyrite is partially converted from an ordered structure with Cu-plane and Fe-planes into a disordered structure. In the thus obtained disordered structure, iron and copper are mixed between two sites in a more random way. Chalcopyrite was decomposed with the loss of iron after its ball-milling in air, while the ball-milling in the presence of surfactant caused iron to enter the chalcopyrite structure.

- In the last decade, there have been significant efforts to understand the nature of high-temperature superconductivity. Very different approaches by researchers were undertaken in the investigations of high-temperature superconductors. In the frame of this program, superconducting $GdBa_2Cu_3O_{7-d}$ ceramics containing ^{155}Gd (s=61000 b) or ^{160}Gd (s = 0.77 b) were irradiated with thermal neutron fluxes up to $4.77 \cdot 10^{20}$ m^{-2}. High-temperature of the samples was not changed after all, the irradiation steps; however, at low temperatures and small fields, the critical current density. The critical current density J_c was slightly enhanced in the ^{155}Gd-123 sample, whereas J_c remained unchanged in ^{160}Gd-123 at all temperatures. This confirmed that the contribution of point defects to flux pinning in high temperature superconductors is rather moderate. Various compounds (Tl-2223, Tl-1223, Tl-2212) as well as material forms (single crystals, thin films, ceramics, tapes) of Tl-based high temperature superconductors were investigated following fast neutrons irradiation. With regard to textured materials, such as Bi-2223 tapes or Nd-123 bulk superconductors, the successful defect modification by neutron-induced collision cascades demonstrated the high potential of this method for the optimization of material properties. Neutron scattering experiments with $YBa_2Cu_3O_{7-d}$ single crystals provided fundamental information on the pairing mechanism in high-temperature superconductors.

- A new experiment with a high-temperature superconductor was also created. The Mössbauer source $^{57}Co/Cr$ was in mechanical contact with $YBa_2Cu_3O_{7-d}$ superconductive powders (T_c=92 K, particle size ~30 mm) under the pressure of $2 \cdot 10^9$ Nm^{-2}. Preliminary results showed possible influence of Mössbauer radiation on super conductor current. However, in order to obtain viable results, further investigations are needed under better defined experimental conditions.

- Various materials, such as $BaLiF_3$, $BaTiO_3$ and high-temperature superconductors, were characterized using neutron diffraction. Neutron diffraction was also used to study the structure of nanometer SiC ceramics. The grain size of SiC ultrafine powder was ~45 nm, while the crystallite size was 5-7 nm as determined by high resolution electronic microscope, 8.0 nm by neutron diffraction and 6.3 nm by XRD. After pressing this material at high temperature, both the grain size and crystallite size of SiC powder increased. The advantages of neutron diffraction in the investigation of nanosize SiC ceramics in relation to the XRD are elaborated. Microporosity is one of the important properties of SiC ceramics. For this reason, SiC powders were mixed with Al_2O_3, B_4C or C additive and hot-pressed. The size and distribution of the pores in these ceramic materials were determined using SANS (small angle neutron scattering). Positron annihilation spectroscopy has been also used to obtain information about the small pore structure of the system $x TiO_2(1-x)SiO_2$, $x = 0.1$ and 0.3. The SANS technique was used to investigate the oxide systems $x TiO_2$-$(1-x)SiO_2$ and $x ZrO_2$-$(1-x)SiO_2$ with $x < 0.1$. The samples were synthesized by the sol-gel method from the corresponding metal alkoxides. For both systems at the gel point, cylindrical clusters or extended linear polymer chains about 10 nm long were found. With prolonged aging, they grow and exhibit mass fractal behavior. The xerogels heated at 120°C showed homogeneous oxide regions with a diameter of about 10-16 nm and pores with an average diameter of 3-4 nm.

- SnO_x films with a thickness of 1 mm were deposited on tin plates of a diameter of 20 mm using d.c. reactive magnetron sputtering in argon-oxygen atmosphere at different oxygen partial pressures. The results showed that the mechanical strength of the films obtained at negative substrate bias was higher, the adhesion of films to substrate was also higher, while the concentration of vacancy defect was smaller than in SnO_x films prepared without substrate bias.

- Elpasolites, of the general stoichiometric structural form Cs_2NaLnX_6 and nonstoichiometric $CsNaLn_{1-x}Ln_xX_6$, where $0.01<x<0.10$, Ln and Ln' are trivalent positive lanthanide ions, and X is chlorine or bromine, are of technological interest due to their luminiscence properties. These compounds were investigated using various techniques with special focus on a neutron diffuse scattering experiment. For this purpose, a new differential acquisition system was built for a neutron diffuse scattering instrument.

- The applications of Mössbauer spectroscopy (MS), deep level transient spectroscopy (DLTS), electron paramagnetic resonance (EPR) and Photoluminiscence (PL) in the investigations of the nature of transition metal dopants in silicon were critically considered.

The following are further results obtained in the framework of the CRP:

Structure

- The nanostructure of SiC has been determined by neutron diffraction. Rietveld refinement for multiphase analysis has been successfully applied.
- The flux line lattice of YBCO single crystal was investigated. The results are discussed in terms of BCS theory.
- A new modified model has been developed for the calculation of vibronic spectra and phonon dispersion relations of the antifluorite structure, e.g. elpasolites.

- Feasibility has been demonstrated for the mechanochemical extraction of noble refractory metals from chalcopyrite ores.
- A new method for the significant reduction of the toxicity of asbestos (crocidolite) has been proven in vitro.
- Chromite minerals have been found to be a mixture of two phases.
- The processing conditions to obtain stoichiometric nickel ferrite and garnets, as single phase, has been developed.

Neutron-induced defects

- Critical current densities J_c are substantially enhanced in Tl-1223 single crystals and in Bi-2223 tapes by fast neutron irradiation
- Fast neutron defects in $YBaCu_3O_{7-d}$ are found to be stable at up to 400°C and over extended periods of time.
- Results of dc susceptibility on irradiated $GdBa_2Cu_3O_{7-d}$ (155, 157, 160 and natural Gd) ceramics were interpreted in terms of structural changes and the Curie-Weiss law.
- An indication of the possible enhancement of critical current densities J_c by point defects in $^{155}GdBa_2Cu_3O_{7-d}$ is found at a pure thermal neutron flux of $4.77 \cdot 10^{20}$ m^{-2}.

Point defects, clusters and multilayers

- Indications of vacancy clusters were found in the Bi-O planes of BiSCCO 2212 single crystals.
- The existence of two types of vacancy defects was found in SnO_x thin films obtained by magnetron sputtering.
- The concentration of defects was lower in SnO_x thin films obtained by magnetron sputtering when the substrate bias was negative.

Impurities and defects in semiconductors

- Co-doped n-type Si shows resonance under special conditions, due to large clusters and not pairs as previously assumed.
- After the ion implantation of radioactive ^{59}Fe, a ^{59}Co-related Deep Level Transient Spectroscopy (DLTS) line was discovered but still not interpreted.
- Photoluminescence experiments on Si samples doped with radioactive phosphorous showed that the daughter element (S) was not photoluminiscent. This indicated an erroneous assignment of S-related PL-lines in the literature.

Development of methods and instruments

- Multiple diffraction analysis: Isomorphic mirrors and anamorphic mirrors in multiple diffraction spectra are shown. A simulation program (MULTI) for multiple diffraction has been developed.
- Neutron diffractometer: Better mathematical description of pulse shapes is achieved. A specific multichannel-router analyzer has been built. A new mathematical foundation for $dd/d\Omega$ extraction from neutron diffraction spectra has been developed.
- Current carriers in HTCS by Mössbauer spectroscopy: A positive effect has been observed in a sample in a close contact with the HTCS, but the zero-velocity test has yet to be repeated.

Inclusions - pores

- Fine porosity: Positron Annihilation Spectroscopy (PAS) and Small Angle Neutron Scattering (SANS) have shown two distinct size distributions, of the mean radii of ~ 0.5

nm and 2 nm, respectively. Doppler broadening of the annihilation g-line give identical defect structures for samples prepared with different H_2O/alkoxide and ethanol/alkoxide molar ratios; a different defect structure is observed for samples with different TiO_2 content and different heat treatment. The nano-structure of $xZrO_2$-$(1-x)SiO_2$, prepared under acidic conditions, was investigated. A correlation between the process parameters and the network structure was found. Average value of pore radius distribution and dispersion for three samples of SiC were obtained. Smaller pore size is probably the reason why the density of hot-pressed SiC is higher than that of not hot-pressed Sic ceramics.

- Iron oxides/hydroxides for Fischer-Tropsch catalysts: A maximum number of small particles at a pH = 7.2 in high concentration is found. Hematite in small particles, containing sodium as an impurity, is found. Ferryhydrite is the major component of nanosized particles.
- Heavy fermion behavior: The data show that the PAL-spectrum depends on four parameters, for which a model was developed: a quantitative analysis in terms of concentration, valence and short range ordering was presented.
- Rare gas inclusions in metals: Three sites are detected: in the matrix, at the interface gas/matrix and within the gas bubble. Their characteristic Mössbauer temperature is derived leading to absolute site populations. Two size classes are discussed: (I) small inclusions (100-1000 atoms) with large θ_M-value, (II) larger soft inclusions with a θ_M -value close to the normal solid rare gas value.

Recommendations

The CRP has opened a new area for further research in this field. The following areas are considered as deserving further research:

Structure

- Neutron diffraction should be extended to nanocomposites SiC-Si_3N_4 and Bi-Sr-Ca-Cu-O powders. The exact phase compositions, and the relative abundance should be determined, in order to optimize the properties of the end product.
- Neutron diffraction on large Y-Ba-Cu-O single crystals should be continued to clarify flux lattice melting, irreversibility lines and the pairing mechanism.
- A study aiming at increasing the mean crystallite size in Pb-doped Bi-Sr-Ca-Cu-O should be performed, in order to allow the application of neutron diffraction and in this way to obtain better quality control during the preparation process.
- Neutron scattering measurements should be done on cubic elpasolites to study the lattice dynamics and to verify the novel model predictions for a better understanding of the factors that influence the efficiency of luminescence in the family of Cs_2NaLnX_6 materials (Ln = lanthanide, X = Br, Cl).
- Research on the amorphous precursors of rare earth iron garnets and the early stages of the ferritization of divalent-transition metals using Mössbauer spectroscopy is recommended.

Neutron-induced defects

- It can be recommended to neutron irradiate Gd-123 ceramics to higher fluxes, in order to arrive at a fundamental understanding of flux pinning by point defects in high-temperature superconductors.
- Gd Mössbauer studies are recommended on Gd-123 ceramics in order to clarify the position of the Gd atom after recoil.

- In view of the results on critical current densities and their enhancements, it is recommended to possibly apply other particle beams providing, e.g., fission tracks (higher energy protons), which have a high potential for the performance improvement of high-temperature superconductors for possible industrial applications.

Point defects, clusters and multylayers

- The application of positron annihilation spectroscopy to investigate defects associated with cation disorder in YBCO (superconductor) single crystal can be recommended.
- It can also be recommended to use channeling experiments to determine the type of position (substation, interstitial, dimmer) of Fe implanted in bcc crystals of Mo and Ta, in order to better understand the nature of the implanted interface.

Impurities and defects in semiconductors

- Further development of neutron diffraction methodology, can be recommended. More attention should be focussed on the neutron diffraction of the samples which are well characterized by complementary techniques.
- The measurement of current carriers in high temperature super conductors by Mössbauer spectroscopy is an interesting idea; however, the experiments must be performed in a much better defined experimental arrangement.

Inclusions-pores

- SANS and PAS instruments for investigation of the porosity of fine powders of ZrO_2-SiO_2 and TiO_2-SiO_2 should be extended to other mixed oxide systems to prove the correlation between the microporosity and processing parameters of the sol-gel synthesis. The applications of SANS and PAS in the investigation of the microporosity of iron oxide catalysts is recommended. Continuation of the experiments on the krypton probe in krypton bubbles is also suggested.

MÖSSBAUER SPECTROSCOPIC CHARACTERIZATION OF FERRITE CERAMICS

S. MUSIĆ, M. RISTIĆ
Rudjer Bošković Institute,
Zagreb, Croatia

Abstract

The principle of Mössbauer effect and the nature of hyperfine interactions were presented. The discovery of the Mössbauer effect was the basis of a new spectroscopic technique, called *Mössbauer spectroscopy*, which has already made important contribution to research in physics, chemistry, metallurgy, mineralogy and biochemistry. In the present work the selected ferrites such as spinel ferrite, $NiFe_2O_4$, and some rare earth orthoferrites and garnets were investigated using Mössbauer spectroscopy. X-ray powder diffraction and Fourier transform infrared spectroscopy were used as complementary techniques. The formation of $NiFe_2O_4$ was monitored during the thermal decomposition of mixed salt $(Ni(NO_3)_2+2Fe(NO_3)_3)nH_2O$. The ferritization of Ni^{2+} ions was observed at 500 °C and after heating at 1300 °C the stoichiometric $NiFe_2O_4$ was produced. The Mössbauer parameters obtained for $NiFe_2O_4$, d_{Fe} = 0.36 mm s^{-1} and HMF = 528 kOe, can be ascribed to Fe^{3+} ions in the octahedral sublattice, while parameters d_{Fe} = 0.28 mm s^{-1} and HMF = 494 kOe can be ascribed to Fe^{3+} ions in the tetrahedral lattice. The effect of ball-milling of $NiFe_2O_4$ was monitored. The formation of oxide phases and their properties in the systems Nd_2O_3-Fe_2O_3, Sm_2O_3-Fe_2O_3, Gd_2O_3-Fe_2O_3, Eu_2O_3-Fe_2O_3 and Er_2O_3-Fe_2O_3 were also investigated. Kvantitative distributions of oxide phases, a-Fe_2O_3, R_2O_3, $R_3Fe_5O_{12}$ and $RFeO_3$, R = Gd or Eu, were determined for the systems $xGd_2O_3+(1-x)Fe_2O_3$ and $xEu_2O_3+(1-x)Fe_2O_3$. The samples, prepared by chemical coprecipitation in the system $xEu_2O_3+(1-x)$ Fe_2O_3, $0 \le x \le 1$, were completely amorphous as observed by XRD, even at the relatively high temperature of the sample preparation (600 °C). Similar behavior was observed during the formation of $Er_3Fe_5O_{12}$. Mössbauer spectroscopy inicated that this "amorphous" phase is actually composed of very small and/or poor crystalline Fe-bearing oxide particles. The nature of these particles was discussed. These results can be of importance for the technology of iron garnet films.

1. Mössbauer spectroscopy

1. 1. The Mössbauer effect

The emission of light from excited atoms and the resonant absorption of the emitted light by the atoms of the same element is a well known process. It might be expected that the same phenomenon should occur for nuclear γ-rays. However, this is generaly not so because in the case of nuclear γ-resonance, the recoil energy and the line-width become very important factors. The recoil energy, **R**, is described by the expression:

$$R = \frac{E^2}{2Mc^2} \qquad (1)$$

where **E** is the photon energy, **M** is the mass of the emitting atom and c is the velocity of light. The energy, **R,** may be about 10^{-11} eV for an optical photon, but for a γ-ray it is about 10^{-1} eV. The width of the resonance is given by the reciprocal of the lifetime of the excited state and may be about 10^{-8} for an optical photon, and about the same or somewhat broader for γ-rays. Thus, in the case of the resonant absorption of light, the recoil energy can be neglected, whereas in the other case, it is large enough to destroy the resonance condition completely.

Rudolf Mössbauer recognized the problems of the degradation of γ-rays energies by nuclear recoil and the thermal energy constraints. The essence of his solution of the problem of nuclear γ-resonance was to eliminate these destructive factors by incorporation of the emitting and absorbing nuclei in a solid lattice for which the lowest (vibrational) excitation energy is greater than the nuclear recoil energy. Under these circumstances, Mössbauer was able to show that a fraction of the γ-rays, **f** , which are emitted, is exempt from the effects of recoil energy and Doppler broadening, and therefore, the fraction, **f** , could be resonantly absorbed by other identical nuclide. The fraction of γ-ray, **f**, usually called the Lamb-Mössbauer fraction, is given by expression:

$$\mathbf{f} = \exp(-k^2\langle x^2\rangle) \qquad (2)$$

where $k=2\pi/l$, l is the wavelength of the γ-ray and $\langle x^2\rangle$ is the mean square displacement of the atom. In 1957, Rudolf Mössbauer discovered the recoil-free absorption of the 129-keV γ-ray by ^{191}Ir in iridium metal [1]. The γ-ray source was ^{191}Os. The transmission of the γ-ray decreased unexpectedly as the temperature was lowered from 370 to 90 K. For this discovery, Rudolf Mössbauer received the Nobel Prize for Physics in 1961. After the discovery of the Mössbauer effect, many other nuclides, ^{57}Fe among them, were found to show the resonant absorption of γ-ray.

The discovery of the Mössbauer effect was the basis of the development of a new spectroscopic technique called *Mössbauer spectroscopy*. In the literature, the alternative name *nuclear gamma resonance* (NGR) *spectroscopy* can also be found. Mössbauer spectroscopy has already made important contributions to research in physics, chemistry, metallurgy, minerology and biochemistry. In this section, only the fundamentals of Mössbauer spectroscopy, which are important for the reader of this publication, will be discussed.

1. 2. Measurement of the Mössbauer effect

In principle, to arrange a Mössbauer experiment the following basic components are needed: a source of γ-ray, an absorber of γ-ray, a driving mechanism to produce a slight change in the γ-ray energy and a detector with a multichannel analyzer.

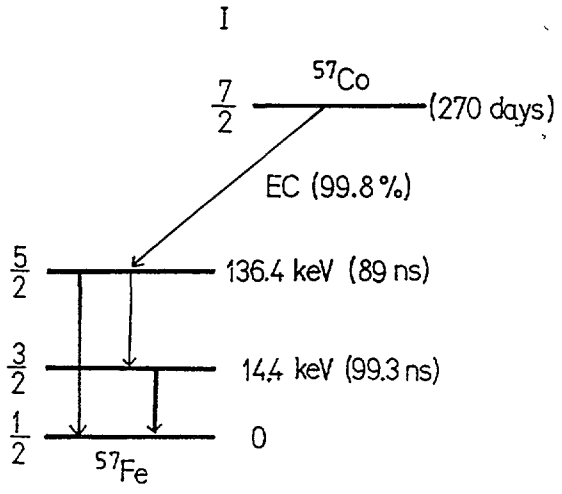

FIG. 1. Decay scheme of ^{57}Co.

Although many nuclides can be used to obtain the Mössbauer effect, to date, the most popular nuclide is ^{57}Fe. It is fortunate that iron, containing ^{57}Fe in its natural nuclidic composition, is an element of great scientific and technological importance. The standard source for the observation of the ^{57}Fe Mössbauer effect is ^{57}Co, which decays by electron capture into the 136.4 keV level of ^{57}Fe. After 89 ns, this level emits a γ-ray of 122 keV. The 14.4 keV level of ^{57}Fe decays after 99.3 ns to the ground state. This transition is generally used to observe the Mössbauer effect in ^{57}Fe. The decay sheme of ^{57}Co is shown in Figure 1. The radionuclide ^{57}Co is formed by the proton irradiation of ^{58}Ni. The irradiated material is refined by ion-exchange procedures to the high standard of chemical purity essential for Mössbauer applications.

Several metals, such as Cr, Cu, Pd, Pt and Rh, are suitable matrices for ^{57}Co because they fulfill the basic requirements regarding the structure, magnetic properties and recoil-free fraction. Other cubic metals do not offer an advantage as matrices or are unsuitable for practical reasons. Stainless steel, popular in early ^{57}Fe Mössbauer works, is no longer applied because self-resonance together with an unresolved isomer shift and quadrupole splittings cause substantial line-broadening. Rhodium possesses the most favorable combination of properties, and is regarded as the best all-round matrix. After ^{57}Fe, ^{119}Sn ranks the second in Mössbauer studies.

As absorbers, synthetic compounds or natural samples containing Mössbauer active nuclides, can be used. In many cases, it is important to perform the measurements at very low temperatures. The Mössbauer source and/or absorber can be cooled using different types of cryostats. The Mössbauer effect can also be studied at high temperatures using a specially designed furnace.

An essential part of the Mössbauer spectrometer is a driving unit capable of producing slight energy changes of the γ-ray generated in recoil-free emission. This slight energy change in the γ-ray is produced by importing a velocity, v, to the source or absorber, and due to the Doppler effect the corrected energy E is given by the expression:

$$E = E_{\gamma} \left(1 \pm \frac{v}{c}\right) \qquad (3)$$

where c denotes the velocity of light. In this way, the extra velocity will either reduce or increase the γ-ray energy just enough to match the energy of the level exactly and allow resonant absorption to take place. For practical reasons the function of the velocity is better to use than the function of the energy.

Different types of detectors can be used in measurements of the Mössbauer effect: scintillation detectors, proportional counters, and Li-drifted Ge and Si detectors. The γ-ray detector selected depends on the type of Mössbauer experiment. Efficiency, resolution and the other properties of the detectors must be considered separately for different Mössbauer sources.

The usual way of monitoring the Mössbauer effect is to display it as a spectrum on a multichannel analyzer used in the multiscaling mode, whereby the number of counts per channel in a fixed time of a few microseconds is shown on a selected number of channels, usually 512 or 1024 chanels. The channel "start" and "advance" signals are synchronized with a signal generator that also drives the Doppler source motion to and from the absorber.

1. 3. Hyperfine interactions

Nuclear γ-resonance is highly sensitive to the variations in the energy of the γ-quanta as a consequence of their extreme resolution ($\Gamma/E_\gamma \sim 10^{-13}$). This is the basis for the measurement of very small energy shifts and the splittings of nuclear levels caused by hyperfine interactions, i. e., interactions of the atomic nucleus with electric and magnetic fields. The three main hyperfine interactions usually measured by Mössbauer spectroscopy are: the isomer shift, electric quadrupole interaction and magnetic dipole interaction. The numerical values of these interactions and their temperature dependence can yield a large amount of information, which is of importance in studies of the lattice, electronic and magnetic properties of the matter in solid state. Additional information can be deduced from line-width data, the sign of the quadrupole interaction and the influence of the relaxation times on the hyperfine parameters.

1. 3. 1. *Isomer shift*

If the Mössbauer nuclei of the both source and absorber are in an identical environment, the minimum of the single Mössbauer line is centered at about zero velocity. The position of the centroid of a Mössbauer spectrum is a function of the difference in the electronic densities at the nucleus in the source and absorber. Any chemical change that influences the electron density at the nucleus of either the source or the absorber will shift the position of the centroid of the spectrum. This shift is usually called the isomer shift (or chemical shift) and is given by expression:

$$\delta = \frac{2}{5\pi Ze^2}\left\{\left|\psi_a(o)\right|^2 - \left|\psi_s(o)\right|^2\right\}\left(R_e^2 - R_g^2\right) \qquad (4)$$

where Z is the atomic number, e is the unit charge, R_e is the radius of the nucleus in the excited state, R_g is the radius in the ground state, and $|\psi(o)|^2$ is the wave function of the electron charge at the nucleus of the absorber and source, respectively. The isomeric term, $\left(R_e^2 - R_g^2\right)$, is a physical property characteristic of each Mössbauer nuclide. On the other hand, the term $\left\{\left|\psi_a(o)\right|^2 - \left|\psi_s(o)\right|^2\right\}$ is of particular interest in the chemical applications of the Mössbauer effect. The *s*-electrons primarily contribute to the electronic charge density at the nucleus. The *p*- and *d*-electrons with little or no charge density at the nucleus contribute indirectly through screening effects on the *s*-electrons. For example, the spectrum of the Fe^{3+} ion is shifted in a positive direction relative to the metallic iron because of a decrease in the electronic charge density at its nucleus following the loss of the 4*s*-electrons. The spectrum of the Fe^{2+} ions is shifted to even higher positive velocities because of of the screening effect of the additional 3*d*-electron on the 3*s*-electrons which increases their radial distribution and further decreases the electron charge density at the nucleus. The magnitude of these effects may vary over wide ranges depending on covalency effects and high- or low-spin states. There are also instances when the isomer shift of low-spin ferrous ions is in the same range as high-spin ferric ions. Since the isomer shift reflects the difference in the electronic charge density at the nucleus of the source compared to the absorber, it is necessary to report shifts relative to a standard reference material; usually, this is α-Fe.

1. 3. 2. *Quadrupole splitting*

Quadrupole splitting is induced by the electrostatic interaction between the electric field gradient (EFG) at the nucleus and the nuclear quadrupole moment (Q). The degeneracy of the nuclear states is partially lifted in the EFG for a nuclear spin I>1/2. For a nuclear level with a spin of I=3/2, which is frequently exploited in Mössbauer spectroscopy, the eigenvalues are given by the expression:

$$E_Q = \frac{e^2qQ}{4I(2I-1)}\left[3m_I^2 - I(I+1)\right]\left(1+\frac{\eta^2}{3}\right)^{1/2} \qquad (5)$$

where q represents the principal component of the EFG and η the asymmetry parameter. γ-transitions occur between the substates of the excited and ground levels. The resultant spectrum is known as a quadrupole doublet. Generally, the contribution of the electric field gradient at the Mössbauer absorber arises from an asymmetric distribution of the surrounding atoms or ligands. The intensities, angular variation and temperature dependence of the quadrupole interaction yield valuable information about the electronic and crystallographic structure, and particularly about the structural symmetry of various chemical compounds.

1. 3. 3. *Magnetic splitting*

Magnetic splitting arises from the interaction of the nuclear magnetic dipole moment with a magnetic field, H, created by the atom's own electrons. The energy for each of the magnetic sublevels is given by the expression:

$$E = -mHm_I/I \qquad (6)$$

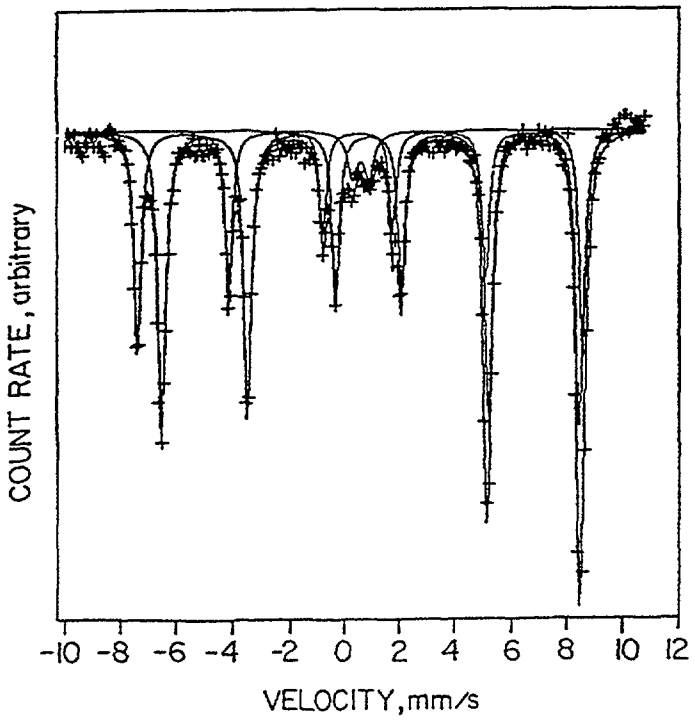

FIG. 2. ^{57}Fe Mössbauer spectrum (RT) of a cervice corrosion product from an isothermal (288 ^{o}C) capsule (Inconel 600).

TABLE I. ^{57}Fe MÖSSBAUER PARAMETERS CALCULATED FOR THE SPECTRUM SHOWN IN FIG. 2.

Lines	δ* (mm s^{-1})	Δ or ΔE_q (mm s^{-1})	H** (kOe)	Γ (mm s^{-1})	Sextet Area (mm s^{-1})	A (%)	Identification
Q_1	0.375	0.589		0.929	0.064	4.81	FeOOH
M_1	0.339	0.119	491	0.295	0.472	34.42	Fe_3O_4
M_2	0.724	0.105	461	0.315	0.795	59.77	Fe_3O_4

*,**Errors:±0.005 mm s^{-1} and ±1 kOe

where m is the nuclear magnetic dipole moment, H is the magnetic field, m_I is the nuclear magnetic quantum number and I is the nuclear spin quantum number. The energy transitions are governed by the selection rule, $\Delta m_I = 0, \pm 1$. Since ^{57}Fe has a ground state of I =1/2 $m_I = \pm 1/2$ and the first excited state of I = 3/2, $m_I = \pm 1/2, \pm 3/2$, the magnetic field will generate six transitions at this nuclide. In this case, a six-line Mössbauer spectrum is obtained. For a thin absorber in which the magnetic moments are randomized, for example in a powder sample, there is ratio of relative peak intensities of approximately 3:2:1:1:2:3. The source of the magnetic field may be either "internal", as in the case of ferromagnetic and antiferromagnetic materials, or it may be an externally applied magnetic field. When the absorber is magnetized perpendicular to the γ-ray direction, the peak intensities ratio is 3:4:1.

In practice, the Mössbauer spectra very often reflect a combination of magnetic and electric quadrupole interactions. The energy levels depend in a complex way on the angles between the principal axes of the EFG tensor and the axes of the magnetic field. Fortunately, symmetry considerations reduce these angles to zero or ninety degrees in a number of important compounds and the expression for the energy levels simplifies. Mössbauer measurements of hyperfine magnetic interactions yield extremly important information about the origin and properties of the magnetism in various materials containing Mössbauer nuclides.

As an illustration for readers, Figure 2 shows the complex Mössbauer spectrum, where different ^{57}Fe contributions to the total Mössbauer effect are present [2]. After the mathematical deconvolution of this spectrum, the values of the ^{57}Fe Mössbauer parameters are obtained (Table I), which serve as the basis for the chemical and physical conclusions. The magnetic splitting components, M_1 and M_2, are ascribed to stoichiometric magnetite, $FeFe_2O_4$, which possesses the structure of spinel ferrite.

2. The ferrites

Ferrites is the general name for a group of mixed metal oxides containing iron ions, which are characterized by specific electric and magnetic properties. They have an appreciably higher (by six orders of magnitude) electric resistance and a lower saturation magnetization than those of silicon steels and permalloys. This reduces eddy-current losses and makes the ferrites sutable for making cores (toroids) which have application in the production of AF and HF transformers, as well as chokes. Ferrites have also found applications as magnetic recording media, wave-guides in microwave techniques, and in magneto-optical

devices. Some type of ferrites have found application as permanent magnets. These important applications of ferrites are a consequence of their unique structural, chemical and physical properties.

Ferrites can generally be considered as the reaction products between Fe_2O_3 and other metal oxides. In general [3], their formula is $\left(Me_2^{k+}O_k^{2-}\right)_{m/2}\left(Fe_2^{3+}O_3^{2-}\right)_n$, where Me is a metal cation with valence k and m and n are full numbers. In addition to ferrites containing oxygen anions, there are ferrites in which oxygen anions are replaced by anions of flourine, chlorine, sulphur, selenium or tellurium. On the basis of their structural properties, ferrites can be divided in four subgroups:

-spinel ferrites with the structure of the mineral spinel, $MgAl_2O_4$,

-hexagonal ferrites with the structure of the mineral magnetoplumbite, $PbFe_{7.5}Mn_{3.5}Al_{0.5}Ti_{0.5}O_{19}$,

-orthoferrites with the structure of the mineral perovskite, $CaTiO_3$, and

-garnet-type ferrites with the structure of the mineral grossular, $Ca_3Al_2(SiO_4)_3$.

Mössbauer spectroscopy is an exellent tool for studying the chemical composition, phase transitions and magnetic properties of the ferrites. In this report, we shall present the capabilities of Mössbauer spectroscopy in the characterization of oxide phases formed during the synthesis of different ferrites, as well as in the investigation of the structural and magnetic properties of these materials. These applications of Mössbauer spectroscopy are not only important from an academic standpoint but are also of great importance for researchers and engineers involved in the commercial production of ferrite ceramics. Selected ferrites, such as spinel ferrite, $NiFe_2O_4$, some rare earth orthoferrites and garnets, will be the subject of discussion.

2. 1. Nickel ferrite

Nickel ferrite, $NiFe_2O_4$, is an inverse spinel in which the tetrahedral or A sites are occupied by Fe^{3+} ions, and the octahedral or B sites by Fe^{3+} and Ni^{2+} ions. This compound is described with the formula $(Fe^{3+})_A(Ni^{2+}Fe^{3+})_BO_4$. The magnetic structure of $NiFe_2O_4$ is of the Néel collinear type in which all the spins at the A and B sites are parallel, while the A and B sublattice magnetizations are antiparallel.

Nickel ferrite and substituted nickel ferrites were the subject of many investigations due to their specific magnetic and microwave energy absorption properties. Different methods were used in the synthesis of $NiFe_2O_4$. Many researchers have observed that the chemical and physical properties of $NiFe_2O_4$ are dependent on the conditions of its synthesis.

Linnett and Rahman [4] performed one of the earliest Mössbauer studies with nickel ferrites, $Ni_xFe_{3-x}O_4$, $0<x<1$. The spectra recorded at RT were deconvoluted into two sextets for $x=0$ and $x=1$, corresponding to Fe_3O_4 and $NiFe_2O_4$, respectively. For $x=0.4$, 0.6 and 0.8, the additional sextets were considered in the mathematical deconvolution of the spectra.

Morrish and Haneda [5] investigated the magnetic structure of small $NiFe_2O_4$ particles. Three kinds of $NiFe_2O_4$ particles having particle sizes of 250±50, 800±200 and 1300±200 Å, and crystallite sizes of 250, 400 and 500 Å, respectively, were investigated. ^{57}Fe Mössbauer spectra, recorded with a longitudinal magnetic field, indicated that a non-collinear magnetic structure exists. Further, the magnetic moment at low temperatures was appreciably lower than the value reported for bulk material. A model was proposed in which the $NiFe_2O_4$ particles consist of a core with the usual spin arrangement and

a surface layer with atomic moments inclined to the direction of the net magnetization. The existence of a non-collinear magnetic structure in the surface layers of γ-Fe_2O_3 and CrO_2 was also found [6]. It was concluded that Mössbauer spectroscopy in conjuction with large magnetic fields is a powerful tool in the study of non-collinear magnetic structures of ferromagnetic and ferrimagnetic fine particles. However, this investigative approch was not convenient for antiferromagnets.

Nickel ferrite has been studied by Mössbauer spectroscopy in the temperature range of $134<T<890$ K [7]. Temperature dependences of the center shift, hyperfine magnetic field and longitudinal relaxation rate were determined for the A and B sites of Fe^{3+} ions. Anomalous behavior in the slope of the center shift and the critical slowing down of the spin fluctuation of Fe^{3+} ions were observed. Typical Mössbauer spectra of $NiFe_2O_4$ recorded at different temperatures are shown in Figure 3.

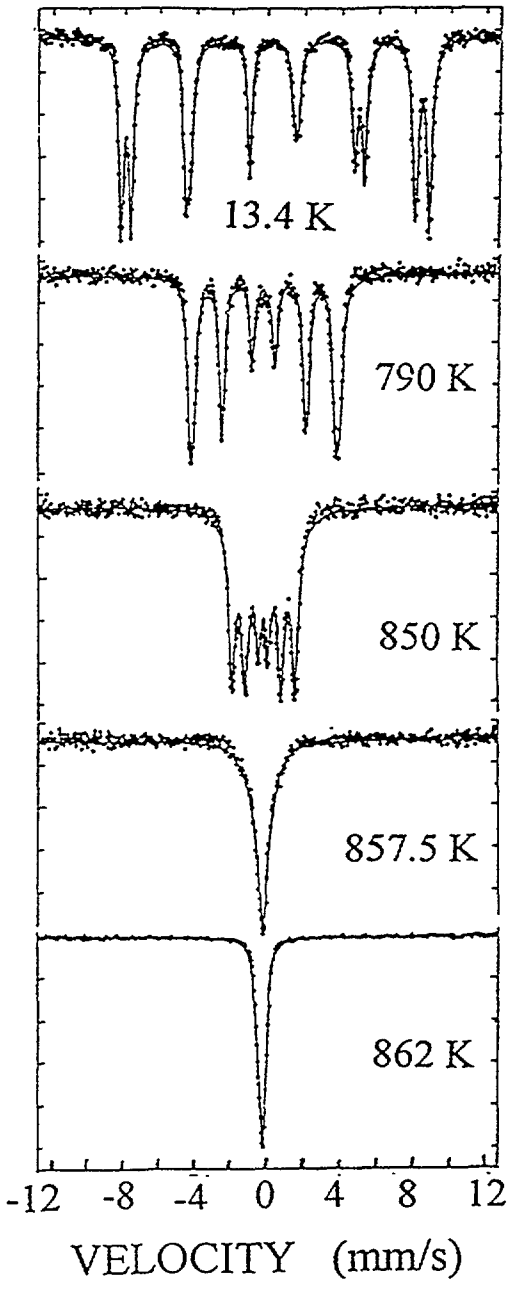

FIG. 3. Typical Mössbauer spectra of $NiFe_2O_4$ at various temperatures. The solid curves are the best two-site fits to the spectra [7].

The reaction of spinel ironsand with NiO in an air inert atmosphere up to 1200 °C was compared with the analogous reactions of synthetic hematite or magnetite with NiO [8]. All three iron oxide phases in reaction with NiO produced $NiFe_2O_4$. Under inert conditions, the reaction products showed larger lattice parameters, thus indicating the presence of Fe^{2+}. Mössbauer spectra suggested that the Fe^{2+} ions in the ferrite spinels were located preferentially at the octahedral sites. Lattice constant calculations suggested that $NiFe_2O_4$ formed in air was not fully inverse, as usually assumed, but contained varying amounts of tetrahedral Ni^{2+}. In the case of ironsand-derived spinels, Ti^{4+} ions were located at the octahedral sites.

For practical reasons, it is very important to understand the early stages of Ni^{2+} ferritization. This is not only of interest for those involved in the commercial production of ferrites but also for corrosion scientists and engineers. Morozumi et al. [9] investigated the hydrothermal synthesis of $NiFe_2O_4$. The formation and growth of nickel ferrite particles were completed within 24 h at temperatures between 100 and 250 °C. Mössbauer spectroscopy gave clear evidence of nickel ferrite formation at all temperatures above 100 °C. Raw [10] applied Mössbauer spectroscopy to study the formation of nickel ferrite as the corrosion product. The principal corrosion product formed in the stainless steel primary cooling circuit of a PWR (Pressurized Water Reactor) is non-stoichiometric nickel

TABLE II. EXPERIMENTAL CONDITIONS FOR THE PREPARATION OF SAMPLES S_2 TO S_9 (HOURS OF HEATING AT GIVEN TEMPERATURES).

	Temperature / °C							
Sample	200	300	400	500	700	900	1100	1300
S_2	1							
S_3	1	1						
S_4	1	1	1					
S_5	1	1	1	1				
S_6	1	1	1	1	1			
S_7	1	1	1	1	1	1		
S_8	1	1	1	1	1	1	1	
S_9	1	1	1	1	1	1	1	1

TABLE III. THE RESULTS OF X-RAY DIFFRACTION PHASE ANALYSIS OF SAMPLES S_1 TO S_9.

Sample	Phase composition	Remarks
S_1	$Ni(NO_3)_2\ 6H_2O + Fe(NO_3)_3\ nH_2O$ (?)	increased broadening
S_2	α-Fe_2O_3 + $Ni(NO_3)_2\ 6H_2O$ + ...	of diffraction lines
S_3	NiO + α-Fe_2O_3	of α -Fe_2O_3 and NiO
S_4	NiO + α-Fe_2O_3	
S_5	NiO + α-Fe_2O_3 + Fe_2O_4	
S_6	$NiFe_2O_4$ + NiO	sharpening of $NiFe_2O_4$
S_7	$NiFe_2O_4$	diffraction lines and no
S_8	$NiFe_2O_4$	shifts of diffraction
S_9	$NiFe_2O_4$	lines

ferrite, $Ni_yFe_{3-y}O_4$, $0.45<y<0.75$. Crud simulants are used extensively in laboratory studies of the properties of reactor corrosion products because the actual products themselves are highly radioactive. Mössbauer spectroscopy has also been applied in studies [11, 12] of the oxidation of the mixed hydroxides $Ni(OH)_2/Fe(OH)_2$ and the thermal decomposition [13] in a vacuum of the mixed hydroxide with the ratios $[Fe^{3+}]/[Fe^{2+}] = 0.22$. and [Ni]/ [Fe] = 0.5. The authors observed the formation of the metallic alloy $Ni_{0.92}Fe_{0.08}$ besides the Ni-substituted magnetite.

The thermal decomposition products of the coprecipitated salts $Fe(NH_4)_2(SO_4)_2 \bullet 6H_2O$ and $Ni(NH_4)_2(SO_4)_2 \bullet 6H_2O$ were analyzed by Mössbauer spectroscopy [14]. The optimum temperature for $NiFe_2O_4$ preparation was 900 °C.

Musić et al. [15] studied the oxide phases generated during the synthesis of $NiFe_2O_4$ using X-ray diffraction, FT-IR and ^{57}Fe Mössbauer spectroscopy. An aqueous solution of $Ni(NO_3)_2/(Fe(NO_3)_3$ of the molar ratio $NiO:Fe_2O_3$ = 1:1 was prepared. The excess water was evaporated using an infrared lamp. The solid residue (sample S_1) was heated at the conditions given in Table II. The results of the X-ray diffraction phase analysis of the prepared samples are given in Table III. The observed phases, α-Fe_2O_3, NiO, $NiFe_2O_4$ and $Ni(NO_3)_2 \bullet 6H_2O$, were identified to the JCPDS-PDF [16] card numbers 13-534, 4-835, 10-325 and 25-577, respectively. Since the lattice constant of $NiFe_2O_4$ is almost twice as large as that of NiO, there are no diffraction lines of NiO independent of the ones of $NiFe_2O_4$. The presence of NiO was proved [17] by comparison of the intensities of the overlapped diffraction lines belonging to both NiO and $NiFe_2O_4$. Besides $Ni(NO_3)_2 \bullet 6H_2O$, sample S_1 contained an additional phase, which may be considered as an iron nitrate hydrate; however, its positive identification by the JCPDS-PDF data was not possible with certainity.

The presence of α-Fe_2O_3 in sample S_1 could not be recognized with certainity on the basis of the FT-IR spectrum because a very strong band at 590 cm^{-1}, with shoulders at 690 and 480 cm^{-1}, was the superposition of several IR bands of different origins. Heating of sample S_1 at 200 °C for one hour caused changes in the corresponding FT-IR spectrum. In the FT-IR spectrum of sample S_2, two new bands at 1532 and 978 cm^{-1} were visible, and also a band at 1324 cm^{-1} instead of the shoulder at 1355 cm^{-1}. This spectrum also showed a separation of bands at 708, 579 and 477 cm^{-1}, and the appearance of a weak band at 389 cm^{-1}. On the basis of the FT-IR spectra of samples, S_1 and S_2 , no conclusion about the presence of α-FeOOH in these samples can be made. Additional heating of sample S_2 at 300 °C for one hour significantly suppressed the relative intensities of the IR bands corresponding to the H_2O molecules and nitrate groups. The FT-IR spectrum of sample S_3 gave more evidence for the presence of α-Fe_2O_3 , but the band at 460 cm^{-1} was an overlap of a band of α-Fe_2O_3 and a band of NiO. The FT-IR spectrum of sample S_4 (additional heating at 400 °C) showed a sharp peak at 1385 cm^{-1} indicating traces of nitrates, while the FT-IR spectrum of sample S_5 (additional heating at 500 °C) indicated that all the nitrates were decomposed. The spectrum of sample S_5 also showed two dominant bands at 589 and 423 cm^{-1} with shoulders at 560 and 454 cm^{-1}. The bands at 584 and 423 cm^{-1} indicated ferritization in sample S_5. The FT-IR spectrum of sample S_6 (additional heating at 700 °C) showed the presence of nickel ferrite on the basis of bands at 600 and 417 cm^{-1}. With further increasing of the heating temperature (900 °C for sample S_7 ; 1100 °C for sample S_8; 1350 °C for sample S_9), the band at 600 cm^{-1} shifted to 604 cm^{-1}, while the band at 417 cm^{-1} shifted to 400 °C. These IR shifts can be ascribed to the crystal lattice ordering and/or to an approach to the full stoichiometry of nickel ferrite.

Figures 4 to 7 and Table IV summarize the results obtained by Mössbauer spectroscopy. The Mössbauer spectra of samples S_1, S_2 and S_3 were interpreted as the superposition of two sextets, M_1 and M_2, while the spectrum of sample S_4 was characterized by one sextet, M_1.

The hyperfine magnetic field, HMF, of sextet M_1 increased from 471 (sample S_1) to 517 kOe (sample S_4), while the HMF of sextet M_2 increased from 439 (sample S_1) to 501 kOe (sample S_3). The HMF value of 517 kOe measured for sample S_4 can be ascribed to α-Fe_2O_3. Samples S_1, S_2 and S_3 showed significantly lower HMF values than sample S4. This can be explained by the presence of poorly crystallized α-Fe_2O_3, probably containing a fraction of Ni^{2+} ions in the α-Fe_2O_3 structure. It is generally known that the substitution of Fe^{3+} ions with certain metal cations can decrease the HMF value of α-Fe_2O_3. An increase in temperature up to 400 ^oC caused the appearance of NiO and ordering in the crystal lattice of α-Fe_2O_3 , reflected in an increase of the HMF value. X-ray diffraction showed a pronounced broadening of the diffraction lines of α-Fe_2O_3 in samples, S_2 and S_3, and to a similar extent, also in sample S_4.

The Mössbauer spectrum of sample S_5 was interpreted as a superposition of the three sextets, due to the presence of nickel ferrite and α-Fe_2O_3 . The spectra recorded for samples S_6 to S_9 were fitted with two sextets corresponding to nickel ferrite. The relative intensities of the spectral lines of the inner sextet, M_2, increased from sample S_6 to sample S_8, and then decreased for sample S_9. The parameters calculated for sample S_9, δ_{Fe} = 0.36 mm s^{-1} and HMF = 528 kOe, can be ascribed to Fe^{3+} cations in the octahedral sublattice, while parameters d_{Fe}=0.28 mm s^{-1} and HMF = 494 kOe can be ascribed to cations in the tetrahedral sublattice. Since the relative intensities of the spectral lines on the inner and outer sextets observed for sample S_9 were almost equal, it could be concluded that sample S_9 contained stoichiometric $NiFe_2O_4$. This conclusion was in agreement with the corresponding X-ray diffraction measurements.

For many years, it has been known that some compounds (synthetic or natural) strongly change their chemical, physical and structural properties during mechanical treatment (for example, by ball-milling). With time, this area of investigation became a separate discipline in chemistry, often reffered to as mechanochemistry. The milling of ferrites into fine powder is important step in their commercial production. For this reason, technologists involved in the production of ferrites are keenly interested in new advanced concerning the mechanochemistry of these materials.

Musić et al. [18] focussed attention was paid to the effect of the ball-milling of $NiFe_2O_4$. The effect of the ball-milling of $NiFe_2O_4$ on its structural properties has been investigated earlier by Pavlyukhin et al. [19]. They published that mechanical treatment had a marked effect on the corresponding Mössbauer spectrum. After ten minutes of ball-milling $NiFe_2O_4$, an intense central doublet was observed at room temperature, while a symmetric central doublet was only present in the room temperature spectrum after 30 minutes. Pavlyukhin et al. [19] concluded that the observed effect is a consequence of the transfer of cations from the tetrahedral to the vacant octahedral sites in the spinel structure. They also suggested that the disordering of the anion and cation sites may lead to an amorphous structure for XRD. In the contrast to the work of Pavlyukhin et al. [19], such a dramatic influence by ball-milling on the properties of $NiFe_2O_4$ was not observed in our work. Table V shows the ^{57}Fe Mössbauer parameters for $NiFe_2O_4$ before and after ball-milling for different times [18]. The room temperature spectra did not show the central quadrupole doublet. However, the calculated Mössbauer parameters indicated a decrease of hyperfine magnetic fields, M_1 from 495 to 485 kOe, and M_2 from 526 to 516 kOe, during a period of ball-milling, up to 27 hours. The parameters of sextet M_1 correspond to the Fe^{3+} cations in the tetrahedral sites, while the parameters of the sextet M_2 correspond to the Fe^{3+} cations in the octahedral sites in $NiFe_2O_4$. The ball-milling of $NiFe_2O_4$ also caused an increase of the spectral line-width and a slight increase of isomer shifts, as shown in Table V.

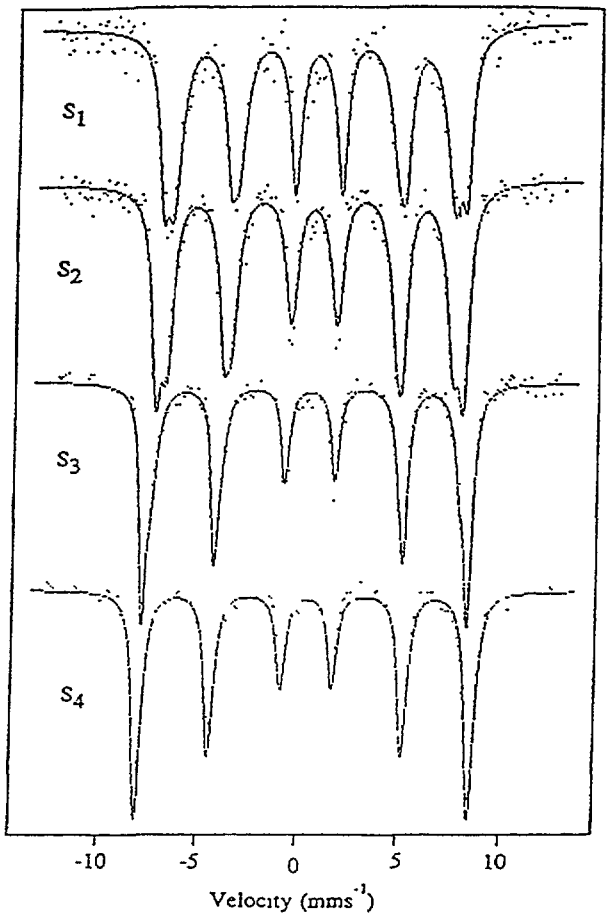

FIG. 4. ^{57}Fe Mössbauer spectra of samples S_1, S_2, S_3 and S_4, recorded at room temperature.

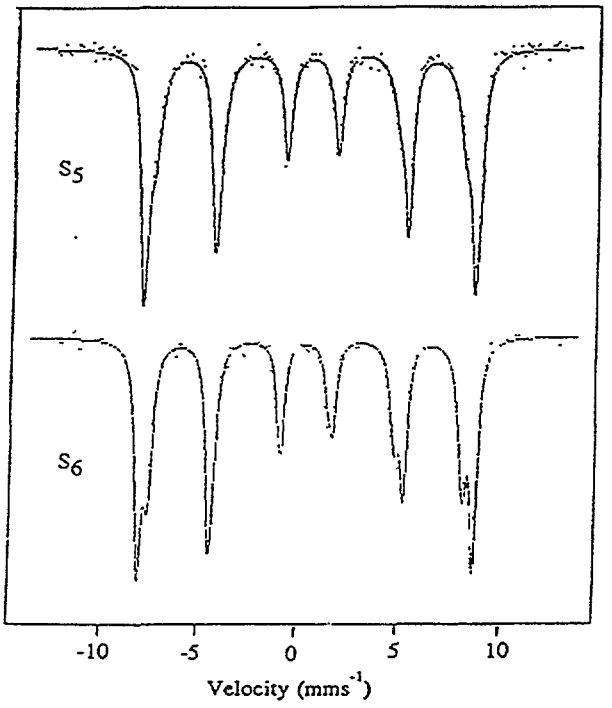

FIG 5 ^{57}Fe Mossbauer spectra of samples S_5 and S_6, recorded at room temperature.

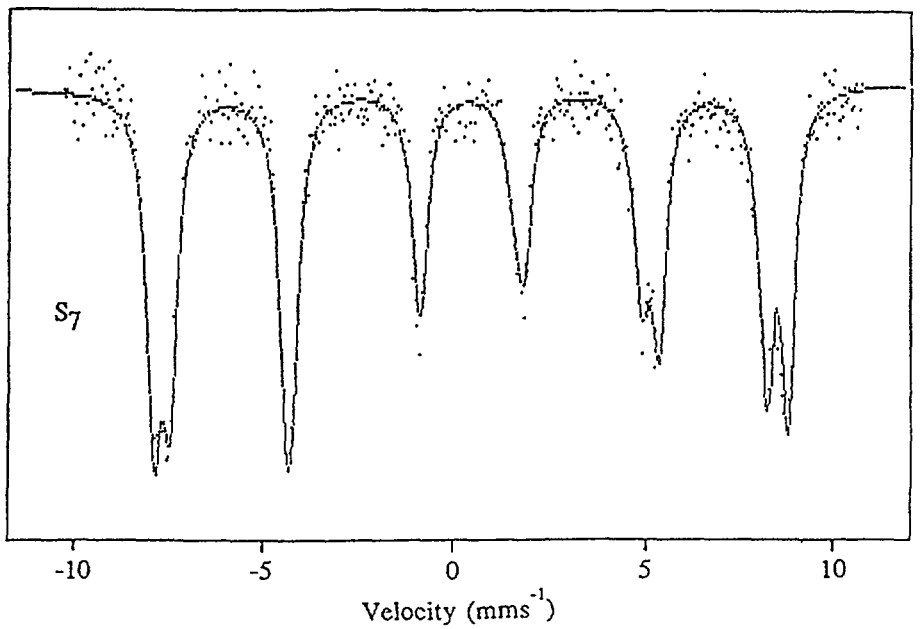

FIG 6 ^{57}Fe Mossbauer spectrum of sample S_7, recorded at room temperature

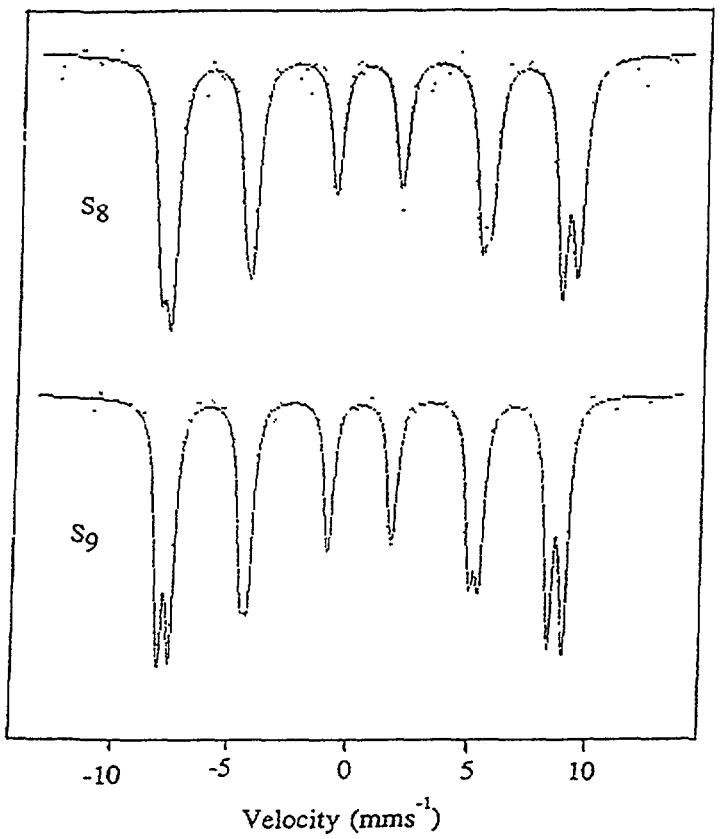

FIG 7 ^{57}Fe Mossbauer spectra of samples S_8 and S_9, recorded at room temperature

TABLE IV. ^{57}Fe MÖSSBAUER PARAMETERS CALCULATED ON THE BASIS OF THE SPECTRA, RECORDED AT ROOM TEMPERATURE.

Sample	Lines	δ*/mm s^{-1}	ΔE_q/mm s^{-1}	HMF/kOe	Γ/mm s^{-1}
S_1	M_1	0.38	-0.21	471	0.45
	M_2	0.37	-0.16	439	0.99
S_2	M_1	0.36	-0.22	478	0.57
	M_2	0.39	-0.16	446	0.75
S_3	M_1	0.38	-0.20	506	0.41
	M_2	0.37	-0.18	501	0.71
S_4	M_1	0.39	-0.14	517	0.54
S_5	M_1	0.37	-0.12	524	0.41
	M_2	0.36	-0.16	513	0.39
	M_3	0.29	-0.01	484	0.83
S_6	M_1	0.36	-0.08	522	0.41
	M_2	0.26	0.01	490	0.55
S_7	M_1	0.36	-0.06	519	0.44
	M_2	0.24	0.01	487	0.50
S_8	M_1	0.35	0.08	535	0.49
	M_2	0.27	0.01	500	0.57
S_9	M_1	0.36	0.04	528	0.42
	M2	0.28	0.01	494	0.47

*Isomer shift is given relative to α-Fe
Errors: $\pm$ 0.01 mm/s and $\pm$ 1 kOe

TABLE V. ^{57}Fe MÖSSBAUER PARAMETERS FOR $NIFe_2O_4$,BEFORE AND AFTER BALL-MILLING FOR VARIOUS LENGTHS OF TIME.

Time of ball-milling (hours)	Spectral component	Isomer shift* δ (mm s^{-1})	Quadrupole splitting ΔE_q (mm s^{-1})	Hyperfine magnetic field H (kOe)	Line width Γ (mm s^{-1})
0	M_1	0.237	-0.002	495	0.480
	M_2	0.352	-0.001	526	0.440
3	M_1	0.240	-0.002	495	0.525
	M_2	0.353	-0.002	526	0.461
6	M_1	0.238	-0.001	495	0.491
	M_2	0.350	-0.001	526	0.437
9	M_1	0.257	0.021	487	0.531
	M_2	0.356	0.010	517	0.449
15	M_1	0.269	0.010	486	0.506
	M_2	0.367	0.002	516	0.463
21	M_1	0.265	0.008	484	0.547
	M_2	0.366	-0.002	515	0.471
27	M_1	0.270	0.011	485	0.529
	M_2	0.368	-0.001	516	0.468

The FT-IR spectra of these samples did not show a significant change in the characteristic FT-IR spectrum of $NiFe_2O_4$ with the time of ball-milling. Small changes in the intensities of the shoulders at 534 and 332 cm^{-1} were visible. On the basis of the Mössbauer and FT-IR measurements in the present work, it cannot be concluded that the formation of an amorphous-like phase is consequence of ball-milling $NiFe_2O_4$ under given experimental conditions. It can be supposed that the ball-milling of $NiFe_2O_4$ has a greater influence on the degree of inversion than on the other structural properties of this spinel. However, we must keep in mind that Ni^{2+} has a high preference for octahedral sites compared to Fe^{2+}. For this reason, further applied field Mössbauer spectroscopic measurements must be performed to obtain a more appropriate conclusion about the effect of ball-milling on the $NiFe_2O_4$ structure. The effect of mechanical grinding on the structural and magnetic properties of $BaFe_{12}O_{19}$ was also monitored by Mössbauer spectroscopy [20]. However, the mechanism of the mechanochemical changes in M-type hexagonal ferrite is different than in the spinel ferrite $NiFe_2O_4$, due to the specific crystal structure of $BaFe_{12}O_{19}$ [20].

2. 2. Rare earth orthoferrites and iron garnets

Rare earth ferrites with perovskite and garnet structures are generally considered to be reaction products between R_2O_3 and Fe_2O_3, R=rare earth. At high temperatures, R_2O_3 and Fe_2O_3 react to produce rare earth orthoferrite in the reaction:

$$R_2O_3 + Fe_2O_3 \rightarrow 2RFeO_3 \qquad (7)$$

In the presence of additional Fe_2O_3, garnet-type ferrites can be also produced at high temperatures:

$$3RFeO_3 + Fe_2O_3 \rightarrow R_3Fe_5O_{12} \qquad (8)$$

Rare earth iron garnets can be prepared using different methods, such as:
-solid state reaction between corresponding oxides,
-thermal decomposition of mixed metal-organic compounds,
-aerosol pyrolysis,
-crystal-growth from the melt,
-film growth on different substrates, for example on GGG (gadolinium gallium garnet),
-"coprecipitation",
-sol-gel etc.

The "coprecipitation" method involves the formation of mixed metal hydroxides, for example $3R(OH)_3 + 5Fe(OH)_3$, and thermal treatment of the mixed hydroxide. The sol-gel method is very useful for the preparation of oxide particles with a narrow size distribution and defined morphology. This method is often used in the preparation of nanosized particles. However, when two or more metal cations are hydrolyzed simultaneously from the corresponding alkoxides, it is difficult to monitor the particle size distribution and morphology because of the different hydrolysis rates of the metal cations. At present, researchers are trying to solve this problem using the microemulsion method. Generally, the chemical methods are more suitable for modifying the chemical and physical properties of rare earth iron garnets than the physical methods. On the other hand, the chemical methods are more sensitive in practice because they depend on many experimental parameters. The physical methods of synthesis need much

higher temperatures than the chemical methods. In the case of the solid state reaction, the sintering effect makes it difficult to control the particle size and morphology of the garnets.

Researchers used very different instrumental techniques to characterize the reaction products which appear during the synthesis of rare earth orthoferrites and iron garnets. Here, we shall report about the application of Mössbauer spectroscopy in the characterization of the Fe-bearing oxide phases formed during the synthesis of the above-mentioned compounds. In this investigation the following oxide systems were selected: Nd_2O_3-Fe_2O_3, Sm_2O_3-Fe_2O_3, Gd_2O_3-Fe_2O_3, Eu_2O_3-Fe_2O_3 and Er_2O_3-Fe_2O_3.

1. 2. 2. 1. The system Nd_2O_3-Fe_2O_3

The chemical and structural properties of the system $(1-x)Fe_2O_3 + xNd_2O_3$, $0<x<1$, were investigated using X-ray diffraction, ^{57}Fe Mössbauer spectroscopy and Fourier transform (FT-IR) spectroscopy [22]. Mixed metal hydroxides, $Fe(OH)_3/Nd(OH)_3$, were coprecipitated from the corresponding nitrate solutions and washed hydroxide coprecipitates were thermally treated at up to 900 ^oC. Tables VI and VII show the initial chemical composition of the samples and the results of the phase composition as determined by XRD.

Table VIII shows the ^{57}Fe Mössbauer parametrs (RT) calculated on the basis of the spectra recorded for the samples $(1-x)Fe_2O_3 + xNd_2O_3$. Hyperfine magnetic splitting is the main characteristic of the ^{57}Fe Mössbauer spectra of samples FN-1 to FN-11. In samples FN-1 to FN-7, X-ray diffraction showed the presence of α-Fe_2O_3 and $NdFeO_3$ which are known to exhibit hyperfine magnetic splitting at room temperature. Therefore, two separable sextets were expected. ^{57}Fe Mössbauer spectra of samples FN-1 to FN-7 showed only the presence of one sextet. However, after the mathematical deconvolution of the spectra, distinct regularities in the changes of the The ^{57}Fe Mössbauer parameters, from sample FN-1 to FN-11, were observed.

The hyperfine magnetic field, HMF = 516 kOe, and quadrupole splitting, ΔEq=-0.208 mm s^{-1}, observed for sample FN-1, can be ascribed to α-Fe_2O_3. In the ^{57}Fe Mössbauer spectra of samples FN-1 and FN-2, a central quadrupole doublet of very small intensity with splitting (Δ=1.030 mm s^{-1}) was measured. With an increase in the Nd_2O_3 molar content in the samples $(1-x)Fe_2O_3 + xNd_2O_3$, there is a gradual decrease of the HMF value. A gradual change of ΔE_q from -0.208 mm s^{-1} for samples FN-1 to zero mm s^{-1} for sample FN-11 was observed. The line-width, Γ, increased gradually with the increase of the initial Nd_2O_3 molar content up to sample FN-5 (Γ = 0.364 mm s^{-1}) and then showed a tendency to decrease, up to sample FN-11. The values of the isomer shift , δ, and quadrupole splitting, ΔE_q, measured for samples FN-8 to FN-11 can be ascribed to Nd_2O_3; however, the measured value of HMF (510-512 kOe) was larger than that reported in the literature for $NdFeO_3$. Eibshütz et al. [22] reported the following Mössbauer parameters for $NdFeO_3$ at room temperature: δ = 0.10 mm s^{-1} ($^{57}Co/Cu$), ΔE_q = 0.0 mm s^{-1} and HMF = 506 kOe.

A strong influence of the atmospheric moisture on the state of the samples (samples exposed to the atmosphere for a longer time are denoted with an asterisk), which contained Nd_2O_3, was observed. On the basis of the FT-IR spectrum of samples FN-7* (Figure 8), it can be concluded that this sample does not contain $Nd(OH)_3$. XRD analysis showed the presence of $NdFeO_3$ (0.60) and α-Fe_2O_3 (0.40) in sample FN-7*. On the other hand, the FT-IR spectrum of sample FN-8* showed a sharp peak at 3606 cm^{-1} and bands at 1513, 1398 and 674 cm^{-1}. The bands at 1513 and 1398 cm^{-1} are due to the presence of carbonates adsorbed by $Nd(OH)_3$. The intensities of the IR bands at 3606 and 674 cm^{-1} increased as the fraction of $Nd(OH)_3$ increased from sample FN-8* to sample FN-11*. Sample

TABLE VI. CHEMICAL COMPOSITION OF THE SAMPLES PREPARED IN THE SYSTEM $(1-x)Fe_2O_3 + xNd_2O_3$

Sample	Molar fraction	
	Fe_2O_3 $(1-x)$	Nd_2O_3 (x)
FN-1	0.99	0.01
FN-2	0.97	0.03
FN-3	0.95	0.05
FN-4	0.90	0.10
FN-5	0.85	0.15
FN-6	0.80	0.20
FN-7	0.70	0.30
FN-8	0.50	0.50
FN-9	0.30	0.70
FN-10	0.10	0.90
FN-11	0.05	0.05
FN-12	0	1

TABLE VII. THE RESULTS OF X-RAY DIFFRACTION PHASE ANALYSIS OF SAMPLES FN-1 TO FN-12.

Sample	Phase composition (approx. molar fraction)
FN-1	α-Fe_2O_3 + $NdFeO_3$ (0.02)
FN-2	α-Fe_2O_3 + $NdFeO_3$ (0.06)
FN-3	α-Fe_2O_3 + $NdFeO_3$ (0.10)
FN-4	α-Fe_2O_3 + $NdFeO_3$ (0.20)
FN-5	α-Fe_2O_3 + $NdFeO_3$ (0.30)
FN-6	α-Fe_2O_3 + NdFeO3 (0.40)
FN-7	$NdFeO_3$ + α-Fe_2O_3 (0.40)
FN-8	$NdFeO_3$ + Nd_2O_3 (0.10)
FN-9	Nd_2O_3 + $NdFeO_3$ (0.50)
FN-10	Nd_2O_3 + $NdFeO_3$ (0.20)
FN-11	Nd_2O_3 + $NdFeO_3$ (0.10)
FN-12	Nd_2O_3

TABLE VIII. ^{57}Fe MÖSSBAUER PARAMETERS (RT) CALCULATED ON THE BASIS OF RECORDED SPECTRA FOR THE SAMPLES PREPARED IN THE SYSTEM Fe_2O_3-Nd_2O_3.

Sample	Lines	Isomer shift, δ* (mm s^{-1})	Quadrupole splitting Δ or ΔEq (mm s^{-1})	Hyperfine magnetic field, HMF (mm s^{-1})	Line width Γ (mm s^{-1})
FN-1	Q	0.304	1.030		0.300
	M	0.367	-0.208	516	0.319
FN-2	Q	0.306	1.030		0.300
	M	0.369	-0.207	515.9	0.322
FN-3	M	0.370	-0.205	515.7	0.350
FN-4	M	0.370	-0.194	514.8	0.350
FN-5	M	0.369	-0.180	514.5	0.364
FN-6	M	0.369	-0.168	515.1	0.324
FN-7	M	0.368	-0.131	514.7	0.338
FN-8	M	0.372	-0.0	510.3	0.308
FN-9	M	0.370	-0.0	511.1	0.314
FN-10	M	0.381	-0.0	511.9	0.286
FN-11	M	0.369	-0.0	511.8	0.308

FN-12 transformed to $Nd(OH)_3$ (sample FN-12*) after exposure to the atmosphere for a prolonged time. In order to confirm the latter conclusion, we recorded the FT-IR spectrum (Figure 9) of a sample asreceived from Trona, Lindsay Chemical Corporation, West Chicago, and declared to be Nd_2O_3.

Figure 8 also shows the FT-IR spectrum of this sample, recorded immediately after calcination at 900 ^oC for 2h. It is obvious that the Trona sample was dominantly $Nd(OH)_3$ with adsorbed carbonates. After calcination the sample consisted only of Nd_2O_3 , which was also confirmed by XRD. During the transformation, the light-rose color of the powder changed to light blue. When it was exposed again to atmospheric moisture and CO_2, the Nd_2O_3 powder slowly became rose colored, thus indicating the reversibility of this process. Figure 9 shows that Nd_2O_3 is characterized by a very strong IR band with a transmittance minimum at 463 cm^{-1}.

2. 2. 2. The system Sm_2O_3-Fe_2O_3

The physical properties of garnets, with rare earth sites fully or partially occupied by Sm^{3+} ions, were previously subjected to several investigations because of applications in advanced technologies. We shall focus our attention on the formation of the oxide phases in the system Sm_2O_3-Fe_2O_3 [23]. The solid state reaction was used to prepare the samples. Proper weights of oxide powders were mixed and mechanically activated in a planetary mill before the sintering of the mixture of corresponding oxides. Table IX shows the experimental conditions for the preparation of the samples in the system Sm_2O_3-Fe_2O_3 [23]. The results of the XRD phase analysis of the samples are given in Table X. XRD analysis of the Sm_2O_3, supplied by Ventron, showed that this chemical was actually a mixture of $Sm(OH)_3$ and B-Sm_2O_3 (sample SM1). After heating this mixture at 900 ^oC for 2 hours, a

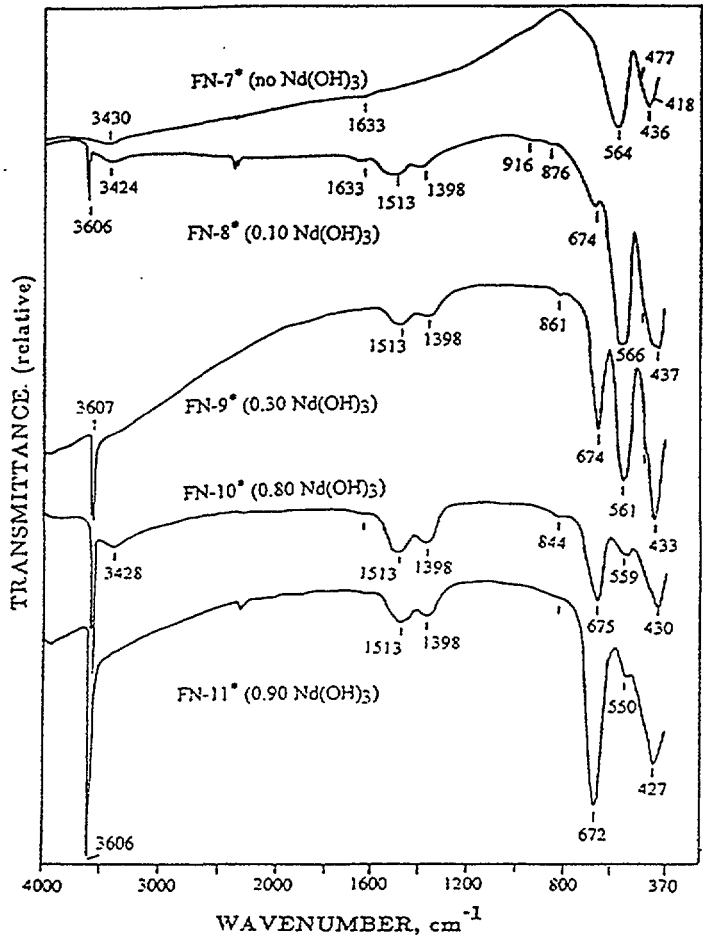

FIG. 8. FT-IR spectra of samples FN-7 to FN-11*, recorded at room temperature.*

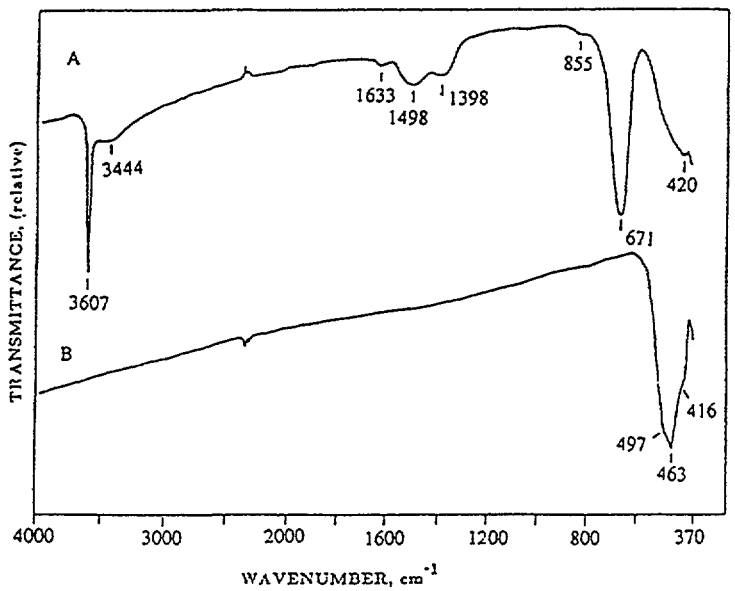

FIG. 9. FT-IR spectra of (A) Nd_2O_3 as-received by Trona, and (B) after calcination of this chemical at 900 °C.

TABLE IX. EXPERIMENTAL CONDITIONS OF THE PREPARATION OF SAMPLES IN THE Fe_2O_3-Sm_2O_3 SYSTEM.

Sample	Molar ratio (Fe_2O_3:Sm_2O_3	Temperature of heating / °C	Time of heating / hours
SM1	Sm_2O_3, as received by Ventron		
SM2	Sm_2O_3, as received by Ventron	900	2
	1:1	200	1
	1:1	300	1
	1:1	400	1
SM3	1:1	500	24
	1:1	200	1
	1:1	300	1
	1:1	400	1
	1:1	500	1
SM4	1:1	600	5
	1:1	200	1
	1:1	300	1
	1:1	400	1
	1:1	500	1
	1:1	600	1
SM5	1:1	700	5
	1:1	200	1
	1:1	300	1
	1:1	400	1
	1:1	500	1
	1:1	600	1
	1:1	700	1
SM6	1:1	800	5
SM7	1:1	1000	2
SM8	1:1	1200	2
	5:3	200	1
	5:3	300	1
	5:3	400	1
SM9	5:3	800	5
SM10	5:3	1000	2
SM11	5:3	1100	2
SM12	5:3	1200	2
SM13	5:3	1300	2

TABLE X. RESULTS OF THE XRD PHASE ANALYSIS.

Sample	Phase composition (approx. molar fraction)	Remarks
SM1	$Sm(OH)_3$ + B-Sm_2O_3	
SM2	B-Sm_2O_3 + C-Sm_2O_3	
SM3	C-Sm_2O_3 + B-Sm_2O_3 + α-Fe_2O_3 (0.30) (0.20) (0.50)	Sharpening of diffraction lines
SM4	C-Sm_2O_3 + B-Sm_2O_3 + α-Fe_2O_3 (0.30) (0.20) (0.50)	
SM5	C-Sm_2O_3 + B-Sm_2O_3 + α-Fe_2O_3 (0.30) (0.20) (0.50)	
SM6	C-Sm_2O_3 + B-Sm_2O_3 + α-Fe_2O_3 + $SmFeO_3$ (0.25) (0.17) (0.43) (0.15)	
SM7	$SmFeO_3$	
SM8	$SmFeO_3$	Sharpening of diffraction lines of $SmFeO_3$
SM9	$SmFeO_3$ + α-Fe_2O_3 (0.05)	
SM10	$SmFeO_3$ + α-Fe_2O_3 (0.03)	
SM11	$SmFeO_3$ + α-Fe_2O_3 (0.02)	
SM12	$Sm_3Fe_5O_{12}$ + $SmFeO_3$ (0.15)	
SM13	$Sm_3Fe_5O_{12}$	Sharpening of diffraction lines of $Sm_3Fe_5O_{12}$

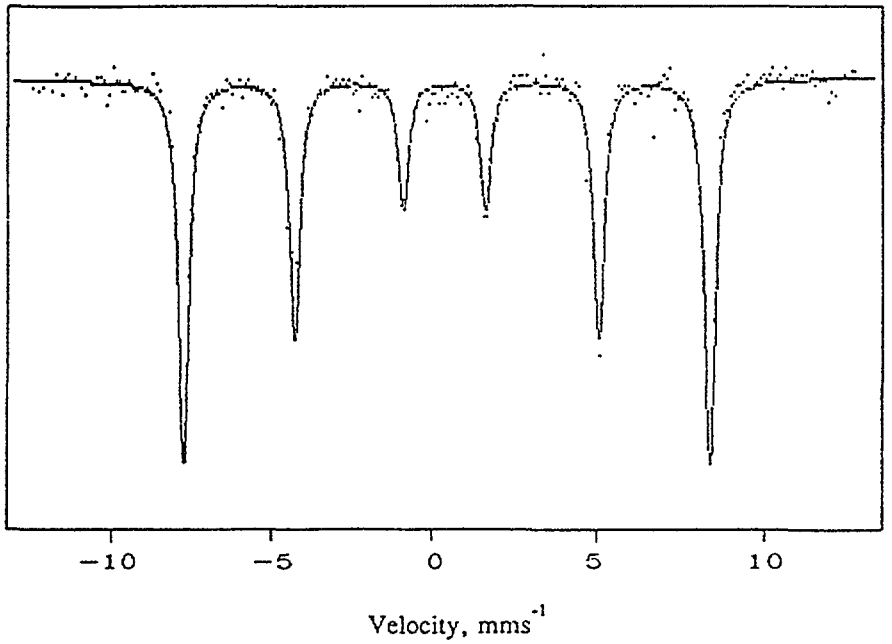

FIG. 10. ^{57}Fe Mössbauer spectrum of sample SM8, recorded at room temperature, indicating hyperfine magnetic splitting of samarium orthoferrite, $SmFeO_3$.

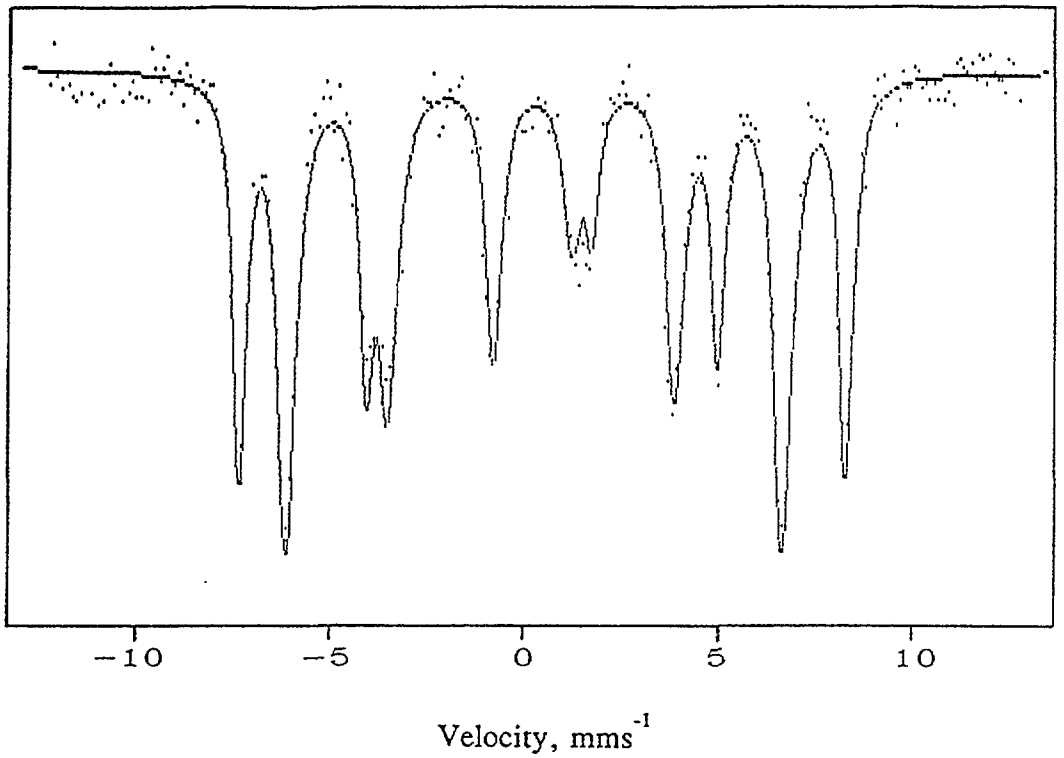

FIG. 11. ^{57}Fe Mössbauer spectrum of sample SM13, recorded at room temperature, indicating the superposition of two sextets of spectral lines corresponding to iron ions at a- and d- sites with hyperfine magnetic fields of 486 and 398 kOe, respectively.

TABLE XI. MÖSSBAUER PARAMETERS (RT) CALCULATED FOR $SmFeO_3$ AND $Sm_3Fe_5O_{12}$

Compound	Lines	d_{Fe}/mm s^{-1}	DE_q/mm s^{-1}	HMF/kOe
$SmFeO_3$	M	0.39	-0.07	500
$Sm_3Fe_5O_{12}$	M_a	0.40	0.08	486
	M_d	0.19	0.10	398

Errors: HMF = 1kOe, δ and ΔE_q = 0.01 mm s^{-1}

mixture of B-Sm_2O_3 and C-Sm_2O_3 was obtained (sample SM2). Heating a mixture of Sm_2O_3-Fe_2O_3 = 1:1 up to 700 °C did not cause the formation of samarium orthoferrite, $SmFeO_3$ (samples SM3, SM4 and SM5). $SmFeO_3$ was detected as one of the oxide phases in sample SM6, which was produced at 800 °C, and as a single phase at 1000 or 1200 °C (samples SM7 and SM8, respectively). When the mixture Fe_2O_3-Sm_2O_3 = 5:3 was heated to 800 °C, the formation of $SmFeO_3$ as the dominant component and α-Fe_2O_3 as the minor component was detected (sample SM9). With increasing temperature, the molar content of α-Fe_2O_3 decreased (samples SM10 and SM11). A mixture of $Sm_3Fe_5O_{12}$ and $SmFeO_3$ was generated at 1200 °C (sample SM12), and $Sm_3Fe_5O_{12}$ as a single phase (sample SM13) at 1300 °C. The oxide phases, α-Fe_2O_3, $SmFeO_3$ and $Sm_3Fe_5O_{12}$, show specific Mössbauer spectroscopic behavior due to their different structural and magnetic properties. α-Fe_2O_3, which possesses the crystal structure of corundum (α-Al_2O_3), is characterized by a hyperfine magnetic splitting spectrum (one sextet) at room temperature. The shape of the spectrum depends on the crystallinity of the α-Fe_2O_3, particle size and the partial substitution of Fe^{3+} ions by other metal ions. Due to these effects, the HMF of α-Fe_2O_3 can be significantly

reduced. For example, in the case of ultra fine α-Fe_2O_3 particles, six spectral lines may collapse into one doublet at room temperature. The orthoferrites of lanthanide elements possess a distorted perovskite lattice with iron having the same environment throughout the lattice. At room temperature, they are characterized by a hyperfine magnetic splitting spectrum. The Mössbauer spectrum of $SmFeO_3$ (sample SM8) is shown in Figure 10.

Lanthanide iron garnets, $R_3Fe_5O_{12}$, possess the crystal structure of the mineral grossular. Fe^{3+} ions occupy octahedral (*a*) and tetrahedral (*d*) sites, while R^{3+} ions are in dodecahedral (*c*) sites. Figure 11 shows the fitted Mössbauer spectrum of sample SM13 corresponding to $Sm_3Fe_5O_{12}$. It is characterized by two hyperfine magnetic fields at room temperature, HMF (*a*) = 486 kOe and HMF(*d*) = 398 kOe. The ^{57}Fe Mössbauer parameters (RT) calculated for $SmFeO_3$ and $Sm_3Fe_5O_{12}$ are given in Table XI.

2. 2. 3. The system Gd_2O_3-Fe_2O_3

X-ray diffraction and Mössbauer spectroscopy were used to monitor the formation of the oxide phases in the system Gd_2O_3-Fe_2O_3 [24]. The solid state reaction between the corresponding oxides (molar ratio Gd_2O_3:Fe_2O_3 = 1:1 or 3:5) was applied. Experimental conditions for the preparation of the samples are given in Table XII. Oxide phases, detected by XRD in the samples prepared in the system Gd_2O_3-Fe_2O_3 , are presented in Table XIII, while ^{57}Fe Mössbauer parameters, calculated on the basis of the spectra recorded at room temperature, are presented in Table XIV. The hyperfine magnetic field measured for $GdFeO_3$ was found to be between 500 and 503 kOe. The sample FG-6, obtained at the maximum heating temperature of 1200 °C was deconvoluted into two sextets. HMFs of 494 kOe for iron ions at *a*-sites and 402 kOe for *d*-sites were calculated. The results indicated that $GdFeO_3$ is intermediate phase in the formation of $Gd_3Fe_5O_{12}$ by the solid state reaction between Gd_2O_3 and Fe_2O_3.

TABLE XII. EXPERIMENTAL CONDITIONS FOR THE PREPARATION OF THE SAMPLES IN THE SYSTEM Fe_2O_3-Gd_2O_3.

Sample	Molar ratio (Fe_2O_3:Gd_2O_3)	Temperature of heating (°C)	Time of heating (h)
	Only Gd_2O_3	200	1
	Only Gd_2O_3	300	1
	Only Gd_2O_3	400	1
G-1	Only Gd_2O_3	800	5
G-2	Only Gd_2O_3	1000	2
G-3	Only Gd_2O_3	1200	2
	1:1	200	1
	1:1	300	1
	1:1	400	1
FG-1	1:1	800	5
FG-2	1:1	1000	2
FG-3	1:1	1200	2
	5:3	200	1
	5:3	300	1
	5:3	400	1
FG-4	5:3	800	5
FG-5	5:3	1000	2
FG-6	5:3	1200	2

TABLE XIII. OXIDE PHASES DETECTED BY XRD IN THE SAMPLES PREPARED IN THE SYSTEM Fe_2O_3-Gd_2O_3.

Sample	Maximum heating temperature (°C)	Phase composition (approximate molar fraction)
G-1	800	Gd_2O_3
G-2	1000	Gd_2O_3
G-3	1200	Gd_2O_3
FG-1	800	$GdFeO_3$ + Gd_2O_3 + α-Fe_2O_3 (>0.5)
FG-2	1000	$GdFeO_3$ + Gd_2O_3*
FG-3	1200	$GdFeO_3$
FG-4	800	Gd_2O_3 + $GdFeO_3$ + α-Fe_2O_3 (0.4)
FG-5	1000	$GdFeO_3$ + α-Fe_2O_3 + Gd_2O_3 (0.8)
FG-6	1200	$Gd_3Fe_5O_{12}$ + $GdFeO_3$*

*Small amount. All samples exhibited sharp, well-defined X-ray diffraction lines.

TABLE XIV. ^{57}Fe MÖSSBAUER PARAMETERS CALCULATED ON THE BASIS OF THE SPECTRA RECORDED AT ROOM TEMPERATURE.

Sample	Lines	Isomer shift, δ^a (mm s^{-1})	Quadrupole splitting, ΔE_q (mm s^{-1})	Hyperfine magnetic field, HMF (kOe)^b	Identification
FG-1	M_1	0.39	-0.23	516	α-Fe_2O_3
	M_2	0.38	0.02	502	$GdFeO_3$
FG-2	M_1	0.37	0.02	502	$GdFeO_3$
FG-3	M_1	0.37	0.03	503	$GdFeO_3$
FG-4	M_1	0.38	-0.22	515	α-Fe_2O_3
	M_2	0.37	0.03	500	$GdFeO_3$
FG-5	M_1	0.37	-0.22	516	α-Fe_2O_3
	M_2	0.38	0.02	503	$GdFeO_3$
FG-6	M_a	0.39	0.06	492	$Gd_3Fe_5O_{12}$
	M_d	0.17	0.01	402	$Gd_3Fe_5O_{12}$

^{a}δ-values referred to α-iron. ^{b}1 kOe = 79.58 kA m^{-1}.

The formation of oxide phases in the system $(1-x)Fe_2O_3+xGd_2O_3$, $0<x<1$, was also investigated [25] using X-ray diffraction and Mössbauer spectroscopy. The samples were prepared by chemical "coprecipitation" and the thermal treatment of hydroxide "coprecipitate" up to 900 °C. The distribution of the oxide phases (molar fractions) present in the system Fe_2O_3-Gd_2O_3, as a function of the molar content of Gd_2O_3, is shown in Figure 12. All the oxide phases present in samples Fe_2O_3-Gd_2O_3, prepared at the final temperature of 900 °C, are well crystallized showing sharp X-ray diffraction lines which are well resolved in the spectral components $K\alpha_1\alpha_2$ at higher Bragg angles.

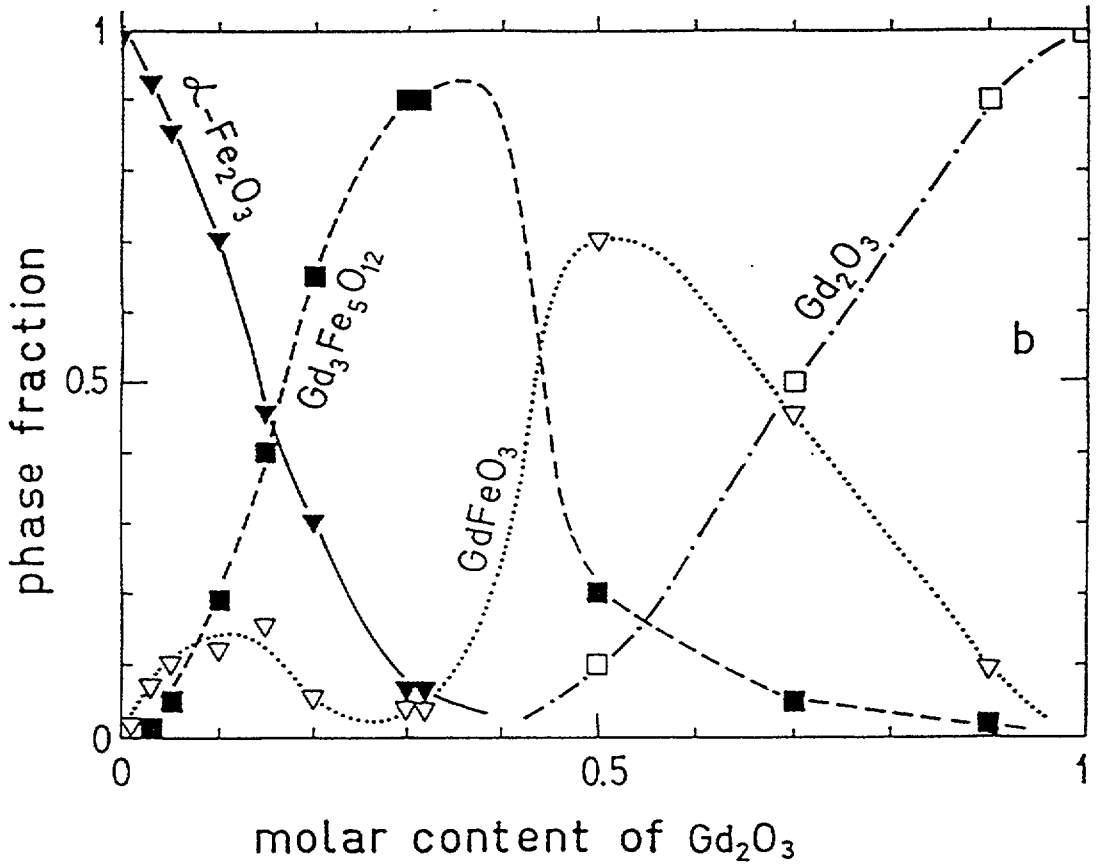

FIG. 12. Distribution of oxide phases (molar fractions) present in the system Fe_2O_3-Gd_2O_3, as a function of molar content Gd_2O_3.

TABLE XV. PHASE COMPOSITION OF SAMPLES $(1-x)Fe_2O_3+xEu_2O_3$ PREPARED AT A MAXIMUM TEMPERATURE OF 600 °C.

Molar fraction of Eu_2O_3, x	Phase composition (approximate molar fraction)	Remarks
0.01	α-Fe_2O_3	BDL
0.03	α-Fe_2O_3	BDL
0.05	α-Fe_2O_3(0.8) + amorphous fraction (0.2)	BDL
0.10	α-Fe_2O_3(0.5) + amorphous fraction (0.5)	BDL
0.20	amorphous	
0.30	amorphous	
0.50	$EuFeO_3$ + Eu_2O_3 + amorphous fraction	*PC
0.70	Eu_2O_3 + $EuFeO_3$ + $Eu_3Fe_5O_{12}$ + amorphous fraction	*PC
1	Eu_2O_3	PC

BDL: broadened diffraction lines
PC: poorly crystallized
*PC: approximate molar fractions not determined because of poor crystallinity

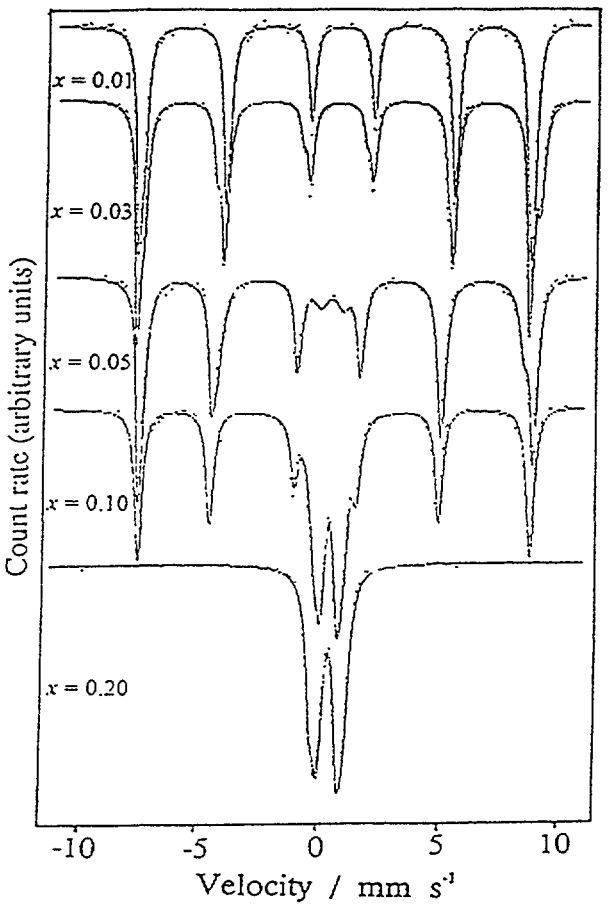

FIG. 13. ^{57}Fe Mössbauer spectra at RT of $(1-x)Fe_2O_3+xEu_2O_3$ with x=0.01, 0.03, 0.05,0.10 and 0.20 Samples were prepared at a maximum temperature of 600 ^oC.

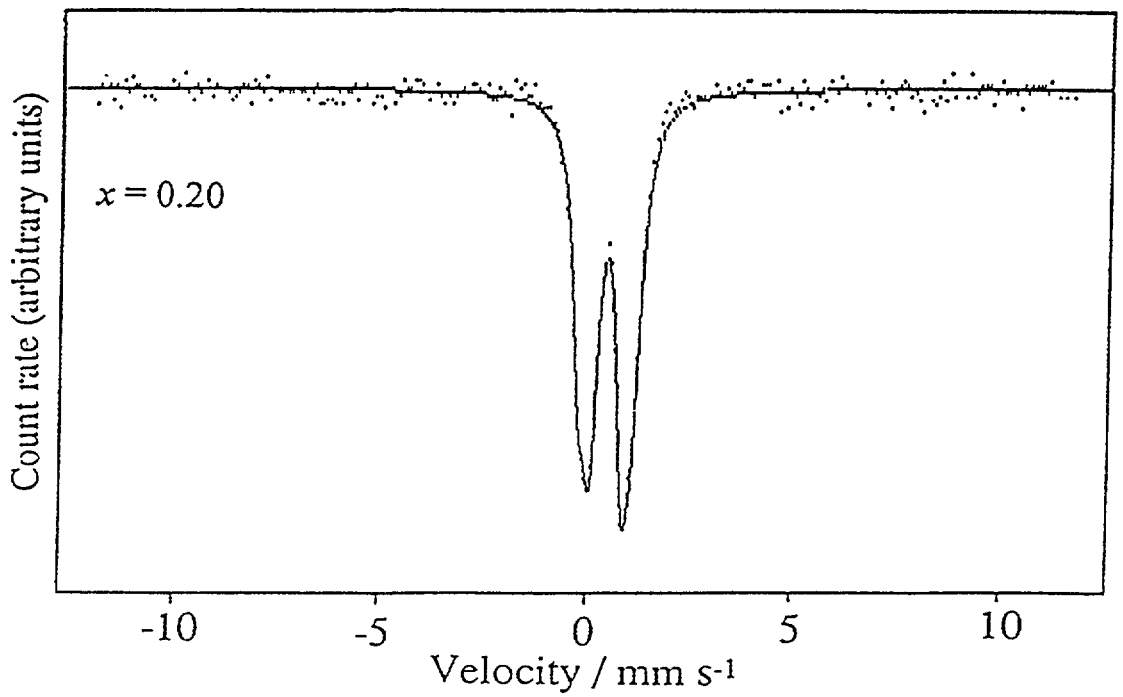

FIG. 14. ^{57}Fe Mössbauer spectrum at 80 K of 0.8 Fe_2O_3 + 0.2 Eu_2O_3. The sample was prepared at a maximum temperature of 600 ^oC.

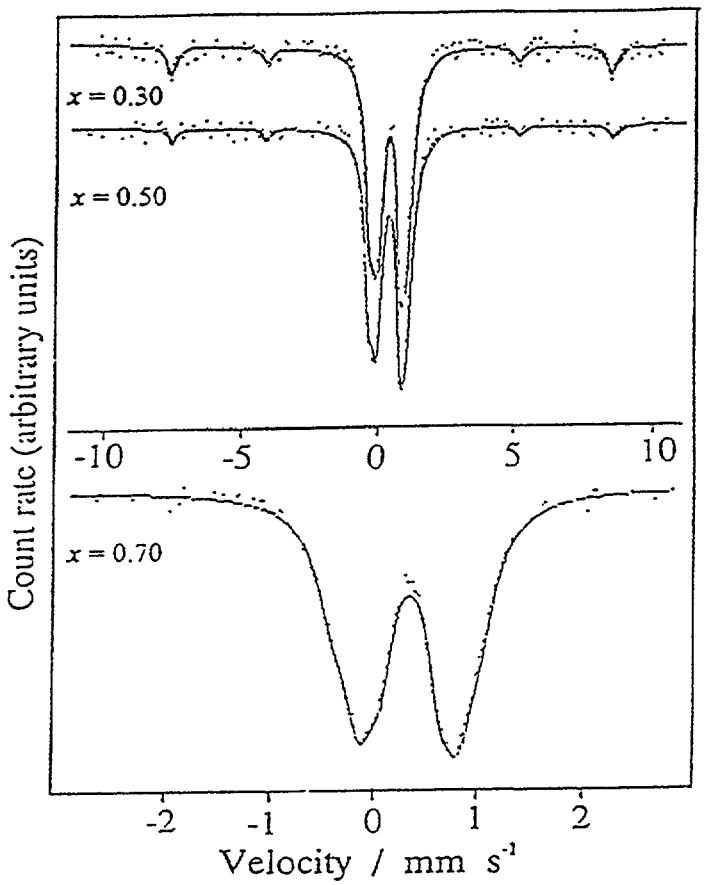

FIG 15 ^{57}Fe Mossbauer spectra at RT of $(1-x)Fe_2O_3 + x\,Eu_2O_3$ with x =0.30, 0 50 and 0 70 Samples were prepared at a maximum temperature of 600 °C

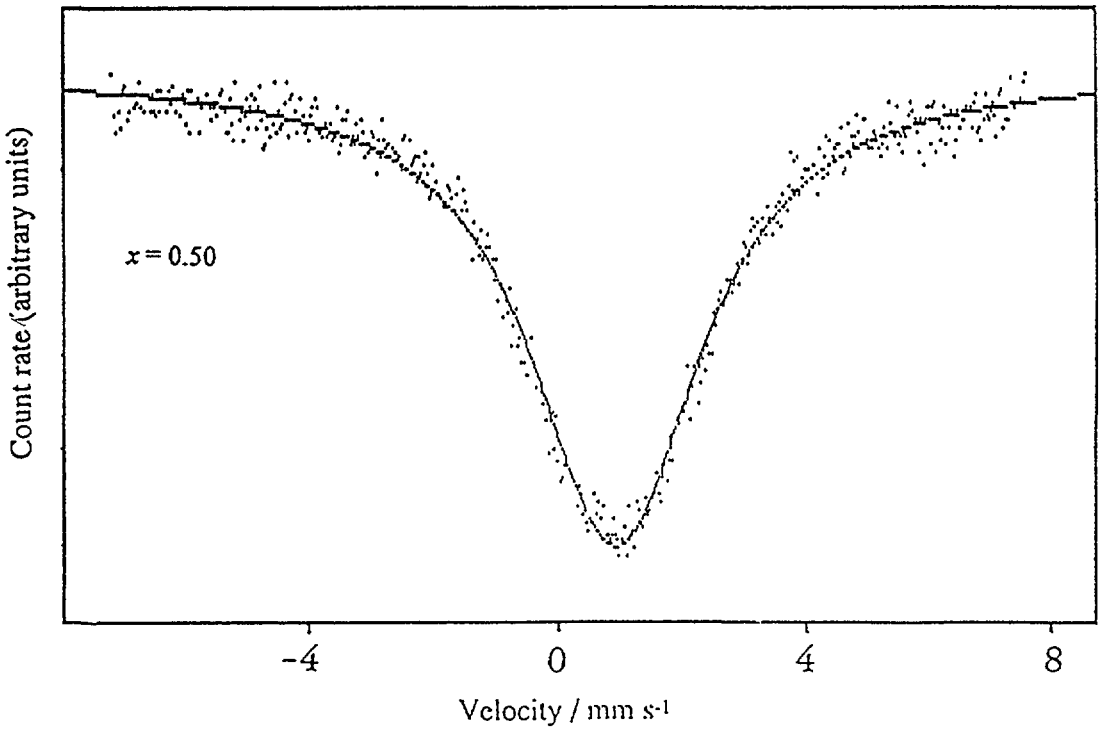

FIG 16 ^{151}Eu Mössbauer spectrum at RT of $0.5Fe_2O_3 + 0.5Eu_2O_3$ The sample was prepared at a maximum temperature of 600 °C

2. 2. 4. The system Eu_2O_3-Fe_2O_3

The samples were prepared using the method of chemical "coprecipitation" [26]. The $Fe(OH)_3$-$Eu(OH)_3$ "coprecipitates", at given molar fractions, were heated for 1h at 200 °C, 1h at 300 °C, 1h at 400 °C and 5h at 600 °C ("step by step" heating). The initial chemical composition and the results of XRD analysis of the samples $(1-x)Fe_2O_3+xEu_2O_3$, $0<x<1$, are given in Table XV. A significant amorphous fraction was observed in all the samples for $0.05<x<0.70$, while for x =0.20 and x=0.30 the samples were completely amorphous for XRD.

The chemical and structural changes in the system Fe_2O_3-Eu_2O_3 also affected the corresponding Mössbauer spectra of ^{57}Fe and ^{151}Eu. The characteristic Mössbauer spectral results are summarized in Figures 13 to 16 and in Table XVI. ^{57}Fe Mössbauer spectra at RT, recorded for x=0.01 and 0.03, are the superposition of two sextets, M_1 and M_2. These sextets can be assigned to α-Fe_2O_3 particles in which Fe^{3+} ions were partially substituted by Eu^{3+}, thus forming a solid solution. For x=0.05, a weak quadrupole doublet, Δ=0.901 mm s^{-1}, is observed and assigned to the amorphous phase detected by XRD

TABLE XVI. ^{57}Fe MÖSSBAUER HYPERFINE PARAMETERS AT R T OBTAINED FOR THE SAMPLES $(1-x)Fe_2O_3+xEu_2O_3$. THE SAMPLES WERE PREPARED AT A MAXIMUM TEMPERATURE OF 600 °C.

Molar fraction of Eu_2O_3, x	Component	δ** (mm s^{-1})	ΔE_q (mm s^{-1})	H (kOe)	Γ (mm s^{-1})
0.01	M_1	0.403	-0.048	517.0	0.286
	M_2	0.404	-0.043	503.9	0.365
0.03	M_1	0.416	0.108	519.1	0.315
	M_2	0.401	-0.049	515.3	0.321
0.05	Q	0.325	0.901		0.696
	M_1	0.403	0.403	518	0.335
	M_2	0.352	0.187	501	0.533
0.10	Q_1	0.350	1.203		0.506
	Q_2	0.381	0.702		0.437
	M	0.400	0.409	514.9	0.382
0.20	Q1	0.334	1.324		0.453
	Q_2	0.363	0.795		0.406
0.30	Q_1	0.312	1.367		0.469
	Q_2	0.355	0.850		0.413
	M	0.416	-0.07	501.6	0.427
0.50	Q_1	0.294	1.389		0.459
	Q_2	0.335	0.875		0.411
	M	0.441	-0.051	499.1	0.350
0.70	Q_1	0.297	1.419		0.402
	Q_2	0.327	0.926		0.424
	Q_3	0.340	0.554		0.264

*M=sextet, Q=quadrupole doublet

**Isomer shift, δ, is given relative to α-Fe.

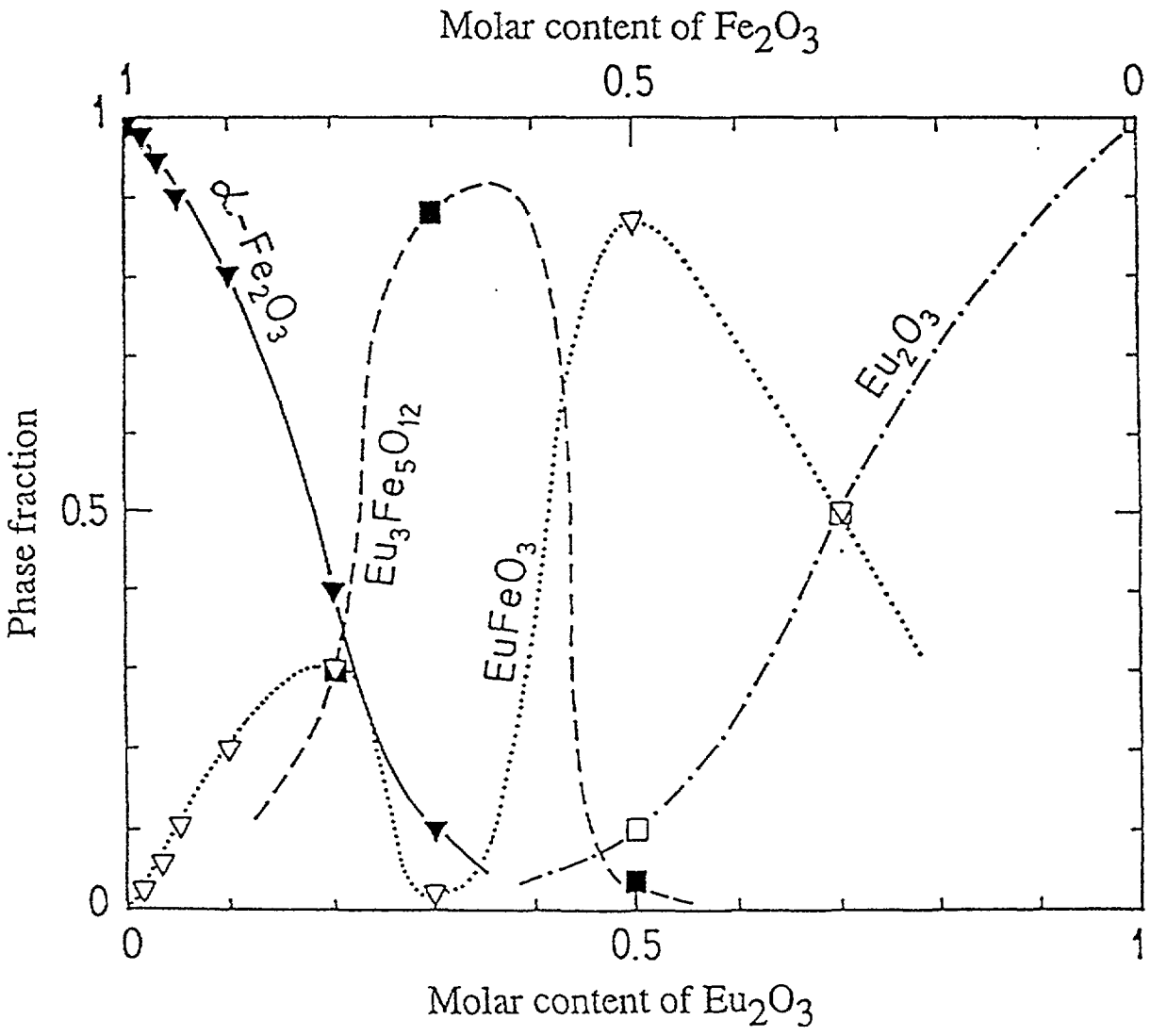

FIG. 17. Distribution of oxide phases in the system (1-x)Fe_2O_3 + xEu_2O_3. Samples were prepared at a maximum temperature of 900 °C.

in the same sample. For x=0.10, the relative intensity of this asymmetric quadrupole doublet increases. This doublet was deconvoluted into two quadrupole split components. For x=0.20, ^{57}Fe Mössbauer spectra at RT (Figure13) and 80 K (Figure 14) show only an asymmetric quadrupole doublet. ^{57}Fe Mössbauer spectra at RT, recorded for x=0.30 and 0.50, additionally show the presence of hyperfine magnetic split components of very small relative intensity (Figure 15). For x=0.70, an asymmetric quadrupole doublet is recorded at RT and analyzed as the superposition of three doublets, Q_1, Q_2 and Q_3. Two doublets, Q_1 and Q_2, can be assigned to the amorphous phase, as for samples with $0.10<x<0.70$. Since XRD analysis showed the presence of $EuFeO_3$ and $Eu_3Fe_5O_{12}$, besides the amorphous fraction, it can be supposed that the doublet Q_3 reflects the presence of $EuFeO_3$ and $Eu_3Fe_5O_{12}$ of poor crystallinity and very small particle size. Figure 16 shows the ^{151}Eu Mössbauer spectrum at RT, recorded for the samples with x=0.50 which was prepared at a maximum temperature of 600 °C. A very broad spectral line is obtained with the parameters δ_{Fe} = 0.914 mm s^{-1} and Γ = 3.351 mm s^{-1}.

Additional heating of sample width x=30 at 900 °C for 6 hours generated the following phase composition, as determined by XRD: $Eu_3Fe_5O_{12}$ (0.88) + α-Fe_2O_3 (0.10) + $EuFeO_3$ (0.02).

The corresponding molar fractions are given in parathensas. The ^{151}Eu spectrum of this sample shows hyperfine splitting as a consequence of the presence of $Eu_3Fe_5O_{12}$ (europium iron garnet, EuIG) in which the Eu^{3+} is magnetically ordered by the exchange polarization effects due to iron.

De Souza, Jr., et al. [27] also investigated the formation of oxide phases as a function of the heating temperature of mixed Eu(III)/Fe(III)-hydroxide (atomic ratio Eu:Fe = 1:9). The Mössbauer spectrum of the sample heated at 500 °C for 12 hours showed one sextet at RT (H=224 kOe) and also at 85 K (H = 465 kOe), which were ascribed to poorly crystallized α-Fe_2O_3. The sample thermally treated at 1000 °C showed one sextet at RT corresponding to α-Fe_2O_3. For the same sample XRD also indicated the presence of $EuFeO_3$ .This result was confirmed by a Mössbauer measurement at 85 K. After heating the sample at 1250 °C, it was found to be 83 % α-Fe_2O_3 and 17 % $Eu_3Fe_5O_{12}$.

In the present work, we observed a disappearence of the amorphous phase in all the samples after additional heating at 900 °C. The quantitative distribution of oxide phases, a-Fe_2O_3, $Eu_3Fe_5O_{12}$, $EuFeO_3$ and Eu_2O_3 in the samples, obtained after cooling the samples from 900 °C to room temperature, is given in Figure 17. These quantitative data were obtained by the application of the doping method. One can see in Figure 17 that the fraction of α-Fe_2O_3 continously decreases as the initial content of europium oxide, x, increases. The fraction of the garnet-type ferrite, $Eu_3Fe_5O_{12}$, increases with x, having a maximum at x~0.4, and then decreases with a further increase of x.

The orthoferrite, $EuFeO_3$, already appears at x~0.01. Its fraction slowly increases, with x having a small maximum at x~0.15 and a pronounced maximum at x~0.50. The fraction of $EuFeO_3$ decreases for x>0.50. The phase Eu_2O_3 appears at x>0.50 and its fraction increases with x. All the phases present in samples Fe_2O_3-Eu_2O_3, prepared at 900 °C, are well crystallized, showing sharp X-ray diffraction lines which are well-resolved in the spectral doublet components $K\alpha_1\alpha_2$ at higher Bragg angles. In these samples, according to X-ray diffraction analysis, the solid solutions are not formed.

2. 2. 5. The system Er_2O_3-Fe_2O_3

In the previous section (2. 2. 4.), it was shown that the presence of an amorphous fraction in the samples of the system $(1-x)Fe_2O_3+xEu_2O_3$, $0<x<1$, was detected, even at the relatively high temperature of the sample preparation (600 °C). The importance of this amorphous fraction in the formation of EuIG was recognized. This finding can be also of importance for the technology of garnet films. In order to learn more about this phenomenon, we continued with the investigation of analogous the system Er_2O_3-Fe_2O_3.

The mixed hydroxide, $3Er(OH)_3+5Fe(OH)_3$, was "coprecipitated" from an aqueous solution of the corresponding nitrate salts. After isolation from the mother liquor and washing, the mixed hydroxide was dried. It is important to note that Er^{3+} ions show amphoteric character; therefore the "coprecipitation" and washing of the mixed hydroxide must be performed carefully. The samples heated at 800 °C and higher temperatures were previously sintered. Table XVII. shows the conditions for the preparation of the samples by heating the mixed hydroxide with a molar ratio of, Er_2O_3 : Fe_2O_3 = 3:5.

The results of the X-ray powder diffraction analysis of samples ER-1 to ER-6 are given in Table XVIII. Samples ER-1, ER-2 and ER-3 were amorphous, as found by XRD. The characteristic part of the XRD pattern of sample ER-3 is shown in Figure 18. Sample ER-4 was a mixture of $ErFeO_3$ and $Er_3Fe_5O_{12}$, together with Er_2O_3 and α-Fe_2O_3.

TABLE XVII. THE CONDITIONS FOR THE PREPARATION OF THE SAMPLES BY HEATING THE MIXED HYDROXIDE WITH THE MOLAR RATIO OF Er_2O_3:Fe_2O_3 =3:5.

Sample	Temperature of heating (°C)	Time of heating (h)	Remark
ER-1			Mixed hydroxide with molar ratio, Er_2O_3 : Fe_2O_3 = 3 : 5, was used as starting material
ER-2	500	4	
	500	4	
ER-3	650	4	
	500	4	
	650	4	
ER-4	750	4	
	500	4	
ER-5	800	4	After the heating at 500 °C, the powder was ground and then sintered into the tablet.
	500	4	
ER-6	1300	4	

TABLE XVIII. PHASE COMPOSITION OF THE SAMPLES AS OBTAINED BY X-RAY DIFFRACTION.

Sample	Phase composition	Remark
ER-1	amorphous	
ER-2	amorphous	
ER-3	amorphous	
ER-4	$ErFeO_3$ + $Er_3Fe_5O_{12}$ + + Er_2O_3 + α-Fe_2O_3	little broadened diffraction lines (diffraction lines of α-Fe_2O_3 masked by stronger ones?)
ER-5	$Er_3Fe_5O_{12}$ + $ErFeO_3$	little broadened diffraction lines
ER-6	$Er_3Fe_5O_{12}$ + α-Fe_2O_3 (<1 mol %)	sharp diffraction lines

With prolonged contact of sample ER-4 with atmospheric moisture, the presence of $Er(OH)_3$ could be found due to high the hygroscopic nature of Er_2O_3. A similar effect was observed during the investigation of the system Nd_2O_3-Fe_2O_3 (section 2. 2. 1.).

Sample ER-5 contained only $Er_3Fe_5O_{12}$ and $ErFeO_3$. Samples ER-4 and ER-5 exhibited slightly broadened diffraction lines. After heating the starting material up to 1300 °C, $Er_3Fe_5O_{12}$ was formed showing sharp diffraction lines. The presence of α-Fe_2O_3 traces in sample ER-6 could be explained by the incomplete solid state reaction or the mode of the sample cooling to room temperature (in furnace).

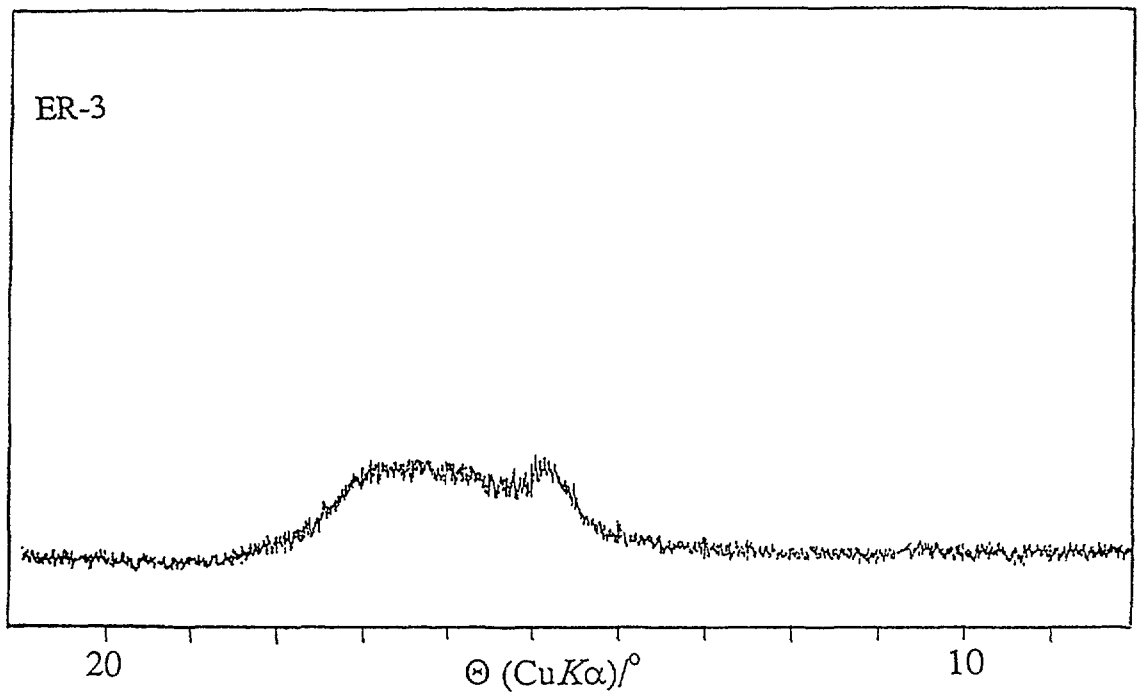

FIG. 18 Characteristic part of the X-ray diffraction pattern of sample ER-3.

Figure 19 shows the FT-IR spectra of samples ER-1 to ER-6. Sample ER-1 shows broad IR bands with transmittance minima at 661, 491 and 403 cm^{-1}, while for sample ER-3 the transmittance minima are at 565, 443 and 327 cm^{-1}. For sample ER-4, additional IR bands were observed, such as shoulder at 658 and bands at 603, 365, and 304 cm^{-1}, thus indicating the presence of additional oxide phases, in accordance with the XRD results (Table XVIII). Samples ER-5 and ER-6, produced at higher temperatures than samples ER-2 to ER-4, showed a gradual evolution of the IR bands typical for rare earth iron garnets. The FT-IR spectrum of sample ER-6 can be ascribed to $Er_3Fe_5O_{12}$.

Since the FT-IR spectra did not yield more information about the amorphous fraction found by XRD, the samples were additionally characterized by Mössbauer spectroscopy. The Mössbauer spectra of samples ER-1 to ER-6, recorded at room temperature, are shown in Figure 20 and 21, while the corresponding Mössbauer parameters are given in Table XIX. The spectrum of sample ER-1 is characterized by a central quadrupole doublet (δ_{Fe}=0.38, Δ=0.80 and Γ=0.50 mm s^{-1}). After heating sample ER-1 at 500 °C and cooling to room temperature, changes in the corresponding Mössbauer spectrum (sample ER-2) were observed. The spectrum of sample ER-2 was considered as the superposition of two quadrupole doublets (Δ_1 = 0.78 and Δ_2=1.29 mm s^{-1}) and one sextet of very small intensity with H = 455 kOe. The H value of 455 kOe is less than those which are known for well crystallized α-Fe_2O_3 and $ErFeO_3$. This H value can be ascribed to very small and/or poor crystalline Fe-bearing oxide particles. Furthermore, the value Δ_2=1.29 mm s^{-1} indicates the presence of an additional Fe-bearing oxide phase. With an increase of the heating temperature to 650 °C the relative intensity of the sextet was slightly increased. The value of the magnetic splitting was also increased to 506 kOe (sample ER-3). Similar results were observed in an analogous system $(1-x)Fe_2O_3+xEu_2O_3$, $0<x<1$, where the samples obtained at 600 °C contained poorly crystallized phases and an amorphous fraction (samples with x=0.20, 030 and 0.50) (see section 2. 2 4.).

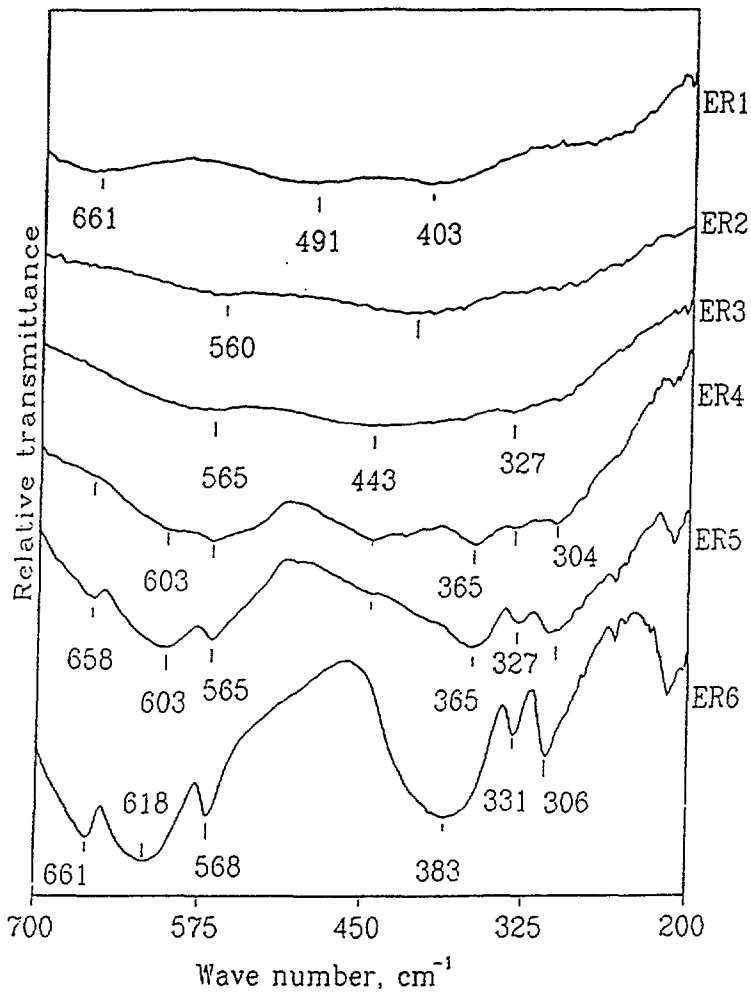

FIG. 19. FT-IR spectra of samples ER-1 to ER-6, recorded at room temperature.

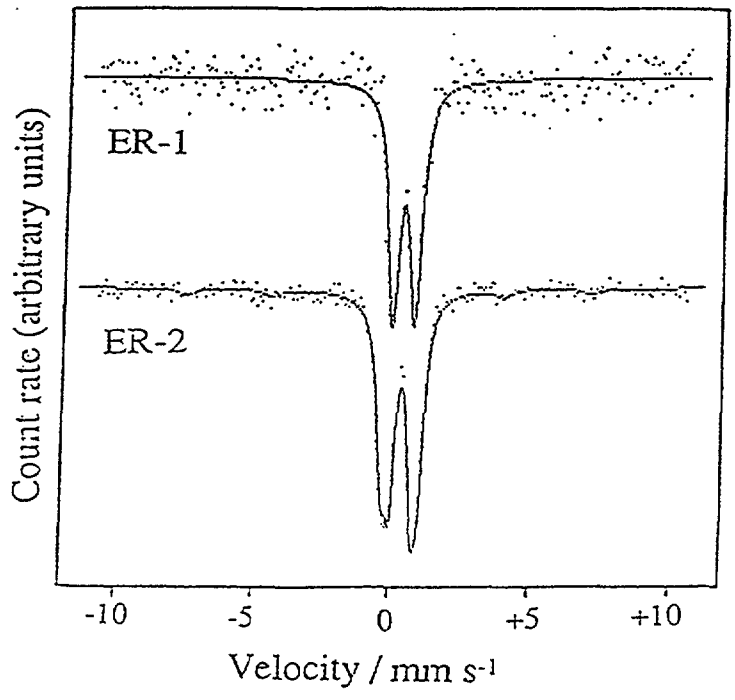

FIG. 20. ^{57}Fe Mössbauer spectra of samples ER-1 and Er-2, recorded at room temperature.

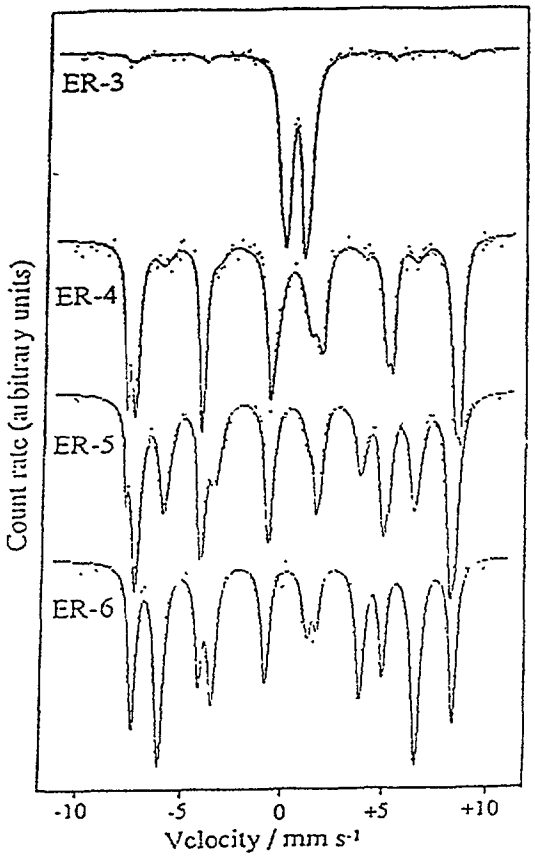

FIG. 21 ^{57}Fe Mossbauer spectra of samples ER-3, ER-4, ER-5 and ER-6, recorded at room temperature

TABLE XIX ^{57}Fe MOSSBAUER HYPERFINE PARAMETERS AT RT CALCULATED FOR OXIDE PHASES FORMED IN THE SYSTEM Er_2O_3-Fe_2O_3.

Sample	Spectral component	δ (mm s^{-1})	ΔEq (mm s^{-1})	H (kOe)	Γ (mm s^{-1})
ER-1	Q	0.38	0.80		0.50
ER-2	Q_1	0 37	0 78		0.38
	Q_2	0.33	1.29		0.49
	M	-0.19	0.01	455	0.62
ER-3	Q_1	0.35	0 83		0 40
	Q_2	0.33	1 35		0.47
	M	0.45	-0.20	506	0 78
ER-4	Q	0.33	1.74		0.84
	M_1	0.23	0.05	395	0 88
	M_2	0.40	0.02	496	0.43
	M_3	0 41	0.11	516	0.27
ER-5	M_1	0 20	-0.02	388	0.65
	M_2	0.40	0.00	487	0.49
	M_3	0.37	0 09	510	0.25
ER-6	M_1	0.17	0.01	394	0.51
	M_2	0.41	0.02	489	0.40

*Isomer shift, δ, is given relative to α-Fe.

REFERENCES

[1] GREENWOOD, N. N., GIBB, T. C., Mössbauer Spectroscopy, Chapman and Hall Ltd, London, 1971.

[2] LEIDHEISER, H., Jr., GRANATA, R. D., SIMMONS, G. W., MUSIĆ, S., VEDAGE, H. L., Metal Cation Inhibitors for Controlling Denting Corrosion in Steam Generators, Report EPRI NP-2655, 136 pp., Electric Power Research Institute, Palo Alto, California (1982).

[3] LETYUK, L. M., ZHURAVLEV, G. I., Chemistry and Technology of Ferrites (in Russian), Khimiya, Leningrad, 1983.

[4] LINNETT, J. W., RAHMAN, M. M., Mössbauer studies of Fe^{2+} ions in $Ni_xFe_{3-x}O_4$, J. Phys. Chem. Solids, 33 (1972) 1465-1473.

[5] MORRISH, A. H., HANEDA, K., Magnetic structure of small $NiFe_2O_4$ particles, J. Appl. Phys. 52 (1981) 2496-2498.

[6] MORRISH, A. H., HANEDA, K., Surface magnetic properties of fine particles, J. Magn. Magn. Mater. 35 (1983) 105-113.

[7] UEN, T. M., YANG, F. H., Critical slowing down of the spin relaxation and center shift anomaly in $NiFe_2O_4$ observed with Mössbauer spectroscopy, Jpn. J. Appl. Phys. 27 (1988) 955-961.

[8] MacKENZIE, K. J. D., CARDILE, C. M., The formation of nickel ferrite from hematite, magnetite and spinel ironsand, Thermochim. Acta, 165 (1990) 207-222.

[9] MOROZUMI, T., FUJII, T., KOZAKI, T., OHASHI, H., Structural analysis of hydrothermally synthesized nickel ferrite, Bull. Fac. Eng., Hokaido Univ. No. 141 (1988) 183-191.

[10] RAW, G., The Synthesis and Characterisation of Magnetites and Nickel Ferrites, Report AERE-R-10777, Harwell, Oxfordshire, U.K., April 1983.

[11] REFAIT, PH., GÉNIN, J.-M. R. The oxidation of Ni(II)-Fe(II) hydroxides in chloride containing aqueous media, Corrosion Sci. 34 (1993) 2059-2070.

[12] REFAIT, PH., DRISSI, H., MARIE, Y., GÉNIN, J.-M. R., The substitution of Fe^{2+} ions by Ni^{2+} ions in green rust one compounds, Hyp. Interact. 90 (1994) 389-394.

[13] POURROY, G., FERLAY, S., DORMANN, J.-L., Ni/Fe alloy-magnetite composites. Stability in vacuum, Eur. J. Solid State Inorg. Chem. 32 (1995) 313-323.

[14] PEEV, T. M., BOZADJIEV, L., STOILOVA, T., NIKOLOV, S., Mössbauer study of the thermal decomposition of co-precipitated $Fe(NH_4)_2(SO_4)_2 \cdot 6H_2O$ and $Ni(NH_4)_2(SO_4)_2 \cdot 6H_2O$, J. Radioanal. Nucl. Chem. Letters, 85 (1984) 151-162.

[15] MUSIĆ, S., POPOVIĆ, S., CZAKÓ-NAGY, I., DALIPI, S., Characterization of oxide phases generated during the synthesis of $NiFe_2O_4$, Croat. Chem. Acta, 67 (1994) 337-346.

[16] International Centre for Diffraction Data, Joint Committee on Powder Diffraction Standards, Powder Diffraction File, 1601 Park Lane, Swarthmore, Pa. 19081, USA.

[17] MUSIĆ, S., POPOVIĆ, S., DALIPI, S., Formation of oxide phases in the system Fe_2O_3-NiO, J. Mater. Sci., 28 (1993) 1793-1798.

[18] MUSIĆ, S., GOTIĆ, M., CZAKÓ-NAGY, I., POPOVI], S., BALZAR, D., A Study of the Mechanochemistry of Nickel Ferrite by Mössbauer Spectroscopy, Conference Proceedings Vol. 50, ICIAME-95, Rimini (ITALY), 10-16 Sept. 1995., Societa Italiana di Fisica, Bologna 1996, p. 267-p. 270.

[19] PAVLYUKHIN, YU. T., MEDIKOV, YA., YA., BOLDYREV, V. V., On the consequence of mechanical activation of zink and nickel ferrites, J. Solid State Chem., 53 (1984) 155-160.

[20] CAMPBELL, S. J., WU, E., KACZMAREK, W. A., JAYASURIYA, K. D., A Mössbauer effect study of barium ferrite ball-milled in air, Hyp. Interact., 92 (1994) 933-941.
[21] MUSIĆ, S., Mössbauer Spectroscopic Characterization of the Mixed Oxides Containing Iron Ions, in Handbook of Ceramics and Composites, Editor CHEREMISINOFF, N. P., Marcel Dekker Inc., New York-Basel-Hong Kong, 1992, pp 423-463.
[22] MUSIĆ, S. POPOVIĆ, S., RISTIĆ, M., SEPIOL, B., Chemical and structural properties of the system Fe_2O_3-Nd_2O_3, J. Mater. Sci., 29 (1994) 1714-1718.
[23] RISTIĆ, M., POPOVIĆ, S., CZAKÓ-NAGY, I., MUSIĆ, S., Formation of oxide phases in the system Fe_2O_3-Sm_2O_3, Croat. Chem. Acta, 67 (1994) 315-326.
[24] MUSIĆ, S., POPOVIĆ, S., CZAKÓ-NAGY, I., GASHI, F., Formation of oxide phases in the system Fe_2O_3-Gd_2O_3 Part II, J. Mater. Sci. Lett., 12 (1993) 869-873.
[25] MUSIĆ, S., ILAKOVAC, V., RISTIĆ, M., POPOVIĆ, S., Formation of oxide phases in the system Fe_2O_3-Gd_2O_3, J. Mater. Sci., 27 (1992) 1011-1015.
[26] RISTIĆ, M., POPOVIĆ, S., CZAKÓ-NAGY, I., MUSIĆ, S., Formation and characerization of oxide phases in the system Fe_2O_3-Eu_2O_3, Mater. Lett., in press.
[27] DE SOUZA, P. A., Jr., GARG, R., DE JESUS FILHO, M. F., SANTANA, G. P., GARG, V. K., NOWIK, I., Mössbauer Hyperfine Interaction in Mössbauer Treated Europium Iron Mixed Oxide, Proceeding of International Conference on the Applications of Mössbauer Effect, Rimini (Italy), Sept. 10-16, 1995.

DRASTIC REDUCTION OF ASBESTOS TOXICITY BY MICROWAVE RADIATION

H. POLLAK*, Z. L. NKOSIBOMVU*, M. GULUMIAN**,***,
K. AMBARAM***

* Department of Physics, Mösbauer Laboratory, Witwatersrand University
**Biochemistry Research Section, National Centre for Occupational Health
***Department of Medical Biochemistry, Medical School, Witwatersrand University

Johannesburg, South Africa

Abstract

The origin of airborne particles of asbestos is found to be related to the crystallographical structure of the asbestos allied with electrostatic charges of the fibres. The small strips of mineral, four to five cations wide, break due to the electrostatic repulsion between the strips. A microwave irradiation increases the bulk number of positive charges, and as consequence reduces the electrostatic repulsion between fibers and hence the probability of airborne particles. The increase of the number of positive charges in the bulk is shown by Mössbauer spectroscopy. As the peroxidation is the main mechanism of inducing fibrosis and two types of cancers viz bronchogenic and mesothelioma, one expects a major reduction of the toxity of the microwave irradiated fibres compared to untreated fibres.

1. Introduction

Asbestos, one of the oldest minerals used by humans, are today bannded in many applications due to its toxicity. The production of crocidolite, one of the most toxic mineral asbestiforms known, is presently almost zero when it was 130 000 tons 15 years ago. The success of asbestos as an industrial product is due first to its intrinsic properties and secondly to the fact that it is a cheap product. This would have ensured an extremely lucrative business. However, its usage is prohibited because of its toxicity. They are two environmental health hazards because they can cause fibrosis of the lung and two types of malignancies [1].
-bronchogenic carcinoma, a tumour of the epithelial cells lining the upper airways, and
-mesothelioma, a tumour of the serosal cells lining the pleural and peritoneal cavities.
Therefore, lot of efforts have been put for finding substitutes for asbestos, but no one succeeds effectively. Another way, and perhaps the most realistic is to find a way to reduce the toxicity of asbestos. Attempts have therefore been made to modify these fibres to decrease or abolish fibrogenic and carcinogenic effects, and yet retain their desirable physical characteristics. The rationale behind one such treatment due to Flowers [2], is that the human body protects itself against harmful effects of fibres by forming ferruginous bodies, which consists of organic ferric oxides such as ferritin, hemosiderin and organic ferric hydroxides. The process involved the treatment of the fibres with ferric oxide salts to form a metal-micelle polymer to prevent physiological reactions with the mineral. This method indeed coats the fibres, but the protection is lost when the fibres must be machined later on.

In this paper we discuss the origin of the toxicity of some asbestos. The emphasis is put on the crystal structure of the fibres and their rupture surfaces that are at the origin of the surface charges inducing airborne particles and hence toxicity when they are inhaled by human. Knowing the origin of the toxicity we propose a way of reducing it, by changing bulk properties on an atomic scale without changing physical properties. The ideas and methods described in this contribution are patented.

1. 1. Physical structure of crocidolite

To understand the origin of the toxicity of the asbestos crocidolite, we analyse the crystallographic structure of this fibrous riebeckite. The crystal structure is well determined, and even the positions of the hydroxyl groups are known. The five cationic sites are A, M1, M2, M3 and M4 of which only the last four are fully occupied [3]. The extra large site A, when populated, contains almost exclusively Na. The cations in crocidolite are in strip or ribbon made of an alternate succession of rows of four and three sites.

Since the strips are sandwiches between two silicon tetrahedrally oxygenated sites, there is a slight mismatch between the parametes of two types of strips, which induced a tilted distortion of the whole sandwich and is responsible of the helicoidal structure of the crocidolite. This favours the fibrous state and hindered in some way the building of a massive crystal, thus producing fibrils or very small fibres that bundle more or less together. A 3D representation of the crystal is depicted in Figure. 1. The sendwiches are bounded together via the M4 sites

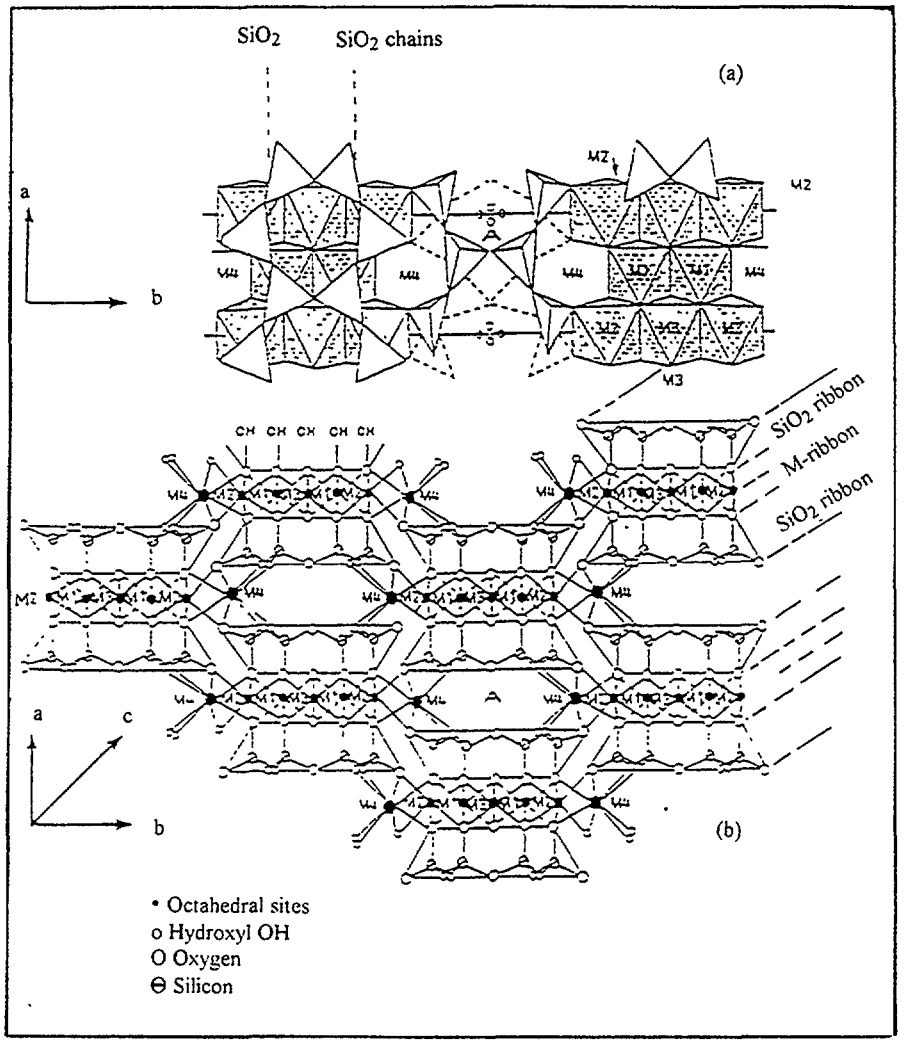

FIG. 1. Crystal structure of crocidolite. (a) Polyhedral representation of the crocidolite structure projected down the a-axis. (b) This representation shows clearly the strip that can be formed by the cation, the rupture layers with the burgeoning group of OH^-, and the large empty A-site that famous the formation of fibers.

leaving large empty sites in between the strips This explains why crocidolite forms fibrils as small as 2 nm which is almost 4 atomic sites wide Five to thirty-five fibrils or strips make up a fibre [4] Note that this structure is favoured by the absence of a cation in the A site. The fibrils have two distinguishable rupture surfaces One is parallel to the a-axis and arises from rupture of the cross-sectional face of the ribbons The other is prependicular to a-axis exposes to b-c planes of the ribbons Two types of hydroxyls groups are thus found at the surface of the fibrils First those not completely bound to the lattice site due to rupture surfaces and therefore not charge compensated and secondly that arising at vacant sites in the bulk octahedral M-ribbon The charge deficiency is at the origin of the negative zeta potential of the crocidolite [5].

1. 2. Toxicity of asbestos

The role of iron in the toxicity of asbestos fibres has been recently reviewed [1, 5] The abilities of iron to reduce oxygen and to decompose hydrogen peroxide and produce hydroxyl radicals are proposed to be some of the reasons for this toxicity [6-9]

$$Fe^{++} \rightarrow Fe^{+++}$$
$$O_2 \rightarrow O_2^-$$
$$H_2^{\bullet} + O_2^- \rightarrow H_2O_2$$
$$Fe^{++} + H_2O_2 \rightarrow Fe^{+++} + HO^{\bullet} + OH^-$$

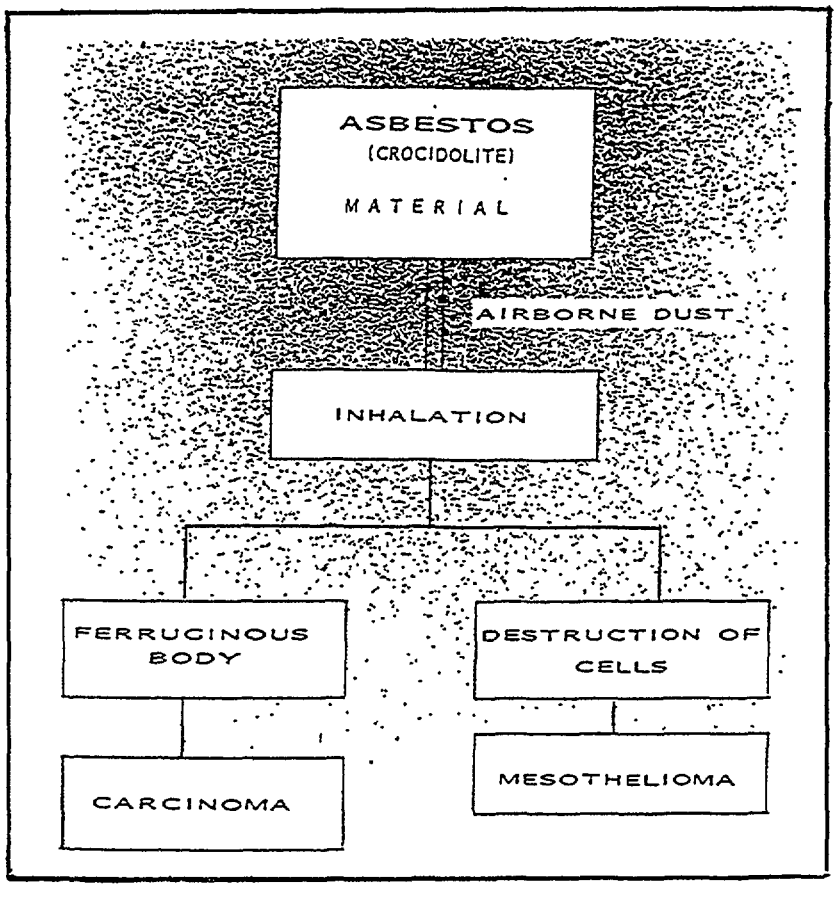

FIG. 2. Effect of asbestos fibers on human bodies.

It is proposed that the hydroxyl radicals ($HO^{\bullet}$) produced from these reactions can attack biological macromolecules, such as membrane lipids, and lead to their peroxidation. The latter process can, in turn, generate other free radicals as well as carbonyl end products, and amplify the demage [10]. The lipid peroxidation through a Fenton reaction is the origin of cancer induced effects. The effect of toxicity of asbestos on human bodies is depicted in Figure 2.

1. 3. Origin of the airborne particle of asbestos

Figure 3 depicts a bundle of crocidolite fibres where the fibres divide themselves in smaller fibre that at their turn divide in fibrils, and this goes on up to strips of a few ions in width (Figure 3a). The fibrils are negatively charges due the surface repture that are like branches with flowers of OH^- groups (Figure 3b). The negative charges on the extremely narrow fibrils or strips repelled each other and they break (Figure 3c and 3d). Due to the presence of the other fibrils still attached to the bundle the extremely small broken parts are expelled from the bundle and are airborne. These particles are of a few microns in length.

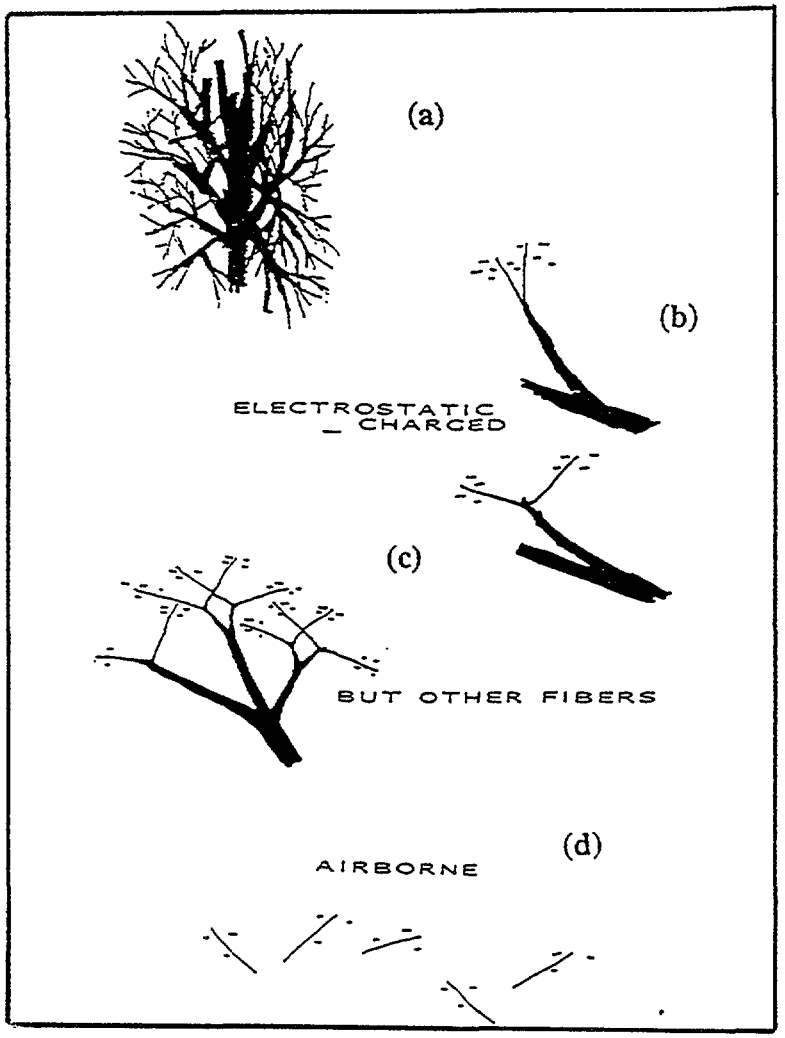

FIG. 3. Airborne of crocidolite dust. This figure emphasised the formation of small particles of crocidolite due to the electrostatic repulsion between fibrils. (a) A bundle of crocidolite fibres. (b) Extremity of a fibre showing the negatively charged fibrils, (c) The fibrils bent due to the electrostatic repulsion, (d) The fibres break and get airborne.

Now these airborne particles are inhaled and go in the lungs of human bodies where they provoke pernicious effect due mainly to peroxidation Fenton reaction catalysed by ferrous ions (Fe^{++}). To reduce the toxicity of crocidolite, the probability of airborne particles must decrease, or the peroxidation mechanism must be inhibited to some extend. The first method is definitively the most effective. The easiest way to reduce the number of airborne particles is to decrease the number of breaks within the fibrils. This requires the reduction of the electrostatic repulsion of the electric charge of this fibrils. This should be acheived by increasing the number of positive charges in the bulk of the bundle of the fibres. Crocidolite normally contains about fifty per cent of its iron in ferrous state and the other in the ferric state as shown by Mössbauer spectroscopy data. All the chemical elements, besides iron presents in crocidolite normally have only valance state. Therefore the only possibilities to increase the bulk positive charge is either to inject positive ions or to change a ferrous ion into a ferric ion. This last process should have another advantage as the number of ferrous ions is reduced, the catalytic effect of the ferrous ions in the Fenton reaction is also decreased. This means that this method should provide a multiplicative effect on the reduction of the toxicity: reduction of airborne particles times the reduction of the peroxidation reaction. Microwave irradiation can induce the transformation of Fe^{++} into Fe^{+++} and thus achieve the above effects.

2. Materials and Methods

The crocidolite was South Africa commercial fibres obtained from the company EVERITE. The fibres were crushed by a mechanical crusher to minimise orientation effects in the Mössbauer studies. The crushed samples ranged between 5 and 10 μ in length and 3 μ in diameter. Some of the fibres were irradiated for 20 min by 2.3 GHz microwaves with a power of 7.5 kW. The temperature of the fibres did not exceed 300 °C. This preserves the structure, as crocidolite lost water at 360 °C. Mössbauer spectra were recorded in a conventional geometry at room temperature and 80 K for both the normal and the irradiated samples. ^{57}Co source was used. Velocity calibrations were performed using a Michelson interferometer, and each spectrum was fitted with Lorenztian lines as the samples thickness was such that no correction was needed. Crocidolite samples, before and after microwave irradiation, were also used to study the ability of the samples to initiate lipid peroxidation. Crocidolite was added to linoleic acid in Tris buffer at pH 7.4 and they were incubated at 37 °C for 21 hours. Preparation of the fibre suspensions in buffer was relatively easier for the original fibres than the irradiated samples. Detection of aldehydic end products from the peroxidation of linoleic acid was achieved by gas chromatography-mass spectrometry detection (GC-MD) [11]. At the end of the incubation, sodium borohydride was added and the samples further incubated at room temperature. After reduction of the pH to 1 with hydrochloric acid, an extraction was done with dichloromethate. The extracts were evaporated under nitrogen and the residue treated with pyridine and N,O-Bis(trimethylsilyl)tri-fluorocetamide and injected in the GC-MSD.

3. Mössbauer data

The Mössbauer spectra measured at room temperature of the crocidolite samples, before and after radiation, are depicted in Figures 4 and 5. The spectra were deconvoluted with quadrupole doublets corresponding to Fe at various lattice sites in either ferric or ferrous oxidation states [13, 14]. Table I shows Mössbauer parameters measured for the original and the microwave irradiated samples. Fe-site population shown in this table indicates that the original sample, M1 site contained both oxidation states of iron in proportions of 25 % Fe^{++} ions. M2 site contained Fe^{+++} only (21 %), and M3 contained Fe^{++}

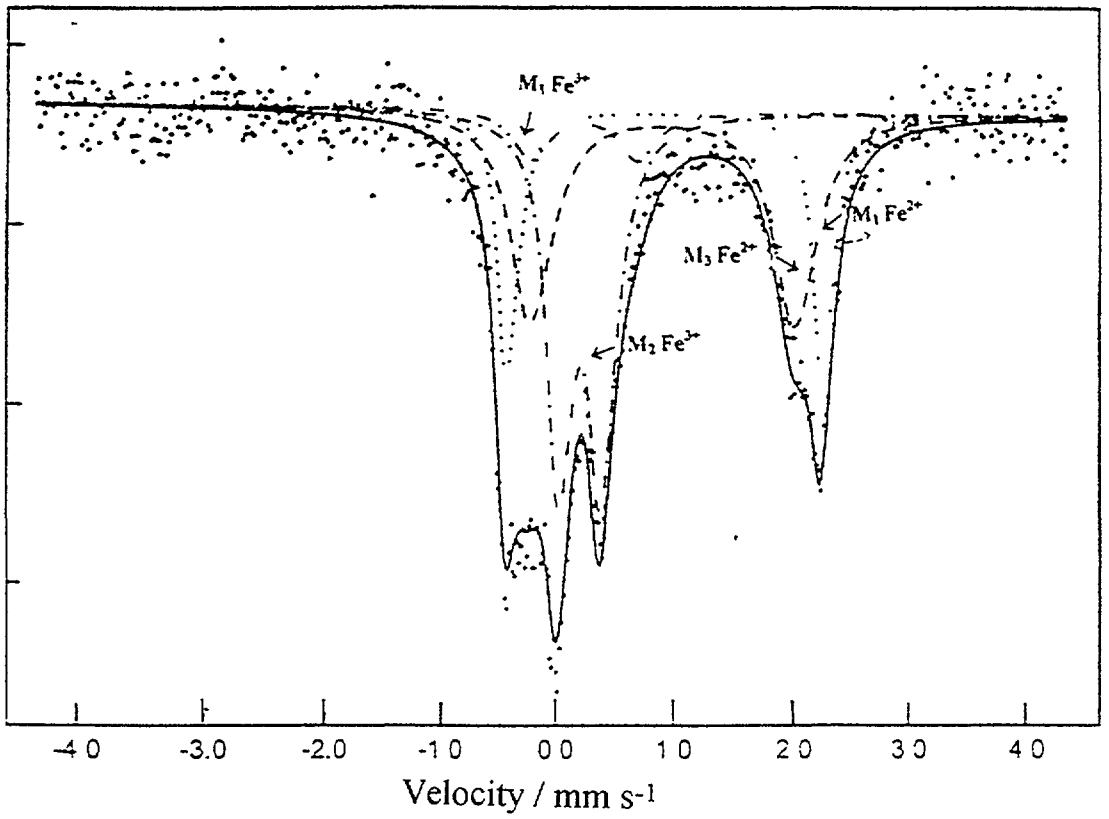

FIG 4 Mossbauer spectrum of commercial crocidolite. Note the four quadrupole doublets representing the four iron sites including charged states

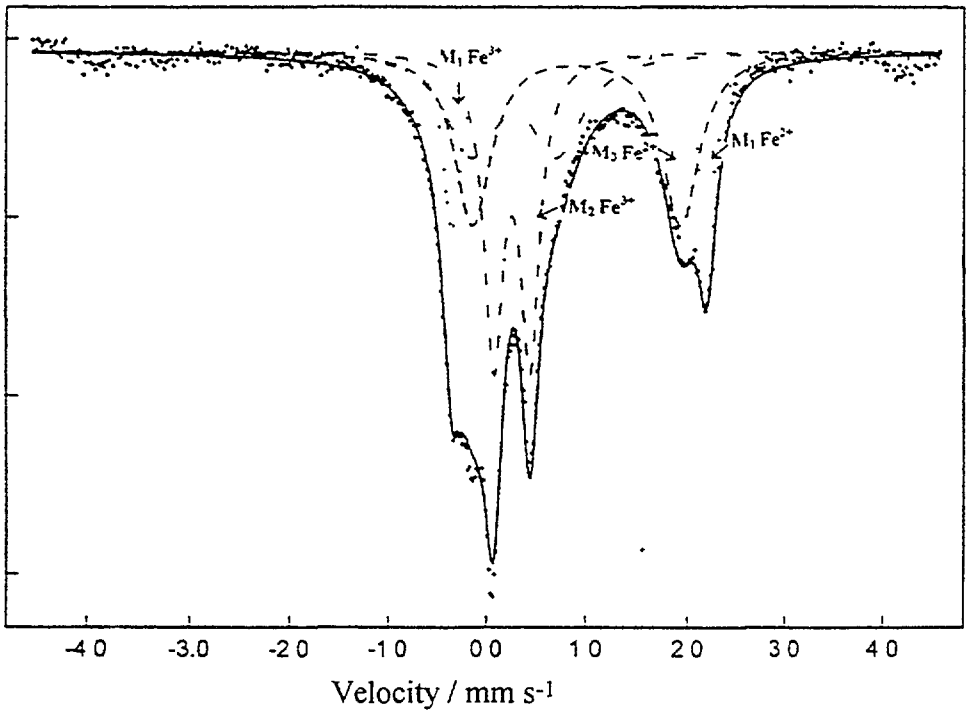

FIG 5 Mossbauer spectrum of microwave irradiated crocidolite This picture is to be compared with Figure 4 The main difference is in the intensity of the high velocity peaks that have noticeable decrease, thus clearly indicating a reduction of the ferrous content

TABLE I. MÖSSBAUER PARAMETERS OF CROCIDOLITE BEFORE AND AFTER MICROWAVE IRRADIATION.

Site	δ (mm s^{-1})	Δ (mm s^{-1})	A (%)	Ratio Fe^{++}/Fe^{+++}
Initial sample				
M1	0.97	2.59	25	1.35
M3	1.06	2.00	33	
Total Fe^{++}		58		
M1	0.22	0.73	22	
M2	0.33	0.34	21	
	Total Fe^{+++}	43		
Microwave irradiated sample				
M1	0.91	2.50	16	0.90
M3	0.89	2.10	31	
Total Fe^{++}		47		
M1	0.23	0.75	32	
M2	0.24	0.37	21	
Total Fe^{++}		53		

δ: Isomeric shift is versus α-Fe, error ±0.03 mm s^{-1};
Δ: Quadrupole splitting, error ±0.03 mm s^{-1};
A: Relative intensity, error ±3%

only (33 %). Site occupation of ferric and ferrous ions agreed with the results obtained with UICC (Union International Contre le Cancer) crocidolite samples (tested earlier but differed only a little in their per cent distribution at the corresponding site [11, 12]. Note that UICC crocidolite is a mixture a various crocidolite originating from various minerological sites all over the world. From the table, it can be seen that the microwave irradiation of the samples decreased the ferrous population of the M1 site from 25 % to 16 % and has increased the ferric population from 22 % to 32 %. This treatment however, did not affect the ferrous population at the M3 site (31 %) not the ferric population at the M2 site (21 %). The treatment has therefore changed the ratio of Fe^{++}/Fe^{+++}, in the M1 site, from 1.14 to 0.50 by coverting the ferrous ions into the ferric ions.

4. Lipid peroxidation

The effect of the change in the ionic oxidation state at M1 site on the ability of the two types of fibres to initiate peroxidation of linoleic acid was investigated. The five of the identified carbonyl end products from the peroxidation are represented in Table II. In the control samples containing linoleic acid, only hexanal and 4-hydroxynonenal could be identified. The addition of the original crocidolite fibres could change the number of the products detected and could also increase the level of the hexanal and 4-hydroxynonenal detected in the control samples.

Table II.1 are presented the two identified BSTFA-derivatives of alcohols obtained from the reduction of their corresponding peroxides produced from the peroxidation of linoleic acid in the absence (control) and the presence of 1 mg/ml original commercial crocidolite or 1 mg/ml radiated crocidolite. The values of each product were calculated as the area under the peaks obtained from mass spectra.

TABLE II.1

SAMPLE	9-HOPDE	13-HOPDE
Control	2 679 130	634 490
Original	9 121 272	1 565 987
Irradiated	3 723 737	557 418

In Table II.2 are presented the five identified BSTFA-derivatives of alcohols obtained from the reduction of their corresponding aldehydes produced from the peroxidation of linoleic acid in the absence (control) and the presence of 1 mg/ml original commercial crocidolite or 1 mg/ml radiated crocidolite. The values of each product were calculated as the area under the peaks obtained from mass spectra.

Table II.2

SAMPLE	Hexanal x 10^6	Heptanal x 10^5	2-heptanal x 10^6	Nonenal x 10^5	4-hydroxy nonenal x 10^6
Control	13.27	0.00	0.00	0.00	8.15
Original	46.14	4.95	4.51	10.31	51.29
Irradiated	16.39	1.72	2.55	1.96	29.08

The addition of irradiated samples to the radiation mixture, on the other hand, could produce the same end products detected with the original samples but of much reduced levels of all the detected products. These reactions therefore indicate that the microwave radiation treatment could reduce the ability of crocidolite to initiate lipid peroxidation and/or to decompose the preexisting lipid hydroperoxide and produce the carbonyl end products. In previous work [14] conversion of ferric ions into ferrous ions by reduction could produce a more active fibre, attributed to an increase of ferrous ions occupying the M1 site [15]. This is indeed a consistency prove of our idea that the peroxidation is related mainly to the relative content of ferrous ions.

5. Conclusion

From the earlier results of the Mössbauer spectroscopy [12, 13] and from those presented in the present work, it can be suggested that, by changing the oxidation state of iron, especially of the iron ions occupying the M1 site, it is possible to change the activity of the crocidolite fibres. The valency of iron seemed to be an important factor which determined the activity of the crocidolite fibres. This confirmes early, preliminary, observations by other authors [16, 17]. Further tests are, however, required to confirm the reduced toxicity of the treated fibres towards cells in culture in the presence of various biological available reducing as well as chelating agents. These studies are necessary to investigate the behaviour of oxidized iron in the M1 site under these conditions. Mössbauer studies have revealed that

substantial changes occur in crocidolite when it is irradiated by means of microwave radiation. The modifications in the bulk material include a change of ferrous ions into ferric ions principally at the M1 site. These valence changes may modify the electrostatic properties as indicated by the the difficulty to suspend these fibres in aqueous solutions and also inhibit the ability of airborne particles. Morever, the decrease in ferrous ions produced a decrease in the ability of the fibres to initiate the peroxidation of linoleic acid. The reduction of the toxicity arises from a multiplicatie effect, the first one is a reduction of the probability of the fibres to be airborne and the second in a reduction in the ability of peroxidation. Therefore, we observe a drastic reduction in the toxicity of the fibres.

Acknowledgment

The authors thank Dr. G. Tumback for the microwave radiation and Mr Enoch Mogomotsi for determining the size distribution of the fibres. This work was possible through FRD and IAEA grants (contract 8394/RB).

REFERENCES

[1] AUST, A. E., in NATO ASI Series, Vol. H85, Cellular and Molecular Effects of Mineral and Synthetic Dust and Fibres, p. 53, 1994, ed. DAVIS, J. M. G. and JAURAND, M. C., Springer Verlag, Berlin.
[2] FLOWERS, S. E., Proc. Nat. Workshop on Subsitutes for Asbestos, Arlington, VA, USA (1980) 489.
[3] HAWTHORNE, F. C., Can. Miner. 16 (1978) 31; 187.
[4] BONNEAU, L., BUGUET, C., MALAROL, C., PEZERAT, H., Environ. Res. 41 (1986) 41.
[5] BARON, P. A., Deye, G., Am. Ind. Hyg. Assoc. J., 51 (1990) 63.
[6] HARDY, J. A., AUST, A. E., Chem. Rev. 95 (1995) 97.
[7] GULUMIAN, M., van Wijk, J. A., Chem. Biol. Interact. 62 (1987) 89.
[8] WEITZMAN, S. A., and GRACEFFA, P., Archiv. Biochem. Biophys., 228 (1984) 373.
[9] ZALMA, R., BONNEAU, L., GUIGNARD, J., PEZERAT, H., JAURAND, M. C., Can. J. Chem. 65 (1987) 2338.
[10] ESTERBAUER, H., SCHAUR, R. J., ZOLNER, H., Free Rad. Biol. Med., 11 (1991) 81.
[11] GULUMIAN, M., AMBARAM, K., VERDOON, G. G., in NATO ASI Series, Vol. H85, Cellular and Molecular Effects of Mineral and Synthetic Dust and Fibres, p. 417, 1994, ed. DAVIS, J. M. G. and JAURAND, M.-C., Springer Verlag, Berlin.
[12] POLLAK, H., De WAARD, H., GULUMIAN, M., S. Afr. J. Sci., 89 (1993) 401.
[13] HEARNE, G. R., KOLK, B., POLLAK, H., Van WIJK, J. A., GULUMIAN, M., J. Inorg. Biochem., 50 (1993) 145.
[14] GULUMIAN, M., BHOOLIA, D. J., THEODOROU, P., ROLLIN, H. B., POLLAK, H., Van WIJK, J. A., S. Afr. J. Sci., 89 (1993) 405.
[15] GULUMIAN, M., BHOOLIA, D. J., Du TOIT, R. S. J., RENDALL, R. E. G., POLLAK, H., Van WIJK, J. A., RHEMPULA, M., Environ. Res., 60 (1993) 193.
[16] ZALMA, R., BONNEAU, L., GUIGNARD, J., PEZERAT H., JAURAND, M. C., Toxicol. Environ. Chem., 13 (1987) 171.
[17] FONTECAVE, M., JAOUEN, M., MANSUY, D., COSTA, D., ZALMA, R., PEZERAT, H., Biochem. Biophys. Res. Comm., 137 (1990) 912.

THE REDUCTION OF MAGNETITE BY Al AND Mg INDUCED BY MECHANICAL ALLOYING

L. TAKACS
Department of Physics, Maryland University,
Catonsville, Maryland,
United States of America

H. DLAMINI
Department of Physics, University of the Witwatersrand,
Johannesburg, South Africa

H. POLLAK
Department of Chemistry, Applied Chemistry and
Chemical Technology Unit, University of the Witwatersrand,
Johannesburg, South Africa

Abstract

The reduction of magnetite by Al and Mg has been induced by mechanical alloying. Milling initiated self propagating thermal "explosion" in these systems after some incubation period. Mössbauer spectroscopy and X-ray diffraction have been used to investigate the reaction products. The shortest incubation time before explosion was measured close to the stoichiometric composition for the reduction of magnetite by Al, but far from stoichiometry when Mg was used.

1. Introduction

The initation of self propagating combustive reactions during the mechanochemical reduction of a metal oxide by a more reactive metal has been demonstrated in a number of systems [1-3]. Combustion can be avoided by using appropriate milling conditions if ball milling of the same mixtures is used to prepare oxide-metal nanocomposites [4].

In this paper the reaction of magnetite by Al and Mg is investigated. The reaction heat associated with the displacement of one mole of oxygen. DQ and the ratio of the reaction heat and the room temperature heat capacity, DQ/C, are given in Table I. DQ/C characterises the self heating of the reaction, a useful parameter when evaluating whether a reaction can become combustive. The data suggest that both reactions are highly exothermic and an explosive reaction should occur after a short incubation time.

TABLE I. THERMODINAMIC PROPERTIES OF THE INVESTIGATED REACTIONS

Reaction	DQ (kcal/mole)	DQ/C (K)
$3Fe_3O_4 + 8Al \rightarrow 9Fe + 4Al_2O_3$	66.9	6130
$Fe_3O_4 + 4Mg \rightarrow 3Fe + 4MgO$	77.0	5770

2. Experimental

Mixtures of $3Fe_3O_4 + xAl$ and $Fe_3O_4 + yMg$ were milled using SPEX 8000 Mixer/Mill and round ended hardened steel vials. The stoichiometric compositions corresponded to x=8 and y=4, off stoichiometric mixtures were milled for $6<x<16$ and $1.4<y<5.5$. The values of x and y are used to label the samples. The combustion reaction was detected by measuring the temperature of vial using a thermocupole. Mössbauer spectra were recorded at 298 K and 80 K in the conventional mode, using a $^{57}Co(Rh)$ source and a constant acceleration transduser.

3. Results

Fe_3O_4-Al mixture

The room temperature Mössbauer spectrum (x=8 in Figure 1) is determined by the sextet of pure α-Fe as anticipated. As the amount of Al is increased or decreased, very different changes of the spectra occur (x=6 and 11 in Fig. 1). The incubation time strongly depends on the Al content (Figure 3.) with a minimum close to the stoichiometric composition. The reaction products identified by X-ray diffraction and Mössbauer spectroscopy are listed in Table II. When the Al composition is below stoichiometry, full reduction of the iron oxide to metallic iron is not possible. For example, the Mössbauer spectrum for sample 6 shows the presence of magnetically split component and a broad quadrupole split doublet. The magnetic component can be described by two sextets with

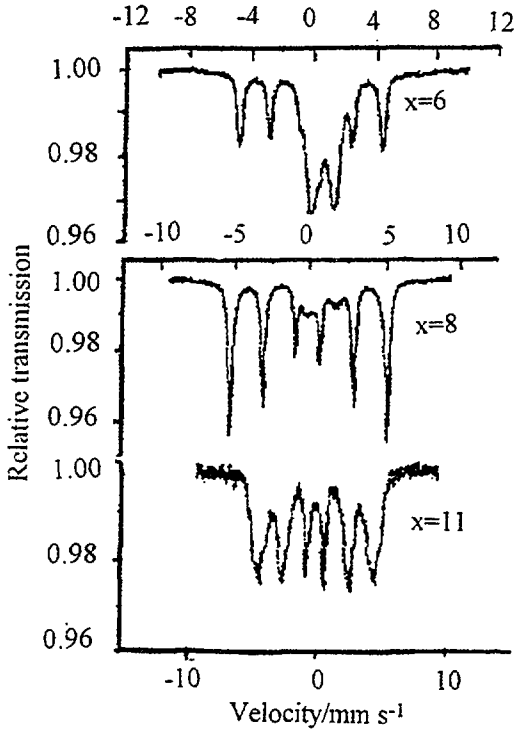

FIG. 1. Mössbauer spectra of milled Al and Fe_3O_4 powders (X=Al composition).

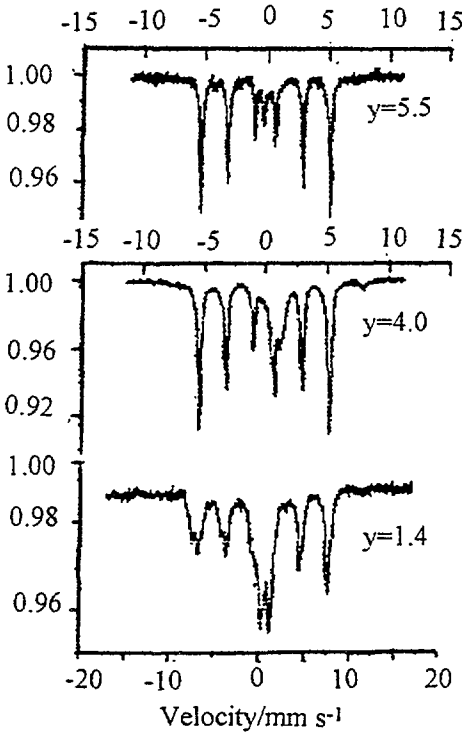

FIG. 2. Mössbauer spectra of milled Mg and Fe_3O_4 powders (Y=Mg composition).

TABLE II. THE VARIATION OF THE REACTING PRODUCTS AND INCUBATION TIME WITH AL COMPOSITION

Sample	Incubation time (min)	Reaction products
6	53	α-Fe, $FeAl_2O_4$
8a	10	α-Fe, $FeAl_2O_4$, (α-Al_2O_3, γ-Al_2O_3)*
8b	8	α-Fe, Fe_3O_4, $FeAl_2O_3$, (α-Al_2O_3, γ-Al_2O_3)
11	14	α-$Fe_{0.6}Al_{0.4}$
16	56	α-$Fe_{0.4}Al_{0.6}$, $Fe_{0.5}Al_{0.5}$

*Phases identified by XRD
Sample 8b was interrupted 10 s after combustion.

hyperfine fields due to the perturbed environments around the Fe nuclei. Data obtained at 80 K can be described by a single hyperfine field of 32.4 T. The larger and less uniform reduction of the hyperfine field at room temperature suggest that the small particle size and high defect concentration results in the lowering of the Curie temperature as well as the reduction of the local magnetisation. The paramagnetic doublet corresponds to the presence of the normal spinel hercynite with Al substituting in both the A and B site of magnetite [5]. The low Al content does not favour the formation of α-Al_2O_3 and γ-Al_2O_3 contrary to the chemical equation suggested in Table I. When stoichiometric amount of Al used to reduce magnetite the product is dominated by α-Fe. The lattice defects and small particle size result in the reduction of the hyperfine field as before, but the deviation from the bulk value is less, the hyperfine fields of the two components are H=32.5 T, H=31.3 T. Any alloying into this phase can be excluded as it would result in spectral components with smaller hyperfine fields. The non magnetic component corresponding to the spinel is still present, but with reduced intensity. XRD data show the presence of α-Al_2O_3 and γ-Al_2O_3, not seen for low amounts of Al. When milling is interrupted after the beginning of combustion (sample 8b) a very complicated mixture containing the above phases and also some of the starting materials is found. This suggests that the combustion reaction does not extend to the full volume of the milling vial, completion of the reduction is only achieved after further milling. In the presence of exccess Al, α-Al_2O_3 and a crystalline Fe(Al) solid solution form. The average hyperfine field of 23 T and the width of the hyperfine distribution are comparable to those of Fe-Al alloys prepared by sputtering. [6].

Fe_3O_4-Mg mixture

Some typical Mössbauer spectra are shown in Figure 2, the ones with stoichiometric (y=4) and higher Mg content are taken after combustion. No combustion was observed for y=4, but gradual reaction was induced by 2 hours of milling. No minimum of the incubation time has been found close to the stoichiometric composition of y=4, instead an almost linear decrease has been observed with a decreasing Mg content from y=5.5 to below 2 as shown in Figure 4. At very low Mg contents the reaction turns gradual within a narrow composition range. In spite of the apparent lack of correlation between off-stoichiometric and incubation time the reaction products relate to off-stoichiometry similar to the Fe_3O_4-Al

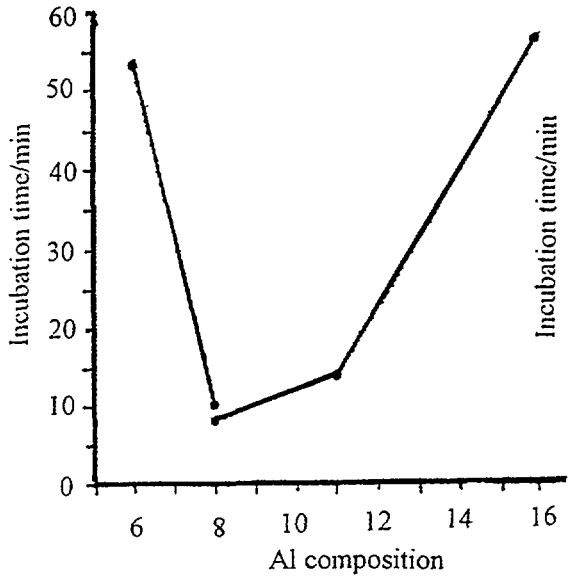

FIG. 3. The variation of the incubation time with Al composition

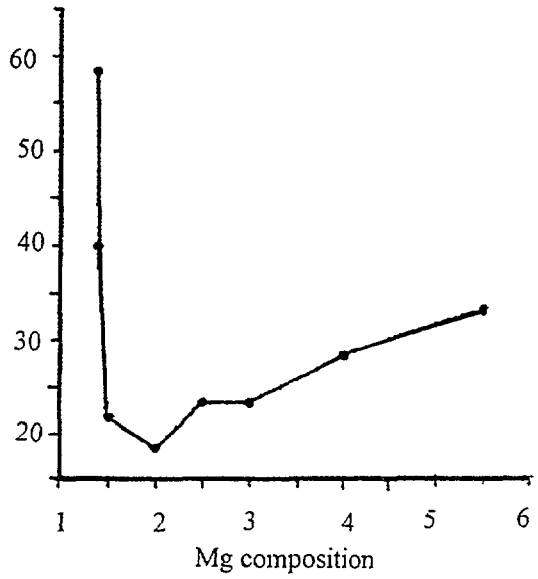

FIG. 4. The variation of the incubation time with Mg composition

system. The main difference is that the solubility of Mg in Fe is very limited. As a consequence, the hyperfine field of the α-Fe is not reduced by the dissolved Mg, any extra Mg remains unreacted. The isomer shift of the little paramagnetic singlet is 0.04 mm s^{-1} suggesting metallic iron. A small amount of fcc phase was indeed found by X-ray diffraction. The stoichiometric sample y=4 shows some residual oxidised iron, as if some Mg had been lost from the reaction. This could happen due oxygen contamination or plating of some Mg metal onto the inner surface of the milling vial. A paramagnetic doublet is observed with a very large isomer shift, corresponding to Fe^{3+}. This suggest Fe^{3+} inclusion in an MgO matrix to give an Fe(Mg)O phase. A small amount of magnetite is also observed. As the amount of Mg is decreased, the relative intensity of the ferrous doublet increases as expected. At the lowest Mg content of y=1.4 magnetite is gradually reduced to an oxide containing ferrous iron only. According to the reaction stoichiometry, some metallic iron could be produced for any Mg content above y=1. A very small α-Fe component has indeed been found by X-ray diffraction, but the corresponding Mössbauer lines are masked by overlapping.

3. Conclusions

The reduction of magnetite by Al or Mg have similar thermodynamic properties. Nevertheless, ignition of combustion is very different in the two systems. Combustion starts much easier (with small balls) and after a short activation time when Al is used. The activation time before ignition has a minimum close to the stoichiometric composition for Al but not for Mg. The reasons for these differences are not understood yet.
In spite of the differences in the initation of combustion, the reaction products relate to stoichiometry in very much the same way in both systems. There are two differences: (a) Al is soluble in Fe while Mg is not. Therefore, an FeAl alloy forms if excess Al is available, but no alloying of Mg into Fe is found. (b) Intermediate mixed oxides play an important role in the process, but these oxides are different due to the different valencies of Al and Mg. The spinel $FeAl_2O_4$ is produced with Al and Fe(Mg)O mixed oxide forms with Mg. These conclusions are consistent with Mössbauer spectroscopy and X-ray diffraction data.

Acknowledgement

The authors thank the IAEA for the contract 8394/RB

References

[1] SCHAFFER, G. B., McCORMICK, P. G., Mater. Sci. Forum, 779 (1992) 88-90.
[2] TAKCS, L., Mater. Lett., 13 (1992) 119.
[3] SHEN, T. D., WANG, K. Y., WANG, J. T., QUAN, M. X., Mater. Sci. Engin., A151 (1992) 189.
[4] PARDAVI-HORVATH, M., TAKACS, L., IEEE Trans. Magn., 28 (1992) 3186.
[5] MURAD, E. and JOHNSTON, J. H., (1987), in Mossbauer Spectroscopy Applied to Inorganic Chemistry, Vol. 2, edited by LONG, J. H., (Plenum Publ. Corp.) pp. 507.
[6] HSU, J. J., CHIEN, C. L., Hyp. Int., 69, (1991) 451.

INFLUENCE OF PREPARATION CONDITIONS ON PRECIPITATED IRON OXIDES AND HYDROXIDES: A MÖSSBAUER SPECTROSCOPY STUDY

H. DLAMINI, H. POLLAK, N.J. COVILLE, J.A. VAN WYK
University of the Witwatersrand,
Johannesburg, South Africa

XA9949652

Abstract

A mixture of hematite and an amorphous Fe(III) hydroxide species are formed during the preparation of precipitated iron based catalysts. The percentage of the two phases varies with the change in the preparation conditions. Mössbauer spectroscopy reveals that maximum hematite was formed between pH 6-7 and C_{Fe3+}/C_{Na2CO3} of 0.33-0.375 corresponding to an increase in product crystallinity as determined from XRD line broadening analysis. The change in the product distribution with preparation conditions suggests the presence of two competing reactions. Particle size distribution of the hematite phase indicates that nucleation and particle growth occur at the same time.

1. Introduction

The preparation of catalysts through precipitation has always proved to be unpredictable, because of the variables involved in the preparation. The use of precipitated iron based catalysts in the Fischer-Tropsch process dates back to the time when the process was discovered. However, recent literature reviews [1-3] have pointed out the lack of fundamental knowledge on the effect of the preparation conditions on the physico-chemical nature and catalytic behaviour of the precipitates. The conditions which can affect the precipitate are, the final pH of the precipitate, the concentration of the solutions used, the time over which the precipitation occurs, the precipitation temperature, the type of precipitating agent used etc. The information often obtained from catalyst characterisation pertains to phase composition, particle size and morphology, surface composition, crystallinity, as well as pore dimensions. Information on phase and surface composition may be difficult to obtain for small particles, as these become transparent to most spectroscopies except Mössbauer spectroscopy.

In our study we have attempted to relate the conditions used in the synthesis of iron based catalysts to the iron phases, crystallite size, pore volume and surface area as well as magnetic properties of the precipitates thus formed.

2. Results and Discussion

The Mössbauer spectra of samples prepared at pH 9.8, 7.2 and 4 are shown in Figure 1. The spectra show the presence of a sextet (M) and a paramagnetic doublet (P). The hyperfine parameters of the sextet, as well as XRD analysis, suggest the presence of hemetite (α-Fe_2O_3). This forms with a distribution of particle sizes to give a sextet with broad lines (Γ=0.35 mm s^{-1}). Lattice deffects or the inclusion of Na+ in the hematite structure would explain the reduced hyperfine field of hemetite and brodened XRD peaks. Mössbauer spectra obtained at 80 K show an increase in the intensities of the magnetic component. This increase is due to hematite with a particle size less than 8 nm which exhibits paramagnetic behaviour at 298 K and magnetic ordering at 80 K. The paramagnetic doublet (δ=0.217 mm s^{-1}, Δ=0.684 mm s^{-1}, Γ=0.52 mm s^{-1} with respect to BCC Fe) can be assigned to a mixture of ferric oxide and hydroxide. This component results in XRD peaks at low angles corresponding to large *d*-values indicating the presence of an amorphous phase.

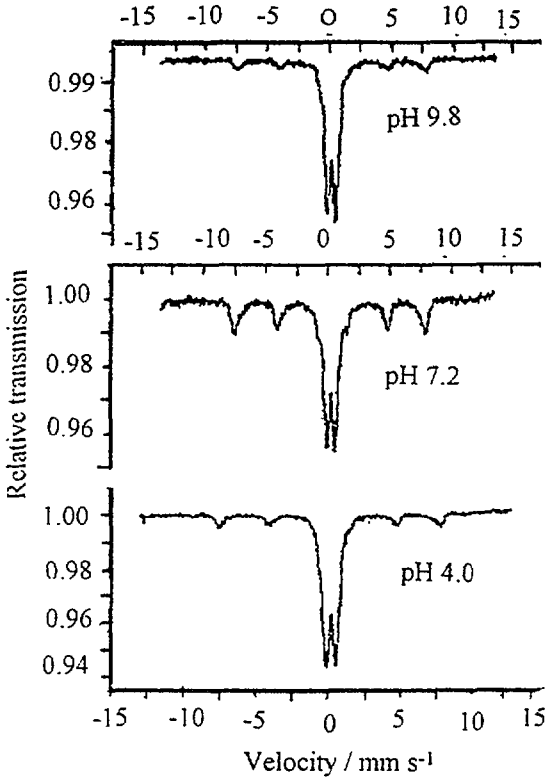

FIG. 1. Mössbauer spectra of precipitates prepared at different pH's at 289 K.

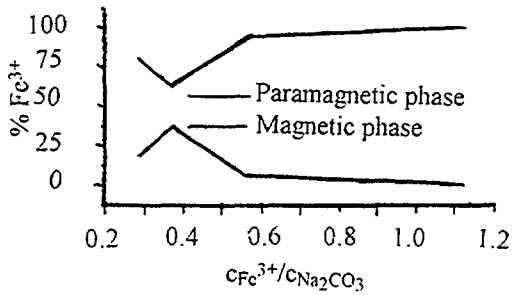

FIG. 2. The variation of %Fe^{3+} in P and M phases with concentration ratio

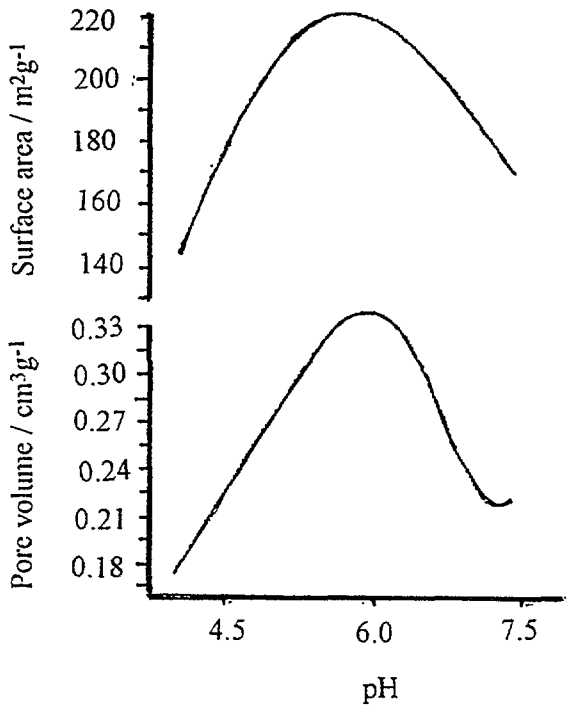

FIG. 3. The change in surface area and pore volume with pH.

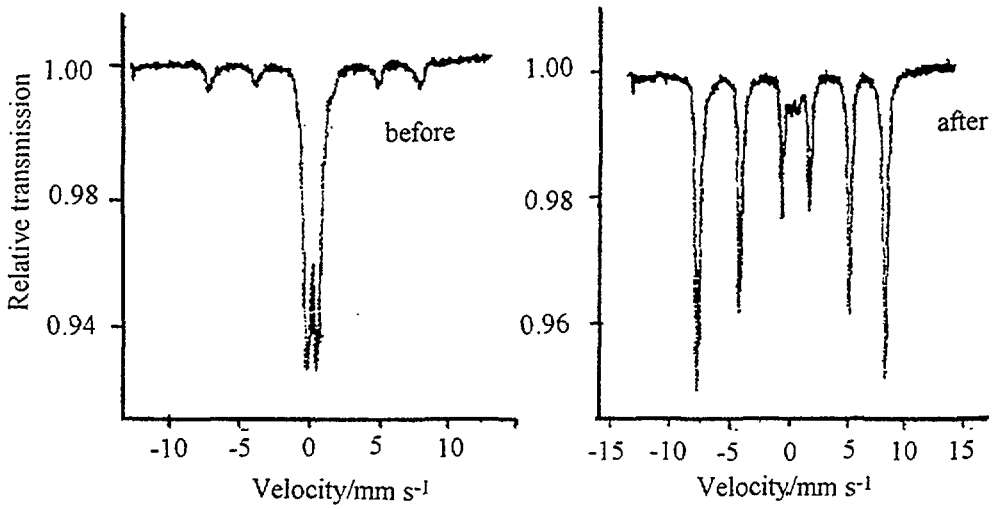

FIG. 4. Mössbauer spectra of the sample prepared at pH 9.8 before and after ESR (heated under air from 25 to 300 °C).

Figure 2 shows the effect of the ratio of Fe^{3+}/Na_2CO_3 concentrations on the amount of iron in the magnetic and paramagnetic components. A maximum amount of the hematite forms at $C_{Fe3+}/C_{Na_2CO_3}$ of 0.38. No change in the type of iron phase formed is observed. The surface area and pore volume of the precipitates varies with preparation conditions as shown in Figure 3.

These reach a maximum at pH 6-6.5 corresponding to $C_{Fe3+}/C_{Na_2CO_3}$ of 0.33-0.38. Decreasing the precipitation time and hence the ageing time of the precipitate favors the formation of the hydroxyl species. Similarly low temperatures slow down the hydrolysis reaction of ferric ions.

ESR spectroscopy shows the presence of a peak which disappeares at 573 K and is irreversible as expected. The room temperature Mössbauer spectra of the pH 9.8 sample, before and after ESR experiment was done, are shown in Figure 4. The sample after ESR shows an increase in the magnetic component with a small paramagnetic doublet. This increase in the magnetic phase can be a result of the transformation and re-arrangement of iron hydroxide species such $Fe_5HO_8 \cdot 4H_2O$ to give α-Fe_2O_3 which explains the reversible nature of this resonance peak. The small paramagnetic component is a result of the presence of small particles of hematite as observed before. Heat treatment studies confirm that the paramagnetic component is composed of the unstable hydrolysis products which convert to hematite on heating. Changing the order of addition of the reacting salts results in the formation of goethite with no hematite. This is suggestive of a change in the reaction pathway for the precipitation process.

3. **Conclusions**

The major phases formed during preparation of precipitated iron based catalysts from iron nitrate and sodium carbonate are hematite and a hydroxyl species whose ordering at 80 K is similar to that of ferrihydrite. On changing the preparation conditions one observes a shift in the relative amounts of iron present in the P and M component. The hematite phase presents a particle size distribution with about 8.5 % of the material being

smaller than 8 nm, which is paramagnetic at 298 K. This shows that both crystal growth and nucleation are taking place simultaneously during precipitation. Hematite forms by the hydrolysis of the Fe^{3+} hexa-aqua ion. We have observed that rapid precipitation, low temperatures and highly acidic as well as as highly basic conditions inhibits the hydrolysis process, resulting in the formation of an amorphous phase with a paramagnetic Mössbauer spectrum. A maximum amount of hematite was formed at pH 6-7 and C_{Fe3+}/C_{Na2CO3} of 0.33-0.38. Particle size distribution of hematite suggests that growth of this phase happens via nucleation at higly basic pH with crystal growth occuring once supersaturation has been attained in the reactor. The phase transformation of the unstable hydrolysis products into either goethite (α-FeOOH) or hematite (α-Fe_2O_3) depends strongly on the order of addition of the reacting salts.

References

1. DRY, M. E., in Catalysis-Science and Technology, Vol. 1 edited by ANDERSON, J. R. and BOUDART, M. (Springer, Berlin), (1981), 159.
2. DIFFENBACH, R. A., FAUTH, D. J., J. Catal., 97 (1986) 121.
3. RAO, V. U. S., STIEGEL, G. J., CINQUEGRANE G. J., SRIVASTAVA, R. D., Fuel Processing Technology, 30 (1992) 83.
4. POLLARD, R. J., Mössbauer Spectra of Iron Oxides and Oxyhydroxides in Applied Magnetic Fields., Internal report, Dept. of Physics, Monash University (1992).

BALL MILLING OF CHALCOPYRITE: MÖSSBAUER SPECTROSCOPY AND XRD STUDIES

H. POLLAK, M. FERNANDES, D. LEVENDIS, L. SCHONIG
Mössbauer Laboratory, Departments of Physics and Chemistry,
University of the Witwatersrand,
Johannesburg, South Africa

Abstract

The aim of this project is to study the behavior of chalcopyrite under ball milling for extended periods in order to determine how it's decompose or transform. Tests were done with chalcopyrite mixed with iron and zinc with and without surfactant. The use of surfactants has various effects such as avoiding oxidation and clustering of the fine particles. In all case magnetic chalcopyrite is transformed into a paramagnetic component showing a disordered structure, thus reveailing that Cu atoms have replaced Fe atoms. In the case of ball milling in air, chalcopyrite is decomposed with the lost of iron, while in milling under surfactants, iron enters into the chalcopyrite structure.

1. Introduction

Iron in chalcopyrite is present in the ferric state with high spin d5 electron configuration Fe^{3+} [1]. This means that iron is in tetrahedral site, Cu is Cu^{+}, and sulphur is S^{-}. The crystal structure of chalcopyrite $CuFeS_2$ has been extensively investigated by Hall [2] as well as the isomorphous compounds talnakhite, mooihoekite and haycockite. The principal structural aspect of the last three minerals is the presence of extra metallic atoms located at interstitial sites and can be considered as superstructure of chalcopyrite [3]. Chalcopyrite is antiferromagnetic at room temperature [4]. Chalcopyrite decomposes at 663 K in air [5]. Various studies of the effect of grinding chalcopyrite have been published, mostly by a Tchek group leads by Tkacova [6-9]. Discussing these results, they consider that iron goes from the high spin to the low spin form and that sulphur changes its valence from 2^{-} to 6^{-}. This result seems somewhat curious, especially that the authors assume the formation of copper sulphates and ferric oxides. Changes in the structure of chalcopyrite brought by mechanical activation causes exothermic oxidative reactions to proceed at temperatures as 180 °C lower than in non activated sample [8].

2. Experimental methods

2. 1. X-ray powder patterns

All samples were run with the same setting; i. e. 40 kV and 20 mA, without spinning. Two types of scan differing only in the 2Θ range and collection time were used. The 2Θ ranges used were 5-140 °C in 45 minutes and 42-60° in 30 minutes for the different scans.

2. 2. Mössbauer spectroscopy

The samples were those used for the XRPD measurements. The samples of about 5 mg were mixed with "cremona" to avoid any broadening due to tickness effects. All spectra were recorded with more than 750 000 counts in each of the 512 channels obtained after folding. All analysis were done using either in-house computer algorithms or MOSFUN [10].

2. 3. TGA and DSC procedures

The original chalcopyrite sample was run in order to see if phases' transitions or losses of material occurred and at what temperature. The TGA and DSC traces were obtained using 10 °C and 1 °C per minute scans. The typical temperature ranges used for TGA were 25-750 °C at both scan rates. The typical temperature range used for the DSC traces were 25-500 °C. Traces were obtained under air and inert atmosphere (He).

2. 4. SEM and EDS

Initial and 30 hour ball milled samples were examined for particle size and an elemental analysis was done by EDS.

2. 5. Magnetic susceptibility

Magnetic susceptibility measurements were done at CNRS, Laboratory of Magnetism, Bellevue, France by Dr.. J-L. Dormann.

2. 6. Ball milling

Chalcopyrite (2.009 g) and irons (0.673 g) were mixed together using an agate hand mill until a fine powder was obtained. Then, the powder was placed in the milling container made of agate balls of an approximate diameter of 8 mm. The mill changes the direction of rotation every 2 minutes. The ratio of the chalcopyrite and iron corresponds roughly to a 33.3 % $Fe/CuFeS_2$ mixture. Some other experiments have been done such as ball milling Zn and chalcopyrite as well as chalcopyrite and pyrite. The results of these experiments will not be discussed in this report, but will be used in the general discussion.

3. Experimental results: TGA and DSC

The reason of this study is to get insight on the possible effect of the ball milling. Ball milling induces an increase of temperature in common in both experiments the conditions are quite different. In TGA or DSC the gradient of temperature is slow, while in milling one expects explosions due to sudden change in temperature.

3. 1. TGA

When chalcopyrite is analyzed in air there is a slight increase in mass of the sample in the range of 360-450 °C followed by a steady decrease in mass. This would indicate that chalcopyrite oxidizes in the ranges of 360-450 °C, most probably to copper and iron sulphate. The mass decrease could most probably be attributed to the formation of elemental sulphur and compounds such as SO_2, SO_3 and SO_4^{2-}. Run under nitrogen, the traces are similar, because most probably water in the nitrogen reacts with chalcopyrite. Run under He (Figure 1), the traces indicate a slight decrease in mass from 93 °C to 360 °C, followed by a large mass decrease after 393 °C that is due to elemental sulphur liberation. An observation during the annealing experiments was that the furnace silica tube was stained with at least three compounds that had come off the sample. Two of the compounds had a metallic appearance, one with gray color and the other with a gold/copper color. When washing the silica tube neither of these compounds could be removed with soap and water. However treatment with nitric acid removed these strains implying that they were composed of metal. The third stain was composed of a white chalky material that was not removed by acid, that suggests a sulphur component. The three compounds were most probably, copper, iron and a compound of sulphur.

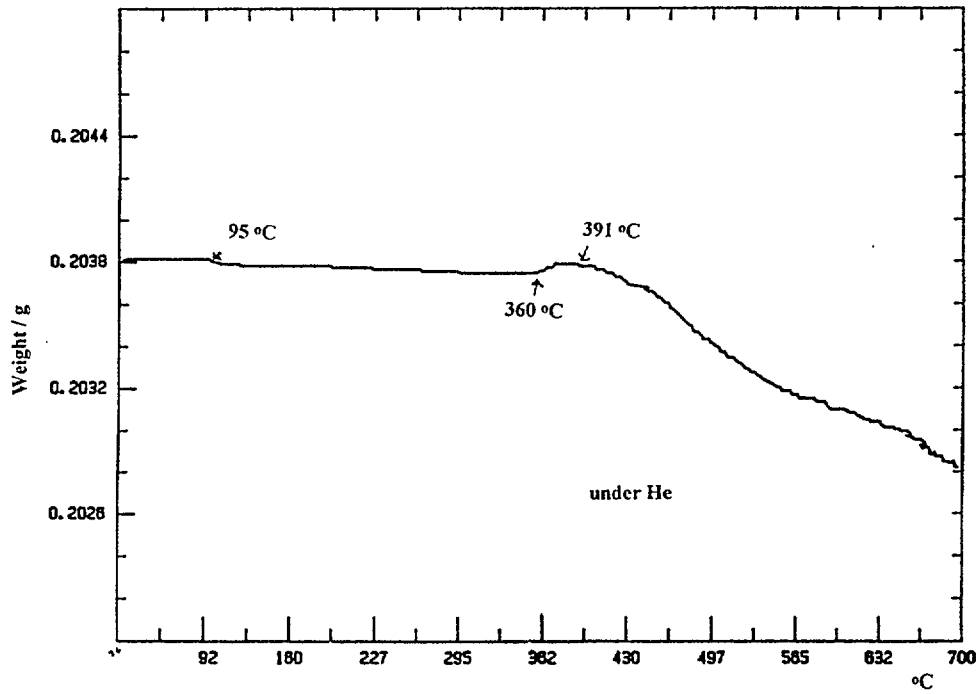

FIG. 1. TGA curve of chalcopyrite run under He. The curve is very flat up to 360 °C were the first weight lost occurs. This indicates a change in the structure above this temperature but not a phase transformation. (He eliminated external oxidation)

3. 2. DSC

DSC under He (Figure 2) indicates that they are two temperatures at which some compound comes off 62 °C and 124 °C. The peaks are small indicating that very small quantities of materials come off. Run in the reverse direction (Figure 3), the peaks were not detected, indicating that they are not due to a phase transition. The high temperature exothermic peaks at 351° and 450 °C arise from sulphur reacting with surrounding impurity gases of the helium.

3. 3. SEM and EDS

If the SEM images reveal (Figures 4) that the overall "particle" size is 100 μm for the initial sample and 2 mm for the ball milled one, these are not elementary particles and represent agglomerate of smaller particles. The EDS results are given in the Table I with the calculated chemical formula.

3. 4. Mössbauer spectroscopy of ball milling chalcopyrite in function of time of milling

The Mössbauer spectra of the reference sample (Figure 5) present the superposition of a magnetic sextet and a quadrupole double doublet. The sextet is the signature of the antiferromagnetism of chalcopyrite while the main quadrupole doublet represents a non magnetic phase due to a randomization of the distribution of the cations (Fe-Cu) between the two possible cationic sites. The doublet with small intensity is considered as a silicate impurity and will be taken out all further discussions. The Figure 6 shows the crystal structure of chalcopyrite. Notice the planes of cations that are parallel to the ab plane. In perfect chalcopyrite all planes are equivalent and only differ by the replacement of Cu by Fe and Fe by Cu. The sextet and the main doublet are charecteristic of chalcopyrite as find from the literature. The Mössbauer parametrs (Table V) that we obtained from all the

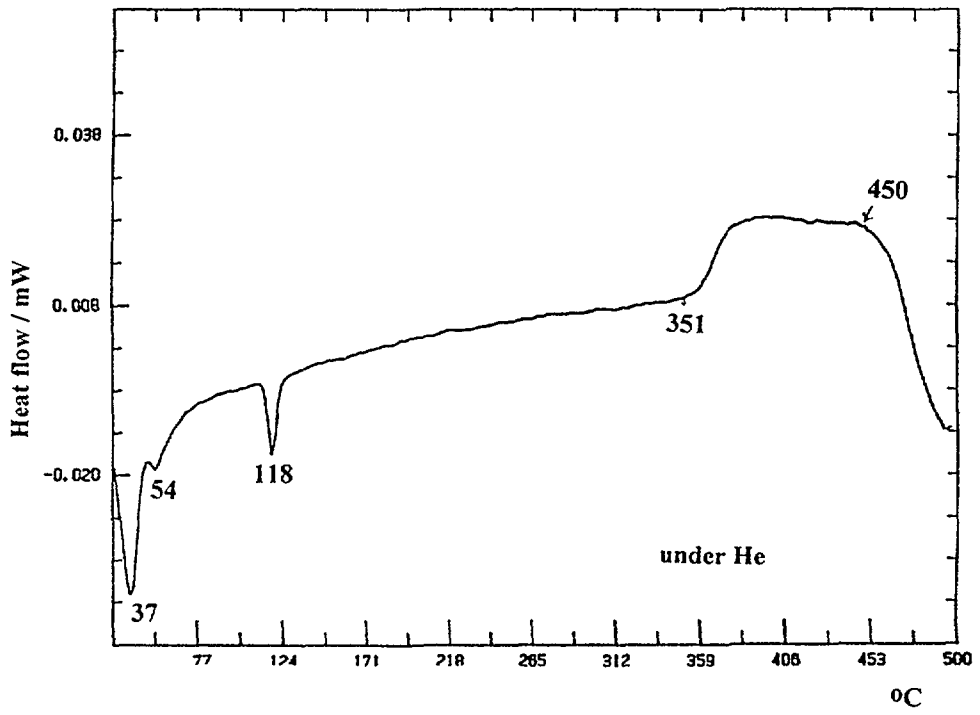

FIG 2 DSC curve of chalcopyrite run under He DSC curve indicates various dips at low temperature (64 and 124 °C) They are small, so they can arise from lost of small quantities of materials, perphaps impurities

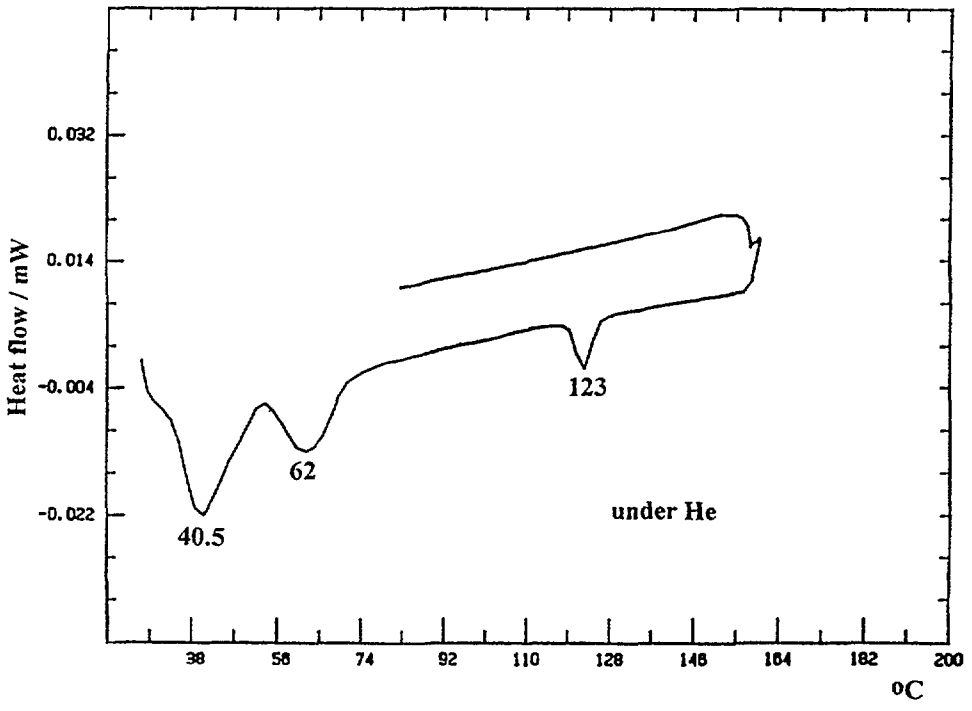

FIG 3 DSC curve of chalcopyrite run under He in the reverse direction (decreasing temperature) He avoid spurious oxidation This curve is to be compared with Figure 2, taken with increasing temperature The fact that no peaks (dips) appear at low temperature confirm the fact that the dips seen in the direct direction (increasing temperature) are not due to phase transition

FIG. 4. SEM micrograp of the initial chalcopyrite (large magnification). This micrograph shows that some grains are of the order of 10 m.

TABLE I. EDS ANALYSIS OF VARIOUS CHALCOPYRITES.

Sample	%Cu	%Fe	%S	%at sample	Formula
Initial	25.29	17.03	48.23	90.65	$Cu_{1.05}FeS_2$
30 h ball milled in air	22.58	16.48	48.57	87.63	$Cu_{0.93}Fe_{0.68}S_2$
Gencor values	23.4	26.6	21.9?	71.9	

Notice the relative reduction of iron in the chalcopyrite after milling.

samples are in excellent agreement with these published in the literature [11-12]. The pure sextet of the chalcopyrite gives place in function of the time of milling to the quadrupole doublet assuming arising from the disoredred phase (Figures 7, 8, 9). By disordered phase, we mean a chalcopyrite in which iron and copper are irregurlarly distributed between the cationic planes parallel to the ab plane. The fact that the increase in intensity arises from sextet is proved by the spectrum run at 80 K (Figure 10) showing that some part of the paramagnetic doublet is converted back into the sextet. This means that the doublet is, at least in part, due to superparamagnetism. This one arises from iron having a limited number of other iron neighbors up to 5 to 10 atomic distances. The superferromagnetism, indeed in this case, super antiferromagnetism is assessed by the important shoulders on the inner sides of the external peaks [13]. They arise from a distribution of particle sizes in the region of 10 nm, or of magnetic domains of that dimension within the chalcopyrite.

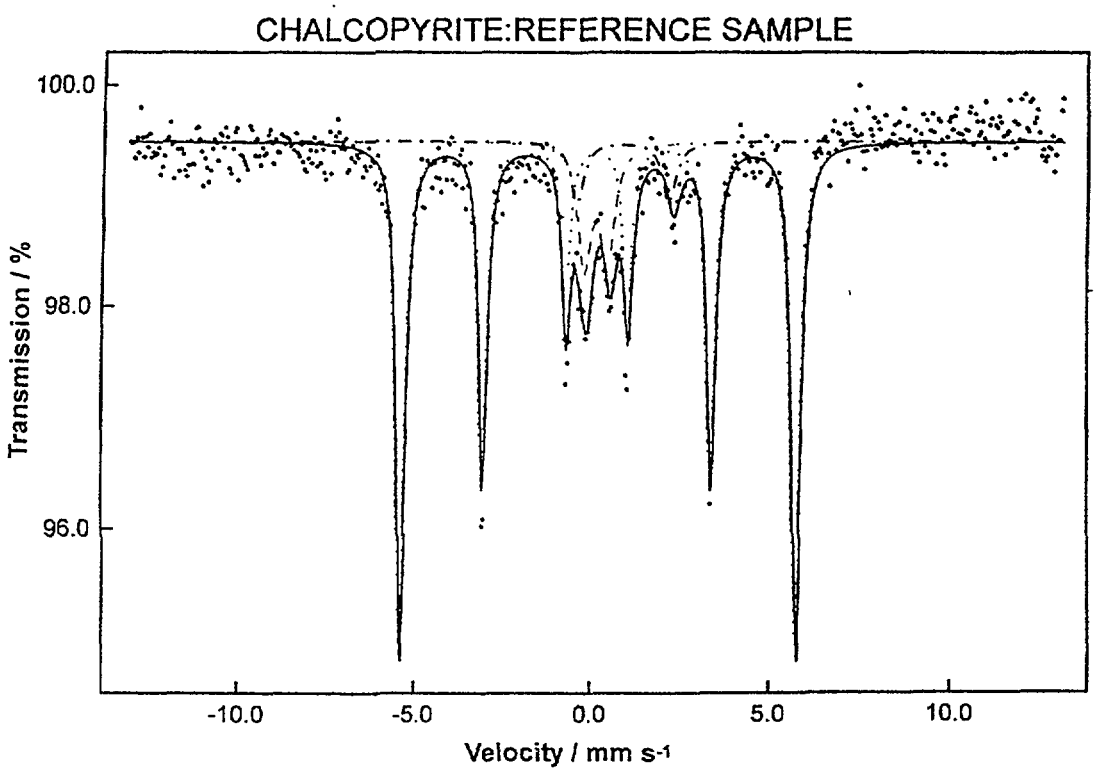

FIG. 5. Mössbauer spectrum of natural chalcopyrite . Note the two components: the sextet arise from large particles, while the central doublet is due to a silicate impurity within the sample.

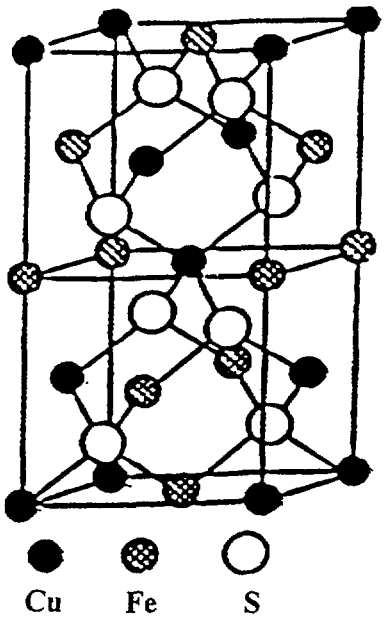

FIG. 6. Crystal structure of chalcopyrite. Note the regular arrangement of the Fe and Cu atom. If this arrangement is perturbed, e. g., by permuting any pair of Fe-Cu, the magnetic order is destroyed and the Mössbauer spectrum will be a doublet and not the sextet.

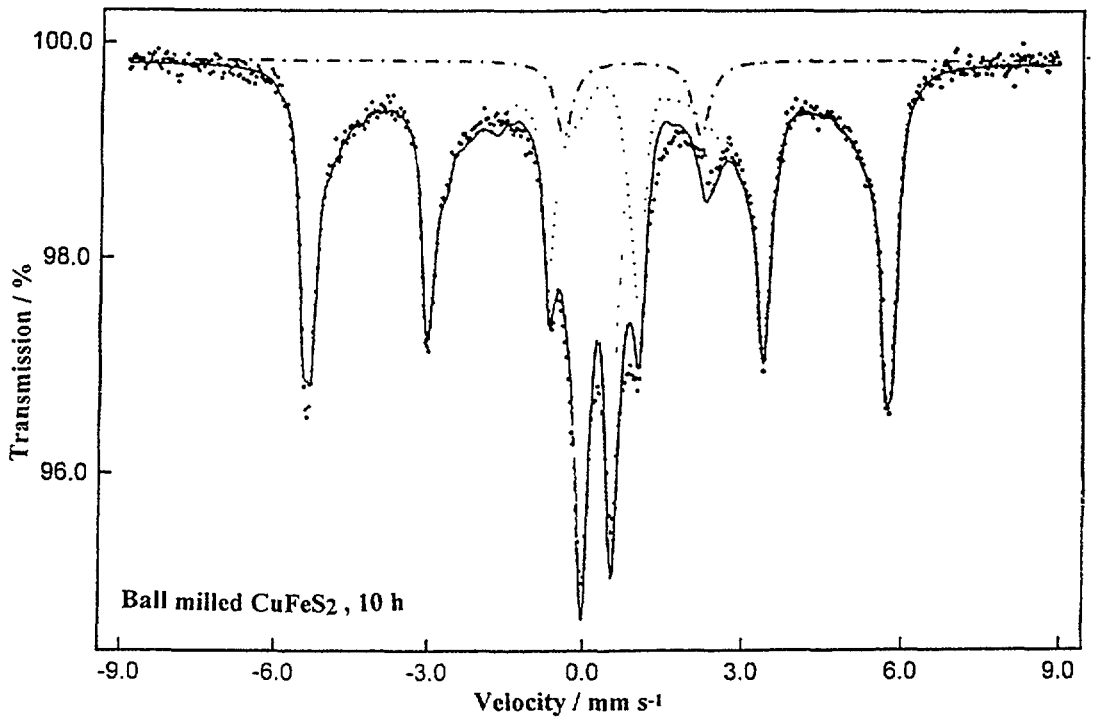

FIG. 7. Mössbauer spectrum of ball milled chalcopyrite for 10 hours. Note the increase of the doublet due to the destruction of the magnetic order by moving Cu and Fe atoms and also form small particles.

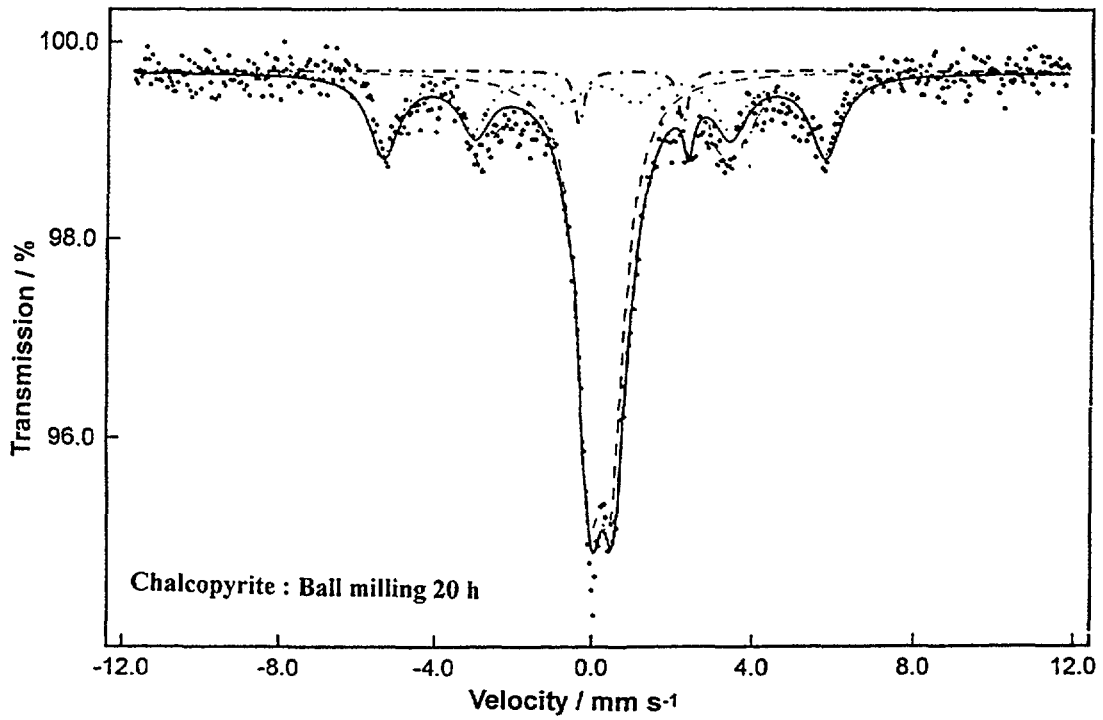

FIG. 8. Mössbauer spectrum of ball milled chalcopyrite for 20 hours. Note the almost disappearance of the magnetic order at room temperature.

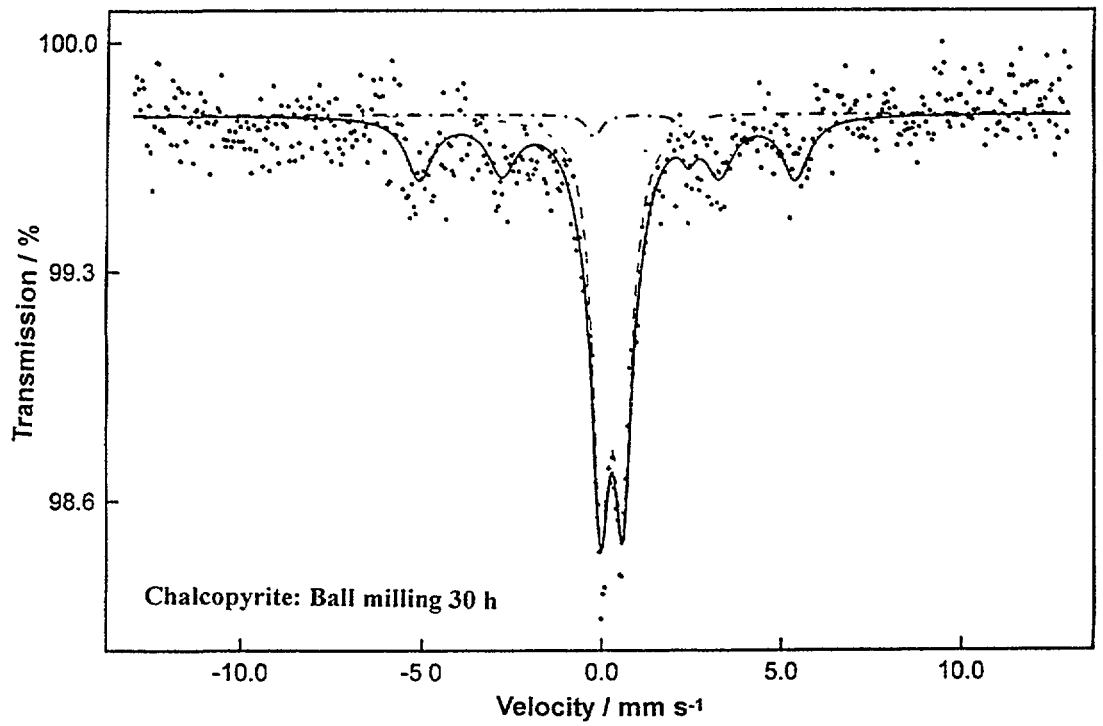

FIG. 9 Mössbauer spectrum of ball milled chalcopyrite for 30 hours. Almost no magnetic order is conserved

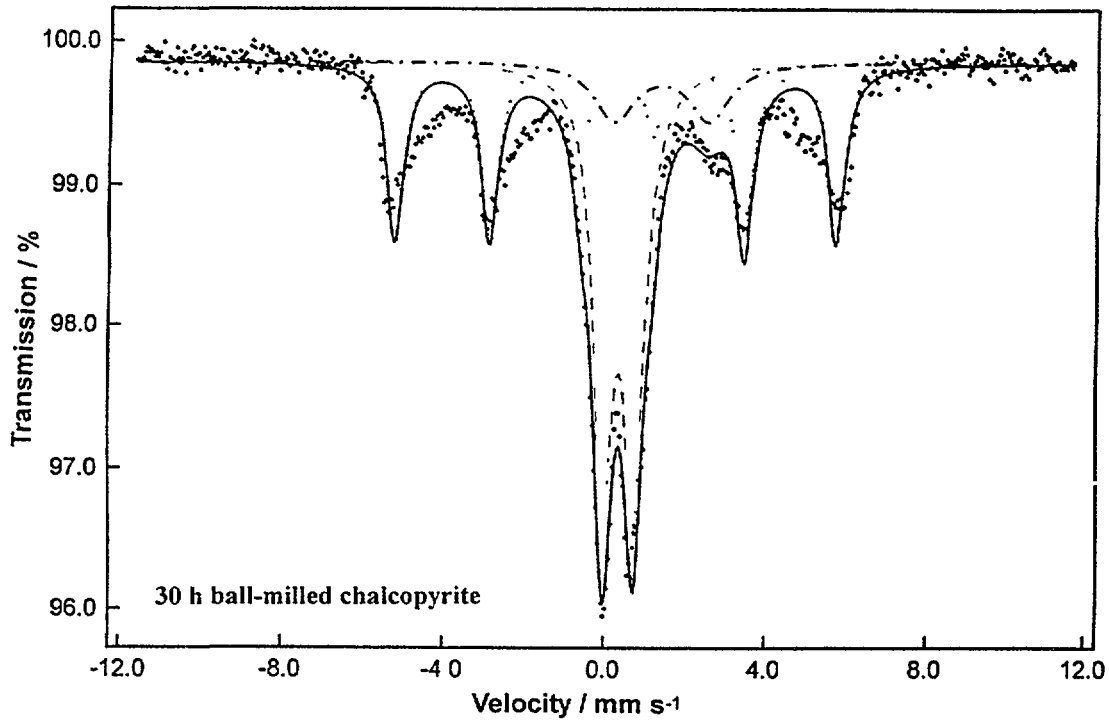

FIG. 10. Mössbauer spectrum of ball milled chalcopyrite (the same sample as in Figure 9), taken at 80 K. The magnetic order is partially restored, indicating that part of the lost of magnetic field at room temperature is due to the formation of small particles as an effect of the milling. That indicates that the particle size is in the range of 10 nm.

3. 5. Magnetic susceptibility measurements

Table II summarizes all results done at the CNRS in France. They clearly indicate that the magnetic domains are much smaller in the ball milled sample than in the initial sample. This confirming on results of the Mössbauer spectroscopy. The magnetization at saturation is reduced by factor 2, meaning that the number of individual magnetic moments is much less in the milled sample. Also, notice of importance in the increase of susceptibility proved the communication of the chalcopyrite and the related disordered phase.

TABLE II. MAGNETIC MEASUREMENTS ON CHALCOPYRITE

Property	Chalcopyrite	Ball milled Chalco.
Antiferromagnetic susceptibility	$7.6 \cdot 10^{-6}$ emu	$12.3 \cdot 10^{-6}$ emu
Magnetization at saturation	0.135 emu	0.065 emu
Remnant magnetism	0.042 emu	0.027 emu
Coercitive field	260 Oe	490 Oe

3. 6. Annealing of chalcopyrite

Fresh chalcopyrite, one hour annealed chalcopyrite and 30 hours ball milled annealed chalcopyrite were run on an XRD machine. The unit cell parameter a and c were determined. The results are given in the Table III.

TABLE III: UNIT CELL OF CHALCOPYRITE AFTER THERMAL TREATMENT.

Material	*a* in nm	% change	*c* in nm	% change
Initial	0.53029		1.0412	
1 hour annealed 600 °C	0.53311	0.53	1.0680	2.57
30 hours ball milled + annealed	0.53080	0.10	1.0638	2.17

These measurements clearly indicate that the chalcopirite, after ball milling and annealing, are very similar. The main effects of ball milling and of annealing are almost identical, an increase in the cell volume due to a randomization of Fe and Cu between the two normal cationic sites. The X-ray diffractograms are given in Figures 11, 12 and 13. Figures 12 and 13 are identical to Figure 11, but are taken on extended scales. Another conclusion, indeed confirmed by Mössbauer spectroscopy, the ball milling did not create any of the superlattice crystals of chalcopyrite such as talnakite, mooihoekite and haykokite (Figure 14). The Mössbauer spectra of these "superlattice" of chalcopyrite all present very different Mössbauer finger printers than these we obtained [14]. The change in the Mössbauer spectra is very similar to that observed on measuring chalcopyrite under pression. In this case the quadrupole

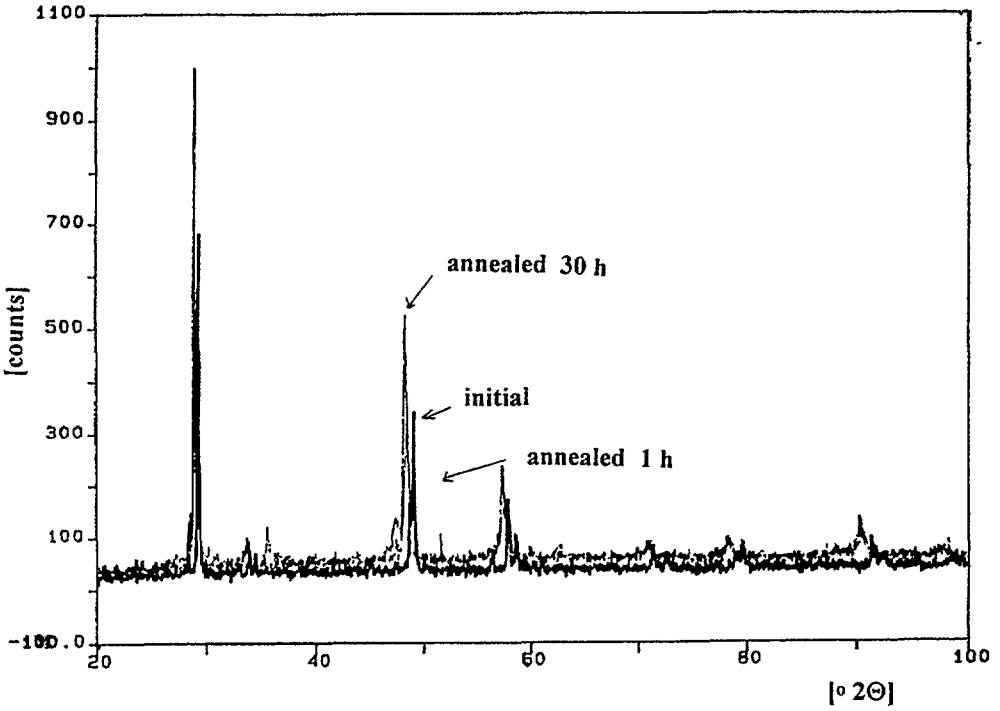

FIG. 11. XRD diagrams of chalcopyrite. The graph is superposition of the initial mineral and 30 hours ball milled, then annealed for 1 hour at 600 °C. We notice a slight shift of the lines toward small angles, but, with the same regularity.

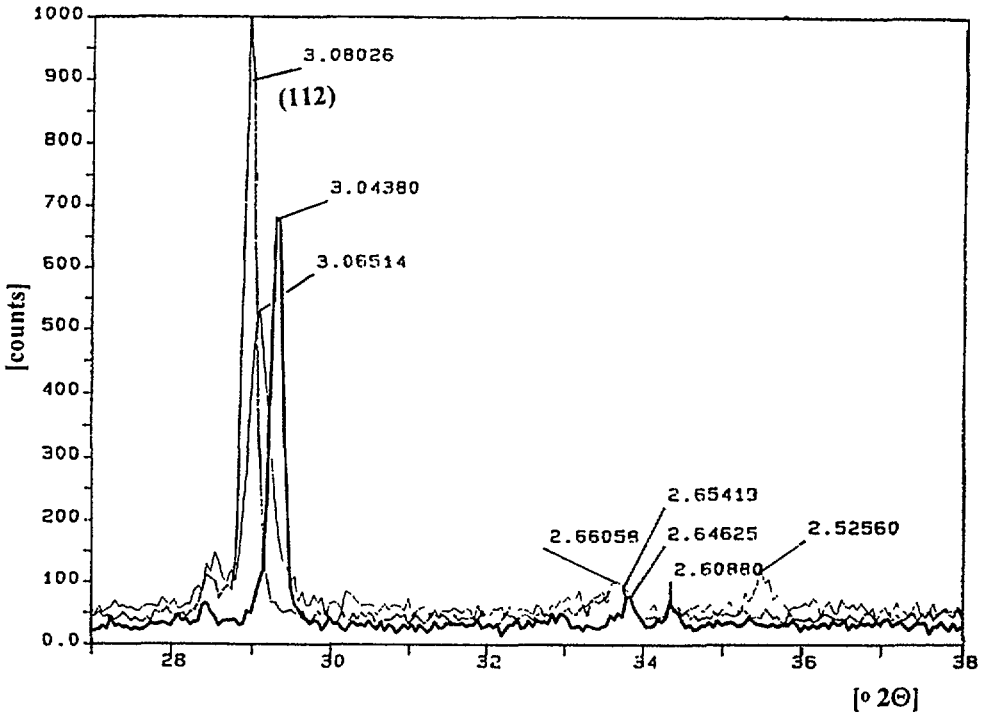

FIG. 12. XRD diagrams comparing 30 hours ball milled chalcopyrite, and then annealed 1 hours at 600 °C and the initial sample. Note the change in intensity in the lines. The figure is the same as figure 13 for the small angles, but on a larger scale showing better the line shifts.

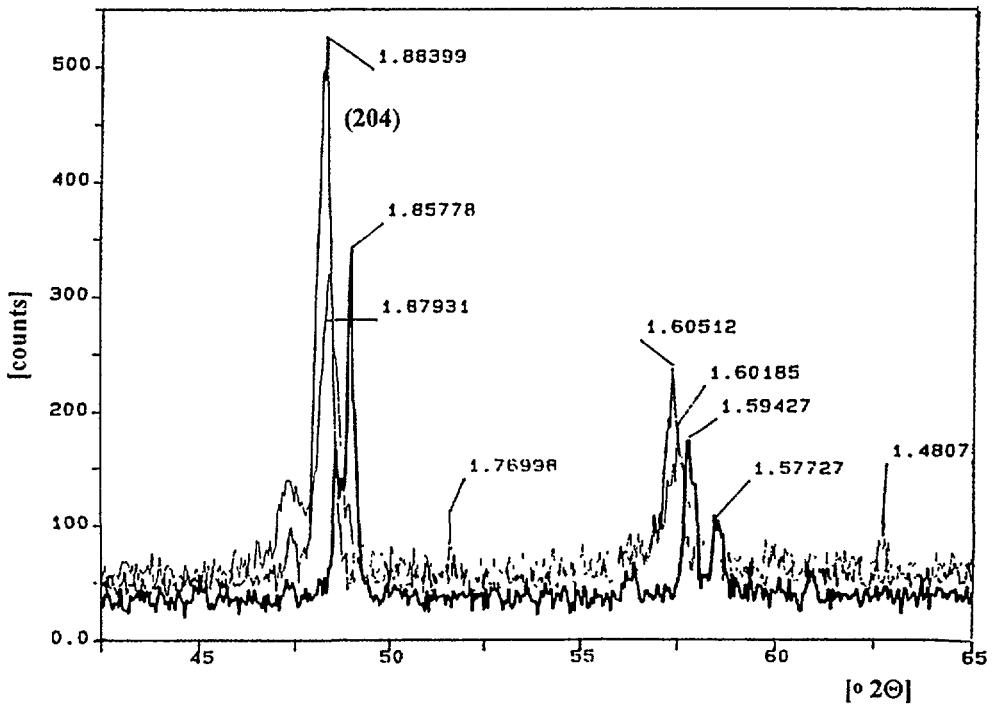

FIG. 13. XRD diagrams comparing 30 hours ball milled chalcopyrite, and then annealed 1 hour at 600 °C and the initial sample. Note the change in intensity in the lines. The figure is the same as figure 13 for the large angles, but on a larger scale showing better the line shifts.

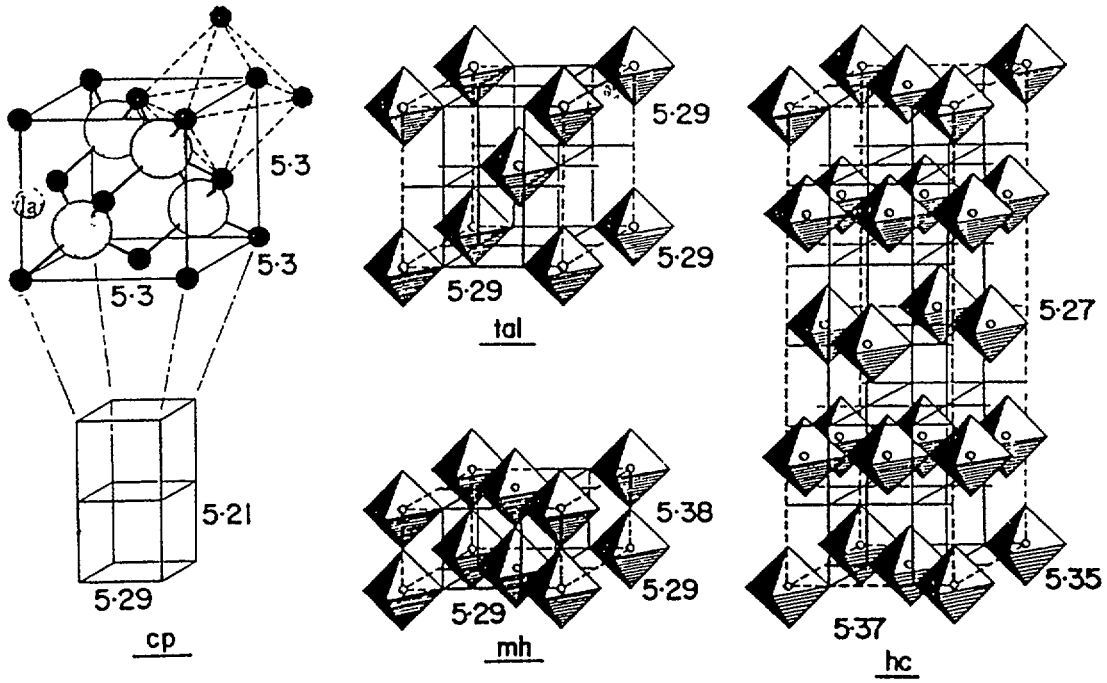

FIG. 14. The crystal structures of chalcopyrite (cp), talnakhite (tal), mooihoekite (mh) and haycockite (hc) are shown schematically in terms of sphalerite-type "cubes" of metals and sulphurs (detailed in the upper-left corner), and in terms of interstatial metal-octahedra. The a, b and c dimensions of the "cubes" are given (in angstroms) for each structure.

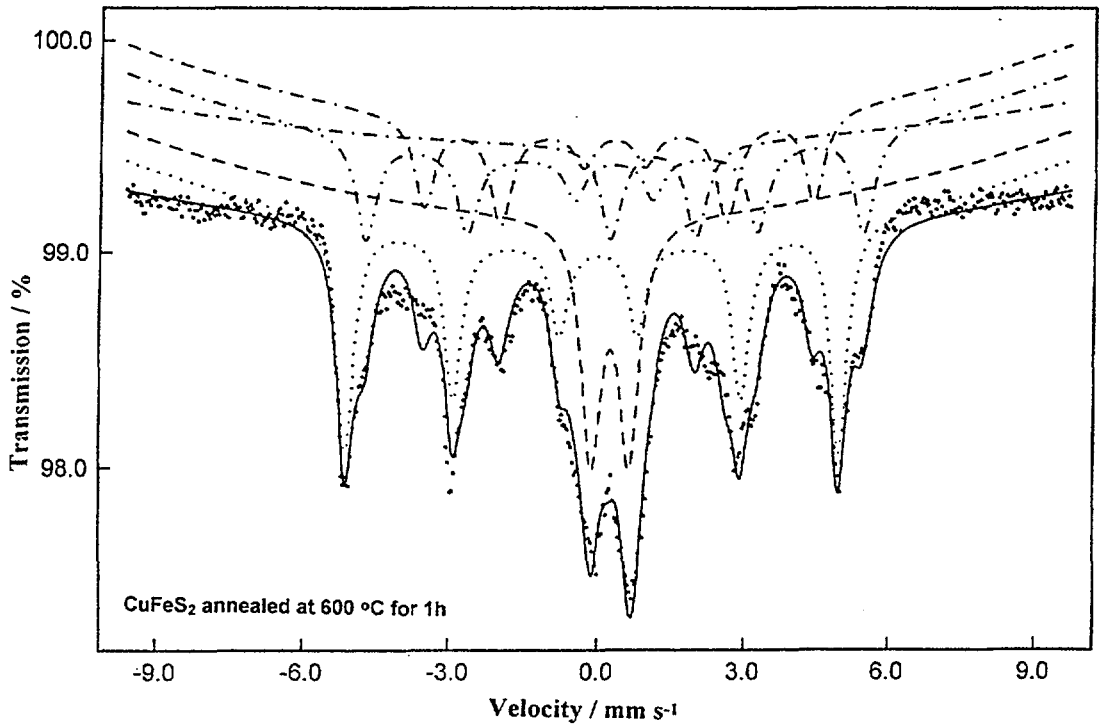

FIG. 15. Mössbauer spectrum of annealed chalcopyrite after being ball milled. The structure is complete different from the initial sample. Three magnetic components at least seem to exist with a strong quadrupole doublet.

TABLE IV: EFFECT ON BALL MILLING OF Fe AND CHALCOPYRITE AS DETERMINED BY MÖSSBAUER SPECTROSCOPY AND XRD. THE RATIOS OF Fe:$CuFeS_2$ AS QUATED ARE RATIO OF DIRECT INTENSITIES OF EXPERIMENTAL SIGNALS, SEE TEXT FOR EXPLANATION. FOR SAKE OF COMPARISION, THE PRECEDING VALUES WERE NORMALIZED TO FRESH CHALCOPYRITE.

Sample	Fe/$CuFeS_2$			
	XRD		Mössbauer	
	Measured	Normalized	Measured	Normalized
Initial	0.100	1.00	0.78	1.00
Milled in air	0.134	1.34	1.28	1.66
Milled in ethanol	0.081	0.81	0.67	0.87
Milled in CH_2Cl_2	0.039	0.39	0.45	0.57

doublet also increase at the expense of the sextet [15], but on releasing the pressure on goes back to the initial conditions. In the case of ball milling the "reaction" is irreversible even with annealing. In fact, the fitting of the ball milled and annealed sample Mössbauer data presents difficulties. Thus the identification all the iron sites was not performed. It seems that the annealing produces a limited re-ordering of the cations in the two sites, thus presenting two different distributions of magnetic fields. Our mathematical tool of fitting was unable to accommodate the above assumption due to very similar parameters of the two assumed magnetic fields (Figure 15).

3. 7. Milling chalcopyrite with iron

Chalcopyrite has been ball milled during 15 h with iron in a proportion of one to one in Cu in chalcopyrite to iron in metallic iron. Measurements were done by XRD and Mössbauer spectroscopy. As the powders, iron and/or chalcopyrite, have a tendency to agglomerate and to make clusters, a series of experiments was done with surfactants: ethanol and dichloromethane CH_2Cl_2. The first was chosen as it was used by many other authors in the past, while we choose the second due to the presence of chlorine that should add an extra reactivity. This was indeed the case as the reader can see from the table below.

The intensity of the chalcopyrite in the Mössbauer data comprises both the typical chalcopyrite sextet and the doublet. Figure 16 gives the X-RDP diagramme of the initial chalcopyrite as well as this of iron and also this of the initial mixture. The X-RPD data of the milled chalcopyrite mixed with iron, under various conditions, in air, in ethanol and in dichloromethane, are displzed in Figures 17-20 while the Mössbauer data are displyed in Figures 21, 22 and 23, for the same conditions. However, for sake of comparasion all the figure includes the spectrum of initial sample.

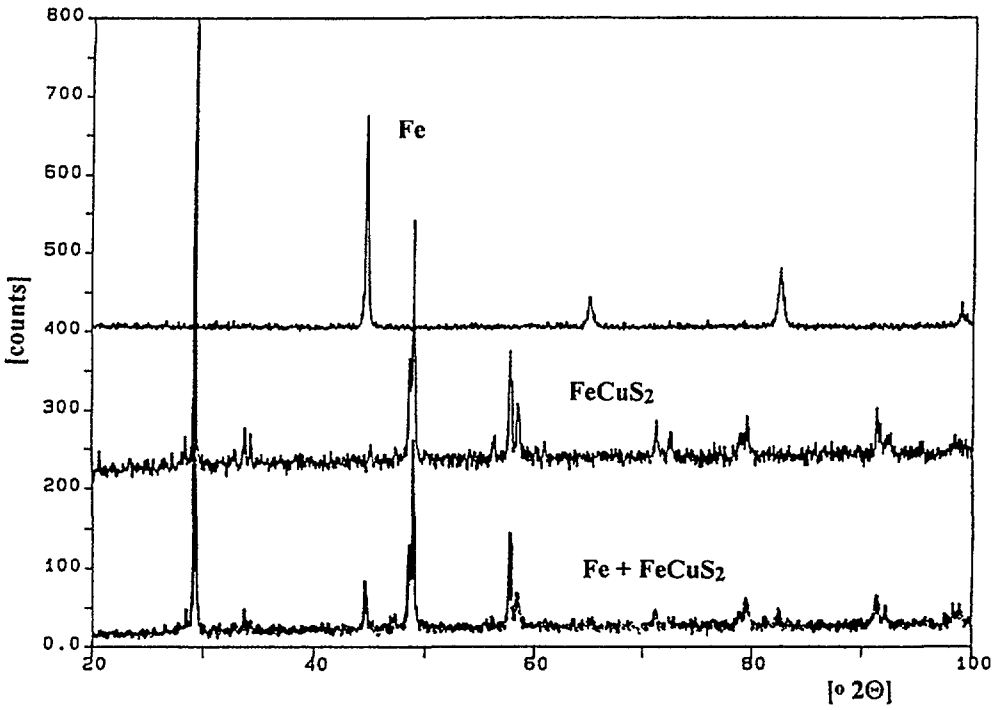

FIG. 16. XRD diffractograms of chalcopyrite with 33 % in weight of Fe. For comparasion the diffractograms of Fe and pure chalcopyrite are given.

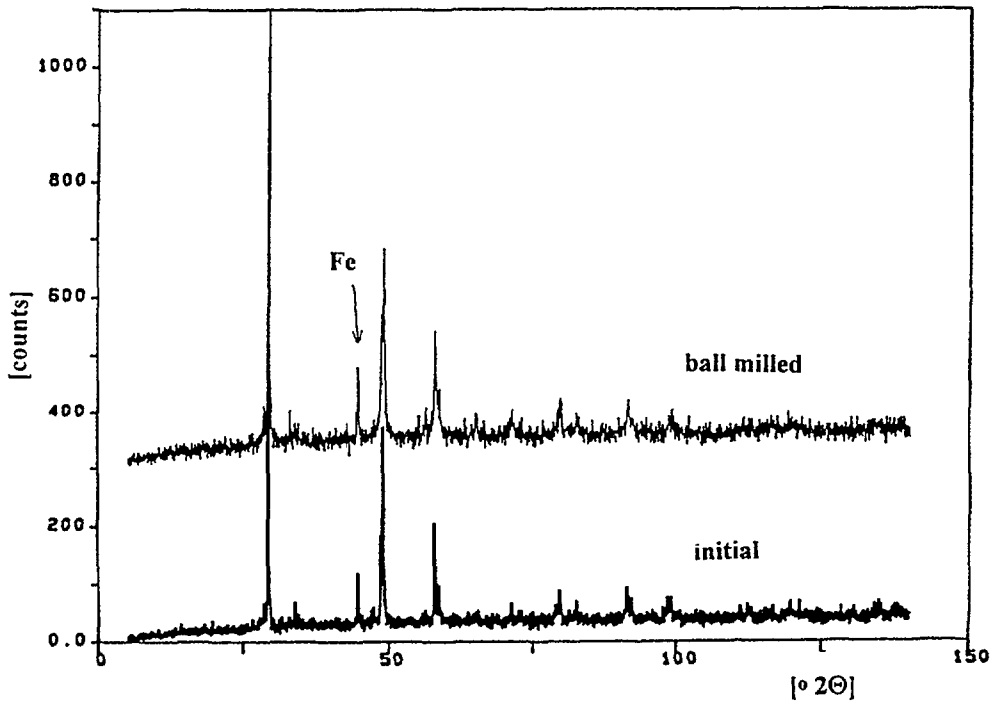

FIG 17. The XRD diagram of ball milled in air chalcopyrite with iron (33 w. %) compared with the initial mixture. Note the relative increase of the Fe lines.

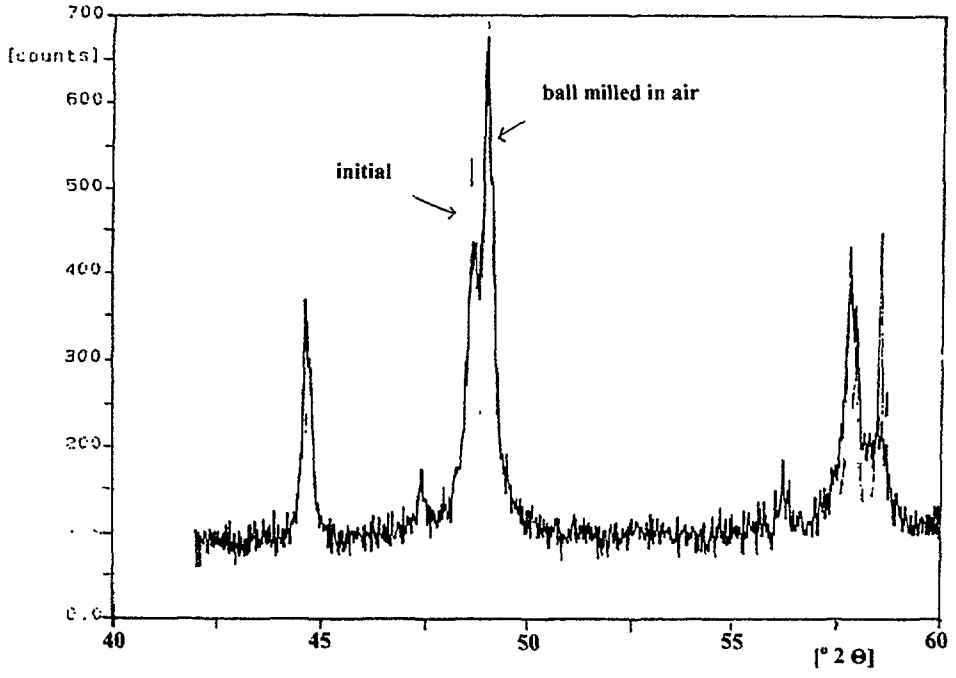

FIG. 18. The XRD diagram of ball milled in air chalcopyrite with iron (33 w. %) compared with the initial mixture, but on a larger scale.

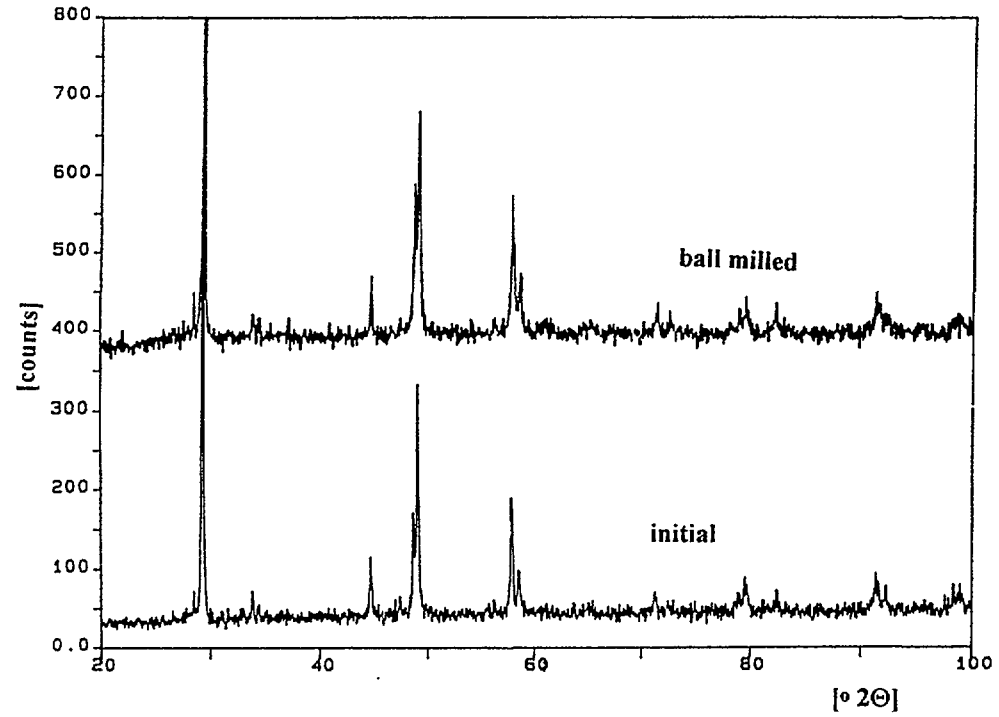

FIG. 19. The XRD diffractogram of ball milled chalcopyrite under ethanol. See the change in intensity compared with the initial sample. No new compound appears in the milling. Note the relative reduction of the Fe lines.

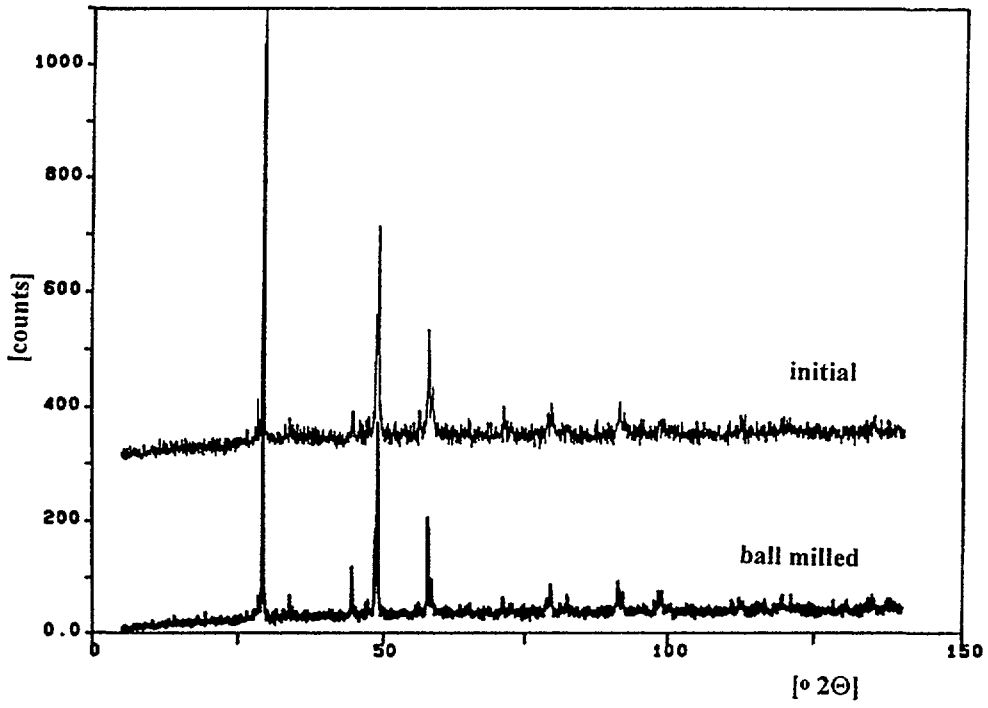

FIG. 20. The XRD diagram of ball milled chalcopyrite under dichloromethane as surfactant.

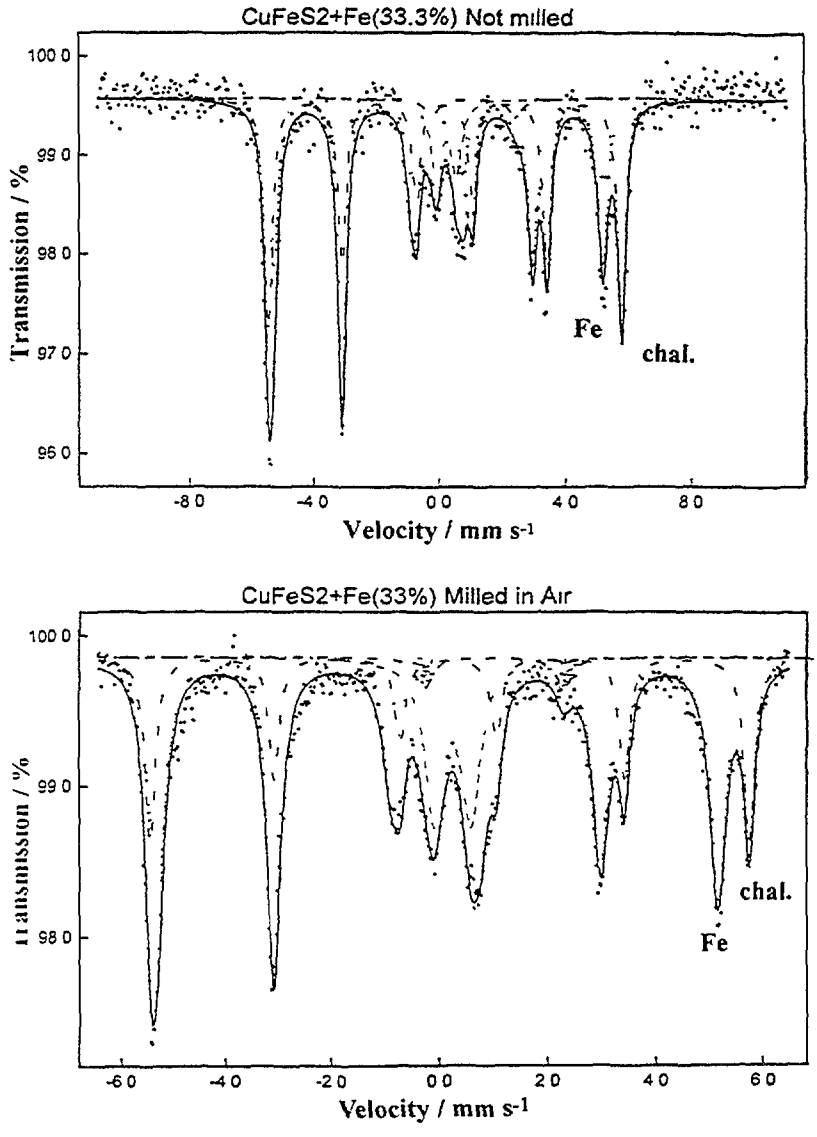

FIG 21. Mössbauer spectrum of the sample milled with iron under air with the initial sample. XRD given in Figure 19. Here the relative increase of metallic iron is well seen.

4. GENERAL DISCUSSION

Examining the above data, one sees an overall agreement with the figures of both experiments, the Mössbauer spectroscopy and XRD Both indicate: when one ball mills iron with chalcopyrite in air, the quantity of iron increases or the amount of chalcopyrite decreases, and milling the same mixture under surfactants shows the opposite trend The relative amount of the iron species is decreased or the chalcopyrite amount has increases. However, a much larger effect has been noticed for dichloromethane surfactant than for ethanol

4. 1. Discussion of XRD measurements

Only one peak of iron is clearly visible (Figure 17) on the mixture of chalcopyrite and iron, it is located at 2Θ of 44.67°. The effect of milling in the different solutions was judged by noting the changes occuring to this peak relative to the chalcopyrite peaks at 2Θ of

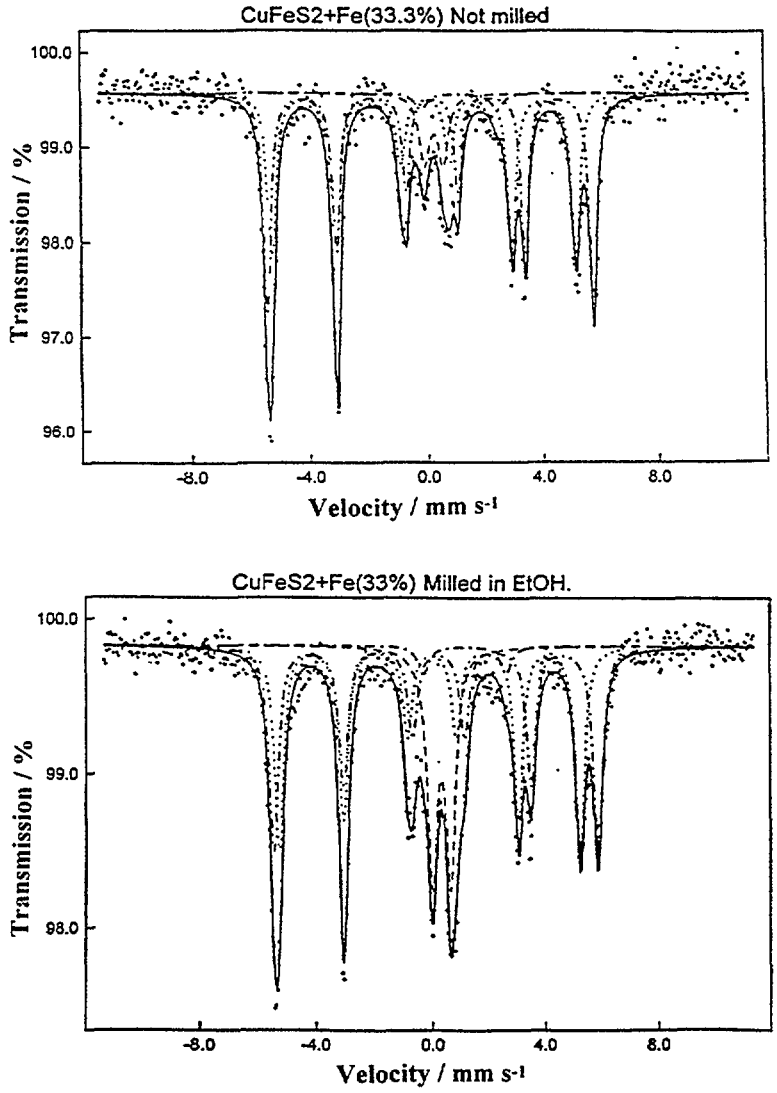

FIG. 22. Sample with iron milled under ethanol. Note now that iron line decreases compared to the chalcopyrite. Chalcopyrite definitively "absorbs" iron.

48.61, 49.02, 57.83 and 58.51° (Figures 18, 19 and 20). Analytically the effect of the different solvents on the milling process was worked out finding a mathematical curve to the iron peak and the chalcopyrite peaks at 2Θ of 48° and 56°. The areas of these peaks were then automatically obtained. A ratio of the iron peak to the chalcopyrite peaks was then calculated for the diffractograms of the different mixtures. The reason for the selection of the chalcopyrite peaks at 2Θ equal 48.61, 49.02, 57.83 and 58.51° for the calculation of the values reported in Table IV was that these peaks did not seem to show preferred orientation or get affected as much as the other peaks.

4. 2. Discussion of Mössbauer data

The Mössbauer spectra (Figures 21, 22 and 23) indicate that after ball milling, whatsoever the conditions are, the paramagnetic component represented by the central doublet of chalcopyrite increases at the expense of the magnetic chalcopyrite represented by a sextet.

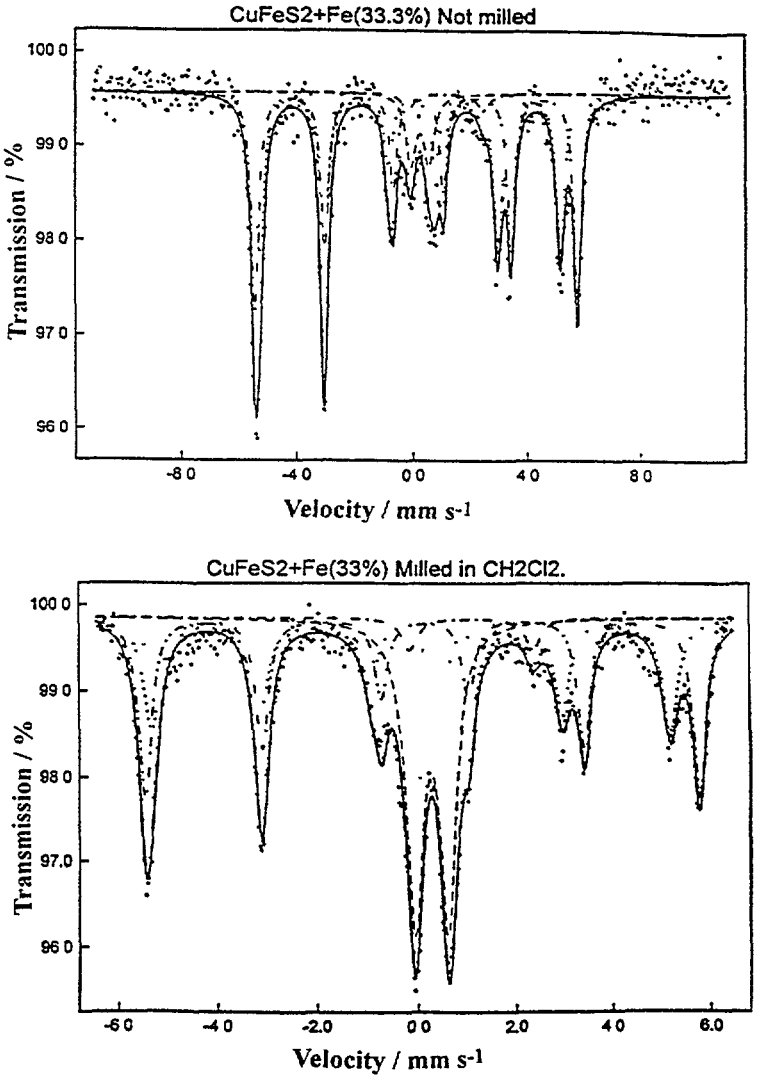

FIG 23 Sample with iron milled under dichloromethane.

The iron typical sextet is very well resolved and allows a neat separation from the sextet of chalcopyrite, even if the left lines overlapped. A comuter programme has no programme to hook itself on the two right lines of the chalcopyrite and the iron to provide reliable results. The good fitting of the data with the three components indicated clearly that no other component should be masked. If another component should be present, a shoulder should be seen somewhere. Also we must notice that if any ferric oxide should be present, even as very small particles (10 nm) one should see a lack of fitting around zero velocity that is not observed indeed. Only a ferrous, small intensity component could be masked, but by looking to the table of all Mössbauer parameters of all the samples, this must be excluded. Therefore, the only possibility that is available is that iron substitutes Cu in the Cu site to a high extend and liberates Cu. This copper must be in the form extremly fine particles below 100 nm or even much less as they are not detected by XRD. This is indeed compatible with the way on how the copper is released: one atom at the time for a typical collision followed by an explosion due the energy stored from kinetic transformation.

The same effects as above was observed when chalcopyrite was ball milled with zinc. The only difference is that the effect of dichloromethane is no much different than this of ethanol.
When ball milled with pyrite, chalcopyrite seems to be decomposed with an increase of iron. This last may arise in this case from either or both the chalcopyrite and pyrite. This means that one necessarily needs to get the reaction going.

4. 3. Dry iron/chalcopyrite ball milling in air

Let us first remember that the samples present clearly agglomerates or clusters. This means that grains, when squeezed between the balls, are an conglomerate and that only external particles are coming in collision. The efficiency of the ball milling process is therefore limited. There is more iron present after ball milling than before (30 to 60 %). Iron must come from the chalcopyrite. So, we assume a decomposition of chalcopyrite to some extends with the liberation of SO_2, SO_3 or SO_4 groups. Copper is maybe also release, but not detected in our experiments. The Mössbauer data indicate also a small increase of the paramagnetic component, that means that some energy liberated by the chocks has been use to move Cu in the Fe sites and Fe into the Cu sites, effect difficult to detect by XRD unless as a small increase on the unit cell parameters. The formation of any iron oxide is ruled out by the Mössbauer data showing no line corresponding to iron oxides. XRD also do not revealed any new species. When mixed with zink (no surfactants used) milled chalcopyrite shows also an increase of metallic iron and no new XRD nor Mössbauer pattern appears.

TABLE V: MÖSSBAUER PARAMETERS OF THE BALL MILLED CHALCOPYRITE UNDER VARIOUS CONDITIONS (AIR AND SURFACTANTS).

Parameter	Initial		Air		Ethanol		CH_2Cl_2	
	Fe	$CuFeS_2$	Fe	$CuFeS_2$	Fe	$CuFeS_2$	Fe	$CuFeS_2$
SEXTET				Chalco	pyrite			
δ								
Δ								
H								
main doublet	Chalco pyrite							
δ		0.31		0.33		0.35		0.36
Δ		0.32		0.34		0.32		0.34
minor doublet				Impuriy				
δ		1.20		1.09		1.21		1.21
Δ		1.33		1.29		1.45		1.26

δ: isomeric shift are given relative to α-Fe in mm s^{-1}. Errors are of ±0.02 mm s^{-1}, except on the minor component where they are ±0.04 mm s^{-1}
Δ: quadrupole splitting is given in mm s^{-1} with an error of ±0.02 mm s^{-1}
H: internal magnetic field expressed in Tesla, estimated errors are of ±0.5T.

The intensities used to evaluated the chalcopyrite amount are always these obtained by adding the typical sextet and the major doublet. The minor doublet is not taking into account as explained next. The minor doublet always seen in the chalcopyrite spectra, is attributed to an impurity in the initial chalcopyrite. From the Mössbauer parameters, we assume that it corresponds to an iron silicate. The intensity of this species is unaffected by all treatments.

4. 4. Wet ball milling of chalcopyrite with surfactants

The effect of surfactants is impressive. The general effect is a relative reduction of the iron species in the mixtures. This means that iron must be incorporated in the chalcopyrite lattice, as it is impossible to conceived that chalcopyrite has been created under the prevailing conditions in the experiments. But, if iron in going into the chalcopyrite lattice where does it really goes. Chalcopyrite has a lot of vacant sites, and it is not impossible that they could accommodate iron atoms, without drastically changing the crystallographic structure. However, if this would be the case, one should see a small change in the XRD diffractograms due to the distortion induced into the lattice by incorporating a foreign atom in a somewhat small site compared to the size of the atom to be incorporated. But, even, if this should be the case, this new populated iron site should have been seen by the Mössbauer spectra because the relative number of iron of 15 or 43 % for milling in ethanol or dichloromethane, respectively, is well above the limit of detection of the Mössbauer spectroscopy assumed to be of a few percent. Considering the system Cu-Fe-S (Figure 24), chalcopyrite (cp) could be transformed under ball milling alone in a large variety of other minerals. If the ball milling induced a lost of iron one could expecte to find talnakhite (tal), idaite (id), and even bornite. Idaite has not been characterized by Mössbauer spectroscopy but well talanakite (14) and bornite (16). Our data do not support any possibility for these minerals. On the contrary, when milling with surfactants, the iron is "absorbed" by the chalcopyrite, but one could consider the possibility of formation of greigite (gr), smythite (sm), mackinawite (mk), pyrrhotite (mpo, hpo) or troilite (tr). Again the comparison with the known Mössbauer data on this minerals do not fit our results [12, 17 and 18].

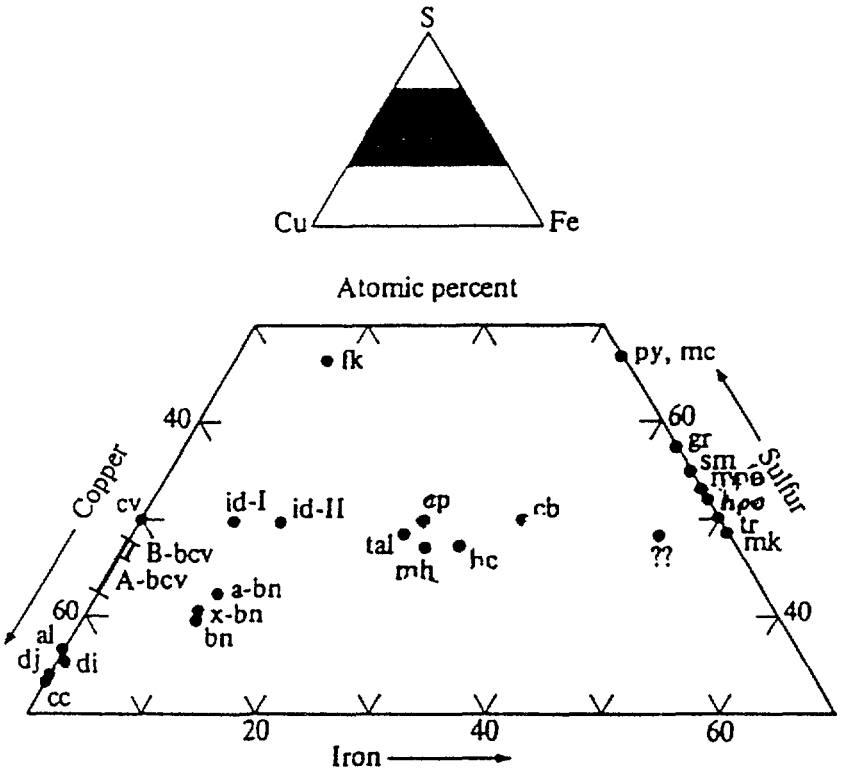

FIG. 24. Stable phases in the system Cu-Fe-S.

minerals. On the contrary, when milling with surfactants, the iron is "absorbed" by the chalcopyrite, but one could consider the possibility of formation of greigite (gr), smythite (sm), mackinawite (mk), pyrrhotite (mpo, hpo) or troilite (tr). Again the comparison with the known Mössbauer data on this minerals do not fit our results [12, 17 and 18].

5. Conclusion

Ball milling of chalcopyrite either alone or with iron or with or without surfactants drastically modifies the chalcopyrite. The antiferromagnetic chalcopyrite is partially transformed from an ordered structure with Cu-plane and Fe-planes, into a disordered structure. In this new structure iron and copper are mixed between the two sites in a more random way. The randomization is much more important in the case of chalcopyrite mixed with iron under surfactants. In this last case, one observed a very intake of iron into the structure of chalcopyrite implying ipso facto a release of Cu. This effect is due to the less reactivity of copper compared to iron. From this result one can expected that any impurity atom that a less reactivity than iron embedded in chalcopyrite, will be released during ball milling under dichloromethane resumably under the metallic form.

Acknowledgment

The authors are pleased to thank the IAEA for the contract 8393/RB, FRD for various grants, and GEMCOR for financial support.

References

[1] ACKERMAN, J., et al., Journal Solid State Chem., 19 (1976) 75.
[2] HALL, S. R., Can. Miner., 13 (1975) 168.; C. L. Herzenberg, Nuovo Cimento, 53B, (1975) 516.
[3 ROWLAND, J. R., HALL, S. R., Acta Cryst., B31 (1975) 2105.
[4] TERANISHI, T., J. Phys. Soc. Japan, 16 (1961)1881.
[5] Di GIUSEPPE, M., et al., Inorg. Chem. 13 (19)1774.
[6] TKACOVA, K., et al., J. Thermal Anal., 34 (1988)
[7] TKACOVA, K., et al., Thermochimica Acta, 170 (1990) 277.
[8] LIPKA, J., et al., Nuclear Instr. and Methods in Physics Research, B76 (1993) 183.
[9] BALAZ, P., TKACOVA, K., AVVAKUMOV, E. G., J. Thermal Analysis, 35 (1989) 1325.
[10] Mosfun, Mössbauer Effect and Data Center, UNCA, Ashville, NC, USA
[11] FINKLEA, S. L., CATHEY, L., Acta Cryst., A32 (1976) 529.
[12] POLLAK, H., STEVENS, G. J., LI SHE, Mineral Data and References Handbook, The Mössbauer Effect and Data Centre, UUNCA, Ashvillee, USA.
[13] MORUP, S.,Industrial Applications of the Mössbauer Spectrometry to Mycrocrystals in: Industrial Applications of the Mössbauer Effect Ed.: LONG, G. J., STEVENS, J. S., Plenun, 1986.
[14] CABRI, L. J., GOODMAN, R. H., Geochem., 7 (1970) 453.
[15] VAUGHAN, D. J., TOSSELL, J. A., Science, 179 (1973) 375.
[16] FISH, Mössbauer spectr. tool for studying hydrometallurgycal treatments of copper iron sulfates. in: Industrial Applications of the Mössbauer Effect, p 523, Ed.: LONG, G. J. and STEVENS, J. S., Plenun, 1986
[17] GREENWOOD, N. N., WHITFIELD, H. J., J. Chem. Soc. A, (1986) 1967.
[18] VAUGHAN, D. J.,Amer. Miner., 55 (1970) 1807.

SUPERCONDUCTIVITY DEGRADATION IN Gd-CONTAINING HIGH TEMPERATURE SUPERCONDUCTORS (HTSC) UNDER THERMAL NEUTRON IRRADIATION

A. PETROV, I. KUDRENITSKIS, A. MAKLETSOV, A. ARHIPOV, N. KARKLIN
Nuclear Research Centre,
Latvian Academy of Sciences,
Salaspils, Latvia

XA9949654

Abstract

The physical properties of ordered crystals are extremely sensitive to the degree of order in the distribution of the various kinds of atoms over the corresponding sites in the crystal lattice. An increasingly popular means of creating disordered states is to use nuclear radiation. The type of radiation defects which appear and the nature and degree of the structural changes in ordered crystals depend on the kind of radiation and the fluence level, the irradiation temperature, the type of crystal structure, the composition and initial disorder of the material, the character of the interatomic forces, etc. There are many such scientific publications where the effects of fast neutron irradiation on high temperature superconductors (HTSC) have been studied in both polycrystalline and single crystalline superconductors. It is known also that the role of thermal neutrons in structural defects forming is negligible in comparison with fast neutrons because of their small (~0,025 eV) energy. But it is evident enough that in superconductors containing isotopes with large thermal neutron cross sections the important results concerning the role of point defects could be obtained. Such point defects are creating due to soft displacements of isotopes having interacted with thermal neutrons. Such the possibility of creating point defects in solids including HTSC is investigating by several groups (Austria, USA, China, Latvia) and these investigations have found the support in the person of IAEA. In this review the authors consider the changes brought about by thermal-neutron irradiation (E~0.025 eV) in the structure, superconducting and magnetic properties of gadolinium containing ordered HTSC with the structure 123, whose extremal electric and magnetic properties continue to attract both research and practical interest. All of the studies reviewed have been done on bulk polycrystalline samples $RBa_2Cu_3O_{7-\delta}$ (where R - natural mixture of Gd isotopes, ^{155}Gd, ^{157}Gd, ^{160}Gd). The sample preparation, irradiation, and measurement techniques are described in detail in the original papers cited.

1. Introduction

Different kinds of radiation in materials result in different radiation defects. Experimental radiation damage data are described in terms of an appropriate theoretical model of accumulation of radiation defects. For fast neutron irradiation the energy of a primary knock-off atom is sufficient for collision cascade initiation thus producing many displacements, per one primary knock-off atom. Interaction of the defects in the primary damaged region with a high local concentration of defects produces a situation where long-term accumulation of damage is controlled by a great number of processes: primary displacement, primary annealing of defects, diffusion-controlled annealing, cluster formation, etc.[1-3]. Consequently, the problem of the physical values estimation for the material becomes complicated due to the abundance of controlling processes.

For low energy irradiation (electrons, γ–quanta in the majority of experiments) cascade damaged regions do not occur. So one can interpret the damage in terms of simpler models than that for cascade defects production. The low-energy damage data are better suited for calculation of defect generation processes for any given mechanism of interacting of irradiation with atoms solids. One of the mechanisms of non-cascade defects production in solids was investigated in [4-7], and is of the highest importance for reactor neutron damage in gadolinium - containing materials. The mechanism is determined by the (n, γ) reactions of thermal neutrons with ^{155}Gd and ^{157}Gd nuclei and the consequent recoil of these nuclei after γ-

quanta emission. High values of the reaction cross sections ($\sigma_c^{(155)} = 6.14 \times 10^4$ b, $\sigma_c^{(157)} = 2.55 \times 10^5$ b) and significant contents of the isotopes in the natural mixture of isotopes of Gd lead to high defect production rates in the irradiated samples. In spite of the fact that no cascades are initiated in this case, the experimentally revealed defect production [3,5,8] occurring due to this mechanism is significantly higher than that for fast neutron defect production under similar reactor radiation.

Unfortunately, we had no a pure thermal neutron flux in all our experiments, i.e., the fast neutrons always were present in the Salaspils' reactor spectrum. Therefore we have carried out also the experiments with our samples using pure fast neutron fluxes in order to account for although partially the role of the fast neutrons. Thus, the impact of thermal neutron irradiation can be drawn out by comparing the experimental pictures of irradiation by reactor neutrons and pure fast neutrons.

A challenging problem which seems to be of great interest is the problem of critical currents in the low and intermediate fluences irradiated $GdBa_2Cu_3O_{7-\delta}$. Pinning force of the gadolinium defects is expected to be very high due to their high enough concentration and perhaps inhomogeneous spatial distribution in the samples.

The first serious indication of possible enhancements of critical current densities J_c by point defects in $^{155}GdBa_2Cu_3O_{7-\delta}$ found at a pure thermal neutron fluence of 4.77×10^{20} m^{-2} was given by Prof. H.Weber in [9].

The mechanism of depression of superconductivity was investigated in detail in terms of radiation damage production in the HTSC $GdBa_2Cu_3O_{7-\delta}$ enriched with ^{155}Gd (up to 91,1%), ^{157}Gd (up to 91,0%) and ^{160}Gd (up to 98,2%), as on natural enriched samples too [10].

2. History of the problem

Our investigations connected with a study of the role of gadolinium isotopes into a change of cooperative properties, which are ferromagnetism and superconductivity, dates back to the 1987th year. We irradiated $Gd_3Fe_5O_{12}$ pellets to study the line width of ferromagnetic resonance in the dependence of the fluence in a mixed spectrum reactor (thermal + fast) neutrons, and we noticed that all pellets already beginning from the value of the total fluence 5×10^{17} n/cm^2 and higher (the temperature of irradiation - 40°C) are breaking. The size of pellets was about 2 - 3 mm. All assumptions connected with the possible temperature gradient, the inhomogeneity of a content or an initial mechanical strains did not result in understanding and reasonable explanations. The pellets have been broken always. The irradiation in cadmium shielding suppressed the thermal component in a reactor neutron spectrum and breaking did not take place, thereby it was distinguished the particular role of thermal neutrons [4].

The further study of a lattice parameter for ferrimagnetics $Gd_3Fe_5O_{12}$ after the irradiation in a mixed reactor flux and after the irradiation only by fast neutrons (E > 0,1 MeV) revealed the large difference in the change of this value in the dependence of these two components. This effect of breaking gave the opportunity to distinguish the contributions of the surface layers and volumes of macroscopically irradiated sample. It should be emphasized that under corresponding conditions the irradiation by thermal neutrons give a chance to create the structural defects only in Gd sublattice.

As a whole the study of the influence of the thermal and fast neutrons on the lattice parameter and Curie temperature T_c (in degrees of Kelvin, K) gave the following [4]:

1. The dependence of the volume fraction of the disordered state C_t upon the irradiation fluence of the thermal neutrons F_{th} was:

$$C_t = 1 - \exp(-\beta_t F_{th}),$$

where $\beta_t = 2{,}5 \times 10^{-20}$ cm^2.

2. The decrease in T_c was caused by the increase of the lattice parameter "a" for $Gd_3Fe_5O_{12}$ ferrite, the fact has been described as the linear relation:

$$\Delta T_C = -\ 1250\text{K} \times (\text{Angström})^{-1} \times \Delta a.$$

3. The X-ray analysis had provided for the possibility to separate the contribution of the thermal and fast neutrons irradiated $Gd_3Fe_5O_{12}$ samples surface from their intrinsic part, irradiated solely by fast neutrons.

The results obtained during such experiments served as the starting-point for our experiments on gadolinium-containing HTSC. As we supposed, in these HTSC materials one can effectively influence by means of corresponding neutrons only on rare-earth sub-lattice without noticeable disturbing other atoms in the structure. We thought also the disappearance of superconductivity after impact of neutron irradiation may "shed light" on the nature of this phenomenon.

3. Superconducting properties of irradiated by fast and reactor neutrons $GdBa_2Cu_3O_{7-\delta}$ ceramic samples

Our HTSC experiments were carried out with neutron irradiated compounds $YBa_2Cu_3O_{7-\delta}$ and $GdBa_2Cu_3O_{7-\delta}$.

The fast neutron irradiation produces in crystals the cascade damaged regions which are the defects with structural and chemical disorder while initial composition remains the same. The size of the defect can be estimated taking into consideration the characteristic energy of the primary knocked-on atom (10^1 - 10^4 eV) for fast neutrons.

The role of thermal neutrons in structural defects forming is negligible in comparison with fast neutrons because of their small (~ 0,025 eV) energy. On the other hand, in Gd-containing HTSC recoil nuclei may become interstitials due to very large neutron-capture cross-section of ^{155}Gd and ^{157}Gd and sufficiently large recoil energy of Gd- nuclei. Upon neutron capture, the Gd nuclei relax to their ground states by X-ray emission. The momentum transferred to the recoiling Gd nucleus by this mechanism can result in the ejection of the Gd nucleus from its lattice site. Because of the low value of the knocked-on atom energy no macroscopic disordered regions are expected. The defect of this type ("Gd defect") should be interpreted as a microscopic point defect having the size of few lattice cell units.

The superconducting and structural properties of the following samples were investigated:

1) $GdBa_2Cu_3O_{7-\delta}$ powder with particle size ~ 20 μm mixed with Al_2O_3 particles of the same size,
2) massive plates of Gd and Y superconductive ceramics,
3) ensembles of particles $YBa_2Cu_3O_{7-\delta}$ with sizes 0,1 - 1,5 μm.

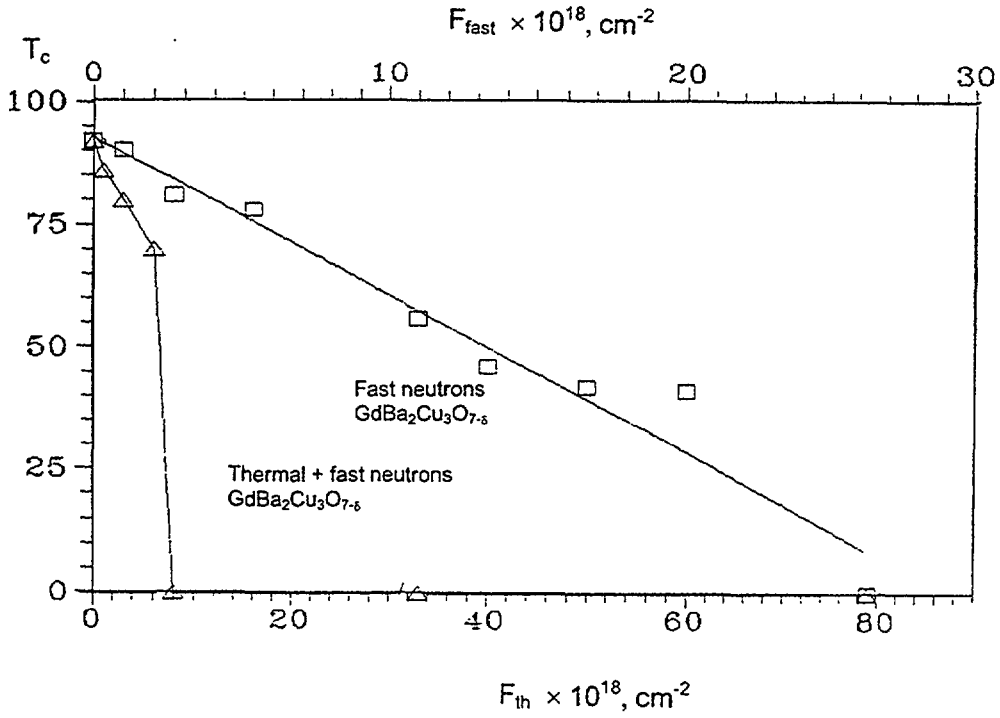

FIG.1.Critical temperature T_c in dependence on neutron fluence value for $GdBa_2Cu_3O_{7-\delta}$ with natural mixture of gadolinium isotopes [5].

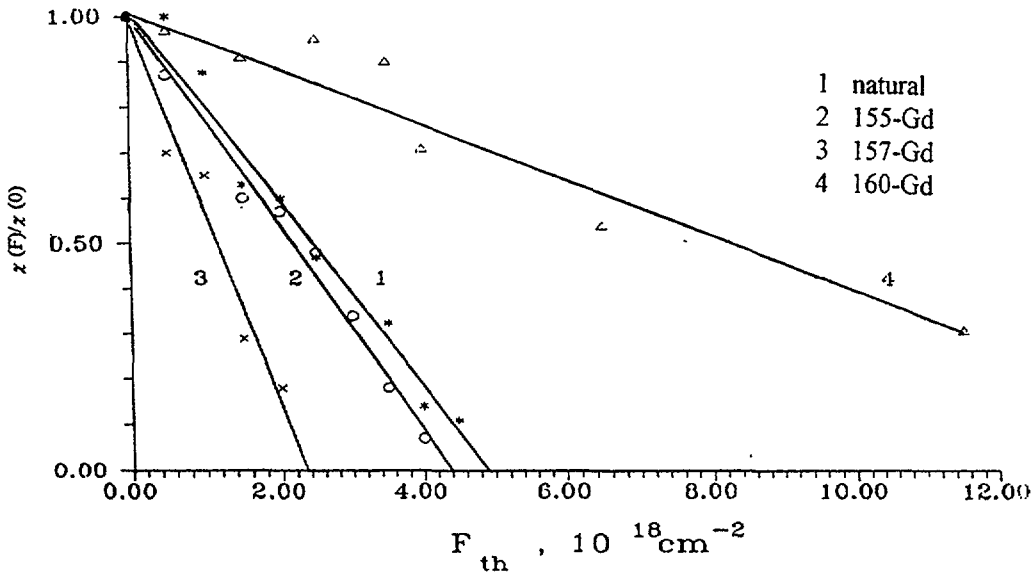

FIG.2. The value of Meissner effect χ (F) / χ (0) versus thermal neutron fluence for samples $RBa_2Cu_3O_{7-\delta}$ (R = natural mixture of Gd isotopes, ^{155}Gd, ^{157}Gd, ^{160}Gd) [10].

The irradiation temperature T_{irr} was 40°C. Half of powdered samples were shielded by cadmium to protect them from thermal neutrons irradiation. In the case of massive ceramics thermal neutrons affected only the surface of the samples as the penetration depth of thermal neutrons is about 20 -30 μm at Gd concentration 6×10^{21} cm^{-3} (the density of Gd atoms in the natural $GdBa_2Cu_3O_{7-\delta}$). The experimental results shown in Figure 1 and Figure 2 demonstrate high sensitivity of T_c and χ (F) / χ (0) of Gd ceramics particles to thermal neutron

irradiation. Sharp decrease of T_c and χ (F) / χ (0) values at the fluences (5 - 8) $\times 10^{18}$ cm^{-2} proved to be characteristic to thermal neutron irradiation. The complete degradation of superconductivity in Gd-containing HTSC ceramics occurs at the unexpectedly low thermal neutrons fluence ~ 7×10^{18} cm^{-2}. At small fluences it is possible to evaluate volumes of non-superconducting phase connected with one knocked-on Gd atom and one primary knocked-on atom using the slope of linear region of relative χ (F) / χ (0) versus fluences F curve [5]. These volumes are equal to 5 and 4×10^3 elementary cell volumes respectively. Such small volume of damage formed by one thermal neutron seems to be connected with short recoil nuclei ^{156}Gd and ^{158}Gd track length due to small recoil energy.

Thus the size of non-superconducting region connected with one "Gd defect" (~10 Angstrom) has an order of coherence length in HTSC. The fluence of thermal neutrons at which strong changes in T_c and c take place also corresponds to the concentration of Gd defects at which the distance between them has an order of coherence length.

Main conclusion derived from these first experiments is the following: essential difference in degradation of superconductivity in the $GdBa_2Cu_3O_{7-\delta}$ ceramic samples with natural mixture of Gd isotopes under the influence of reactor (thermal + fast) and pure fast neutrons was found; the regions of non-superconductivity phase are formed as the result of soft displacement of Gd^{3+} ions.

4. Structural properties of irradiated $GdBa_2Cu_3O_{7-\delta}$ ceramic samples

Structure changes in Gd123 HTSC were investigated on the ceramics plate irradiated by the fluence $F_{th} = 4 \times 10^{19}$ cm^{-2} (fluence on the surface) and $F_{fast} = 2{,}7\times 10^{19}$ cm^{-2}. The depth of thermal neutron damaged layer, taking into account ^{155}Gd and ^{157}Gd burning out, was ~300 μm. X-ray penetration depth was 30 μm. The plate was ground with the step 50 μm to an accuracy of 5 μm.

The influence of fast and thermal neutron irradiation on the interplane distance d_{103} is shown in Figure 3. Different depths of grinding correspond to different effective fluences (they are

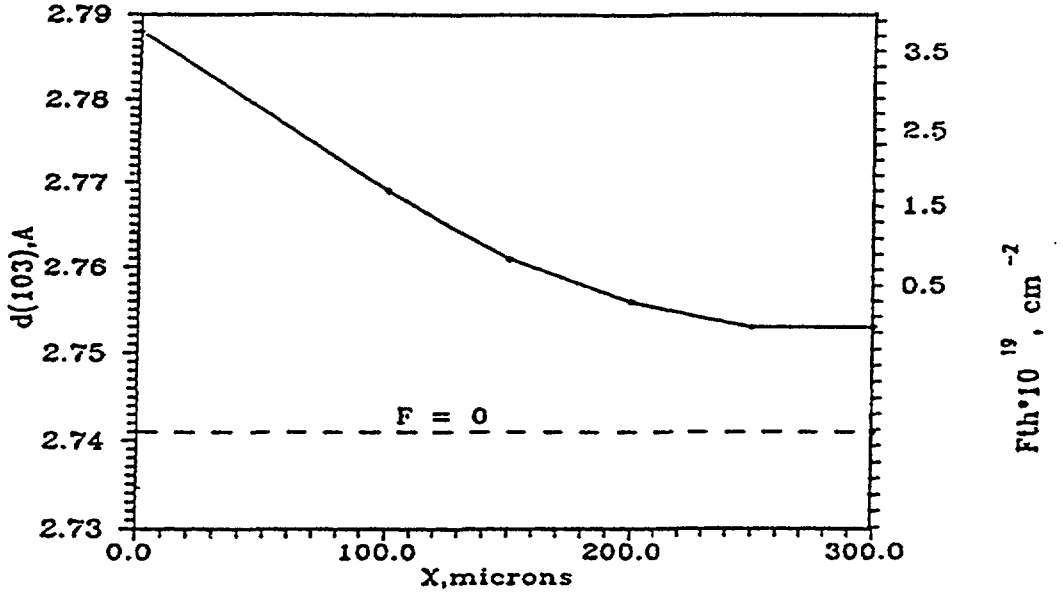

FIG. 3. The influence of fast and thermal neutron irradiation on the interplane distance d_{103} [5].

shown on the right ordinate axis). At the depth more than 300 μm only fast neutrons affect d_{103}. The doublet (200), (020, 006) measured at different depths of grinding was investigated (Figure 4). In the inner region of the irradiated sample the size and shape of doublet is similar to that of an unirradiated material. Closely to the surface the peaks of the doublet are strongly widened and in the surface layer they are transformed to one broad peak. This broadening is possibly due to inhomogenious deformation in the region of Gd defects. At $F_{th} > 2 \times 10^{19}$ cm^{-2} ($x < 100$ μm) the deformations become significant and the structure looks like tetragonal one. This evolution of the doublet strongly differs from the evolution of doublet in HTSC with decreasing oxygen content in 123 ceramics [11].

These data had been added with depth-dependent microhardness measurements [12] of Gd123 irradiated sample-plate of 2 mm thickness with $F_{th} = 4 \cdot 10^{19}$ cm^{-2} on the each surface and $F_{fast} = 2,7 \cdot 10^{19}$ cm^{-2}. The measurement of the microhardness H_v on the cross-section of irradiated sample shows that significant increase of H_v up to 5.4 ± 0.6 GPa takes place in the regions adjoint to the irradiation surfaces while in the depth of the sample the microhardness value is only slightly higher than that of the non-irradiated one (Figure 5).

Thus the fast neutron effect on the microhardness is found to be negligible while the thermal ones cause its considerable change. The difference in the effect of fast and thermal neutrons on the microhardness seems to be connected with formation of different types of defects.

The penetration depth of thermal neutrons can be estimated from the Figure 5. as ~ 700 μm. The same order of magnitude of thermal neutron damaged layer was obtained by X-ray analysis (Figure 3.).

To distinguish the role of each Gd isotope in the change of superconducting properties, the influence of thermal neutrons irradiation on superconducting and structural properties of enriched $RBa_2Cu_3O_{7-\delta}$ (R - natural mixture of Gd isotopes, ^{155}Gd, ^{157}Gd, ^{160}Gd) was investigated. Four samples of isotopic content $RBa_2Cu_3O_{7-\delta}$ were investigated [10]. Sample No.1. -91.0% ^{157}Gd isotopes enriched; No.2.- 91.1% ^{155}Gd isotopes enriched; No.3. - nature mixture of gadolinium isotopes; No.4. - 98,2 % ^{160}Gd isotopes enriched. The sample 4. served as the bearing sample. These samples constituted disks of the 10 mm diameter and the thickness of 1 mm. The axis of crystal texture was the axis "c" perpendicular to plane of disks.

The irradiated samples for structural measurements represented plates with sizes 1 mm × 2 mm × 10 mm, which have been cut by the diamond saw so, that axis " c " was perpendicular to plane of the plate. Plates were placing in hermetically sealed aluminium containers, filled up by gaseous helium. and were irradiating in the water channel of reactor. The irradiation was made by mixed spectrum reactor flux, whose included also the component of fast neutrons (ratio $F_{th}/F_{fast(E>0.1\ MeV)}$ was approximately 5 : 1). Iron irradiation for X-ray measurements of the plates in the range of angles up to $2\theta = 90^{\circ}$ was used.

Usually weak reflections (005), (007) were well-defined on the roentgenograms. The line (006) was the most strong. We have observed in dependence on neutron fluence this line and the intensity of (200), (020, 006) doublet. Exposure has been carried out both from butt-end of the plate and along the axis " c ". It should be mentioned that the ratio of the lines intensity in the doublet differed little from one for non-textured sample.
The maximum fluence achieved by us was $F_{th} = 5 \cdot 10^{19}$ th.n./cm^2 (the fast neutron flux component was $1 \cdot 10^{19}$ f.n./cm^2 correspondingly) during of irradiation of enriched samples. The maximum fast neutron fluence achieved was $F_{fast} = 8 \cdot 10^{19}$ f.n./cm^2 for the irradiation of the sample $GdBa_2Cu_3O_{7-d}$ with natural mixture of gadolinium isotopes.

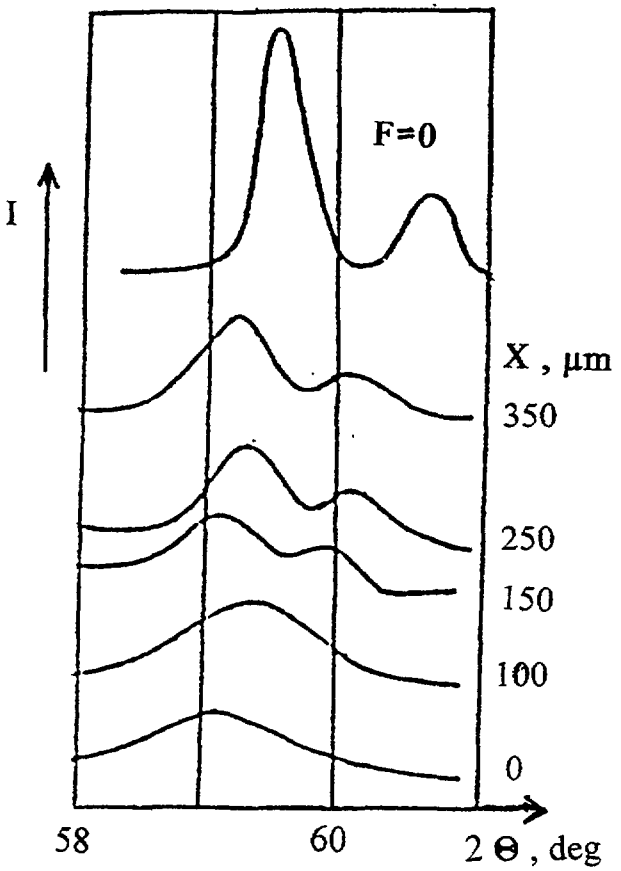

FIG.4. Transformation of (020, 006), (200) doublet with the depth of grinding; x - thickness of the grinded layer [5].

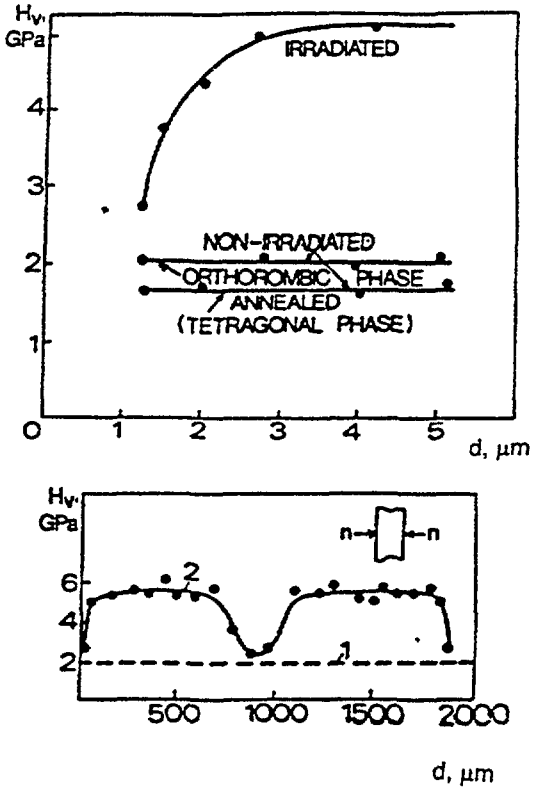

FIG. 5. Microhardness versus indentation depth for irradiated sample and for non-irradiated samples in orthorhombic and tetragonal phase (upper part of figure), and microhardness distribution on cross-section of irradiated samples (lower part of figure) [12].

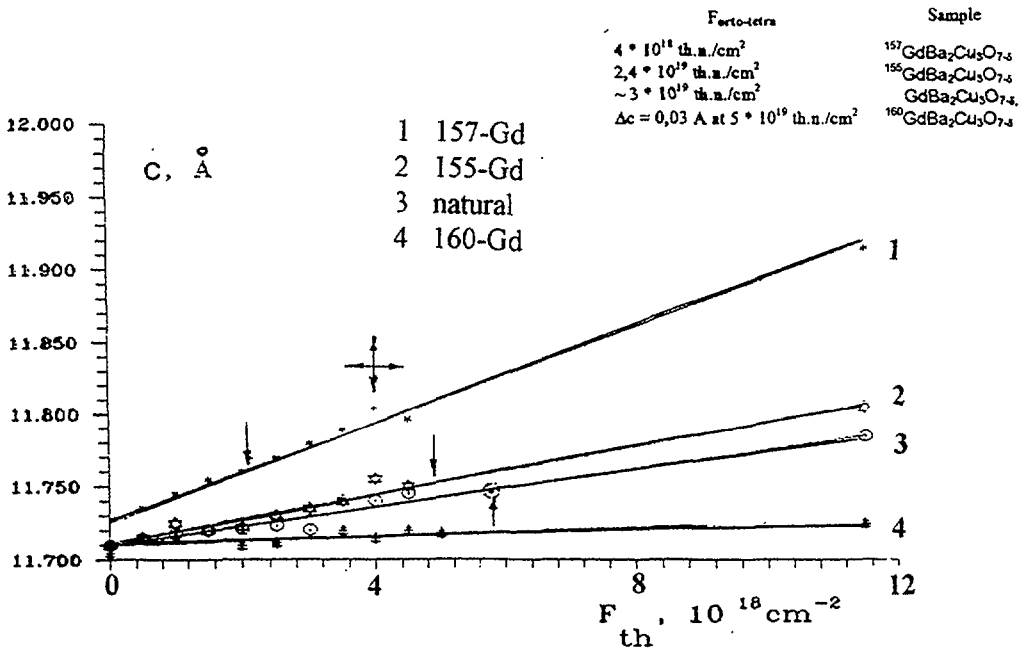

FIG. 6. The dependence of parameter "C" of samples $RBa_2Cu_3O_{7-\delta}$ on the thermal neutron fluence F_{th}.

The main results can be formulated as follows:

1. Structural parameter " C " for all samples No. 1. - 3. depended linearly on the thermal neutron fluence at least up to 10^{19} th.n./cm^2 . In the range of the values 1×10^{19} th.n./cm^2 - 5×10^{19} th.n./cm^2 the rate of increasing of the parameter " C " slightly diminished. The value of the parameter " C " for the bearing sample No.4. changed little and the increasing at the fluence of 5×10^{19} th.n./cm^2 was about 0,03 Angströms (Figure 6.). Measurements were done by using magnetic susceptibility and structural methods. The values of thermal neutron fluences for structure transition ortho - tetra are indicated [12].

2. We suppose that the values Δc for the samples No. 1. - 3. have been defined by the thermal component of the total reactor flux. The complete depression of superconductivity in the samples No. 1.-3. occurred at the practically identical values of Δc = (0,050 ± 0,004) Angströms [10].

3. The sample $^{157}GdBa_2Cu_3O_{7-\delta}$ was became by the tetragonal structure's sample at the fluence about 4×10^{18} th.n./cm^2 , the sample $^{155}GdBa_2Cu_3O_{7-\delta}$ - at the fluence ~ $2,4\times10^{19}$ th.n./cm^2 , the sample $GdBa_2Cu_3O_{7-\delta}$ (the natural mixture of gadolinium isotopes) - at the value of the fluence ~ 3×10^{19} th.n./cm^2 . The sample No.4. for our opinion gradually is getting the sample with the amorphous structure (the weakening of all lines in dependence on neutron fluence). It is observed little by little the damage of the crystal structure under the influence of fast neutrons mainly. The " tetragonalization " of the sample No.3. at the fluence ~ $(3 - 4) \times 10^{19}$ fast n./cm^2 without thermal neutrons component was not observed (earlier our investigation, [5]).

4. It was observed the essential damage of texture of all samples No. 1. - 4. during irradiation. The width of reflection (006) for samples No. 1.-3. was increasing non-linearly with the fluence. It was increasing very little in "superconducting" region ($F < F_{critical\ for\ SC}$) and has undergone the considerable increasing (more than 2 times) at $F > F_{critical\ for\ SC}$.

5. The role of displaced gadolinium ions was revealed also in the effect on neutron irradiation on microhardness [12]. The microhardness has been found to grow from 2 to 5 GPa under thermal neutron impact while the fast neutron irradiation caused only negligible changes of microhardness. We consider the microhardness increase observed is connected with strong lattice distortion due to displacement of Gd atoms under thermal neutron irradiation.
The estimations of several possible superconductivity suppressing mechanisms connected with arising of pressure, d variations and magnetic moments of Gd^{3+} ions in irregular positions of 1-2-3 structure were carried out. The most probable mechanism is supposed to be the last one. The region of suppression has the size about 10 Angströms which is comparable with the coherence length in 1-2-3 materials.

X-ray structure investigations have demonstrated that radiation induced rate of degradation of the orthorhombic structure is significantly lower than the superconductivity degradation rate.
The existence of local lattice distortions due to (n,γ) reaction has been additionally proved by significant increase of microhardness in the regions of thermal neutron impact. Moreover, the difference between the radiation-enhanced microhardness values and those for the samples with especially lowered oxygen content has also strengthened the suggestion of the absence of oxygen removal from the sample under thermal neutron irradiation.

5. Magnetic properties of irradiated $GdBa_2Cu_3O_{7-\delta}$ ceramic samples

An exciting challenge is to understand the interplay between magnetism (or concrete magnetic properties) and superconductivity, including under neutron irradiation. This was addressed in our study of the degradation of superconductivity in irradiated samples $GdBa_2Cu_3O_{7-\delta}$ by thermal along with fast neutrons and by fast ones (E > 0,1 MeV) only. The more interesting results are the data of magnetic moment of superconducting samples m (H,T,F), at the different values of magnetic field H, temperature T and fluences F of thermal neutrons only. The unique data in this sense belong to the group of Prof. H.Weber, who has the opportunity to irradiate superconductors by pure thermal neutrons without the component of fast ones, using the thermal column. This uniqueness consists in selective and strong interaction of thermal neutrons with isotopes of gadolinium ^{155}Gd and ^{157}Gd, prevailing even in the samples $GdBa_2Cu_3O_{7-\delta}$ with natural mixture of gadolinium isotopes. That means the structure changes are mainly in rare-earth sublattice and as far as the gadolinium ion is the strongest (except Tm, for which the total angular momentum I is largest , for Gd the value S is the largest) it may be easy detected by means of measuring the value of magnetic susceptibility. The fast neutrons affect almost on all atoms entering into content of superconductor and it is more difficult to extract (distinguish) an information about Gd ions, for example about their position in the crystal structure of $GdBa_2Cu_3O_{7-\delta}$ (Fig.7., from [13]).

Previous authors have shown [14, 15] that T_c is dramatically affected by subtle changes in oxygen content. Here we try to show that the displacements of Gd both after thermal and fast neutrons irradiation play an important role as well.

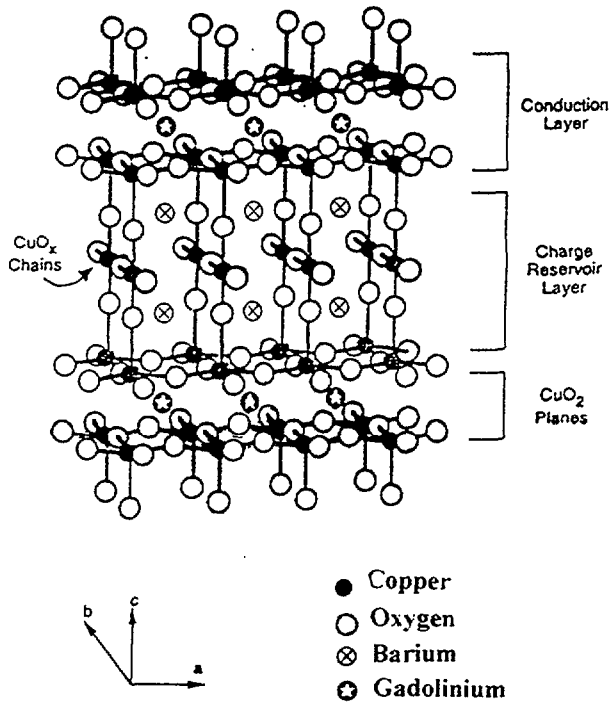

FIG.7. Crystal structure of $GdBa_2Cu_3O_{7-\delta}$ [13].

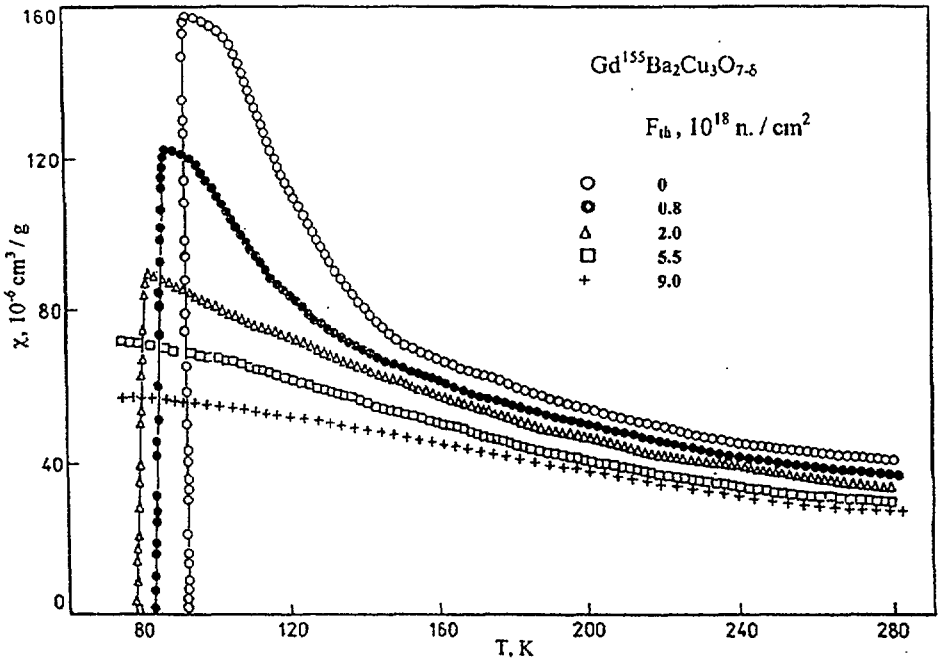

FIG.8. The mass specific susceptibility under impact of thermal neutron irradiation in the dependence on temperature T for the $^{155}GdBa_2Cu_3O_{7-\delta}$ sample. The irradiation was made by mixed spectrum reactor flux, whose included also the component of fast neutrons (ratio F_{th}/F_{fast} approximately 5:1) [10].

5.1. Experimental procedure

Susceptibility measurements using vibrating magnetometer and magnetic balance (method of Faraday) from 300 K down T_c have been carried out (Fiure 8.). For pure $GdBa_2Cu_3O_{7-\delta}$ Currie-Weiss law is nearly perfectly obeyed from T_c to 300 K.

At first sight it seems surprising to see a paramagnetic susceptibility in a superconductor. But the applied field (in our case ~ 15 kOe) is much larger than H_{c1} (~ 100 Oe), so that much of the material of the sample is threaded by flux. Thus, the measured susceptibility χ is a combination of the paramagnetism of the normal part and the diamagnetism of the superconducting part of the sample, for example, any graph of the group of Prof. H.Weber. Because of the large moment of the Gd ions the paramagnetic part dominates, but the diamagnetic part lowers the susceptibility. Nevertheless it is difficult precisely to evaluate the portion of the superconductive part, therefore we decided to process the magnetic susceptibility for normal state of our samples at high temperatures.

On a basis of temperature measurements (T_c - 300 K) of specific magnetic susceptibility and its processing in coordinates ($1/\chi$, T) the values of χ_o, μ and θ, entering into the expression

$$\chi = \chi_o + C\,(\mu) / (T - \theta),$$

where χ - the measured susceptibilty, χ_o - temperature independent summand, μ - the effective magnetic moment of ion Gd^{3-} in units of μ_B, θ - Curie-Weiss constant, have been found for all irradiated by fast neutrons samples, including the sample of $^{157}GdBa_2Cu_3O_{7-\delta}$ which was irradiated by two fluences of thermal plus fast neutrons.

5.2 Results and their discussion

Impact of reactor neutrons (thermal + fast) on $GdBa_2Cu_3O_{7-\delta}$ drastically affect their superconducting properties [5, 6, 8, 10].

The structure of $GdBa_2Cu_3O_{7-d}$ can be viewed as a stacking of three perovskite layers with a plane of Gd atoms every three layers, so that the Gd atoms are separated by CuO_2, BaO, CuO_x, BaO, and CuO_2 planes.

TABLE I. THE MAGNETIC PROPERTIES (MEISSNER EFFECT, MAGNETIC EFFECTIVE MOMENTS AND PARAMAGNETIC CURIE TEMPERATURE) FOR THE $REBa_2Cu_3O_{7-\delta}$ POLYCRYSTAL (CERAMICAL) SAMPLES SERIES, ALONG WITH THEIR "c" PARAMETRS AND RE^{3+} RADII.

RE^{3+} radii, A	Compounds	Meissner effect, %	μ_{eff} (theory)	μ_{eff} (exper.)	θ, K	c, A	T_c (onset)
1,11	$GdBa_2Cu_3O_{7-\delta}$	40*	7,94	7,9* 7,75-7,85	- 0,4*	11,703(3)*	93,8 *
1,07	$DyBa_2Cu_3O_{7-\delta}$	35	10,65	10,45-10,69	-7 - -8	11,668 (2)	93
1,05	$HoBa_2Cu_3O_{7-\delta}$	34	10,61	10,48-10,60	-16 - -19	11,670(2)	93
1,04	$ErBa_2Cu_3O_{7-\delta}$	34	9,58	9,63 - 9,93	-15 - - 16	11,659(2)	92,5
1,04	$TmBa_2Cu_3O_{7-\delta}$	36	7,56	7,53 - 7,69	-35 - - 38	11,656 (2)	92,5
1,00	$YbBa_2Cu_3O_{7-\delta}$	49	4,54			11,650(2)	87-88

Note. The experimental results of the group of superconductivity, Riga, for $GdBa_2Cu_3O_{7-\delta}$, is marked by * .

It is well known, that the initial state for many rare earth metals in the structure $REBa_2Cu_3O_{7-d}$ (RE = Sm, Eu, Gd, Dy, Ho, Er, Tm) does not destroy superconductivity, all these compounds $REBa_2Cu_3O_{7-d}$ can be prepared as single phase and the T_c for these phases remains essentially constant at 90) 3 K (Table I.).

So, when the Gd atoms are places along "c" axis in their right sites, then the T_c is equal to maximal, ~ 93 K, and superconductivity does not disappear. What is changed when the displaced atoms of gadolinium are appeared ? In what state are they ? By what initial non-irradiated state does differ from the irradiated one ?

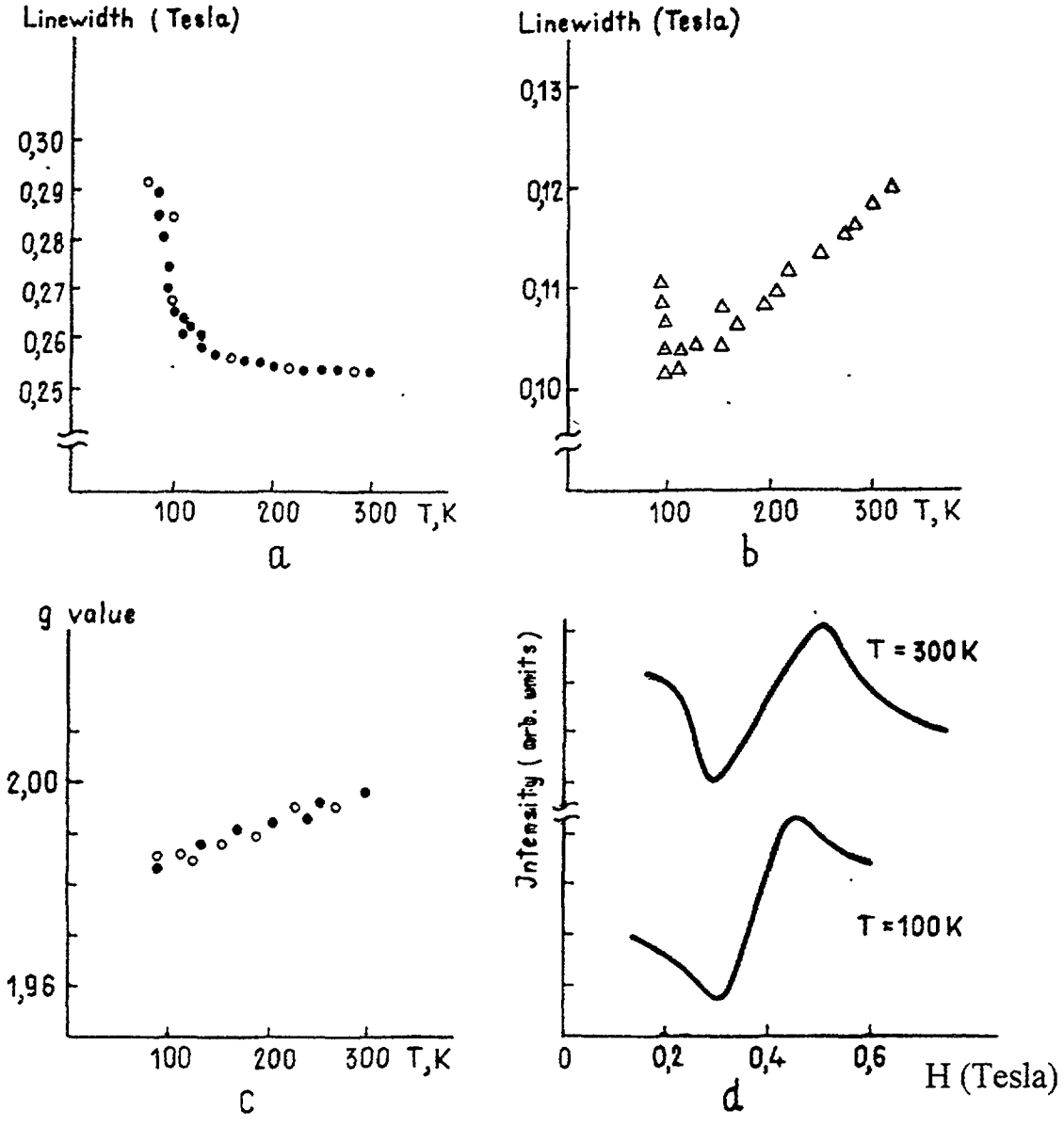

FIG. 9. ESR data for the samples $^{155}GdBa_2Cu_3O_{7-\delta}$ (black dots) and $^{157}GdBa_2Cu_3O_{7-\delta}$ (open dots) on the Fig. 9.a, 9.c. thermal neutron fluence F_{th} = 2'10^{18} th.n./cm^2. The case of non-irradiated sample of $^{155}GdBa_2Cu_3O_{7-\delta}$ is shown on Fig. 9.b; Fig.9.d - the example of recording of ESP spectrum for 2 temperatures

Let us begin with the initial non-irradiated state.

It is considered that there is very little interaction between the magnetic Gd ions and the conduction electrons (or quasi-holes) responsible for superconductivity. Also, ^{155}Gd Mössbauer spectroscopy has provided direct evidence for an absence of conduction electrons at the Gd sites in $GdBa_2Cu_3O_{7-\delta}$ [16, 17]. This suggests that the observed antiferromagnetic ordering at T_N = 2,25 K is not due to the Ruderman - Kittel - Kasuya - Yosida (RKKY) interaction, which is mediated by the conduction electrons, but is rather due to dipole-dipole interaction between the Gd magnetic moments. May be there is even a little admixture of superexchange interaction. More recent neutron diffraction studies on non-superconducting $GdBa_2Cu_3O_{7-\delta}$ (δ = 0,86) compounds have shown c-axes ordering with unit-cell doubling in all three directions. For δ = 0 the unit cell is doubled in all three directions, for δ = 0,5 the c-direction is ferromagnetic [18-20].

In all this it is essential for us only the following: dipole - dipole interaction between the ions Gd^{3+} along the axis "c" may resulting in both antiferromagnetic and also ferromagnetic ordering, what is detected by direct method of neutron diffraction. We are able to fix this after all only indirectly using the value θ.

As has been calculated by J.Felsteiner [21], to a good approximation, all possible configurations when Gd-ions are along the axis "c" have the same dipole-dipole interaction energy; each arrangement of Gd magnetic moments was assumed to have eight sublattices, all the dipoles on a given sublattice being parallel to one another. This is due to the large separation of the Gd ions along the "c"axis which is approximately 3 times that along the "a" and "b" axes.

The ground state of the Gd^{3+} ion from our measurements of the magnetic susceptibility is $^8S_{7/2}$ with the values L = 0, J = 7/2, S = 7/2, so the effect of the crystalline electric field (CEF) on the ground state splitting cannot be strong. Of course, CEF splitting can occur through admixtures of states with non-zero orbital angular moment.

The experimental value of the magnetic moment of the Gd^{3+} for non-irradiated $GdBa_2Cu_3O_{7-\delta}$ is equal to 7,9μ_B, what is very close to the value of the free-ion magnetic moment $\mu = g\mu_B [S (S+1)]^{1/2}$ = 7,937 μ_B for S = 7/2 and g = 2 (the factor of spectroscopical splitting).

Colleagues from the Institute of the New Chemical Problems (Chernogolovka, Russia) [22] have recently reported electron - spin resonance measurements which have indicated the existence of a CEF splitting of about 1,5K in the ground state of Gd^{3+} ions in dilute $Gd_xY_{1-x}Ba_2Cu_3O_{7-\delta}$. Analysis of their measured CEF parameters has further indicated the existence of an easy axis of magnetisation along the "z" direction (the principal axes of the electric field gradient tensor at the Gd sites coincide with the crystallographic axes a, b, c). This explains to some degree the reduction of the value g (g-factor) with decreasing of the temperature (Figure 9.), which was observed by us experimentally. Taking into account the temperature dependence g (T), the values m (Gd^{3+}) for all fluences both for fast neutron irradiation and for thermal + fast neutron irradiated sample of $^{157}GdBa_2Cu_3O_{7-\delta}$ are within limits 7,75 - 7,85 μ_B: We consider that there is not the dependence of magnetic moment m (Gd^{3+}) on fluence and, therefore, on the position of displaced gadolinium ion in our experiments.

Our experiments show that after irradiation by fast neutrons the value θ rushes to change the sign for completely degradated in the sense of superconductivity samples (see Figure 10.). Two black circles on this figure are two fluences of thermal plus fast neutrons irradiation for $^{157}GdBa_2Cu_3O_{7-\delta}$. Figures illustrate the dependence of the values χ and T_c (Figure 11.) and the increase of the temperature independent summand χ_0 (Figure 12.) on the value of fast neutron fluence F.

The such behaviour of the value θ we try to discuss and account for using the conception that the T_c is depressing due to a volume-change effect. In favour of there are the following facts:

1. our experimental data for increasing of the parameter "c" in dependence on fluence (see Figure 6.),

2. the complete depression of superconductivity in the samples of $^{155}GdBa_2Cu_3O_{7-d}$, $^{157}GdBa_2Cu_3O_{7-d}$ and $GdBa_2Cu_3O_{7-d}$ with natural mixture of Gd isotopes occurred at the practically identical values of Dc = (0,050) 0,004) Angströms,

3. soft displacement of Gd^{3+} ions after thermal neutron irradiation do not disturb the orthorhombic modification: for two enriched samples ^{155}Gd, ^{157}Gd and sample with natural mixture of Gd isotopes the transition into tetragonal phase takes place after complete disappearing of superconductivity,

4. the value of the magnetic moment for Gd^{3+} does not depend on the fluence of neutron irradiation,

5.the behaviour of the value q in dependence on fluence for our $GdBa_2Cu_3O_{7-d}$ samples,

6. the correlation between the values q and "c" for other magnetic ions in the rare-earth group $REBa_2Cu_3O_{7-d}$ (Table I.),

7. the directions of the up-to-date returns that the main role in creating of superconductivity belongs to CuO_2 planes [13] (Fig. 7.),

8. the value dT_c / dP along the axis "c" is equal 0.1 K / kbar for the $GdBa_2Cu_3O_{7-d}$ [23]; that means the increase of the value T_c by compression of sample.

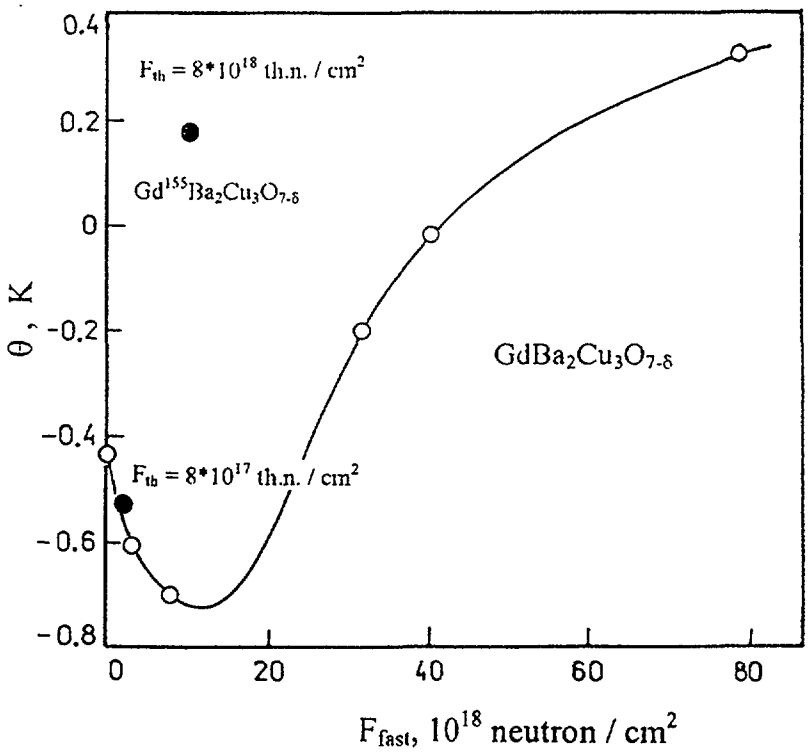

FIG.10. The processing of magnetic data by means of Curie-Weiss law: $\chi = \chi_0 + C / (T - \theta)$ for the $GdBa_2Cu_3O_{7-\delta}$ sample with natural mixture of Gd isotopes. Figure illustrates the dependence of value θ fast neutrons fluences. Two black points are for $^{155}GdBa_2Cu_3O_{7-\delta}$ with fluences indicated near.

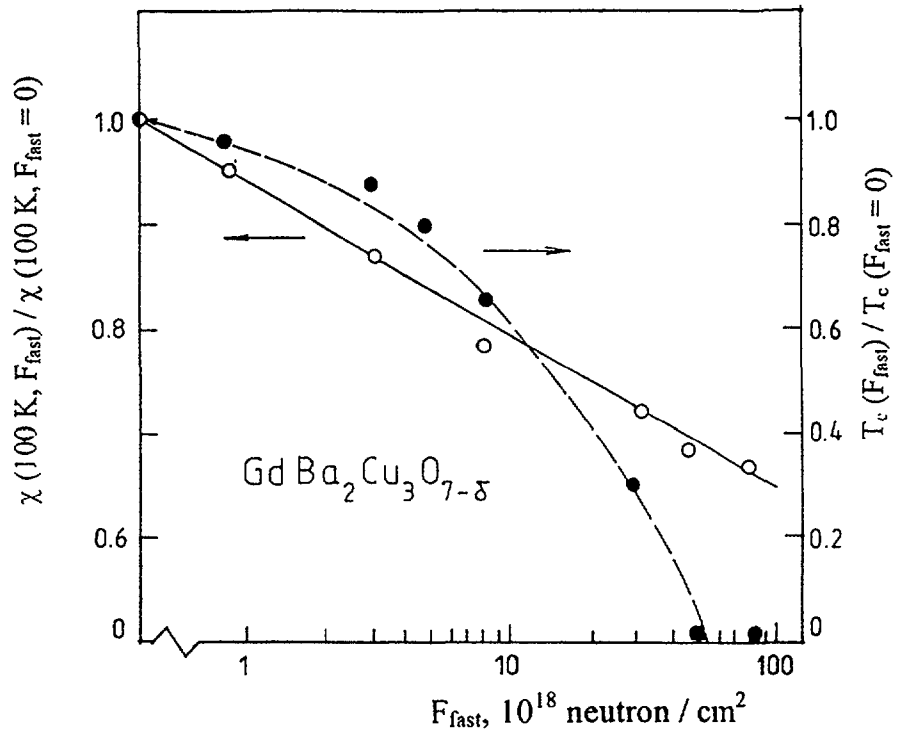

FIG.11. The mass specific magnetic susceptibility and the value of critical temperature in the dependence on fast neutron fluences for temperature T = 100 K.

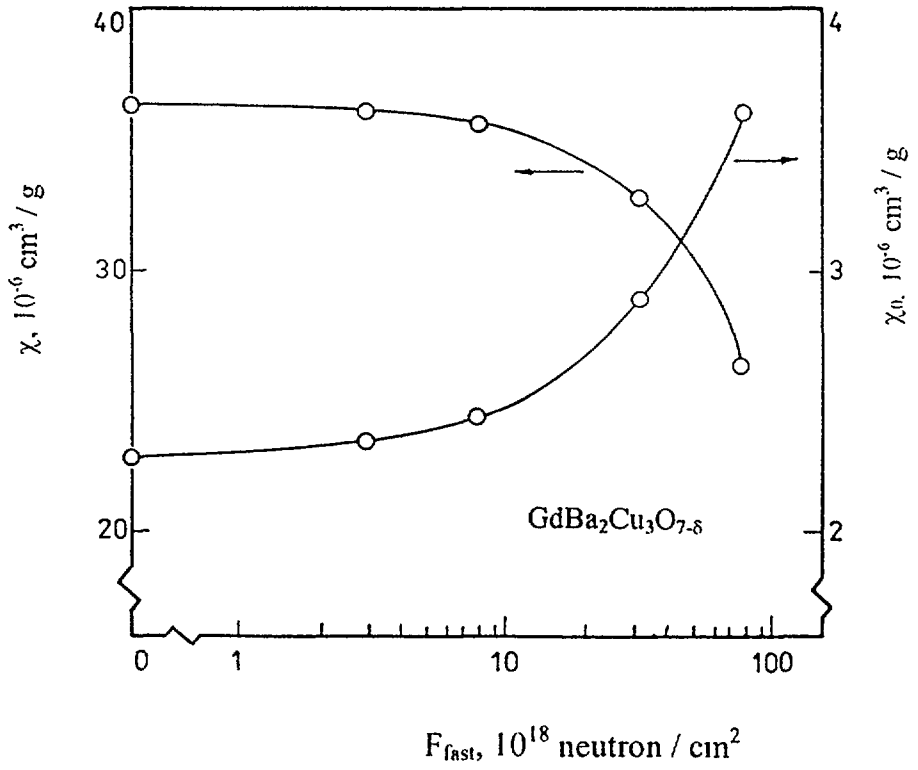

FIG.12. The processing of magnetic data by means of Curie-Weiss law: $\chi = \chi_0 + C / (T - \theta)$ for the $GdBa_2Cu_3O_{7-d}$ sample with natural mixture of Gd isotopes. Figure illustrates the dependence of values χ and χ_0 on fast neutron fluences.

It is interesting to note that during such disorderly process as preparing the samples $GdBa_{2-x}Sr_xCu_3O_{7-d}$ is going on not only the substitution of Ba^{2+} by Sr^{2+}, but is going on the process of mixture of positions of Gd^{3+} and Sr^{2+} . Analysis of X-ray spectra confirms [24,25] that 26 % of ions of Gd^{3+} may occupy the positions Sr^{2+} and the corresponding number of ions Sr^{2+} are in the positions Gd^{3+} in the compound $GdBaSrCu_3O_{7-d}$.
We try using all these data and assumptions to understand where may be the displaced ion of gadolinium after (n,g) reaction.
It is seemed, all this confirms that all displacements of Gd^{3+} may occur only along the "c" axis. In any case we are disposed to consider that the most probable process is the exchange of ions Ba^{2+} and Gd^{3+} along the "c" axis.
The insensitivity of T_c to the presence of magnetic rare earth ions suggests that the superconducting electrons are far away from the magnetic ions.

6. Evaluation of the displacement energy of Gd atoms in $GdBa_2Cu_3O_{7-\delta}$ from experimental data

The processing of the experimental data along with the Meissner effect value variation has made it possible to evaluate the ratio of the degradation rates of $GdBa_2Cu_3O_{7-\delta}$ enriched with ^{155}Gd and ^{157}Gd isotopes respectively [26].
The samples irradiated in the experimental work [10] were specially prepared to significantly reduce the effect of absorption of thermal neutrons in the material and burn up of the ^{155}Gd and ^{157}Gd isotopes. Meissner effect measurements on the samples revealed that the damage introduced is a linear function of irradiation time. That means that the observed Meissner variations are proportional to the amount of damaged non-superconductive phase in the sample and is proportional to the number of displaced atoms.

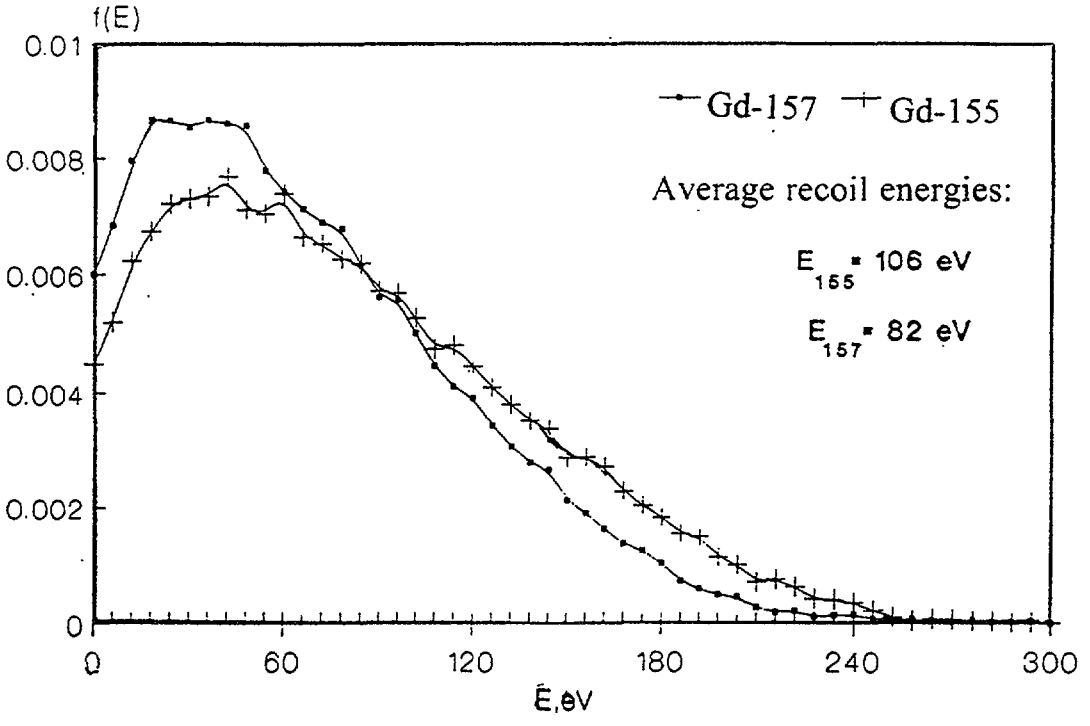

FIG 13. Normalised recoil atom energy spectra for ^{155}Gd and ^{157}Gd [26]

TABLE II. SOME CHARACTERISTICS OF THERMAL NEUTRON-INDUCED RADIATION DAMAGE PRODUCTION IN $GdBa_2Cu_3O_{7-\delta}$: $\sigma_d^{(i)}$ - DISPLACEMENT CROSS SECTIONS FOR A Gd ATOM, $K_i^{(0)}$ - THE DEFECT PRODUCTION RATES.

	$\overline{E^{(i)}}$, eV	$p^{(i)}$	$\sigma_d^{(i)}$, b	$K_i^{(0)}$, dpa/s
^{155}Gd	106	0.023	1.4×10^3	3×10^{-6}
^{157}Gd	82	0.011	2.8×10^3	6×10^{-6}

Note: The value $K_i^{(0)}$ is estimated according to the formula $K_i^{(0)} \sim n_0 F_{th} \sigma_d^{(i)}$,
where n_0 - the estimated total number of displaced atoms per displaced Gd atom ($n_0 \sim 10$),
$F_{th} = 2.0 \times 10^{13}$ th.n. / cm^2 / s - a typical thermal neutron flux for our experiments.

The principal problem for the computation is the fact that the excited nucleous after having absorbed thermal neutrons emits several γ-quanta with different energies E_γ. The total recoil momentum of the nucleous is the vector sum of the individual recoil momenta. No delay should be taken into account in this compution because for the nuclei ^{156}Gd and ^{158}Gd the intra nucleus relaxation time is short compared with that of the atom displacement time. To compute the functions, represented on the Figure 13., we have performed Monte-Carlo simulations of the random process of γ-quanta emission with the given emission probabilities. The probabilities are determined by the energy levels and the inter-level transition probabilities of the excited ^{156}Gd and ^{158}Gd nuclei. The probabilities were investigated experimentally and are available, for instance, in [27], for some transitions from the highest level (5 MeV < E_γ < E_{max}) and for several transitions near the ground state (E_γ < 1 MeV). Transitions in the quasi-continuous spectrum ($E_\gamma \sim$ 2 - 5 MeV) are not resolved and identified so we had to use for the Monte Carlo simulation the accurate energy and probability values for the resolved transitions and approximate values taken from the experimental curves [27] for quasi-continuous γ-spectra.

The results calculated, i.e., the displacement probabilities $p_d^{(155)}$ and $p_d^{(157)}$ for different threshold energies E_d and the threshold energy of Gd atom displacement producing disordered bubbles in $GdBa_2Cu_3O_{7-\delta}$, E_d^* = 150 eV are presented in Figure 13. and Table II. In terms of our approach we can for various displacement energies calculate the mean volume of the structural defect produced by a single displaced nucleus and compare this value with that obtained from experimental data on neutron-induced HTSC degradation (Meisner effect magnitude measurements). The degradation is determined by the radiation-induced formation of disorded non-superconductive "bubbles" When a Gd atom is displaced with energy close to the threshold energy value no "bubbles" are expected but rather some microscopic point defects. Obviously there is a "threshold energy II E_d^* ", being the critical energy of non-superconductive "bubble" formation. The value of E_d obtained and discussed above is actually the value of mentioned "threshold energy II", E_d^*. Having realized the physical meaning of the computed values we can estimate the "normally defined" threshold displacement energy. Estimating the critical volume V_c for "bubble" formation as V~ (3-5) $\times V_o$, where V_o - unit cell volume, the multiplicator (3 - 5) follows from our experiments [5], we should expect that for linear approximation, "threshold energy II " is $E_d^* \sim$ (3-5) $\times E_d$. As our computation yield a "thershold energy II " value of 150 eV, the conventional displacement energy value is $E_d \sim$ 30 - 50 eV.

7. Model of degradation of superconductivity in these samples

At present after all experimental data the picture of disturbance in irradiated by thermal neutrons sample is the following: the regions with strongly distorted structure which surround interstitial ions of Gd^{3+} are of pointed character and contain approximately 10 atoms. The every such a region is surrounded by non- superconducting sphere with the volume of five unit cells [5] and with inhomogeneous deformation within the sphere (bubble or islet). The size of distorted islet or bubble around Gd-defect is comparable with the coherence length in high T_c-superconductors. When these bubbles begin to contact one another then the condensation takes place and the sample abruptly becomes non - superconducting (Figure 14.). The possible reason of depression of superconductivity may be the appearance of strongly paramagnetic ions of Gd^{3+} in "prohibited" sites of the structure not far from the layers CuO_2. In order to define the possible positions of displaced Gd^{3+} it is necessary to use other methods of analysis, for example, Mössbauer measurements.

We assume that displacement of Gd^{3+} may occur along the "c" axis. Due to results, summarized above in the Table I., we are disposed to consider that more probable process is the exchange of ions Ba^{2+} and Gd^{3+} or placing recoiled ion Gd^{3+} near the plane CuO_2.

Taking into account the size of ions Ba^{2+} and Gd^{3+} the distance between the nearest planes of CuO_2 increases and, as far as at present it is considered that superconductivity is caused by conduction mechanism in these layers (planes), superconductivity on the whole sample disappears.

Of course, the such model is one of the possible models and we do not pretend on an establishment of final truth in this question. All in all, the disappearing of superconductivity in the ceramic oxides after neutron irradiation remains a very difficult problem for experimental confirming and demands the further experiments and the processing of data, connected with pure thermal neutron irradiation of gadolinium isotopes enriched samples.

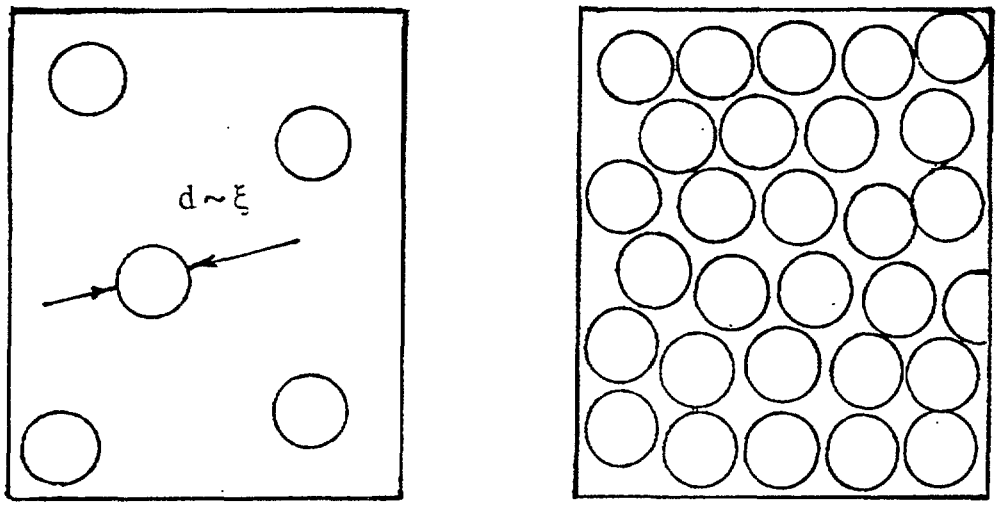

FIG.14. Possible explanation of abrupt transition from superconducting to normal state during thermal neutron irradiation of $GdBa_2Cu_3O_{7-\delta}$.

APPENDIX 1: POSSIBLE DEPENDENCE OF MÖSSBAUER RADIATION ON HTSC CURRENT

In this appendix we would like to discuss the following effect observed by us: the dependence of Mössbauer radiation on the direction of superconductive current. The main idea of the experiment was the following: when current is directed from superconductor to usual conductor, a Cooper pair, coupled by phonon exchange interaction, decays in usual conductor radiating phonon, causing additional lattice excitation in usual conductor, being at the same time a source of Mössbauer radiation. That, in turn, causes an absorption decrease in resonance absorber and increase of counts number on radiation counter.

The experimental routine was the following (Figure15.): Mössbauer source (Co^{57} in Cr pattern) was in mechanical contact with $YBa_2Cu_3O_{7-\delta}$ superconductive powder (T_c= 92 K, particles size ~ 30 μm) under the pressure of 2×10^9 N/m^2. Two indium washers were used as current outputs. Radiation, passed through resonance absorber, was detected by radiation counter. Relative velocity source-absorber was zero.
For every current value a number of counts was measured for three cases: current direction superconductor - usual conductor (N_{s-c}), reverse current direction (N_{c-s}) and zero current (N_o). The following values were considered:

$$\alpha = (N_{s-c}-N_{c-s})/N_{c-s} \quad \text{and} \quad \beta = (N_o-N_{cs})/N_{cs}\,.$$

The experimental results are presented in Table III .

Absolute Mössbauer fraction dependence of superconductor current in the most general form may be described by an additive Debye-Waller factor value linearly depending on superconductor current value

$$(2W + qI),$$

where

W - Debye-Waller factor,
I - superconductor current,

then

$$\alpha = (1-\exp(-qI)) / (\exp(2W)-1).$$

Expanding exp(-qI) into a series and taking into account only the first term of the expansion due to qI negligibility, we obtain linear dependence on superconductive current at fixed temperature. It is evident from the experimental results for the current 20 mA that values of a do not depend on measurement duration (1 or 5 sec) and current parameters sequence order (I_o, I_{c-s}, I_{s-c} or I_o, I_{s-c}, I_{cs}). The measurements at I = 100 mA are more complicated. Due to a considerable voltage drop across the "HTSC - Mössbauer source" contact (4-6 V) the source was appreciably heated by a current flow and cooled down for lack of current. The source heating also caused the resonance absorber "transparence" increase, as well as the source lattice excitation due to superconductor current, that slightly darkened the picture (seeming decrease or increase of the superconductor current effect). However, in any case heating did not cause disappearance of the effect, which exceeded measurement error.

We realize, that our experiment may be interpreted not only in terms of electron coupling due to electron-phonon exchange interaction [28]. But the results are in agreement with the latest works [29], describing HTSC effect in the terms of BCS.

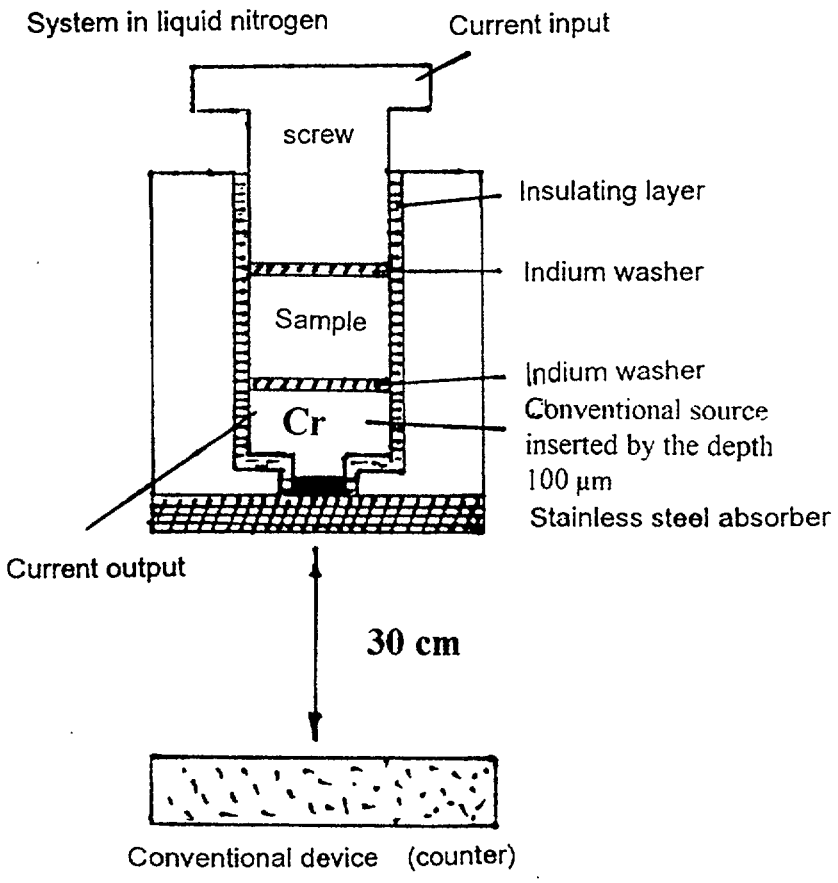

FIG.15. Scheme of the Mössbauer experiment on polycrystalline $YBa_2Cu_3O_{7-\delta}$.

TABLE III. SUMMARY OF RESULTS OBSERVED DURING MÖSSBAUER EXPERIMENT

I-current through the device
U-voltage drop
T-measurement period

T (sec)	Measurement sequence	U (V)	I (mA)	$\alpha \times 10^3$	$\beta \times 10^3$
1	0, c-s, s-c	0.26	20	5.5 ± 3.4	0.9 ± 3.4
1	0, s-c, c-s	0.26	20	6.0 ± 2.2	3.6 ± 2.2
5	0, s-c, c-s	0.24	20	3.9 ± 2.1	- 1.2 ± 1.6
Sum for all measurements			20	5.0 ± 1.6	1.2 ± 1.6
1	0, s-c, c-s	5.5	100	10.0 ± 4.0	- 14 ± 4.0
1	0, c-s, s-c	5.7	100	74.0 ± 4.0	6.0 ± 4.0
5	0, s-c, c-s	5.7	100	34.0 ± 1.7	- 75.0 ±1.7

As far as we know such experiments did not fulfil anywhere, therefore the zero-velocity test has still to be repeated. As it was indicated in [30], an experiment is needed to eliminate other possible origins of the observed effect: (i) the effect should disappear when rising the temperature of the HTSC-sample above T_c, (ii) the effect should disappear when replacing the HTSC-sample by another non-superconducting material.

APPENDIX 2: EXPERIMENTS ON ALIGNED ENSEMBLES OF $YBa_2Cu_3O_{7-\delta}$ FINE PARTICLES

Aligned ensembles of $YBa_2Cu_3O_{7-\delta}$ were obtained with the aim of creating so-called quasi-monocrystals, because it is obvious that the best physical results may be received on monocrystals, obtaining of which in massive state is a great problem still.

The crystallographical orientation of particles with the "c" axes along the direction of magnetic field in H = 1 Tesla have been performed at 77 K. The ordering have been carried out in liquid paraffin matrix with the volume concentration of particles 0.01.The extent of the orientation have been defined by measuring of the roentgen line (006), which have been getting the most strong during the orientation, and this extent have reached the maximum values of 0.5 ÷ 0.8. The value of 1 have not been reached because of sticking of particles. This sticking could not be avoided even by ultrasound dispersion. It should be especially emphasized the interaction among the particles $GdBa_2Cu_3O_{7-d}$ is still stronger due to their paramagnetism and to orientate them is more difficult. So, the obtaining of particles of $YBa_2Cu_3O_{7-d}$ with different sizes gave us the opportunity to study their dimensional properties. The initial ceramics $YBa_2Cu_3O_{7-d}$ was prepared under the usual techology. The scanning microscope photographies showed the obtained $YBa_2Cu_3O_{7-d}$ ceramics had the granular structure with the size of grains 20 - 30 mm. Homogeneity, absence of nonsuperconductive phases and the value d= 0,18 for the samples were determined by X-ray powder diffraction method.

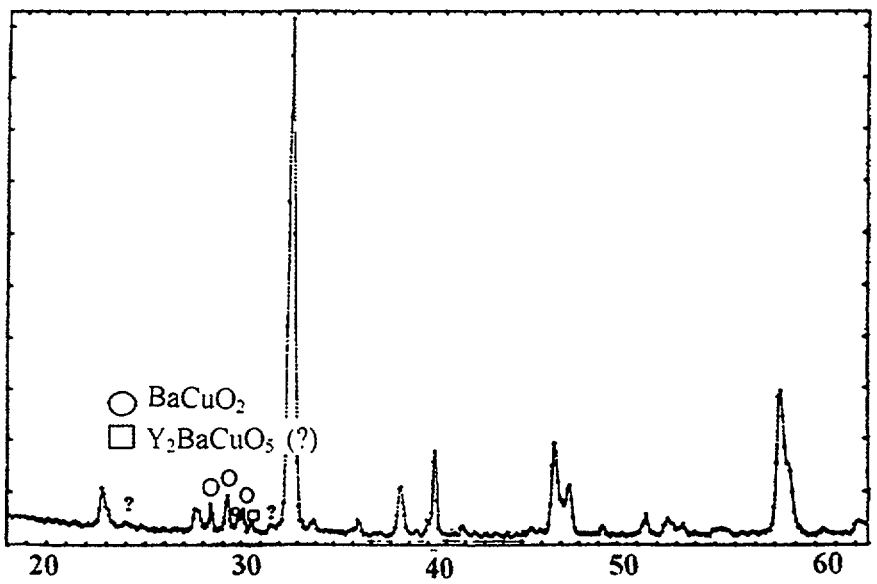

FIG.16. Experimental X-ray diffraction pattern for 0,1 μm $YBa_2Cu_3O_{7-\delta}$ fine particles.

TABLE IV. DATA FOR SUPERCONDUCTING $YBa_2Cu_3O_{7-\delta}$ FINE PARTICLES (H_{c1}- CRITICAL MAGNETIC FIELD MEASURED AT 77 K, ρ- THE DENSITY OF SAMPLES).

d, μm	T_c, K	ΔT_c, K	H_{c1}, Oe,	Δχ, %,	ρ,g/cm^3
bulk	93	5.5	150	50	5.7
1.5	91	12	145	30	4.63
0.5	90	17	133	17	4.5
0.1	90	33	95	9.5	3.8

$YBa_2Cu_3O_{6.82}$ ceramic particles with various size in the range of 0.1 - 1.5 mm were obtained by (1) mechanical dispersion (for 0.1 - 1.5 mm) and by (2) electrodispersion (for 0.1 mm). Variations of dispersion medium in the latter technique had no influence on the mean particle size. The particles had the spherical form with the mean size ~ 0,1mm, but some fraction of them had the size less than 100 nm. The attempts to separate the fractions of particles on the obtained powder were done by sedimentation on the different liquids. In the non-polar liquids the fine fraction formed the agglomerates; in the polar liquids the particles chemically interacted with the liquid and as the result the superconductivity of the powder disappeared. The X-ray investigations showed the lattice parameters and the oxygen content of samples did not change after the dispersion. The slight rest of $BaCO_3$ was observed on the roentgenogram in the case of electrodispersion (Figure 16.)

The superconductive transition temperature T_C value was independent on the particle size within the given size range. Transition width DT_C increased and Meissner effect Dc value decreased significantly with the particle size decreasing. The summary of experimental data is presented in the Table IV.

All these superconductive values were obtained from magnetic measurements. The values of T_c and ΔT_c were obtained by magnetic susceptibility measurements by method described in [5]. The H_{c1} was defined as follows: the function $-4\pi M$ (H) measured by vibrational magnetometer [31] becomes nonlinear and approaches its maximum value for $H \sim H_{c1}$. It is significant, that the T_c value was independent on the particle size within the given size range (with $d > 100$ nm). The similar result was observed for non-contacting particles of low-temperature superconductors (with $d > 10$ nm) [32] and for high-temperature superconductors powders (HTSC) (with $d > 20$ nm) [33]. It may be assumed that the mean length of Cooper pair ζ (ζ ~ 10^3 nm for low-temperature superconductors and ζ ~ 5 nm for HTSC) is not significant there. Transition width ΔT_C increased abruptly with the particle size decreasing. The rise of ΔT_C value is connected with the decrease of homogeneity and structural and surface defectness of the particles. It is notable, that the temperatures of superconductive transition starting are equal for all investigated particles ensembles and are independent of the particles size, but the temperatures of transition end are various for different samples.

Meissner effect value Δχ decreased significantly with particle size decreasing. The decreasing of superconductive phase volume in the samples is supposed to have slight influence on the Δχ decreasing. The dominant reason being the breakup of current paths in the net of weak links of HTSC producing the obstacles for external field screening. The observed decreasing of H_{c1} value confirmed this supposition. The another reason of the Δχ decreasing might be the fact that the magnetic field penetration depth (~ 0.1 μm) is of order of the investigated samples particles size.

APPENDIX 3: ROLE OF SURFACE EFFECTS ON EXAMPLE OF Co FINE PARTICLES

The main reason why we have studied this effect in connection with superconductivity is the following. The particulate matter (especially in the case of complex substance, as HTSC 123) is not homogeneous along the particle's radius, firstly, and particle itself is defective along its diameter, secondly. This defectness arises during its formation, i.e., condensation of vapours of basic substances in the flow of inert gases or mechanical fine grinding from the bulk state. As turned out [34], the irradiation by low fluences of neutrons forces the defects of the content and the structural defects come right partially and partially go out to the surface of particle due to the field of elastic longitudinal stresses [35]. Therefore the layer near the surface of particle enriches by defects what follows to changes of properties connected with the surface.

We have irradiated our ensembles of oxidized particles CoO by reactor's neutrons and have seen the disappearance of the effect of exchange anisotropy, but to see increase of Tc for HTSC 123 after the irradiation, as in [34] for superconductors A15, did not prove. Nevertheless, we consider that it is reasonable to inform shortly about the results obtained on non-irradiated ensembles of cobalt particles.

Cobalt fine particles is a very interesting well-known object for investigation of magnetic properties in dependence on the size of particles. In the case of not fully oxidized state this investigation gives the opportunity to study properties both connected with boundary between ferromagnetic core and oxidized cover, and with the size of core.

We have investigated the phenomenon of exchange anisotropy in small cobalt particles in the range of size 14 - 110 nm. As it is known [36-38], after cooling in a magnetic field the ensemble of partially oxidized cobalt particles shows a shift of magnetic hysteresis loop. This shift is a result of appearing the so-called unidirectional anisotropy. As it is considered, the origin of such an anisotropy is conditioned by interaction between Co ions placed near the surface of the particle and Co ions placed in the cover of cobalt oxide with antiferromagnetic arrangement. Besides this well-known result, we have observed the widening of hysteresis loop during cooling in a magnetic field in comparison with one measured on the ensemble of cobalt particles cooled in the absence of the magnetic field.

We have defined experimentally from the shift of hysteresis loop the constants of exchange surface anisotropy K_{exch} for different size cobalt particles. It was assumed that the direction of the easy axis of the exchange anisotropy coincides with one of an external magnetic field H at which the inducing of the anisotropy was done. As far as the exchange anisotropy is the surface phenomenon it is sensible to introduce the values of K_{exch} per unit of the surface of particle's cobalt core.

Fine particles of cobalt were made by the method of vapours condensation in the flow of inert gas (argon, helium). The single domain particles are only those with the size 14 nm and 23nm [39]. Nevertheless, the multidomain state of the particle should not influence the values of loop shift. The structure analysis of the particles shows the strong lines of cobalt cubic modification (in comparison with bulk cobalt which has hexagonal structure) and Co_3O_4. The lines corresponding to CoO were shown only on the level of sensitivity, thus it is affirmed the thickness of CoO layer is much smaller than the thickness of Co_3O_4 layer. As it was early considered all antiferromagnetic cover of particle consists of CoO [36]. As far as the temperature of antiferromagnetic transition of Co_3O_4 is about 40K, evidently, the thin layer of CoO is situated between the cobalt core and Co_3O_4 layer. That means the antiferromagnetic arrangement exists even in very thin CoO layer. The radius of the cobalt core was defined

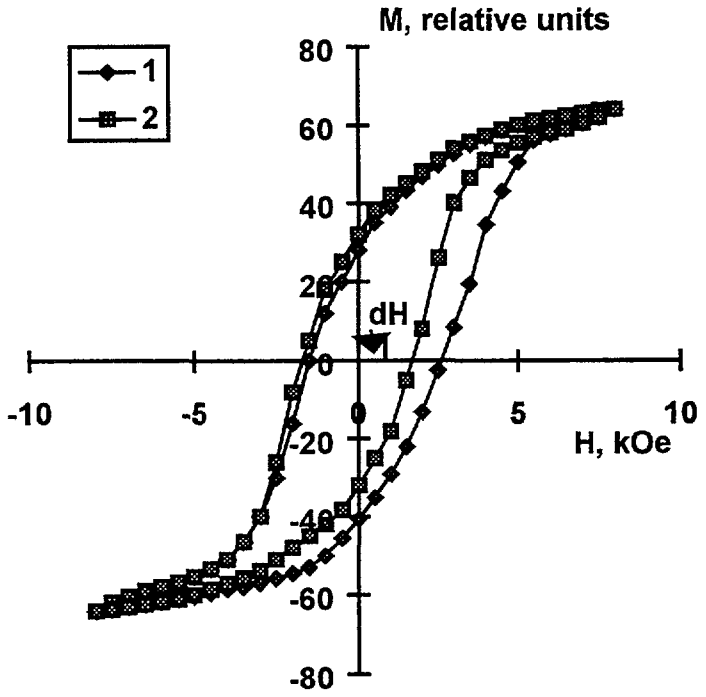

FIG. 17. Experimental hysteresis loops for oxidized Co particles with the size 23 nm (R = 8 nm) at 77 K, cooled with (1) and without (2) presence of the magnetic field.

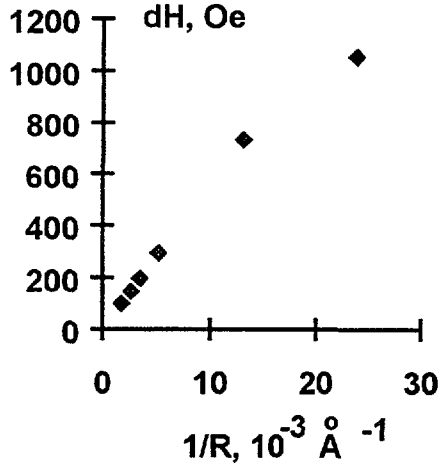

FIG. 18. Experimental data of hysteresis loop shift vs. cobalt ferromagnetic core radius (1/R) of particles.

from the measurements of saturation magnetization M_s in the assumption that the values of M_s do not depend on the size for the given range.

The induction of the exchange anisotropy was held during cooling of the samples from 300K to 77K in the magnetic field about 10 kOe. The hysteresis loops of uncooled in the magnetic field samples were also measured. The measurements were performed using vibrating magnetometer (Fig.17.). The exchange anisotropy results in the shift of the loop dH on the value $dH = 3K_{exch}/M_sR$ (R - the ferromagnetic core radius). It follows from the expression for the particle energy E in the magnetic field. The experimental data [40]

for the particles of all sizes, except the smallest one are well fitting on the line with the value of the slope K_{exch}= 0,29 ± 0,02 erg/cm2 (Fig.18). The smallest particles with R = 4 nm give the value K_{exch}= 0,21 ±0,02 erg/cm^2, that might be connected with the size effect for this value defined, e.g., by the decreasing the thickness of CoO layer or decreasing the value of M_s in dependence on the cobalt core diameter of the particle. It should note, it is impossible to extract the value of K_{exch} from the direct measurements on oriented cobalt particles using an anisometer because of torque measured is proportional to the sum of all kinds of anisotropy.

In order to explain the difference of values of coercivity after cooling in the magnetic field and without its presence we have calculated the hysteresis loops for the case when the axes of exchange anisotropy of the particles are distributed disorderly (it corresponds to cooling without presence of the magnetic field). It gives a narrowing of the loop that qualitatively accounts for the experimental picture; nevertheless, for obtaining the quantitative agreement with experimental results it is necessary to take into account both magnetic crystallographic anisotropy and effective uniaxial anisotropy arising from the magnetostatic interaction between the particles.

References

[1]BEELER, J.R., Radiation Effects, Computer Experiments, North-Holland, Amsterdam (1983), 881 pp.

[2]SIGMUND, P., Rev.Roum. Phys., **17** (1972), p. 823, 969, 1079.

[3]KIRSANOV, V.V., SUVOROV, A.L., TRUSHIN, Yu.V., Processes of Radiation Defects Production in Metals, Energoatomizdat, Moscow (1985), 272 pp (in Russian).

[4]BREZGUNOV, M.M., PETROV, A.E., Ukrainskij Fizicheskij Zhurnal (translated in English), **33** (1988), p.616.

[5]BREZGUNOV, M.M., BELOGUROV, S.V., PETROV, A.E., KUDRENITSKIS, I.V., MAKLETSOV, A.A., KURKIN, V.V., NERSESJAN, A.E., Superconductivity: Phys.,Chem., Technol., **3** (1990). p.894.

[6] MAKLETSOV, A.A., Superconductivity:Phys.,Chem., Technol., **3** (1990), p. 900.

[7]VAISFIELD, A.M., GANN, V.V., PAVLENKO, V.I., SHILYAEV, B.A., YUDIN, O.V., YAMNITSKII, A.M., Vopr. Atomn.Nauki i Techn. Ser.: Fiz. Radiat. Povr. i Radiats. Materialoved., **4** (1984), p.3 (in Russian).

[8]SICKAFUS, K.E., WILLIS, J.O., KUNG, P.J., WILSON, W.B., PARKIN, D.M., MALEY, M.P., CLINARD, Jr., F.W., SALGADO, C.J., DYE, R.P., HUBBARD, K.M., Phys.Rev. B, **46** (1992), p. 11862.

[9]BRANDSTÄTER, G., FRISCHHERZ, M.C., WEBER, H.W., PETROV, A., In: IAEA Report of the 2nd Research Co-ord. Meeting of the Co-ordinated Research Programme on "Nuclear Techniques for Advanced Ceramics and Semiconductors", Leuven, Belgium, October 1995, Annex 3.

[10]BELOGUROV, S.V., BREZGUNOV, M.M., PETROV, A.E., POLIKARPOV, I.V., YAKUBOVSKII, A.Yu., Superconductivity:Phys.,Chem., Technol., **5** (1992), p. 2242.

[11]FARNETH,W.E.,BORDIA,R.K.,McCARRON III, et al.,Solid State Comm.,**66**(1988), p.953-959.

[12]STOLYAROVA,S.V.,SIMANOVSKIS,A.A.,PETROV,A.E., Ferroelectrics, **133** (1992), p.363-7.

[13]DAGOTTO, E., Reviews of Modern Physics, **66** (1994), p. 763-840.

[14]GINSBERG, D.M. (ed), Physical Properties of High Temperature Superconductors I., World Scientific, Singapore - New Jersey - London - Hong Kong, 1989.

[15]TARASCON, J.M., McKINNON, W.R., GREEN, L.H., HULL, G.W., VOGEL, E.M. Preprint, Bell Communications Research, 331 Newman Spring Road, New Jersey 07701-7020.

[16]ALP, E.E., SODERHOLM, L., SHENOY, G.K., HINKS, D.G., CAPONE II, D.W., ZHANG, K., DUNLOP, B.D.,, Phys.Rev. **B36** (1987), p. 8910

[17]SMIT,H.H.A.,DIRKEN,M.W.,THIEL,R.C.,JONGH,L.J.de, Solid St.Commun., **64**(1985), p. 695.

[18]PAUL, D. Mck., MOOK, A., HEWAT, A.W., SALES, B.C., BOATNER, L.A., THOMPSON, J.R., MOSTOLLER, M., Phys. Rev., **B37** (1988), p. 2341.
[19]CHATTOPADHYAY, T., MALETTA, H., WIRGES, W., FISCHER, K., BROWN, P.J., Phys. Rev., **B38** (1988), p. 838
[20]MOOK, H.A., PAUL, D. McK., SALES, et. al., Phys. Rev., **B38** (1988), p. 12008.
[21]FELSTEINER, J., Phys. Rev., **B39** (1989), p.7248
[22]KURKIN, E., private communication (1995).
[23]BUD'KO, S.L., NAKAMURA, O., GUIMPEL, J., MAPLE, M.B., SCHULLER, I.K., Physica, **C185** (1991), p. 1947-1948.
[24]WANG, X.Z., BAUERLE, D., Physica, **C176** (1991), p. 507 - 510.
[25]BARAN, M., DJAKONOV, Y.P., MARKOVICH, V.I., SHIMCHAK, G., Solid State Phys. **36**, (1994) p. 3461 - 3467 (in Russian).
[26]MAKLETSOV, A.A., PETROV, A.E., GANN, V.V., Nucl.Instr. and Methods in Phys. Research, **B94** (1994), p. 203 - 206.
[27]GROSHEV,L.V.,DEMIDOV,A.M.,PELEKHOV,V.J.,SOKOLOVSKII, L.L, BARTHOLOMEW, G.A., DOVEIKA, A., EASTWOOD, K.M., MONARO, S., Nucl. Data Tables, **5** (1968), p. 159.
[28] BELOGUROV, V.N., BORZYAK, A.N., KARKLIN, N.N., Letters to JETP, **48** (1988), p.25-26.
[29]GOFRON, K., CAMPUZANO, J.C., ABRIKOSOV, A.A., LINDROOS, M., BANSIL, A., DING, H., KOELLING, D., DABROWSKI, B., Observation of an "Extended" Van Hove Singularity in $YBa_2Cu_3O_8$ by Ultrahigh Energy Resolution Angle-Resolved Photoemission, Physical Review Letters, **73** (1994), p. 3302 - 3305.
[30]IAEA, Session summaries and Scientific Recommendations of the Report of the 2nd Research Co-ordination Meeting of the Co-ordinated Research Programme on "Nuclear Techniques for Advanced Ceramics and Semiconductors", Leuven, Belgium, October 1995, p. 9.
[31]FERGUSON, G., et al., J.Phys.D: Appl. Phys, **21** (1988), p.1306.
[32]NAUMENKO, I., PETINOV, V., Pis'ma JETP, **15** (1972), p.464.
[33]NAUMENKO, I., et al., In: Physics and Chemistry of Ultradispersed Systems.Abstracts, Riga (1989), p.87 (in Russian).
[34]PLECHKENS, E.S., RADZUS, V.D., PETROV, A.E., Izvestija Akademii Nauk Latviskoj SSR, ser. fiz. (1983), No 4, p.41-45 (in Russian).
[35]PETROV, A.E., Izvestija Akademii Nauk USSR , ser. fiz., (1986), **50**, p.1646-1649.
[36]MEIKLEJOHN, W.H., BEAN, C.P., Phys.Rev. (1956), **102**, p. 1413 -1417.
[37]GANGOPADHAYAY,S.,HADJIPANAYIS G.,C.,et.al., Nano Structured Mat.(1992),**1**,p.449-456
[38]GANGOPADHAYAY, S., YIPING, L., et.al., Physics and Chemistry of Finite Systems: From Clusters to Crystals (1992), **1**, p. 743 - 752.
[39]PETROV, A.E., PETINOV, V.I., GEN, M..J., Fizika Tverdogo Tela (1971, translated in English), **13**, p.1573-1577.
[40]PETROV, A., BELOGUROV, S., KUDRENITSKIS, I. In: 14th Int.Colloqium on Magnetic Films and Surfaces, Düsselldorf (29.08-02.09. 1994), p. 448-449.

Glossary

amorphous (adj.)	describes a solid which has no crystalline structure
bulk (adj.)	see *massive*
ceramics (n.)	the substance in which many small regions (grains not obligatory completely crystallic) all joined together; the grains meet at very defective grain boundaries
Curies's law (n.)	the magnetic susceptibility of a paramagnetic substance is inversely proportional to the thermodynamic temperature
fine powder (n.)	a solid substance in which the particles are very small compared to characteristic lengths of concrete physical phenomena; usually the size of particles in fine powder is less than 0,1 mm.
hysteresis (n.)	an effect, observed in the magnetic behaviour of ferromaterials
hysteresis loop (n.)	the enclosed shape of a hysteresis curve
magnetometer (n.)	an instrument for comparing magnetic moments of samples in dependence on temperature and the value of magnetic field.
massive (adj.)	describes the state of being in large pieces

STRUCTURAL CHARACTERIZATION OF ADVANCED CERAMICS USING THE NEUTRON DIFFRACTOMETER DEVELOPED BY INSTITUTO DE PESQUISAS ENERGETICAS E NUCLEARES (IPEN)

C.B.R. PARENTE, V.L. MAZZOCCHI
Instituto de Pesquisas Energéticas e Nucleares,
Comissão Nacional de Energia Nuclear,
São Paulo, Brazil

XA9949655

Abstract

Application of neutron diffractometer at the Instituto de Pesquisas Enérgeticas Nucleares, São Paulo, Brazil, in the structural investigations of advanced ceramics was presented. Methodology of the analysis of neutron diffraction patterns was tested with $BaLiF_3$ single crystals and also doped with Ni^{2+} or Pb^{2+} ions. The same methodology was used to investigate the HTSC phases in the system Bi-Sr-Ca-Cu-O. The system $Bi_{1.7}Pb_{0.3}Sr_2Ca_{2.2}Cu_{3.5}O_{10.6}$ was also investigated. Addition of Pb^{2+} ions increased the fraction of high-T_c phase 2223. Symmetry in neutron multiple diffraction patterns, obtained for aluminium single crystal, was elaborated. Crystal lattice parameter for aluminium single crystal was determined at different temperatures using neutron multiple diffraction.

1. Development of the methodology for analysis of the crystalline quallity of single crystals

S. Metairon, V. L. Mazzocchi, C. B. R. Parente, S. L. Baldochi

Recently, a study of the crystalline quallity of Czochralski grown $BaLiF_3$ single crystals has been published [1]. In the study, intensity curves (rocking curves)obtained by neutron diffraction are related to several parameters involved in the growth method. Although the methodology employed in the study led to useful results, charcaterization of domains obtained by its employement lacks completeness. The present study is an attept to develop a better methodology for the analysis of the crystalline quality of single crystals by using rocking curves measured by neutron diffraction. Neutrons are better than x-rays for this purpose since they can give information about the bulk of the crystal. X-ray, on the other hand, gives information about very small portion of crystal [1]. Tridimensional Intensity x ω x χ plots, obtained from a single crystal as several Intensity x ω rocking curves for χ stepping in a convenient interval, show, in general, more than a single mosaic domain. In principle, it is possible to determine number of domains, their relative intensities, mosaic spread of each one and angular dispersion between them. From a macroscopic point of view, determination of these characteristic corresponds to an evaluation of the crystalline quality of the single crystal under study. Figure 1 shows a tridimensional plot obtained from a $BaLiF_3$ single crystal and the corresponding contour map. A fit of Gaussians to a few of the individual Intensity x ω rocking curves showed at least 5 mosaic domains. For the reason, one can say that the crystal has a bad crystalline quality. It should be noted that domains for the scans in the χ direction appear much more wider than in the ω direction. This is due to the worst resolution of the Soller colimator in the χ direction. Use of a special collimator for neutron multiple difraction, which colimates in both vertical and horizontal directions, can partially eliminates this problem. Figure 2 is similar to Figure 1, except that it represents a $BaLiF_3$ single crystal with a much better crystalline quality. In fact, Gaussian fittings to a few individual Intensity x ω rocking curves showed no more than 2 mosaic domains, one being dominant over the other.

Figure 3 shows 3 rocking curves obtained from a BTO single crystal. Such curves were measured with reflections 200, 002 and 020. Scattering vector of reflection 200 was parallel to the growth direction [100]. Scattering vectors of reflections 002 and 020 were prependicular to growth direction. Gaussian fittings revealed the existence of several domains in the crystal.

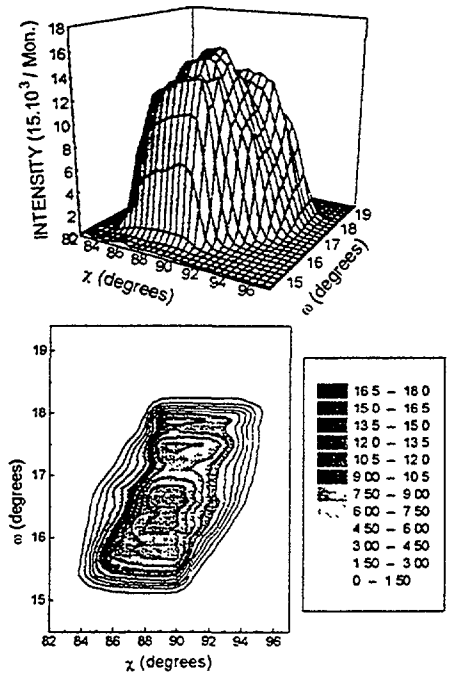

FIG. 1 Tridimensional plot (above) obtained with reflection 111 from a BaLiF3 single crystal and corresponding contour map (below). Crystalline quality is very poor.

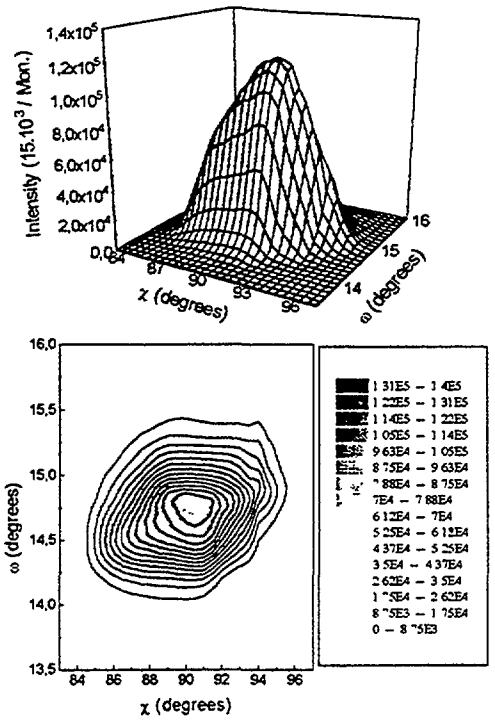

FIG. 2. Tridimensional plot (above) obtained with reflection 111 from a BaLiF3 single crystal and corresponing contour map (below). Crystalline quality is good.

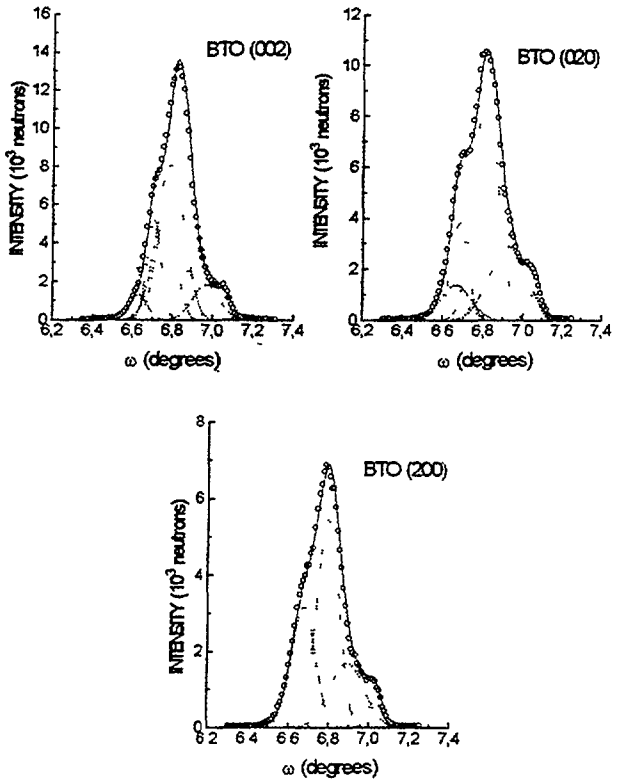

FIG 3. Rocking curves for the growth direction, BTO (200), and for two directions perpendicular to growth direction, BTO (002) and (020) of a BTO single crystal Gaussian fittings to curves reveal number, position and intensity of mosaic domains. Crystalline quality is poor

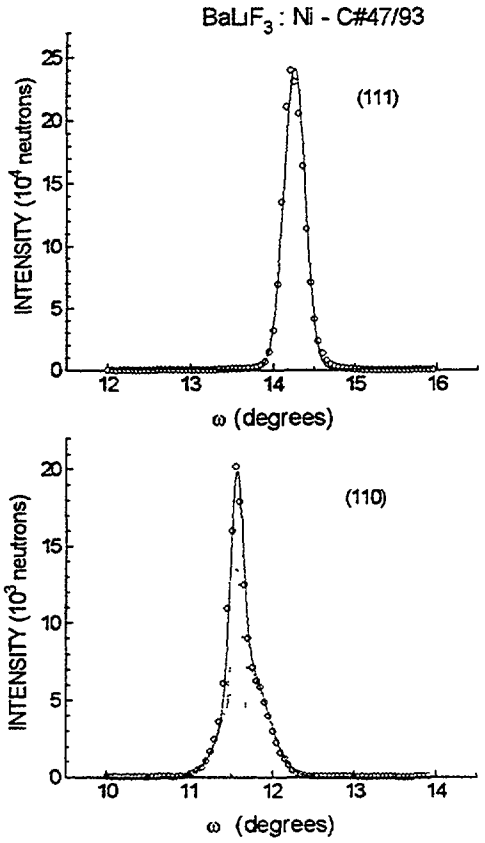

FIG 4. Rocking curves for the growth direction (111) and a direction (110) prependicular to growth direction of a Ni doped BaLiF3 single crystal. Crystalline quality is good.

TABLE I- PARAMETERS FOR THE MOSAIC DOMAINS IN THE BTO SINGLE CRYSTAL, FOUND IN THE GAUSSIAN FITTINGS OF ROCKING CURVES.

	BTO (002)			BTO (020)			BTO (200)		
domain	center pos. (degrees)	f.w.h.m. (degrees)	height (counts)	center pos. (degrees)	f.w.h.m. (degrees)	height (counts)	center pos. (degrees)	f.w.h.m. (degrees)	height (counts)
1	6.6239	0.0876	1314.8	6.6600	0.1503	1387.3	6.6696	0.1182	3169.4
2	6.7007	0.0687	5217.9	6.6772	0.0831	3849.9	6.7899	0.1081	5463.2
3	6.8088	0.0997	5754.9	6.8067	0.1206	8903.5	6.8878	0.1690	1697.3
4	6.8310	0.1345	8112.0	6.9189	0.1855	2899.1	7.0270	0.0725	693.28
5	7.0101	0.1318	1870.8	7.527	0.0624	1081.2			

TABLE II. PARAMETERS FOR THE MOSAIC DOMAINS IN THE NI DOPED $BaLiF_3$ SINGLE CRYSTAL, FOUND IN THE GAUSSIAN FITTINGS OF ROCKING CURVES.

	$BaLiF_3$: Ni(111)			$BaLiF_3$: Ni(110)		
domain	center pos. (degrees)	f.w.h.m. (degrees)	height (counts)	center pos. (degrees)	f.w.h.m. (degrees)	height (counts)
1	14.24	0.1292	240600	11.55	0.0758	13530
2				11.67	0.2488	7173

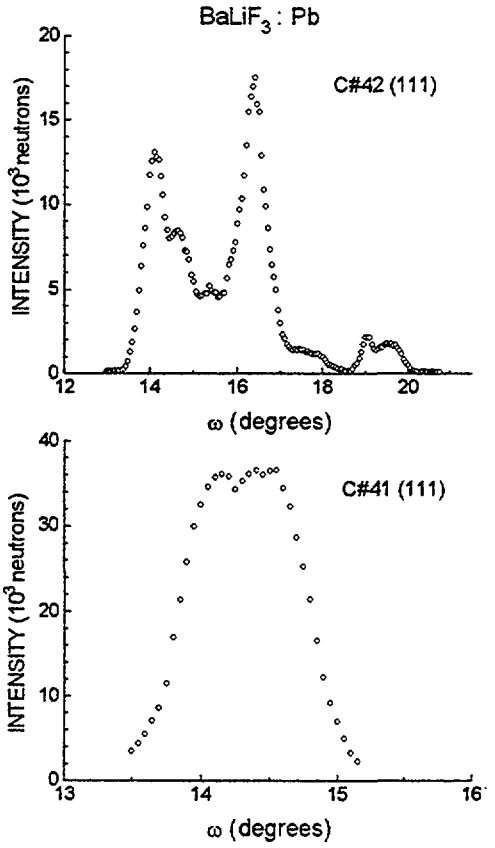

FIG. 5. Rocking curves for the growth direction of two Pb doped $BaLiF_3$ single crystals. Crystals C#41 and C#42 have concentrations 1% wt. and 2 % wt. Pb, respectively. Although both have a bad crystalline quality, C#41 is much better than C#42.

Although obtained from a same crystal, rocking curves BTO (002) and BTO (020) revealed 5 mosaic domains whereas rocking curves BTO (200) revealed only 4 domains. It should be understood that it is impossible to determine unequivocally number and angular positions of domains from bidimensional rocking curves. Table I lists the parameters of the mosaic domains found for the rocking curves of Figure 3.

Figure 4 shows rocking curves obtained with reflections 111 and 110 from a Ni doped $BaLiF_3$ single crystal. Scattering vector of reflection 111 was parallel to the growth direction.

Scattering vector of reflection 110 was prependicular to growth direction. For the growth direction only one domain is observed. The crystal has undoubtedly a quite good quality. As expected for the prependicular direction, the quality is not so good as for the growth direction [1]. A Gussian fitting in the case shows 2 domains with different spreads but very close one to other. Table II lists parameters found in the Gaussian fittings for both curves.

Figure 5 shows rocking curves for two Pb doped $BaLiF_3$ single crystals, both obtained in the growth direction. Crystals were doped with 5 % wt. and 2 % wt. of Pb and called C#41 and C#42, respectively. They were both grown by Czochralski method. Crystal C#42 has a very poor crystalline quality, probably due to extended defects produced by inclusion of Pb in the lattice. The same occurs with crystal C#41, although in a lesser degree owing to the smaller concentration of Pb in the lattice. It is expected that the crystalline quality be improved in next crystals in order to allow n.m.d. measurements. No Gaussian fittings were done for these samples.

2. Phases present in high - Tc ceramic superconductors of the Bi-Sr-Ca-Cu-O system.

R. Muccillo, E. N. S. Muccillo, V. L. Mazzocchi and C. B. R. Parente

In a previous report, Parente and Mazzocchi [2] observed that the singnal-to-backgroundatios, calculated for the peaks in neutron powder patterns of superconductors of the Bi-Sr-Ca-Cu-O system, have very low figures. Peaks are very broad with low intensity. This was ascribed to the small size of the crystallites in the samples. We have also observed that a heat treatment of samples, consisting of annealing at approximately 1000 K for several hours, produced no increase in the mean crystallite size. As a metter of fact, such annealing produced even a decrease in the mean size. Results also included a neutron powder pattern for a sample obtained by addition of lead during sintering of the superconductor. The signal-to-background ratios in this case have even lower figures, indicating that the mean crystalitte size is smaller than in the case of annealed pure superconductors.

In continuation of the research, we have used a different heat treatment which will be described later on. We decided to use samples prepared by addition of lead although, as mentioned above, they produce poor figures for the signal-to-bacground ratio. Addition of lead is reported to increase the fraction of the higher Tc phase 2223 increasing the uniformity in the composition of this phase as well [3]. Both are desirable characteristics of the Bi-Sr-Ca--Cu-O system. For this reason, we have opted for this kind of superconductors. It should be mentioned that addition of Pb provokes a partial substitution of Pb for Bi in the lattice. A general formula, for the superconductor containing Pb can be written as $Bi_{2-x}Pb_xSr_2Ca_2Cu_3O_y$.

Samples of high-Tc ceramic superconductors are being currently prepared in the Materials Science Division at IPEN. A sample containing Pb to be used in this work was prepared by the solution technique [4]. The initial stoichiometry had an excess of 10 % at. of

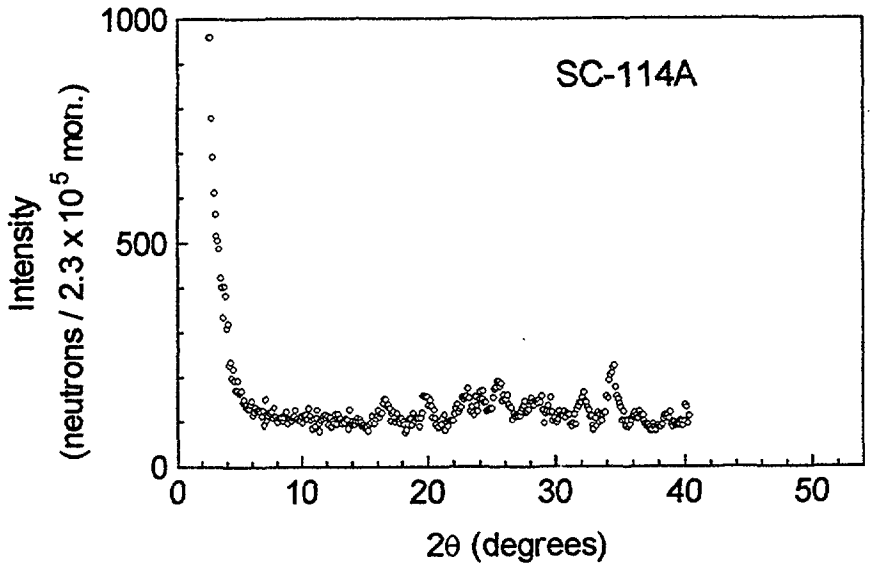

FIG. 6. Neutron powder pattern obtained with the high-Tc superconductor $Bi_{1.7}Pb_{0.3}Sr_2Ca_{2.2}Cu_{3.5}O_{10.6}$ after annealing at 1103 K for 30 h.

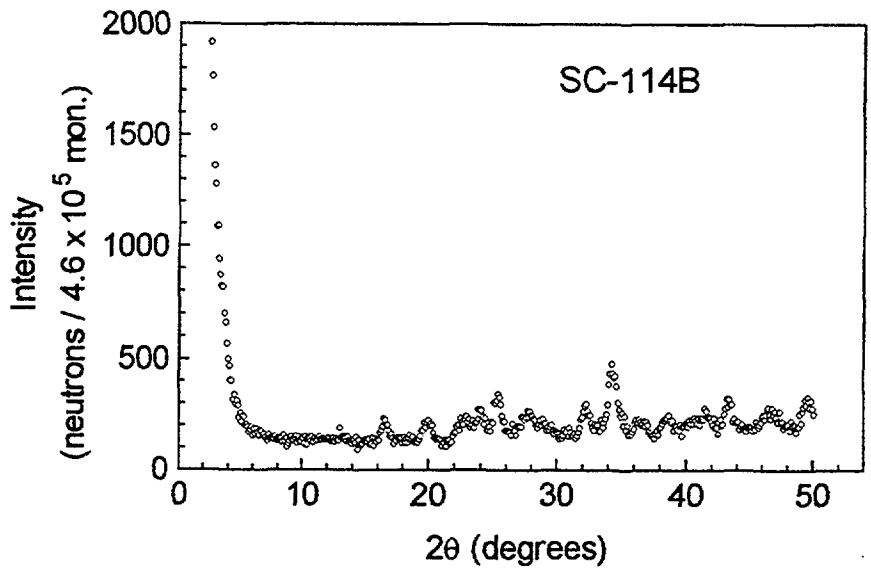

FIG. 7. Neutron powder pattern obtained with the same superconductor of Figure 6 above after a quick second annealing at ca. 1113 K for 30 minutes.

Ca and 16.7 % at. of Cu resulting in the high-Tc superconductor $Bi_{1.7}Pb_{0.3}Sr_2Ca_{2.2}Cu_{3.5}O_{10.6}$. The sample was annealed at circa 1103 K for 30 hours. With this sample, called SC-114A, we obtained the neutron powder pattern showed in Figure 6. After measurements, a new heat treatment was applied to the sample. It consisted of a quick annealing at 1113 K for 30 minutes. This temperature is about 5 K below the eutetic point of the compound. Fig. 7 shows the neutron powder pattern obtained with such sample, called SC-114B. It should be noted that the preset counting for the monitor in SC-114B pattern is twice that in Sc-114A pattern. To allow an easy observation of differences between two patterns, intensity scale in SC-114A has an extension twice that in SC-114B. A simple

qualitative analysis of results shows that peaks for sample SC-114B are slightly greater than peaks for sample SC-114A. Another observation is that the background level in SC-114A is almost twice that in SC-114B. Both are evidences that crystallites in sample SC-114B have slightly greater sizes than in sample SC-114A.

3. Symmetry in multiple diffraction patterns

Contributors: C. B. R. Parente, V. L. Mazzocchi, S. Metairon, J. M. Sasaki, L. P. Cardoso

In 1972, Parente studied the multiple diffraction of neutrons in an aluminium single crystal [5]. He measured a neutron multiple diffraction (m.d.) pattern with the 111 primary reflection from the crystal. The experimental neutron m.d. pattern had an extension sufficient to show two of the symmetry mirrors normally existing in a m.d. pattern. Figure 8 shows the pattern with indexing for the secondary reflections. It can be observed in Figure 8 that, for one of the mirrors (at $\phi = 60^{o}$ in the lower scale), in the unique pair of symmetrical peaks appearing in the pattern, peaks have different intensities. For the other mirror (at $\phi = 30^{o}$) 3 pairs exhibit a perfect symmetry, i. e. peaks are in symmetrical positions around the mirror and have same intensity. The author explained the differences in intensity by showing that a few of the secondary reflections, as well as the coupling reflections, involved in the formation of the peaks had different reflectivities. Different reflectivities imply different intensities. Recently, Sasaki [6] observed the same phenomenon in a X-ray m.d. pattern obtained with Cu$K\alpha_1$ radiation and primary reflection 222 from a galium arsenide (GaAs) single crystal. The crystal was epitaxially grown on top of an indium-galium arsenide (InGaAs) substrate. The pattern obtained with the crystal is shown in Figure 9. Two symmetrical peaks having different intensities are indexed in this Figure.

This work is a systematic search for the phenomenon observed by authors above in X-ray and neutron m.d. patterns. Present authors intend to make a further investigation of the phenomenon by measuring a simulating m.d. patterns for different primary reflections from several different crystals. Simulated patterns are calculated by the computer programs MULTI [7] and MULTX [8], for neutrons and x-rays, respectively. Till now, several simulated m.d. patterns have been calculated, for a full extension of the azimuthal angle ϕ ranging from 0 to 360°. Data were plotted in circular plots, where the intensity axis is radial and the ϕ axis is circular. A circular plot allows a better visualization of the pattern symmetry. Using such a type of plot simulated patterns, we have identified two types of symmetry mirrors. One of them is a normal mirror we called "isomorphic mirror". It produces only pairs of fully symmetrical peaks like those in Figure 8, around $\phi = 30^{o}$ in the lower scale. Other is an abnormal mirror we called "anamorphic mirror". It produces pairs of symmetrical peaks having different intensities like those in Figure 8, around $\phi = 60^{o}$. It should be mentioned that such a type of mirror also produces pairs of fully symmetrical peaks. Another point to be noted is that, depending on some sample characteristics, partially symmetrical peaks can appear with so minute differences that they can be misinterpreted as being fully symmetrical peaks. Figure 10 shows a pair of peaks, simulated by MULTI, corresponding to the experimental pair at $\phi = 60^{o}$ in the lower scale of Figure 8. For the simulations, a cylindrical Al single crystal was considered. By varying radius (r), height (h) of the cylinder and mosaic spread (η) of the crystal, peaks change their shapes and intensities in an astonishing way. It can be easily verified that η plays a much more important role in the shape modification than r or h does. Figure 11 is the equivalent for Figure 10, except that the

simulated pair corresponds to the experimental pair at $\phi = 30^{o}$ in Figure 8 In this case, although a great variation in shape and intensity occurs, peaks are rigorously equal for a same pair

Concerning the existance of isomorphic and anamorphic mirrors, we have simulated several different m d patterns Examples of simulated patterns are shown in Figures 12, 13 and 14 corresponding to the primary reflections 111, 220 and 042 from a cylindrical Al single crystal In cubic symmetry, direction [111] has a 3-fold symmetry, [220] a 2-fold symmetry and [042] As can be readily seen in Figures 12, 13 and 14, each plot form a figure having the symmetry of the corresponding direction Furthermore, circular plots for n odd have both anamorphic and isomorphic mirrors Mirrors of one type intercalate into mirrors of other type, in a regular sequence Circular plots for n even have only isomorphic mirrors The number of isomorphic mirrors equals the order of the symmetry axis parallel to the scattering vector of primary reflection, i e $m_i = n$ For anamorphic mirrors $m_a = m_i = n$, if n is odd, and $m_i = 0$, if n = even Of course, number total of mirrors m_t is given by $m_t = m_i + m_a$ In equalities above m_i is the number of isomorphic mirrors, m_a is the number of anamorphic mirrors and n is the order of symmetry axis It should be noted that, the number of mirrors is twice that in a circular plot, a same mirror passing through a certain azimuthal position also passes through a position 180° from the first one In a normal plot, these two positions are considered as being individual mirrors

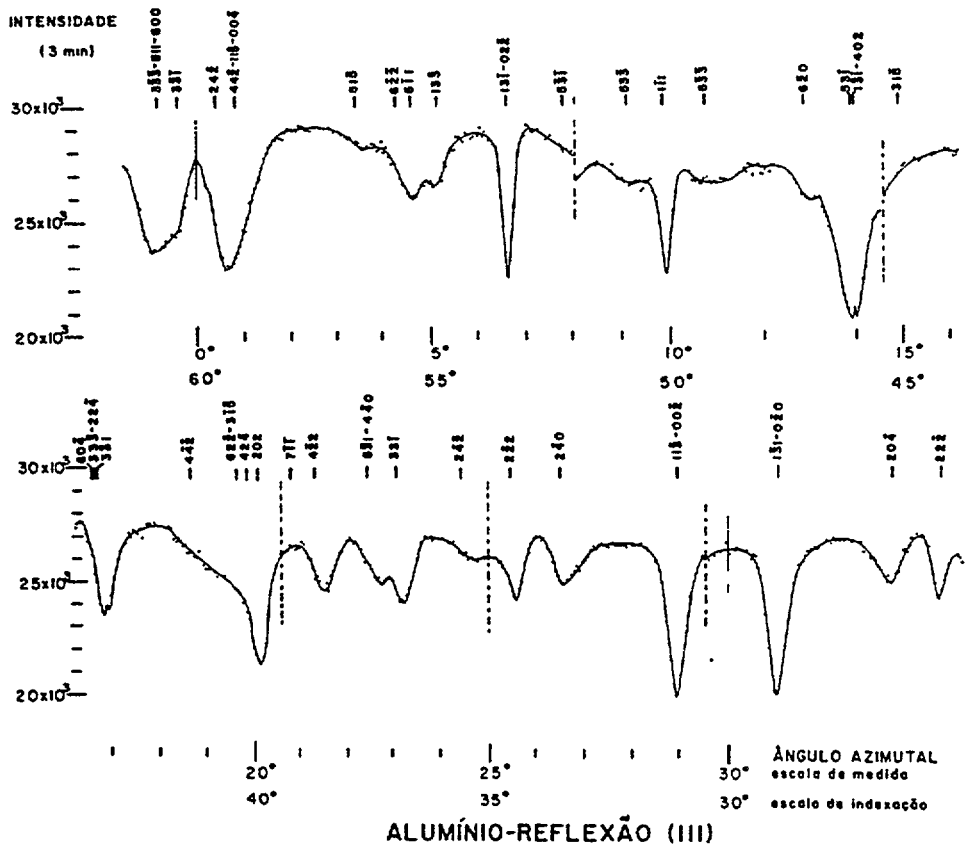

FIG 8 Neutron m.d pattern obtained with reflection 111 from an aluminium single crystal [5]. An anamorphic symmetry mirror is positioned at $\phi = 60^{o}$ in lower scale, an isomorphic at 30^{o}

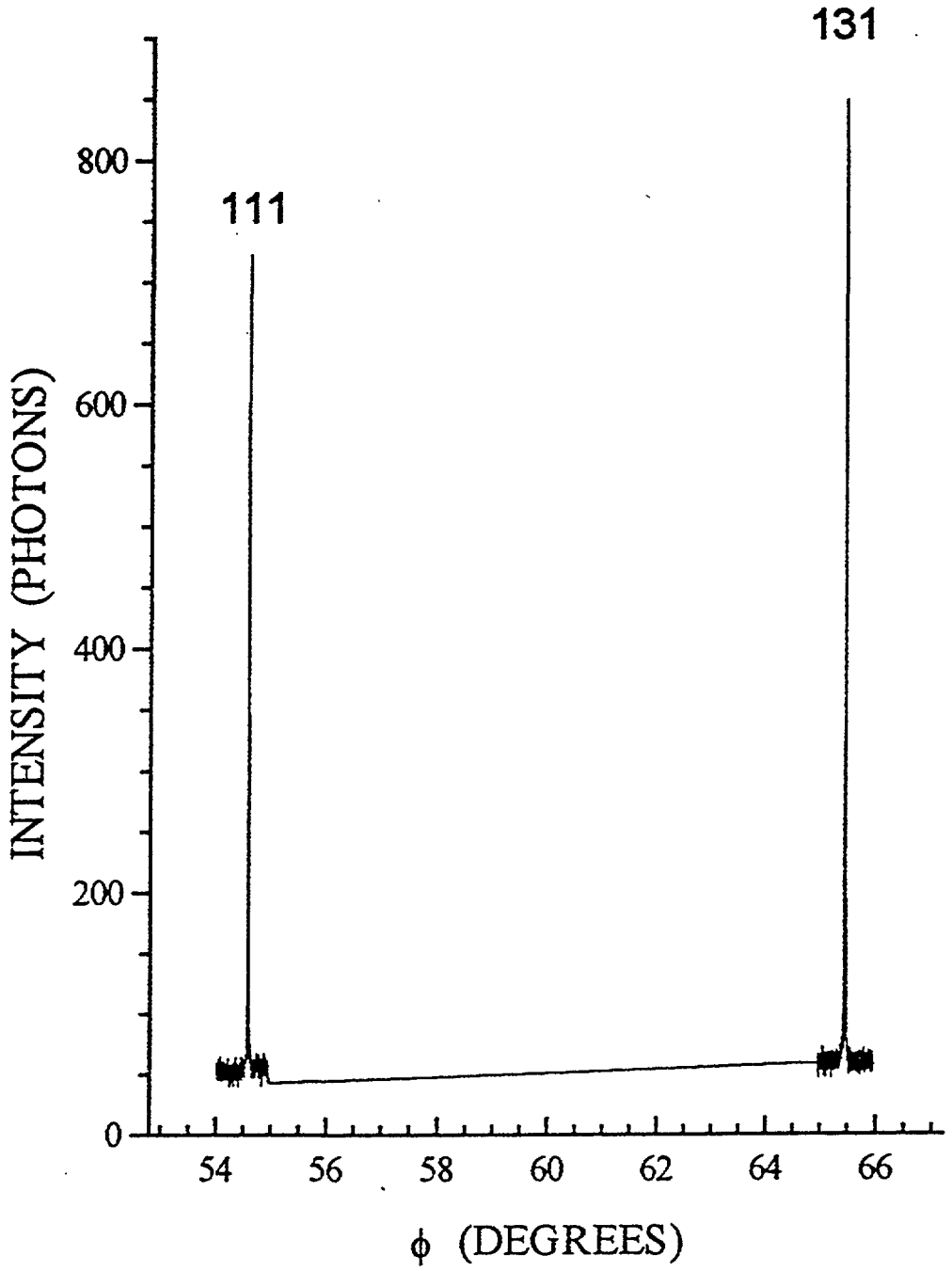

FIG. 9. X-ray m.d. pattern obtained with CuKα1 radiation and reflection 222 from a GaAs/InGaAs single crystal [6]. Symmetrical secondary reflections have different intensities.

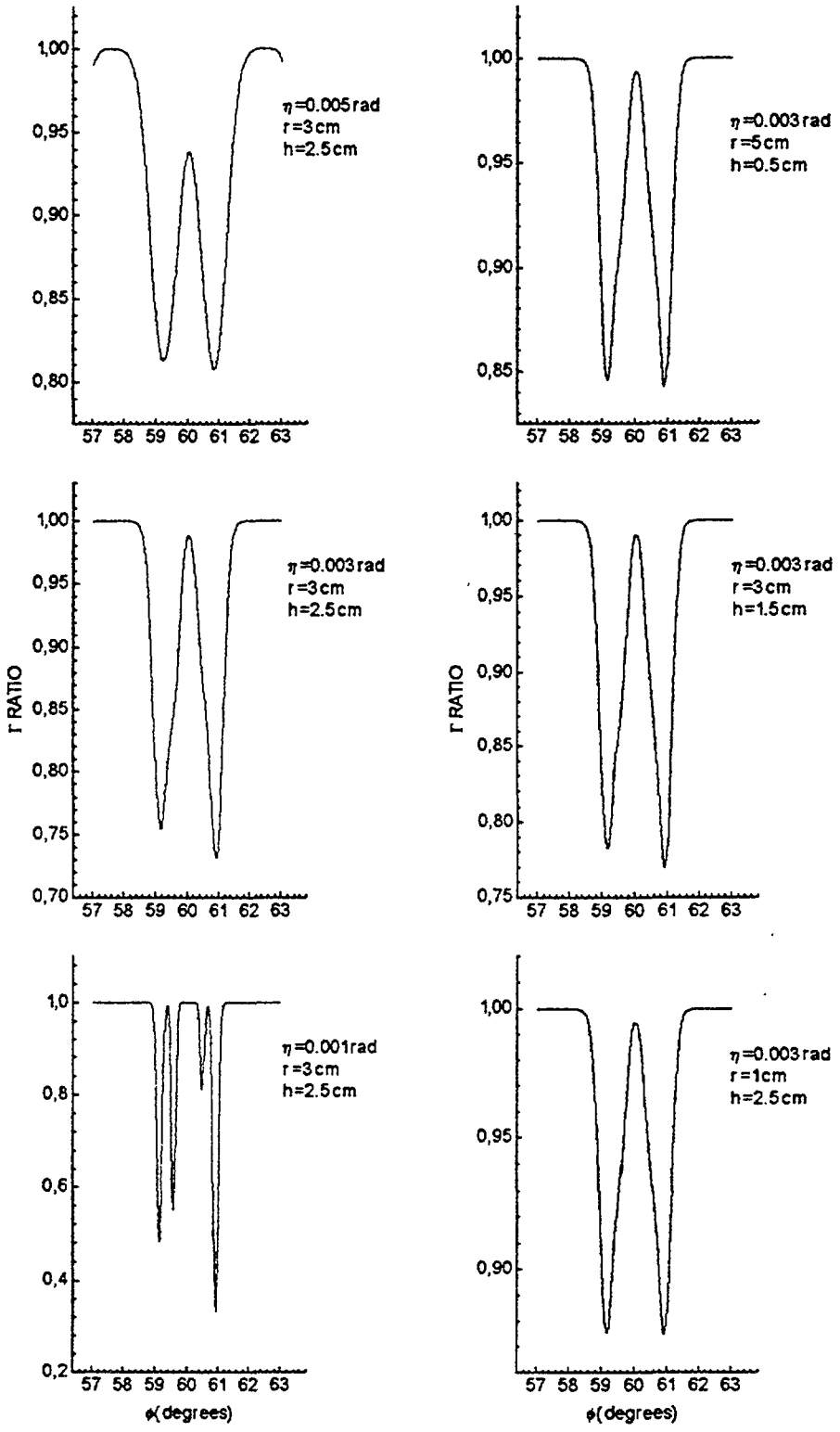

FIG. 10. Al (111) simulated peaks around an anamorphic mirror located at $\phi = 60^{o}$. Different values for the radius (r) and height (h) of a cylindrical single crystal as well as for the mosaic spread (η) were assumed in the calculations.

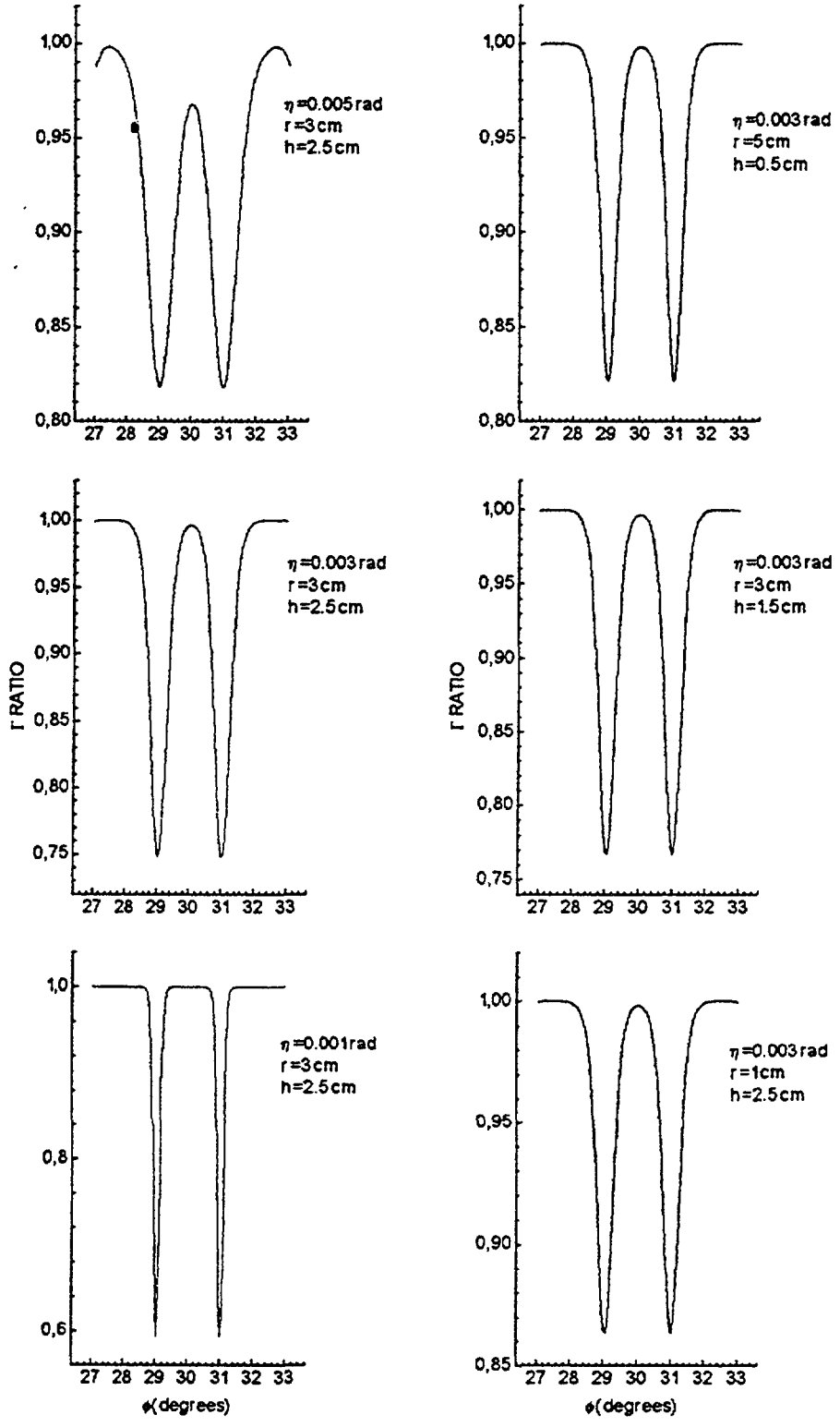

FIG. 11. Al (111) simulated peaks around an isomorphic mirror located at $\phi = 30^{o}$. Different values for the radius (r) and height (h) of a cylidrical single crystal as well as for the mosaic spread (η) were assumed in the calculations.

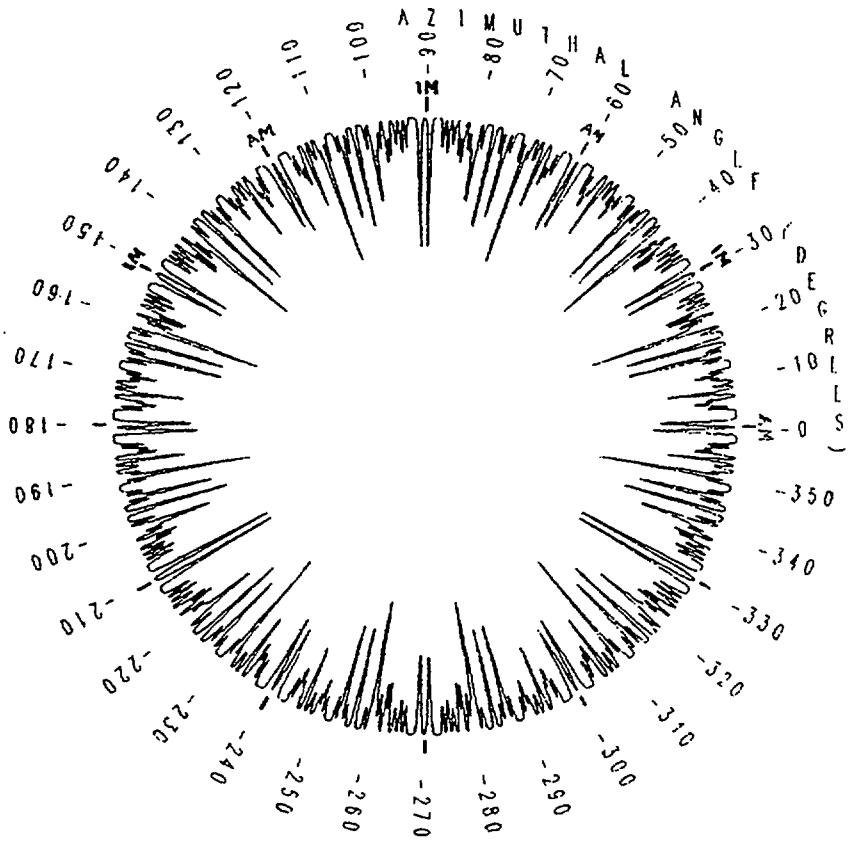

FIG. 12. Simulated Al (111) neutron m.d. pattern in a circular plot. The 3-fold symmetry of direction 111 is clearly visible in the plot. Three isomorphic mirrors (IM) intercalated into three anamorphic mirrors (AM) are shown in the plot.

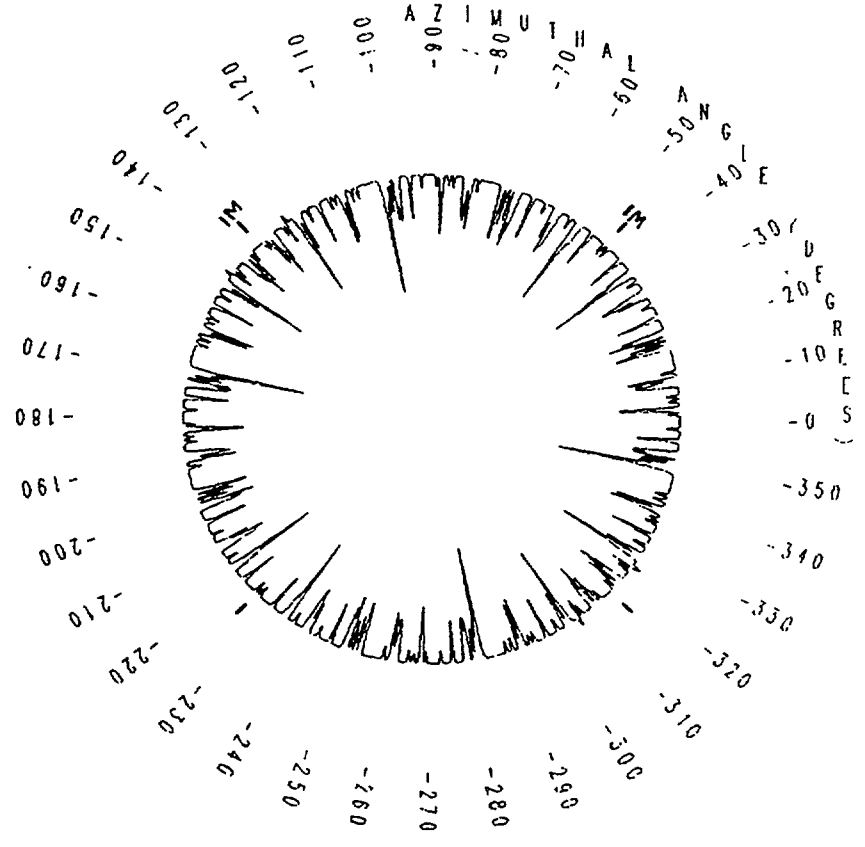

FIG. 13. Simulated Al (220) neutron m.d. pattern in a circular plot. Only two isomorphic mirrors (IM) are defined for the 2-fold symmetry of direction 110.

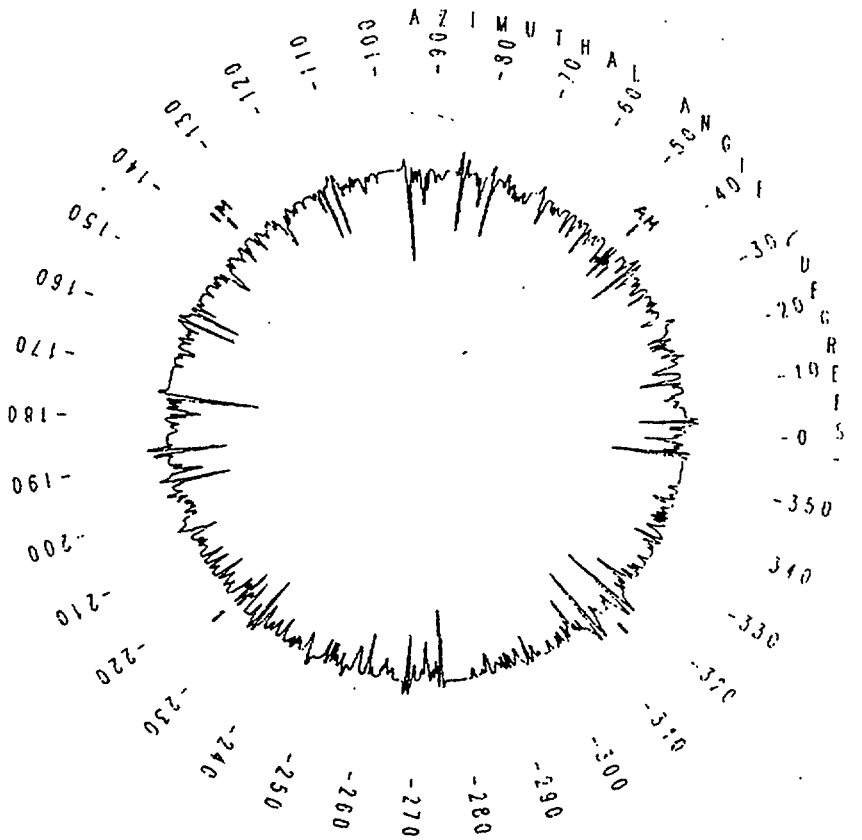

FIG. 14. Simulated Al (042) neutron m.d. pattern in a circular plot. According the 1-fold symmetry of direction 021 only one isomorphic mirror (IM) and one anamorphic mirror (AM) appear in the plot.

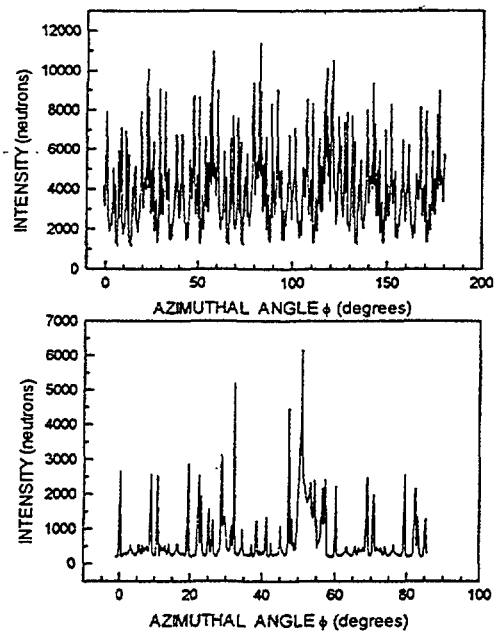

FIG: 15. Neutron m.d. patterns obtained with reflection 00.1 from a quartz (SiO_2) single crystal in phase a (above) and b (below) [9].

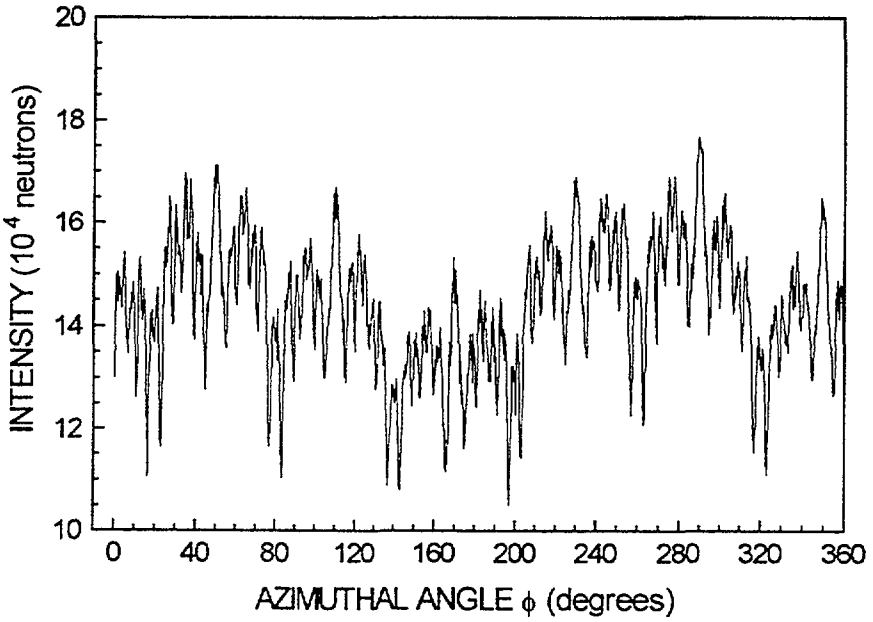

FIG. 16. Full neutron m.d. pattern measured with reflection 111 from a $BaLiF_3$ single crystal.

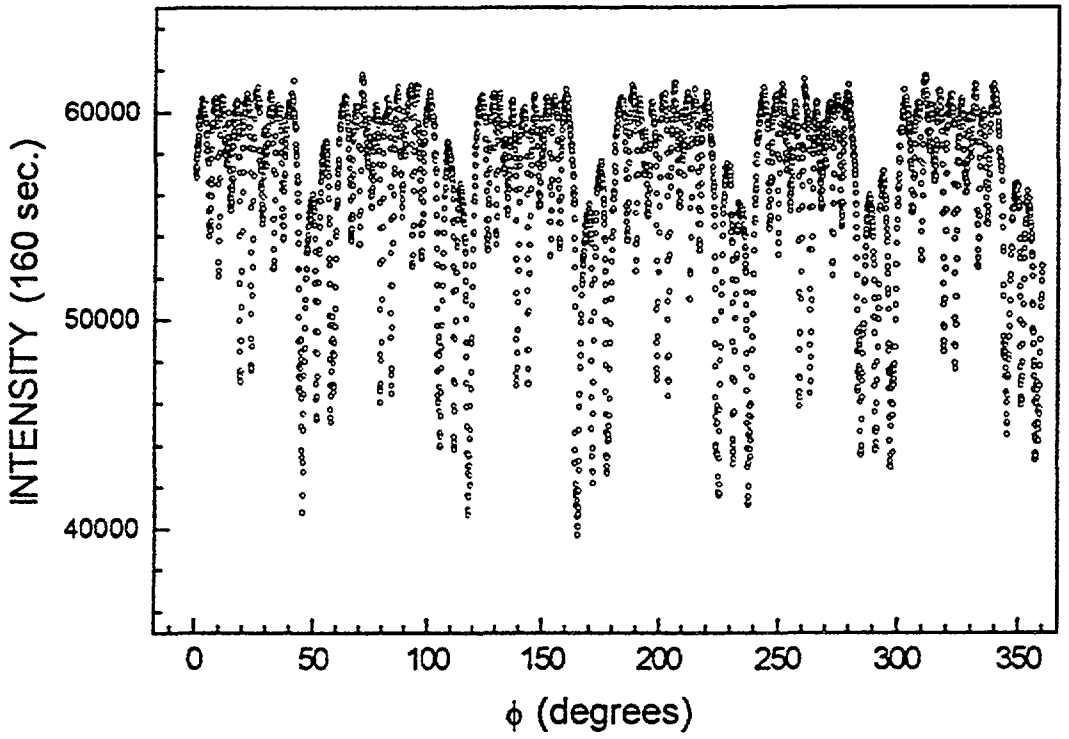

FIG. 17. Full neutron m.d. pattern measured with reflection 111 from a Cu single crystal.

We have also studied several experimental X-ray and neutron m.d. patterns in search for isomorphic and anamorphic mirrors. For instance, we have analysed the experimental 00.1 α- and β-quartz patterns measured by Mazzocchi [9]. We observed that they present no anamorphic mirrors. In this case, in a circular plot, m_a is equal to zero but m_i is still equal to n. It should be mentioned that α-quartz has a hexagonal structure. Consequentely, the [00.1]direction has 6-fold symmetry and $m_i = 6$. On the other hand, β-quartz has a trigonal structure and [00.1] direction has a 3-fold symmetry with $m_i = 3$. The patterns are shown in Figure 15.

Although conclusions like those just above have been drawn from experimental patterns, existing patterns have limited extensions and are, in general, of poor quality. For this reason, we have decided to obtain full experimental patterns with good quality. It should be noted that obtainment of a full (360°) pattern is a very time-consuming procedure, particularly in a low flux reactor like ours. Nevertheless, we have already measured two full patterns. One of them is shown in Fig. 16. It was obtained with the 111 primary reflection from a $BaLiF_3$ single crystal. Other recently measured full pattern was obtained by measuring reflection 111 from a cylindrical copper single crystal. The scattering vector of this reflection was parallel to the cylinder axis. In this case, a quite good pattern was obtained. Fig. 17 shows such a pattern like in the pattern of Fig. 12, intercalated isomorphic and anamorpic mirrors can be observed. It should be noted that copper and aluminium are isostructural. The number of mirrors, 12 in the normal plot, is in accordance with reflection 111 from the copper cubic structure.

4. Determination of the lattice parameter of aluminium at different temperatures by neutron multiple diffraction

C. B. R. Parente, V. L. Mazzocchi

In a m.d. pattern the azimuthal position of a peak depends on the wavelength of the incident radiation as well as on the cell parameters of the crystal under investigation [10]. If the wavelength assumes a fixed value, azimuthal position becomes dependent only on the cell parameters. In this work, the cell parameter a of an Al single crystal is determined for different temperatures. The azimuthal angular positions of several peaks in a neutron Al m.d. pattern, obtained at a certain temperature, are used to determine the a-value for that temperature. In a first method, the absolute position of a peak, i. e. its position referred to an arbitrary origin, is used. In this method, each peak produces an a-value. In a second method, the relative positions of two neighbour peaks are used. In this method each pair of peaks produces an a-value. Values of a are found by comparing the absolute azimuthal position of a peak with azimuthal positions of the corresponding peak in simulated patterns, calculated by assuming different a-values. When the azimuthal position of corresponding peaks match for a particular simulated pattern, the a-value assumed in the simulation is assigned to the peak. In the second method, relative positions, i. e. azimuthal angular distances between two peaks, are used instead. For this method, angular distances are compared to find the a-value for a particular temperature. For both methods, the final a-value can be attained by linear regression of the several individual a-values plotted.

Figure 18 shows partial neutron m.d. patterns obtained with an Al single crystal at 3 different temperatures. The azimuthal positions of the peaks are listed in the bottom of Figure 18. They resulted from Gaussian fittings of the patterns (full lines). Figure 18 ilustrates how the peaks change their positions with temperature. Peak 402, for example, goes to left as

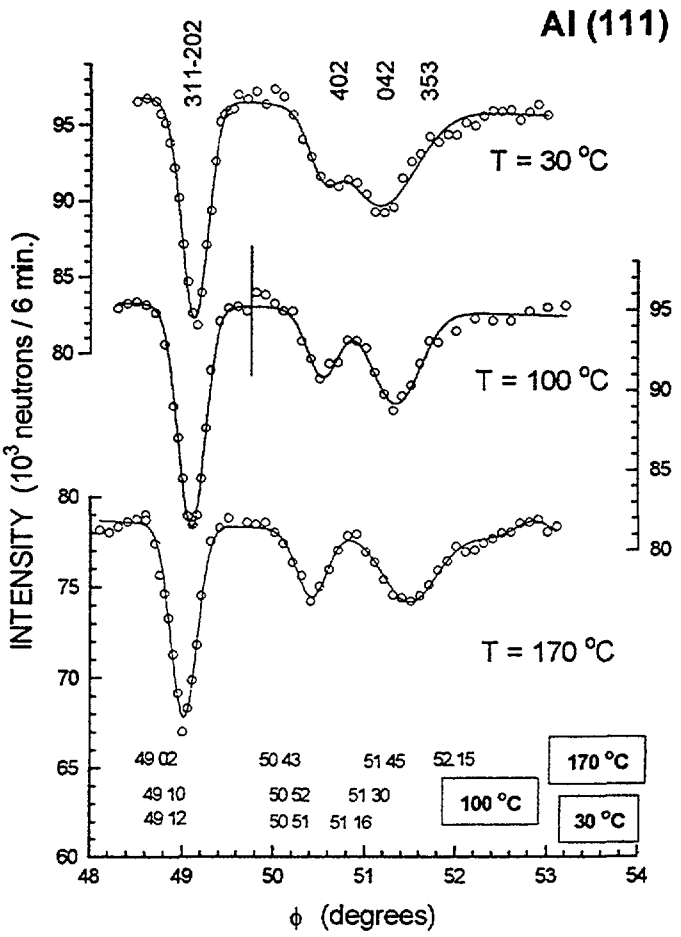

FIG. 18. Partial Al (111) neutron m.d. patterns measured at 30, 100 and 170 °C. They illustrate how peaks change positions with the temperature variation.

the temperature increases. Peak 042, on the other hand, goes to right. They form a pair with opposite behaviours and could be used in the second method. Nevertheless, each one separately could also be used in the first method.

References

[1] Baldochi, S. L., Mazzocchi, V. L., Parente, C. B. R., Morato, S. P., Study of the crystalline quality of Czochralski grown barium lithium fluoride single crystals, Mat. Res. Bull. 29, 12, 1321-1331, 1994.

[2] Parente, C. B. R., Mazzocchi, V. L., Structural characterization of advanced ceramics using the neutron diffractometer developed by Instituto de Pesquisa Energeticas e Nucleares (IPEN). International Atomic Energy Agency - Summary Report for the First Research Co-ordination Meeting of the Coordinated Research Programme on "Advanced Ceramic Materials Charcterization using Thermal Neutrons", National Institute for Industrial Technology and Engineering (INETI/CEN), Sacavem, Portugal, 21-25 de marco de 1994.

[3] Yan, L. C., Stevens, R., J. Amer. Ceram. Soc. 75, 1142, 1150 and 1160, 1992.

[4] Sarkar, B., Reddy, Y. S., Sharma, R. G., A comparative study of the synthesis techniques to obtain high Tc single phase in bismuth based superconductors, Mat. Res. Bull. 28, 263-269, 1993.

[5] Parente, C. B. R. Difracao Multipla de Neutrons em um Cristal de Aluminio, Universidade Estadual de Camoinas, Instituto de Fisica Gleb Wataghin, 1993. (Doctor Thesis).
[6] Sasaki, J. M. Diagrama Renninger com Radiacao de Freamento de Electrons e Sincroton no Estudo de Estruturas Heteroepitaxiais, Universidade Estadual de Campinas, Instituto de Fisica Gleb Wataghin, 1993. (Doctor Thesis).
[7] Parente, C. B. R., Mazzocchi, V. L., Pimentel. F. J. F., Approximate intensity solutions for the multiple diffraction of neutrons in a many-beam case. J. Appl. Cryst., 27, 463-474, 1994.
[8] Salles da Costa, C. A. B., Cardoso, L. P., Mazzocchi, V. L., Parente, C. B. R., Multiple diffraction simulation in the study of epitaxial layers, Defect Control in Semiconductors, vol. II, K. Sumino (ed.), pp. 1535-39, Elsevier Science Publishers B. V. (North-Holland), 1990. Proceedings of the International Conference on the Science and Technology of Defect Control in Semiconductors, Yokohama, Japan, September 17-22, 1989.
[9] Mazzocchi, V. L., Estudo das fases α e β do quartzo com difracao multipla de neutrons, Universidade de Sao Paolo, IPEN-CNEN/SP, 1984. (Master Thesis
[10] Cole, H., Chambers, F. W., Dunn, H. M., Simultaneous diffraction: indexing umweganregung peaks in simple cases, Acta Cryst. 15, 138-144, 1962.

STUDY ON THE STRUCTURE OF NANOMETER CERAMIC SiC USING NEUTRON DIFFRACTION

LI JIZHOU, YANG JILIAN, CHEN DONGFENG, GOU CHENG
China Institute of Atomic Energy,
Beijing

TAN SHOUHONG, HUANG ZHENGREN
High Temperature Structure Ceramics Department,
Shanghai Institute of Ceramics,
Shanghai,

China

Abstract

The nanometer functional heat-resistant ceramic SiC is expected to have enhanced properties (such as structure strength, toughness) compared with the SiC sample consisting of larger crystalline particle. To study on the structure of nanometer SiC, the X-ray diffraction measurements for 4 samples with different size of particle (3000, 800, 100 and 45 nm) were carried out. The results of X-ray diffraction show that the FWHM of the characteristic peak ($2q = 35.5^{o}$) for SiC ceramics are significantly increasing with the decrement of size of particle. They are 0.16^{o}, 0.26^{o}, 0.32^{o} and 1.48^{o} respectively. For last one (45 nm) it is more like an amorphous. The neutron diffraction experiment was performed at a triple-axis spectrometer (used as a higher-resolution powder diffractometer) in China Institute of Atomic Energy. By comparasion with the diffraction pattern of SiC (~3m), the first main peaks for SiC (45 nm) are overlapped to one peak and widening. In addition, under the crystalline peaks there are some wide amorphous peaks obviously. With the aid of a comparasion between the area of crystalline peak and amorphous peak the crystallinity (~75 %) for SiC (45 nm) has been obtained. After deduction of background and amorphous peaks, the multiphase (up to 8 phases) Rietveld profile refinement program FullProf (version 2.2 June 92-ILLJRC) was undertaken for fitting neutron data of SiC (45 nm and 100 nm). The results show that for nanometer SiC (45 nm and 100 nm) the abundances of phases are different with the conventional SiC ceramics (~3m). To evaluate the microstructure of nanometer crystalline grain of SiC ceramics, HREM (High Resolution Electron Microscope) image of sample No. 4 was performed. It shows that a crystalline grain of No. 4 consists of a lot polycrystalline ranges with different phases, and the range-size is about 5-7 nm. Moreover, the microcrystalline-size of SiC sample No. 4 can be obtained by the aid of Scherrer formula according to widening on 12 neutron diffraction peaks, and it is about 8.0 nm.Two results are coincidence.

1. Introduction

It is generally recognized that ceramics frequently offer adventages over metals in their use, such as chemical resistivity, hardness, wear resistance, high melting temperature, low density and low price. However, the use of ceramics has so far been hampered by their brittleness at low temperature. The nanometer crystalline ceramics developed at the middle of 1980s [1] maybe can overcome its disadventage of brittleness. The conventional brittle ceramics can become ductile permitting large plastic deformations at low temperature if a polycrystalline ceramic was generated with a crystal size of a few nm. The ductility seems to originate from the diffusional flow of atoms along the intercrystalline interfaces.

A new concept for developming ceramic with very high strength and fracture toughness is perhaps the combination of micro-composites and nano-composites. Research and development of advanced structural ceramics and ceramic matrix composites with nanometer crystalline ceramics designed for use at high temperatures (up to 1600 ^{o}C) were reviewed [2, 3].

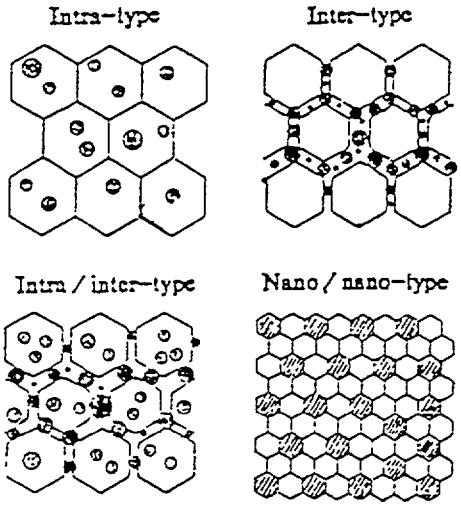

FIG. 1 Classification of ceramic nanocomposites

Ceramic matrix composites include both micro-composites and nano-composites, and nano-composites can be divided into three types: intra-type, inter-type and nano/nano-type (see Figure 1).

Figure 1. shows that for intra-type, inter-type and intra/inter-type nano-composites the particulate dispersions of the nanometer crystalline ceramics take mainly place inside the grain or grain boundary or both of the matrix material. It can not only improve the mechanical properties and the durability at room temperature, but also improve the mechanical properties at high temperature, such as toughness, strength, fracture strength, creep resistance and maximum operating temperature. The nano/nano-type composites consist of nanometer crystalline ceramics dispersion and jointly with nano-size matrix material. It will increase some new functions, such as machinability and superplastic deformation.

In order to obtain the nanocomposites, at first, the nano-size ultrafine powder of ceramics with high-quality must be sintered. On synthesis of ultrafine powder some new methods such as High Temperature Chemical Vapor Deposition (HTCVD) method, Thermal chemical vapor phase reaction method [4], sol-gel synthesis [5], H_2O-catalyzed sintering method [6] and gas-phase chemical reaction by laser [7] or plasma, are used. In this paper, we study on the structure of nano-size ultrafine powder of ceramic SiC sintered by high-temperature chemical vapor deposition method using neutron diffraction technique. The emphasis is focused on the size, shape, phase abundance, crystallinity of resulting particles and so on.

2. Sample preparation

For comparasion of characteristics of SiC ceramics changed with a size of crystalline grains, 4 SiC ceramic samples with different size of particles (~3μ, 800, 100 and 45 nm) are prepared.

The SiC sample No. 1 (~3μ) is a kind of commercial ceramic powder, which was synthesized by reaction within silica (SiO_2) and coke at a temperature of more than 1900 °C. The SiC sample No.2 (800 nm), and No. 3 (100 nm) and No. 4 (45 nm) were prepared in the High Temperature Structure Ceramics Department of Shanghai Institute of Ceramics. The SiC sample No.2 powder was prepared by ball milling method using SiC ceramics powder

FIG. 2. HREM image of SiC sample No. 4.

with larger-size particles, which was sintered again using the commercial SiC ceramic powder as raw and semifinished materials.

The sample No.4 was synthesized using the bichlorosilane plus hydrogen gas at high temperature by High Temperature Chemical Vapor Deposition Method. The synthesis included 3 processes: reaction-nucleation-growth. The SiC powder with different particle size and different extent of nucleation (such as nanometer-size powder) can be produced by means of the control of gas flow rate, mole ratio and temperature. The SiC sample No 3 was processed again at high temperature using nanometer-size (45 nm) SiC powder.

The resulting microstructures (such as particle-size, shape and cluster state) of SiC sample No.3 and No. 4 powder were evaluated by TEM (Transmission Electron Microscopy). The TEM micrograph of SiC sample No.4 powder shows that the nanometer SiC ceramic ultrafine powder synthesized by high temperature chemical vapor deposition method is in size of narrow ranges, equiaxial morphology and a nonagglomerated state. The average partical-size of SiC sample No.4 powder is about 45 nm.

The TEM micrograph of SiC sample No. 3 powder processed with high temperature aftertreatment using nanometer SiC sample No. 4 powder shows that after high-temperature aftertreatment, some nanometer-size powder formed larger crystalline grains. So, the particle-size range wider from 30 nm to 200 nm, and the average particle-size of SiC sample No.3 is about 10 nm.

To evaluate the microstructure of nanometer crystalline grain of SiC sample No. 4 further, the HREM (High Resolution Electron Microscopy) image of a sample No. 4 grain was performed (see Figure 2). It shows that the crystalline grain of SiC sample No. 4 consists of a lot of polycrystalline ranges with different phases, and the range-size is about 5-7 nm.

The electron diffraction measurement for SiC sample No.4 powder was also performed. The electron diffraction diagram of SiC sample No. 4 is shown in Figure 3. The distinct and sharp circles of electron diffraction show that the SiC crystalline grain consists of polycrystalline microstructure with different phases.

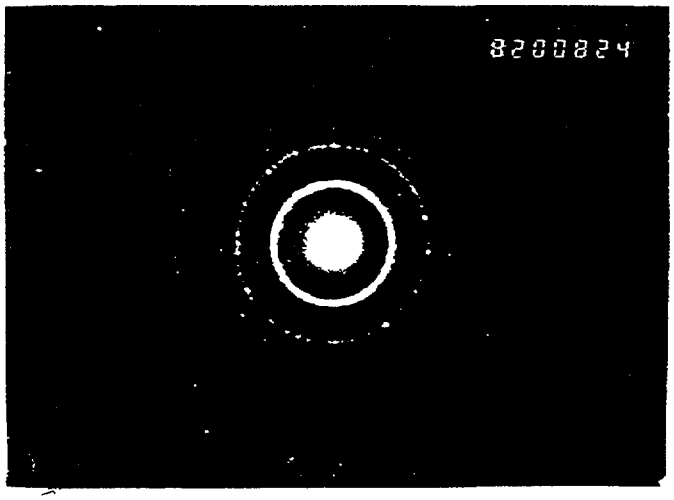

FIG. 3. Electron diffraction diagram of SiC sample No. 4.

3. Experimental procedure

3. 1 X-ray diffraction experiment

To study on the structure of nanometer ceramics SiC, the X-ray diffraction measurements for 4 samples with different particle-size (3000, 800, 100 and 45 nm) were carried out. The X-ray diffraction patterns of SiC sample No. 1, No. 2, No. 3 and No. 4 are presented in Figures 4, 5, 6 and 7. The results of X-ray diffraction show that the FWHM of the characteristic peak (2q=35.5°) for ceramics SiC are significantly increasing with the decrement of particle-size. They are 0.16°, 0.26°, 0.32° and 1.48° respectively. For last one (45 nm) the first 3 main peaks are overlapped to one peak and widening. So, it is more like an amorphous.

3. 2. Neutron diffraction experiment

The neutron diffraction experiments of ceramic SiC sample No.3 and No.4 were performed at a triple-axis spectrometer (used as a higher-resolution powder diffractometer) in Heavy Water Research Reactor of China Institute of Atomic Energy. The SiC sample powder was contained in a 6 mm inside diameter, 0.1 mm walled vanadium can. A neutron wavelength of 1.541Å selected from the (004) planes of a pyrolytic graphite monochromator at a take-off angle of 27.36°. The analyzer was pyrolytic graphite in the (002) setting. The collimation was 29` in-pile, 40` monochromator-sample, 28` sample-analyzer and 40` analyzer-detector.

By comparasion with the diffraction pattern of common SiC ceramics (several microns), which was presented in the first paper [9] of "Study on Functional Heat-Resistant Ceramics SiC Using Neutron Diffraction", the first 3 main peaks in neutron diffraction pattern of sample No. 4 are overlapped to one peak and widening. In addition, there are some wide amorphous peaks obviously under the crystalline peaks.

After deducation of background and amorphous peaks, the neutron diffraction pattern was fitted with three phases: 6H phase (space group C6mc), 15R phase (R3m) and 2H phase (P63mc) using multiphase Rietveld analysis program FullProf for SiC sample No.3 and No.4.

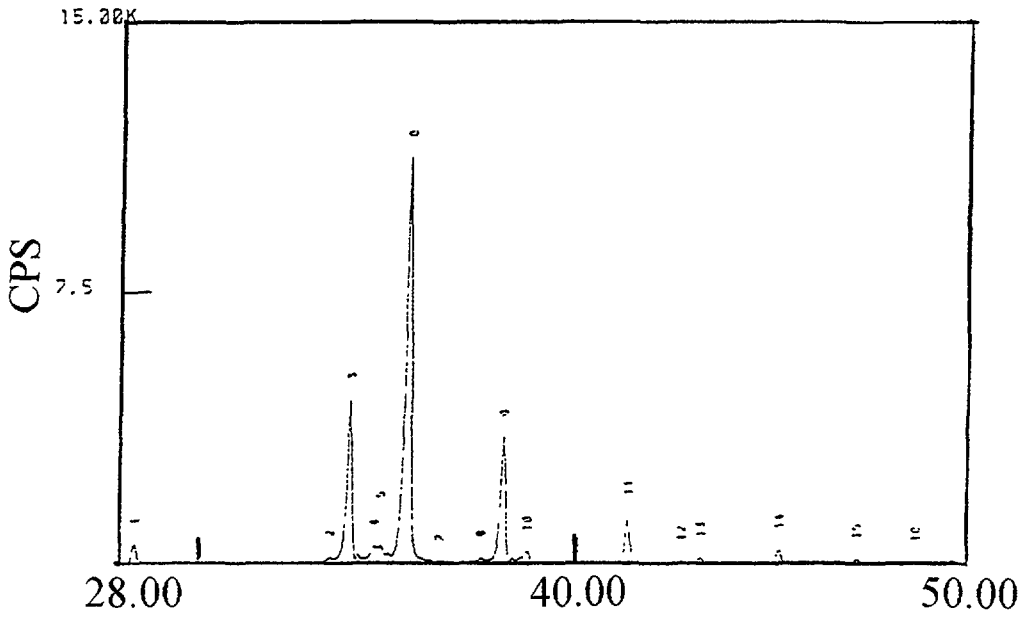

No.	2Theta	TOTAL	BACK	NET	INTEG.W	HEIGHT.W
1	34	38540	3434	34906	.157	.143
2	35.53	107648	7234	100414	.181	.163
3	38.04	30220	1651	28570	.165	.149

FIG. 4. X-ray diffraction pattern of SiC sample No. 1 powder.

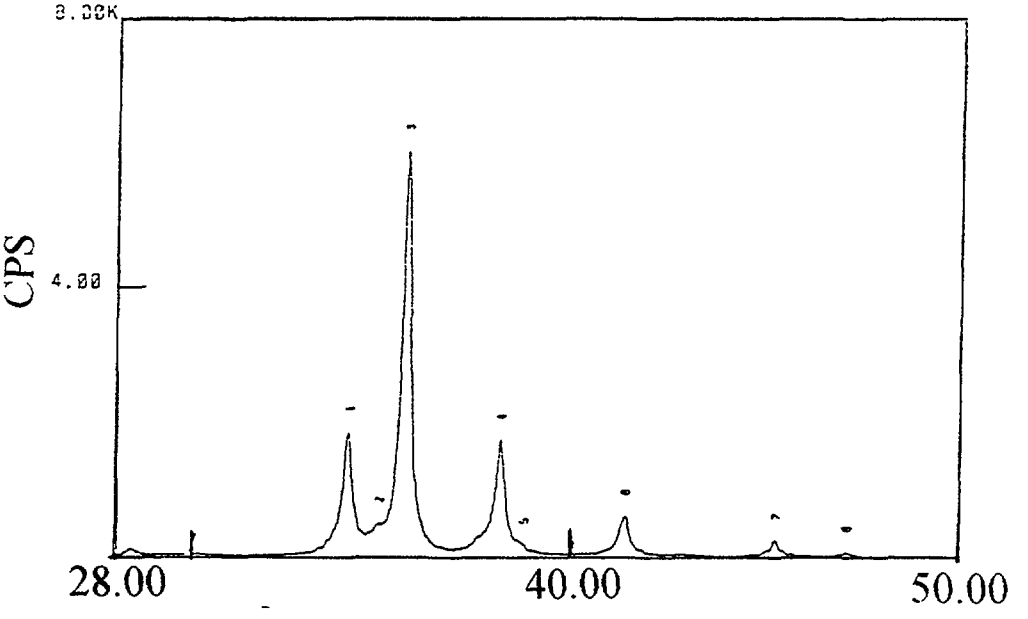

No.	2Theta	TOTAL	BACK	NET	INTEG.W	HEIGHT.W
1	34.09	40586	14664	25922	.325	.258
2	35.62	123625	24731	98894	.342	.259
3	38.15	41802	13665	28137	.359	.266

FIG. 5. X-ray diffraction pattern of SiC sample No. 2 powder.

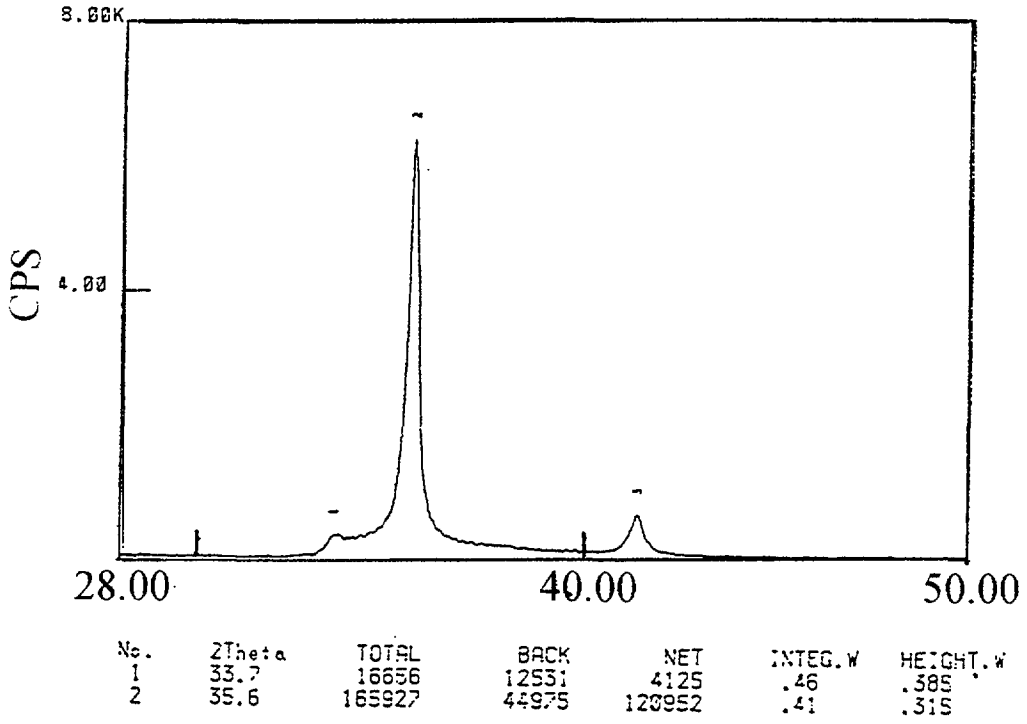

FIG.6. X-ray diffraction pattern of Sic sample No. 3 powder.

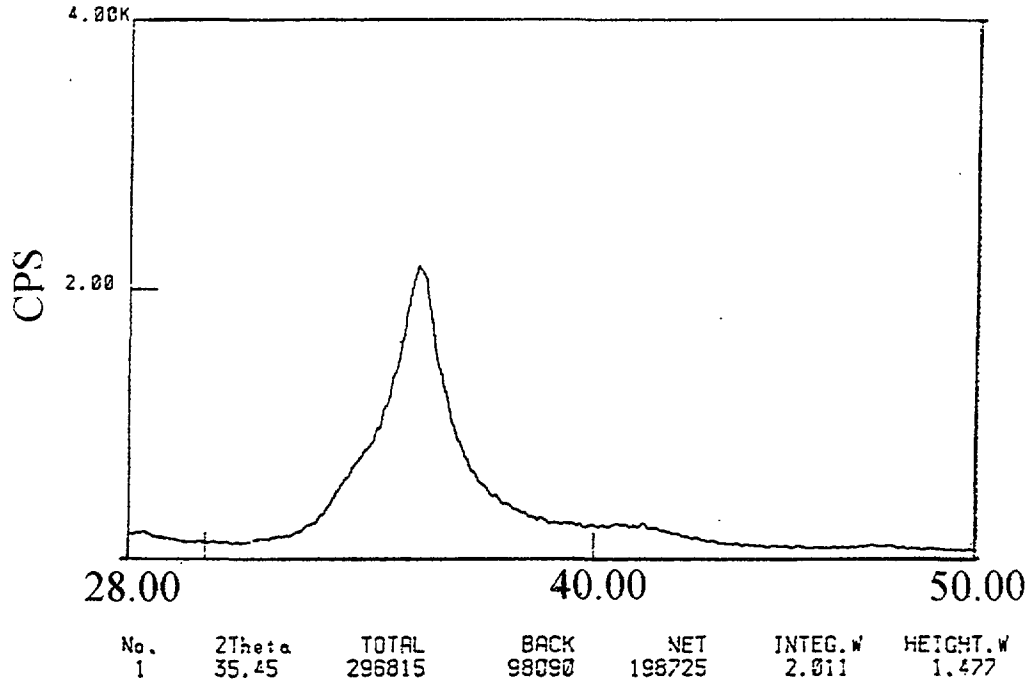

FIG. 7. X-ray diffraction pattern of SiC sample No.4 powder.

TABLE 1: THE CRYSTALLOGRAPHIC DATA OF COMMON STRUCTURE FOR SIC ARE AS FOLLOWS [8]:

Phase	Structure	Unit-cell *a*	dimensions *c*	Space group	Atomic Si	positions C
2H	Hexagonal	3.0817	5.0394	*P63mc*	0 0 0 2/3 1/3 1/2	0 0 3/8 2/3 1/3 7/8
β-SiC	Face-centered cubic	4.349		*F43m*	0 0 0 0 1/2 1/2 1/2 0 1/2 1/2 1/2 0	at 1/8 1/8 1/8 plus Si positions
4H	Hexagonal	3.073	10.053	*C6mc*	0 0 0 0 0 1/2 1/3 2/3 1/4 2/3 1/3 3/4	at 0 0 3/16 plus Si positions
6H	Hexagonal	3.073	15.1183	C6mc	0 0 0 0 0 1/2 1/3 2/3 1/6 1/3 2/3 5/6 2/3 1/3 2/3 2/3 1/3 1/3	at 0 0 1/8 plus Si positions
15R	Rhombohedral	12.69	37.70 (a=13°54.5`)	R3m	0 0 u 1/3 2/3 1/3+u 2/3 1/3 2/3+u u=0,2/15, 6/15,9/15, 13/15	at 0 0 1/20 plus Si positions

TABLE II. NEUTRON DIFFRACTION DATA OF SiC SAMPLE No.3

Phase no. 1 Phase name SiC 6H

No.	Code	H	K	L	Mult	Hw	ETA/M 0.149	2theta	Icalc	Iobs
1	1	0	0	4	2	0.565	0.149	23.173	1.	2.
2	1	0	0	5	2	0.537	0.149	29.080	0.	0.
3	1	0	0	6	2	0.526	0.149	35.067	1179.	1250.
4	1	0	0	7	2	0.536	0.149	41.156	0.	0.
5	1	0	0	8	2	0.570	0.149	47.368	1.	0.
6	1	0	0	9	2	0.627	0.149	53.731	0.	0.
7	1	1	1	0	6	0.701	0.149	59.675	142.	153.
8	1	1	1	1	12	0.706	0.149	60.009	0.	0.
9	1	0	0	10	2	0.709	0.149	60.280	1.	3
10	1	1	1	2	12	0.720	0.149	61.005	0.	0.
11	1	1	1	3	12	0.744	0.149	62.644	0.	0.
12	1	1	1	4	12	0.780	0.149	64.899	0.	0.
13	1	0	0	11	2	0.817	0.149	67.053	0.	0.
14	1	1	1	5	12	0.829	0.149	67.738	0.	0.
15	1	2	0	0	6	0.867	0.149	69.813	0.	0.
16	1	2	0	1	12	0.872	0.149	70.120	0.	0.
17	1	1	1	6	12	0.892	0.149	71.133	117.	120.
18	1	2	0	2	12	0.890	0.149	71.039	831.	847.
19	1	2	0	3	12	0.920	0.149	72.560	0.	0.
20	1	0	0	12	2	0.951	0.149	74.103	35.	11.
21	1	2	0	4	12	0.963	0.149	74.668	68.	29.
22	1	1	1	7	12	0.971	0.149	75.059	0.	0.
23	1	2	0	5	12	1.021	0.149	77.348	0.	0.
24	1	1	1	8	12	1.070	0.149	79.503	0.	0.
25	1	2	0	6	12	1.095	0.149	80.586	1.	2.
26	1	0	0	13	2	1.117	0.149	81.498	0.	0.
27	1	1	1	9	12	1.192	0.149	84.464	0.	0.
28	1	2	0	7	12	1.190	0.149	84.375	0.	0.

Phase: 1

Bragg R-factor: 6.99 Vol: 129.585 Fract(%): 38.55

Rf-factor = 13.1 ATZ: 721.552 Brindley: 1.0000

TABLE II. (cont.)

Phase no. 2 Phase name SiC 15R

No.	Code	H	K	L	Mult	Hw	ETA/M	2theta	Icalc	Iobs
1	1	0	0	12	2	0.539	0.149	28.613	0.	0.
2	1	1	0	1	6	0.528	0.149	33.044	18.	17.
3	1	0	1	2	6	0.528	0.149	33.310	61.	82.
4	1	1	0	4	6	0.527	0.149	34.358	123.	135.
5	1	0	0	15	2	0.527	0.149	35.984	29.	68.
6	1	0	1	5	6	0.527	0.149	35.125	51.	55.
7	1	1	0	7	6	0.528	0.149	37.104	53.	54.
8	1	0	1	8	6	0.530	0.149	38.296	27.	22.
9	1	1	0	10	6	0.537	0.149	41.036	3.	50.
10	1	0	1	11	6	0.543	0.149	42.567	5.	0.
11	1	0	0	18	2	0.547	0.149	43.512	0.	0.
12	1	1	0	13	6	0.561	0.149	45.911	4.	0.
13	1	0	1	14	6	0.573	0.149	47.710	1.	0.
14	1	0	0	21	2	0.603	0.149	51.244	0.	0.
15	1	1	0	16	6	0.606	0.149	51.538	2.	0.
16	1	0	1	17	6	0.627	0.149	53.558	8.	1.
17	1	1	0	19	6	0.677	0.149	57.795	28.	45.
18	1	0	0	24	2	0.696	0.149	59.236	0.	0.
19	1	0	1	20	6	0.707	0.149	60.009	16.	21.
20	1	1	1	0	6	0.697	0.149	59.299	1244.	1288.
21	1	1	1	3	12	0.704	0.149	59.807	0.	0.
22	1	1	1	6	12	0.726	0.149	61.313	0.	0.
23	1	1	1	9	12	0.763	0.149	63.777	0.	0.
24	1	1	0	22	6	0.777	0.149	64.619	36.	43.
25	1	0	0	27	2	0.827	0.149	67.558	0.	0.
26	1	0	1	23	6	0.817	0.149	67.016	30.	31.
27	1	1	1	12	12	0.820	0.149	67.143	0.	0.
28	1	0	2	1	6	0.856	0.149	69.173	5.	5.
29	1	2	0	2	6	0.859	0.149	69.329	19.	16.
30	1	0	2	4	6	0.870	0.149	69.951	44.	42.
31	1	1	0	25	6	0.910	0.149	71.998	6.	6.
32	1	1	1	15	12	0.897	0.149	71.353	235.	240.
33	1	2	0	5	6	0.879	0.149	70.416	20.	20.
34	1	0	2	7	6	0.903	0.149	71.649	25.	26.
35	1	2	0	8	6	0.918	0.149	72.415	14.	18.
36	1	0	1	26	6	0.962	0.149	74.585	6.	3.
37	1	0	0	30	2	0.999	0.149	76.306	1.	1.
38	1	0	2	10	6	0.955	0.149	74.241	2.	0.
39	1	2	0	11	6	0.977	0.149	75.299	3.	2.
40	1	1	1	18	12	1.000	0.149	76.362	0.	0.
41	1	0	2	13	6	1.030	0.149	77.698	3.	3.
42	1	1	0	28	6	1.082	0.149	79.967	1.	1.
43	1	2	0	14	6	1.060	0.149	79.037	1.	0.
44	1	0	1	29	6	1.150	0.149	82.769	0.	0.
45	1	1	1	21	12	1.135	0.149	82.151	0.	0.
46	1	0	2	16	6	1.131	0.149	81.993	2.	10.
47	1	2	0	17	6	1.171	0.149	83.609	7.	33.

Phase: 2

Bragg R-factor: 12.0 Vol: 323.500 Fract (%): 37.13

Rf-factor = 18.4 ATZ: 601.455 Brindley: 1.0000

TABLE II. (cont.)

Phase no. 3 Phase name SiC 2H

No.	Code	H	K	L	Mult	Hw	ETA/M	2theta	Icalc	Iobs
1	1	1	0	0	6	0.527	0.149	33.251	28.	34.
2	1	0	0	2	2	0.526	0.149	35.478	36.	50.
3	1	1	0	1	12	9.528	0.149	37.828	21.	19.
4	1	1	0	2	12	0.586	0.149	49.412	10.	0.
5	1	1	1	0	6	0.701	0.149	59.675	223.	241.
6	1	1	0	3	12	0.786	0.149	65.258	28.	26.
7	1	2	0	0	6	0.867	0.149	69.813	8.	8.
8	1	1	1	2	12	0.896	0.149	71.383	131.	133.
9	1	2	0	1	12	0.921	0.149	72.622	8.	12.
10	1	0	0	4	2	0.972	0.149	75.087	1.	1.
11	1	2	0	2	12	1.101	0.149	80.826	6.	23.
12	1	1	0	4	12	1.196	0.149	84.628	0.	3.

Phase: 3
Bragg R-factor: 14.3 Vol: 42.707 Fract (%): 24.32
Rf-factor= 15.3 ATZ: 160.388 Brindley: 1.0000

TABLE III. NEUTRON DIFFRACTION DATA OF SiC SAMPLE No. 4

Phase no. 1 Phase name SiC 6H

No.	Code	H	K	L	Mult	Hw	ETA/M	2theta	Icalc	Iobs
1	1	0	0	4	2	1.319	0.149	23.965	0.	0.
2	1	0	0	5	2	1.281	0.149	30.082	0.	0.
3	1	0	0	6	2	1.250	0.149	36.289	425.	441.
4	1	0	0	7	2	1.227	0.149	42.608	0.	0.
5	1	0	0	8	2	1.213	0.149	49.066	0.	0.
6	1	0	0	9	2	1.212	0.149	55.695	0.	0.
7	1	1	1	0	6	1.220	0.149	60.387	45.	47.
8	1	1	1	1	12	1.220	0.149	60.742	0.	0.
9	1	0	0	10	2	1.226	0.149	62.534	0.	0.
10	1	1	1	2	12	1.224	0.149	61.798	0.	0.
11	1	1	1	3	12	1.230	0.149	63.535	0.	0.
12	1	1	1	4	12	1.240	0.149	65.925	0.	0.
13	1	0	0	11	2	1.261	0.149	69.630	0.	0.
14	1	1	1	5	12	1.257	0.149	68.934	0.	0.
15	1	2	0	0	6	1.272	0.149	71.121	0.	0.
16	1	2	0	1	12	1.274	0.149	71.447	0.	0.
17	1	1	1	6	12	1.282	0.149	72.532	37.	36.
18	1	2	0	2	12	1.281	0.149	72.421	236.	236.
19	1	2	0	3	12	1.295	0.149	74.033	0.	0.
20	1	0	0	12	2	1.324	0.149	77.046	13.	13.
21	1	2	0	4	12	1.316	0.149	76.269	23.	19.
22	1	1	1	7	12	1.320	0.149	76.695	0.	0.
23	1	2	0	5	12	1.347	0.149	79.113	0.	0.
24	1	1	1	8	12	1.375	0.149	81.412	0.	0.
25	1	2	0	6	12	1.391	0.149	82.553	0.	0.
26	1	0	0	13	2	1.424	0.149	84.867	0.	0.
27	1	1	1	9	12	1.453	0.149	86.690	0.	0.
28	1	2	0	7	12	1.452	0.149	86.585	0.	0.

Phase: 1

Bragg R-factor: 2.87	Vol: 119.967	Fract (%):	19.93
Rf-factor= 2.55	ATZ: 721.552	Brindley:	1.0000

TABLE III. (cont.)

Phase no 2 Phase name SiC 15R

No	Code	H	K	L	Mult	Hw	ETA/M	2theta	Icalc	Iobs
1	1	0	0	12	2	1 294	0 149	27 904	0	0
2	1	1	0	1	6	1 262	0 149	33 833	15	22
3	1	0	1	2	6	1 262	0 149	34 081	50	61
4	1	1	0	4	6	1 256	0 149	35 059	111	113
5	1	0	0	15	2	1 256	0 149	35 082	49	49
6	1	0	1	5	6	1 253	0 149	35 778	49	51
7	1	1	0	7	6	1 245	0 149	37 636	57	70
8	1	0	1	8	6	1 240	0 149	38 758	30	44
9	1	1	0	10	6	1 231	0 149	41 346	3	14
10	1	0	1	11	6	1 227	0 149	42 796	7	0
11	1	0	0	18	2	1 228	0 149	42 405	0	0
12	1	1	0	13	6	1 218	0 149	45 971	5	10
13	1	0	1	14	6	1 215	0 149	47 684	2	9
14	1	0	0	21	2	1 212	0 149	49 915	0	0
15	1	1	0	16	6	1 211	0 149	51 334	3	9
16	1	0	1	17	6	1 211	0 149	53 264	12	11
17	1	1	0	19	6	1 213	0 149	57 317	40	52
18	1	0	0	24	2	1 214	0 149	57 662	0	0
19	1	0	1	20	6	1 217	0 149	59 436	23	50
20	1	1	1	0	6	1 219	0 149	60 310	405	425
21	1	1	1	3	12	1 221	0 149	60 788	0	0
22	1	1	1	6	12	1 225	0 149	62 210	0	0
23	1	1	1	9	12	1 234	0 149	64 539	0	0
24	1	1	0	22	6	1 231	0 149	63 853	54	73
25	1	0	0	27	2	1 239	0 149	65 708	0	0
26	1	0	1	23	6	1 241	0 149	66 150	45	57
27	1	1	1	12	12	1 249	0 149	67 726	0	0
28	1	0	2	1	6	1 271	0 149	71 029	4	9
29	1	2	0	2	6	1 272	0 149	71 175	15	24
30	1	0	2	4	6	1 276	0 149	71 761	36	37
31	1	1	0	25	6	1 270	0 149	70 923	9	22
32	1	1	1	15	12	1 276	0 149	71 722	213	221
33	1	2	0	5	6	1 280	0 149	72 199	17	17
34	1	0	2	7	6	1 289	0 149	73 361	22	26
35	1	2	0	8	6	1 295	0 149	74 084	13	21
36	1	0	1	26	6	1 289	0 149	73 402	10	12
37	1	0	0	30	2	1 296	0 149	74 139	1	3
38	1	0	2	10	6	1 311	0 149	75 809	1	2
39	1	2	0	11	6	1 321	0 149	76 809	3	3
40	1	1	1	18	12	1 318	0 149	76 485	0	0
41	1	0	2	13	6	1 346	0 149	79 080	3	14
42	1	1	0	28	6	1 340	0 149	78 554	1	4
43	1	2	0	14	6	1 362	0 149	80 349	1	11
44	1	0	1	29	6	1 373	0 149	81 232	0	1
45	1	1	1	21	12	1 383	0 149	81 997	0	0
46	1	0	2	16	6	1 399	0 149	83 154	2	6
47	1	0	0	33	2	1 398	0 149	83 067	0	0
48	1	2	0	17	6	1 422	0 149	84 689	8	24

Phase 2

Bragg R-factor	17 1	Vol	311 159	Fract (%)	51 27
Rf-factor=	18 2	ATZ	601 455	Brindley	1 0000

TABLE III. (cont.)

Phase no.: 3 Phase name SiC 2H

No.	Code	H	K	L	Mult	Hw	ETA/M	2theta	Icalc	Iobs
1	1	1	0	0	6	1.529	0.149	34.407	20.	21.
2	1	0	0	2	2	1.528	0.149	34.687	21.	21.
3	1	1	0	1	12	1.241	0.149	38.683	18.	25.
4	1	1	0	2	12	1.213	0.149	49.660	6.	22.
5	1	1	1	0	6	1.223	0.149	61.613	165.	175.
6	1	1	0	3	12	1.235	0.149	64.839	13.	20.
7	1	2	0	0	6	1.282	0.149	72.531	4.	4.
8	1	1	1	2	12	1.284	0.149	72.680	88.	87.
9	1	0	0	4	2	1.288	0.149	73.197	3.	3.
10	1	2	0	1	12	1.305	0.149	75.182	10.	16.
11	1	2	0	2	12	1.396	0.149	82.966	4.	12.
12	1	1	0	4	12	1.403	0.149	83.446	1.	3.

Phase: 2

Bragg R-factor: 14.4 Vol 1: 40.452 Fract (%): 28.80

Rf-factor = 11.3 ATZ: 160.388 Brindley: 1.0000

They are presented in Figures 10 and 11, respectively. Scattering lengths of 4.149 and 6.6484 fm (10-13 cm) were taken for Si and C. The corresponding neutron diffraction data (such as observed (Iobs) and calculated (Icalc) diffraction intensities of 3 phases and agreement factors (Bragg R-factor and Rf-factor) of SiC samples No. 3 and No. 4 are listed in Table 2 and Table 3, respectively.

4. Results, discussion and conclusions

4.1. Results discussion

4. 1. 1. Multiphase analysis

According to neutron diffraction pattern Figures 8 and 9 of nanometer ceramic SiC sample No.3 and No.4 the multiphase analysis can be completed with FullProf program, although the neutron diffraction peaks are widening. The abundances of 3 phases for sample No.3 and No.4 are as follows:

Sample	Phase name	Space group	Abundance (%)
No. 3	6H	*C6mc*	38.55
	15R	*R3m*	37.13
	2H	$P6_3mc$	24.32
No. 4	6H	*C6mc*	19.93
	15R	*R*3m	51.27
	2H	$P6_3mc$	28.80

Multiphase analysis for nanometer SiC sample No.4 shows that the main phase of newly synthesized nanometer SiC No.4 powder (45 nm), using HTCVD method is 15R phase, differs from α-SiC ceramics with main phase of 2H. Since SiC sample No. 3 was processed again at high temperature using sample No. 4 powder, the phase abundances are different from those of No. 4. Comparing phase abundances of sample No. 3 with No. 4, some 15R phase transformed into 6H phase.

4. 1. 2. Crystallite size

The determination of microcrystalline-size for nanometer SiC ceramics is very important and interesting. As we know, the X-ray and neutron diffraction peaks are considerably broadened due to the small crystallite-size. Applying the Scherrer formula [10] an average crystallite diameter can be deducated.

Scherer formula is

$$L_{hkl} = \frac{K\lambda}{\sqrt{B^2 - B_0^2}Cos\theta} \qquad (1)$$

in which L_{hkl} is crystallite diameter vertical to (hkl) plane, λ is wavelength (Å) and θ is Bragg angle, B_0 and B are FWHM of corresponding diffraction peak for common sample and

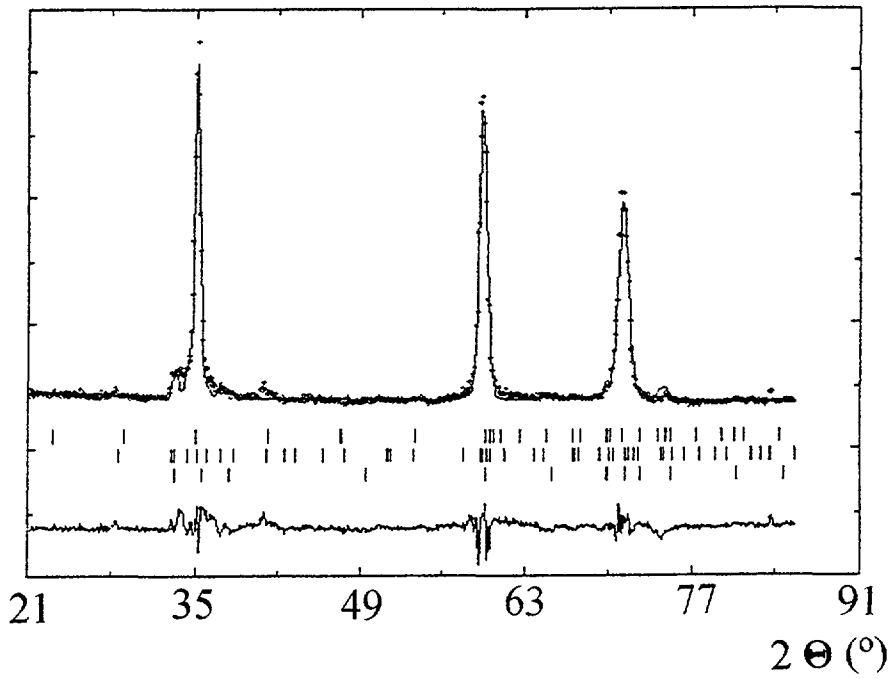

FIG. 8. The neutron diffraction pattern fitted with 6H phase (space group C6mc), 15R phase (R3m) and 2H phase (P63mc) using multiphase Rietveld analysis program FullProf for SiC sample No.3.

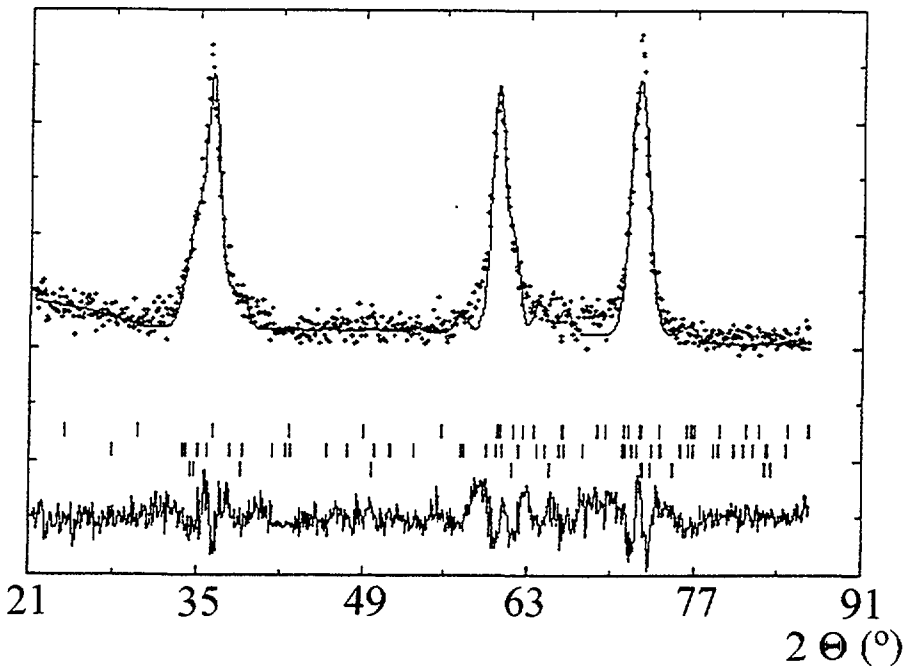

FIG. 9. The neutron diffraction pattern fitted with 6H phase (space group C6mc), 15R phase (R3m) and 2H phase (P63mc) using multiphase Rietveld analysis program FullProf for SiC sample No. 4.

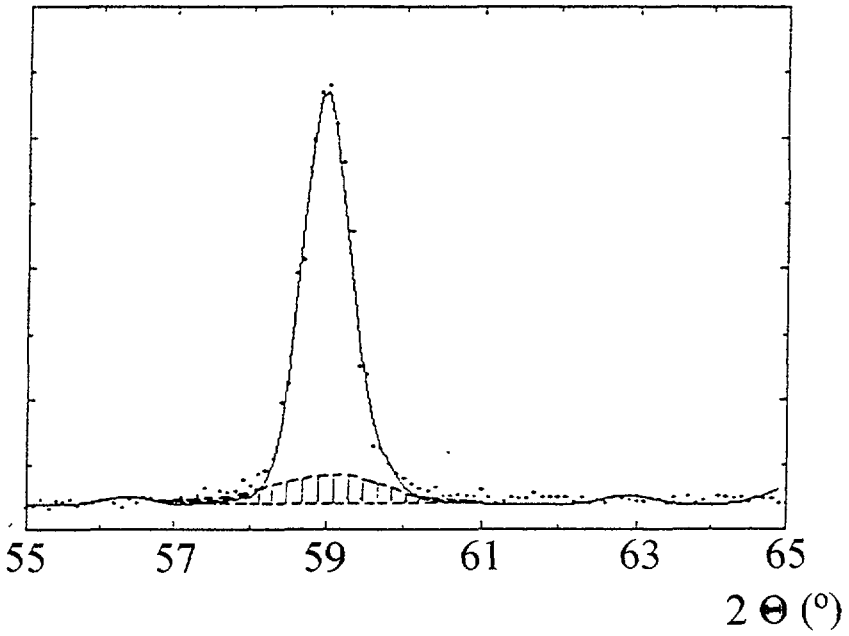

FIG. 10. Amorphous peak in neutron diffraction pattern for sample No. 3.

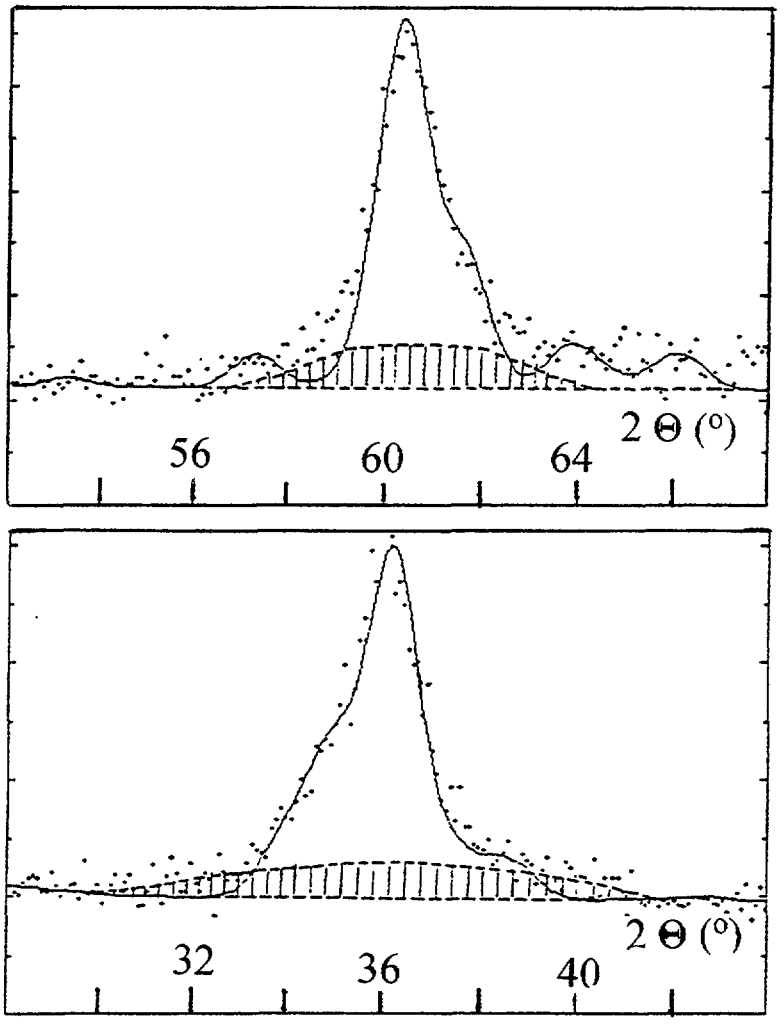

FIG. 11. Amorphous peaks in neutron diffraction pattern for sample No. 4.

measured nanometer sample respectively. Crystalline shape factor K of 0.89 is assumed, if B_0 and B are defined as FWHM of diffraction peak with Gauss distribution.

By the aid of Scherrer formula (1), according to X-ray diffraction patterns Figures 4, 6 and 7 a crystallite diameter of 6.3 nm was deducted for SiC sample No.4, and 26.8 nm for sample No.3. According to neutron diffraction patterns (Figures 9 and 8) an average crystallite diameter of 8.0 nm was deducted for SiC sample No. 4, and 21.5 nm for sample No.3. It must be pointed out that results of average crystallite-size for No.3 and No.4 using neutron data were based on broadening on 12 main neutron diffraction peaks of 3 phases, but results using X-ray data are only concerned with one or two diffraction peaks. In this connection, neutron diffraction is of adventage.

4. 1. 3. **Crystallinity**

In neutron diffraction patterns Figures 8 and 9 some wide amorphous peaks are under crystalline peaks obviously. For demonstration, corresponding peaks are widened as shown in Figures 10 and 11, in which small and wider amorphous peaks are shadowing. With the aid of a comparasion between the area of crystalline peak and amorphous peak, a crystallinity of 75 % is obtained for SiC sample No. 4, and 85 % for sample No. 3. The result of crystallinity for sample No. 4 coincides with the demonstration in HREM image of Figures 4, in which some indistinct regions indicate amorphous existance.

4. 2. Conclusions

1. The newly synthesized nanometer SiC ceramic ultrafine powder by HTCVD method is in size of narrow ranges (~45nm), equiaxial morphology and a nonagglomerated state, in which the crystallite size is 5-7 nm by HREM, an average value of 8.0 nm by neutron diffraction and a value of 6.3 nm by X-ray diffraction. The main phase is 15R phase (R3m) which differs from common α-SiC ceramics by means of multiphase analysis of neutron diffraction. The crystallinity is about 75 % according to a comparasion of peak area between crystalline and amorphous.
2. After above nanometer SiC ultrafine powder was processed again at high temperature, some nanometer-size powder formed larger crystalline grains, and the average grain-size is about 100 nm, in which the crystallite size is also larger than that of above powder. An average value of 21.5 nm was obtained by neutron diffraction and a value of 26.8 nm by X-ray diffraction. The main phases are 6H and 15R. It seems that some 15R phase transformed into 6H phase with aftertreatment. The crystallinity is about 85 %.
3. The neutron diffraction pattern for nanometer-size SiC ceramics has more obvious peaks comparing with X-ray (see Figures 9 and 7), so neutron diffraction is more advantageous in multiphase analysis, determination of crystallite-size and evaluation of crystallinity.

References

[1] J. Karch, R. Birringer, H. Gleiter, "Ceramics Ductile at Low Temperature", Nature, 330 (1987) 556.

[2] Guo Jingkun, Xu Yueping, "State-of-art of Nanocrystalline Ceramics", J. Chin. Ceramic Soc., 20 (1992) 286.

[3] Shi Keshun, "Development of High Temperature Ceramics Composites", J. Chin. Ceram. Soc., 22 (1994) 239.

[4] Xu Yuqing, Hu Guojun, Ding Zishang, "Synthesis of Nanometer SiC-Si3N4 Composite Ultrafine Powder by Thermal Chemical Vapor Phase Reaction Method", J. Chin. Ceramic. Soc., 21 (1993)296.
[5] Xiao Hanning, Du Haiqing, "Sol-gel Synthesis of SiC/B Composite Ultrafine Powder", J. Chin. Ceram. Soc., 21 (1993) 296.
[6] Yoshio Sakka, Donald D. Bidinger, Ilhan A. Aksay, "Processing of Silicon Carbide-Mullite-Alumina Nanocomposites", J. Am. Ceram. Soc., 78 (1995) 479.
[7] Sui Tongbo, Wang Tingji, "Study on Physico-Chemical Process of Laser Synthesis of Ultrafine SiC Powder", J. Chin. Ceram. Soc., 21 (1993) 33.
[8] P. T. B. Shaffer, " A Review of the Structure of Silicon Carbide", Acta Crystallographica, B25 (1969) 477.
[9] Li Jizhou, Yang Jilian, Kang Jian, Ye Chuntang, "Study on Functional Heat-Resistant Ceramics SiC Using Neutron Diffraction", IAEA"s Research Coordination Meeting, 21-25 March 1994, Sacavem, Portugal.
[10] H. K. Klug and L. E. Alexander, "X-ray Diffraction Procedures for Polycrystalline and Amorphous Materials", Second edition, John Wiley and Sons, New York, Chapter 9, pp. 687-708, 1974.

STUDY OF FREE VOLUME HOLE DISTRIBUTIONS IN $xTiO_2(1-x)SiO_2$ BY POSITRON ANNIHILATION SPECTROSCOPY

XA9949657

M.A. MISHEVA, N. DJOURELOV
Faculty of Physics,
Sofia University,
Sofia, Bulgaria

M.A. MARGACA
Physics Department,
ICEN/INETI,
Sacavém, Portugal

F.I. SALVADO
University of Aveiro,
Portugal

G. PASSAGE
Institute of Nuclear Research and Nuclear Energy,
Sofia, Bulgaria

Abstract

Positron annihilation spectroscopy has been used to get information about the small pore structure of the system $xTiO_2.(1-x)SiO_2$ (x=10,30 mol.%). The pore radius and volume probability distribution functions have been received from the ortho-Positronium lifetime probability distribution function, obtained by the lifetime spectra processing with CONTIN (PALS-2) program. The linearity of the S versus W-parameters has been used to check the similarity (or not) of the defect structure of the samples prepared under different experimental conditions.

1. Introduction

Glasses of the system $TiO_2.SiO_2$ have a high refractoriness and low thermal expansion coefficient. Their preparation is very difficult using the traditional oxide melting method because of the high melting point of TiO_2. Furthermore, devitrification can not be avoided for αTiO_2 content larger than ca. 12% [1].

Materials of system $xTiO_2.(1-x)SiO_2$ can be prepared by sol-gel, e. g. alkoxide method for any value of x at low temperature [2]. However, the final product is porous and densification occurs by heat-treatment.

The often used methods for investigation of the pores - the photochromic and fluorescence spectroscopy when the free volume holes in a material are only of a few angstroms in size (2-20 Å) are not suitable for their studies. The small angle neutron and X-ray scattering cannot effectively reveal the hole properties also [3].

Recently Positron Annihilation Lifetime (PAL) spectroscopy has been successfully used for studying the free volume holes in porous materials as protective coatings [4], silica gels [5] and polymers [6,7,8]. The method is based on the established fact that ortho-positronium "atom" (o-Ps), a bound state of the positron and the electron, is preferentially localised in the free-volume holes, where o-Ps lifetime is relevant to the hole size [5,9]. It is considered that o-Ps formation probability is proportional to the concentration of holes.

In this paper we present results on positron annihilation in the system $xTiO_2(1-x)SiO_2$ (x=10,30 mol %), obtained by means of lifetime technique and Doppler broadening of annihilation 511 keV γ-line.

2. Experimental

2.1. Samples

The xTiO$_2$.(1-x)SiO$_2$ glasses with x=10 and 30 mol % were prepared using tetraethylorthosilicate (TEOS) and titanium isopropoxide (i-PrTi) as raw materials. TEOS was first hydrolysed for two hours with magnetic stirring at room temperature with water, ethanol and HCl. After this first step , i-PrTi dissolved in ethanol was added to hydrolysed TEOS solution. Next, water was added until the final molar ratio H_2O/alkoxides, R, was attained.

The solutions obtained were left in a glass container covered with a plastic foil at 60°C for gelation. After a period of 15 day the gels were heat treated at 120°C for 48 hours, after which one pair of the samples was heat treated for 5.5 hours at 850°C. The heating rate to 850 ^{0}C was equal to 60°C.h^{-1}.

The experimental conditions of samples are shown in table 1.

TABLE I. EXPERIMENTAL CONDITIONS OF SAMPLES

No	TiO_2 (mol %)	R	heat-treatment
#1	10	4	120°C
#2	10	4	120°C
#3	10	40	120°C
#4	10	40	850°C
#5	30	40	120°C

The samples #1 and #2 were prepared with different ethanol/alkoxides molar ratio which for the latter was three times that used in the former.

2.2.Positron annihilation lifetime

The lifetime spectrometer was a standard fast-fast coincidence apparatus based on Pilot U scintillators, XP 2020 - Q PMT and ORTEC electronics. It provides a time resolution ~ 260 ps FWHM. The channel width of multi-channel analyzer was Δ=36 ps/ch. The positron source prepared by ^{22}NaCl solution evaporated on and covered by 1 mg/cm Kapton foils was sandwiched between two identical glass samples. The activity of the source was 12±1 μCi. Approximately 3x10^5 counts could be collected for one hour. As a rule several lifetime spectra were recorded for each pair of samples.

2.3.Data analysis of PAL spectra

2.3.1.Analysis with POSITRONFIT EXTENDED program [10]

In this case it is considered that positrons annihilate in several strictly definite states and a finite-term model spectrum is supposed. The lifetime spectrum, N(t), obtained from a positron annihilation experiment is represented by the convolution of the instrumental resolution function, I(t), and the decay curve of positrons, C(t),

$$N(t)=N_s I(t)*C(t) \quad (1)$$

$$C(t)=\sum_{i=1}^{n} \alpha_i \lambda_i \exp(-\lambda_i t) \quad (2)$$

where n is the number of annihilation modes, α_i is the fraction of positrons annihilating with lifetime τ_i= 1/λ_i and N_s is the total number of the annihilation events.

Instrumental resolution function in our analysis was represented by one gaussian with ~260 ps FWHM. As we were interested in the longer lifetime components, we summarized the content of the adjacent channels two by two to obtain spectra with Δ=72 ps/ch. These spectra were analysed into four components. Corrections for positron annihilation in the source have been made.

2.3.2.Analysis with CONTIN (PALS-2) program [6,11,12]

In fact, in many cases, e.g. in polymers or porous materials an assumption of lifetimes distribution due to heterogeneity of the local environment in which positrons annihilate is more realistic. In these cases equation (2) is necessary to be replaced by integral,

$$C(t)=\int_0^\infty \lambda\,\alpha(\lambda)\exp(-\lambda t)\,d\lambda \qquad (3)$$

where $\alpha(\lambda)$ is the annihilation rate probability density function (PDF). The fraction of positrons annihilating with rates between λ and $\lambda+d\lambda$ is given by $\alpha(\lambda)d\lambda$ with

$$\int_0^\infty \alpha(\lambda)d\lambda=1 \qquad (4)$$

The necessary transformations for converting positron annihilation rate PDF to the corresponding lifetime, radius, and free volume PDFs are given in [6].

The computer program CONTIN, originally developed by Provencher [11] and modified by Gregory and Zhu [12,13,6] CONTIN (PALS-2) is widely used for the analysis of the positron lifetime spectra in heterogeneous materials. In CONTIN (PALS-2) PDF is obtained by using a reference spectrum of the specimen with a single well defined positron lifetime. In the present study, the lifetime spectrum of a well annealed and chemically polished Cu sample with τ=121 ps was used as a reference spectrum. The total counts of both sample and reference spectra were about 9 millions each.

We installed CONTIN(PALS-2) on our IBM 486DX PC using F77-EM/32 Fortran 77, ver.5.20 under DOS 6.2.

2.4. Doppler broadening of annihilation γ-line

The 511 keV annihilation γ-line was measured using a high purity germanium detector of energy resolution 1.17 keV at 514 keV γ-line of ^{85}Sr. Each spectrum, containing more than 10^6 counts was collected for 10^4 s. Eight spectra have been recorded for each pair of samples.

The annihilation γ-line was characterized with usual shape S and W-parameters. The S-parameter is defined as a ratio of the counts in the annihilation line central region ($0<|\Delta E|<0.933$keV) and the total counts number N_{tot} in the line. The W-parameter is the ratio of the counts in the annihilation line (2.33 keV$<|\Delta E|<$7.31 keV) wings and N_{tot} .

Liszkay et al. [14] suggested a method for data analysis which directly shows that the same vacancy defect can be present in a set of samples by checking the linearity of the S versus W parameter. Obviously, the method remains valid not only when positrons annihilate from the bulk state and only one defect state, but also when the annihilation take place in two distinct types of defects only. Furthermore, it is easy to be proved that the linear dependence between S and W parameters is valid also in the case of three distinct positron states provided that the relative intensities of two of them remain constant. In fact, the average value of S (W) parameter for a sample in which three definite states with relative intensities f_1, f_2, $f_3 = 1-f_1-f_2$ and $f_1=af_2$ (where a is a constant) exist, can be written as

$$S = af_2S_1 + f_2S_2 + (1-af_2-f_2)S_3$$
$$W = af_2W_1 + f_2W_2 + (1-af_2-f_2)W_3$$

where $S_1(W_1)$, $S_2(W_2)$, $S_3(W_3)$ are characteristic for respective states. By eliminating the fraction f_2, a linear dependence between S and W can be obtained. In the presence of four states, the linear dependence is possible if the condition $f_1:f_2:f_3 = a:b:c$, (a, b, c - constants) is valid.

Let we used the term "defect structure" to designate briefly the presence of a combination of several positron states in a sample, between the relative concentrations of which exist the above mentioned ratios. Then one can say generally that the linear relationship between S and W parameters exists for samples with the same defect structure.

3. Results and discussion

3.1.Results, obtained by POSITRONFIT EXTENDED program

Four component analysis of the PAL spectra have been done. The results are shown in table 2.

TABLE II. THE POSITRON LIFETIMES AND INTENSITIES OBTAINED BY POSITRON FIT EXTENDED PROGRAM

sample	τ_1(ps) I_1(%)	τ_2(ps) I_2(%)	τ_3(ps) I_3(%)	τ_4(ps) I_4(%)	(I_3+I_4) (%)
#1	198(4) 19.5(8)	439(3) 70.3(7)	2031(80) 8.2(6)	3708(329) 2.0(7)	10.2
#2	180(3) 26.4(9)	441(4) 67.0(7)	1469(83) 3.7(2)	7579(205) 2.8(1)	6.5
#3	174(3) 23.5(7)	431(3) 67.8(6)	1547(44) 6.24(15)	6267(166) 2.50(8)	8.74
#4	215(5) 29.9(2)	457(6) 61.8(1)	1695(85) 4.9(2)	6605(195) 3.3(1)	8.2
#5	195(4) 24.7(9)	433(3) 71.2(8)	1649(81) 2.8(1)	6853(308) 1.27(6)	4.07

As it is known from the studies by techniques other than positron annihilation [15], xerogels heat treated at 120°C consist of homogeneous regions of about 12 nm average diameter and pores of about 3.6 nm average diameter located in the free space left by the contact of those regions. It is believed that the samples heat-treated at 120°C contain a very large concentration of chemisorbed hydroxyls on the surface of the pores. Thermal treatment in the range 500-800°C desorbs these hydroxyls and decreases the pore diameter.

Taking into account the above, the first component $\tau_1 \approx$175-215ps is attributed mainly to p-Ps (singlet Ps) and free positron annihilation. We consider that the second component $\tau_2 \sim$ 430-450 ps is due to positron annihilation in vacancy type defect in the homogeneous regions of the samples. The last two components $\tau_3 \approx$1500-2000 ps and $\tau_4 \approx$3700-7500 ps, as it is commonly accepted, are due to o-Ps annihilation in the free volume holes with two different average sizes.

By the measurements of the Infrared absorption of samples #3 and #4 heat treated at 120°C and 850°C respectively, the presence of hydroxyl radicals in sample #3 was established by the appearance of 3650 cm^{-1} absorption band. By the comparison of $\tau_3(I_3)$ and $\tau_4(I_4)$ values for samples #3 and #4 (table 2), one can say that the difference between them is the somewhat smaller size of the largest holes and the increasing of the concentration of the smaller ones. The presence of the hydroxyl groups on the surface of the holes apparently has no influence on the positron annihilation in this case.

3.2. Results from data processing with CONTIN(PALS-2)

These results are consistent with results, obtained by POSITRONFIT EXTENDED program. Figure 1 shows as an example the positron annihilation rate probability distribution functions for samples #3 and #4 obtained by CONTIN(PALS-2) program.

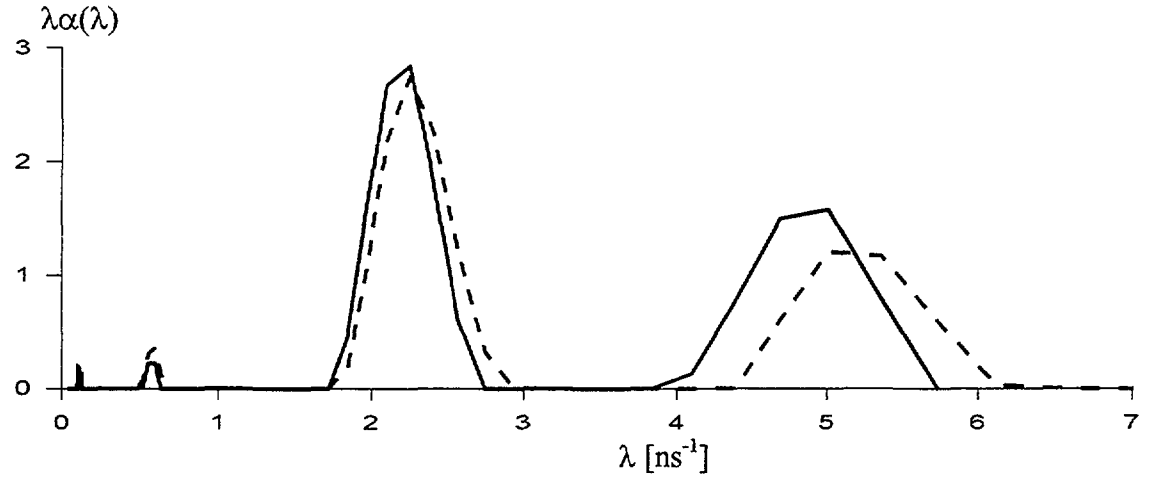

FIG.1. The positron annihilation rate PDFs for samples #3 and #4(----)

The shortest lifetime (longest annihilation rate λ) distribution is not very reliable since the lifetime resolution of ~ 260 ps of the spectrometer. The influence of this resolution on τ_3 and τ_4 is not significant [5,6].

A semiempirical equation between the measured o-Ps lifetime and the free-volume hole radius R has been obtained [16,17]

$$\tau = 1/2\ [1 - R/(R + R_w) + (1/2\pi)\sin(2\pi R/(R + R_w))]^{-1} \qquad (5)$$

where τ and R are expressed in ns and Å, respectively and R_w takes the value 1.656 Å.

Using the corresponding transformation formulas from [6] and equation (5), the radius and free volume PDFs were obtained from the Ps lifetime probability distribution function. The fraction of positrons, annihilating in cavities with radii between R and R+dR is f(R)dR, where f(R) is the radius PDF and is given by

$$f(R) = |2R_w\{\cos 2\pi R/(R + R_w) - 1\}\alpha(\lambda)/(R + R_w)| \qquad (6)$$

The free-volume PDF assuming a spherical cavity is $g(V) = f(R)/4\pi R^2$. The fraction of positrons annihilating in cavities with volumes between V and V+dV is g(V)dV.
The radius and free-volume PDFs are presented in Figures 2 and 3.

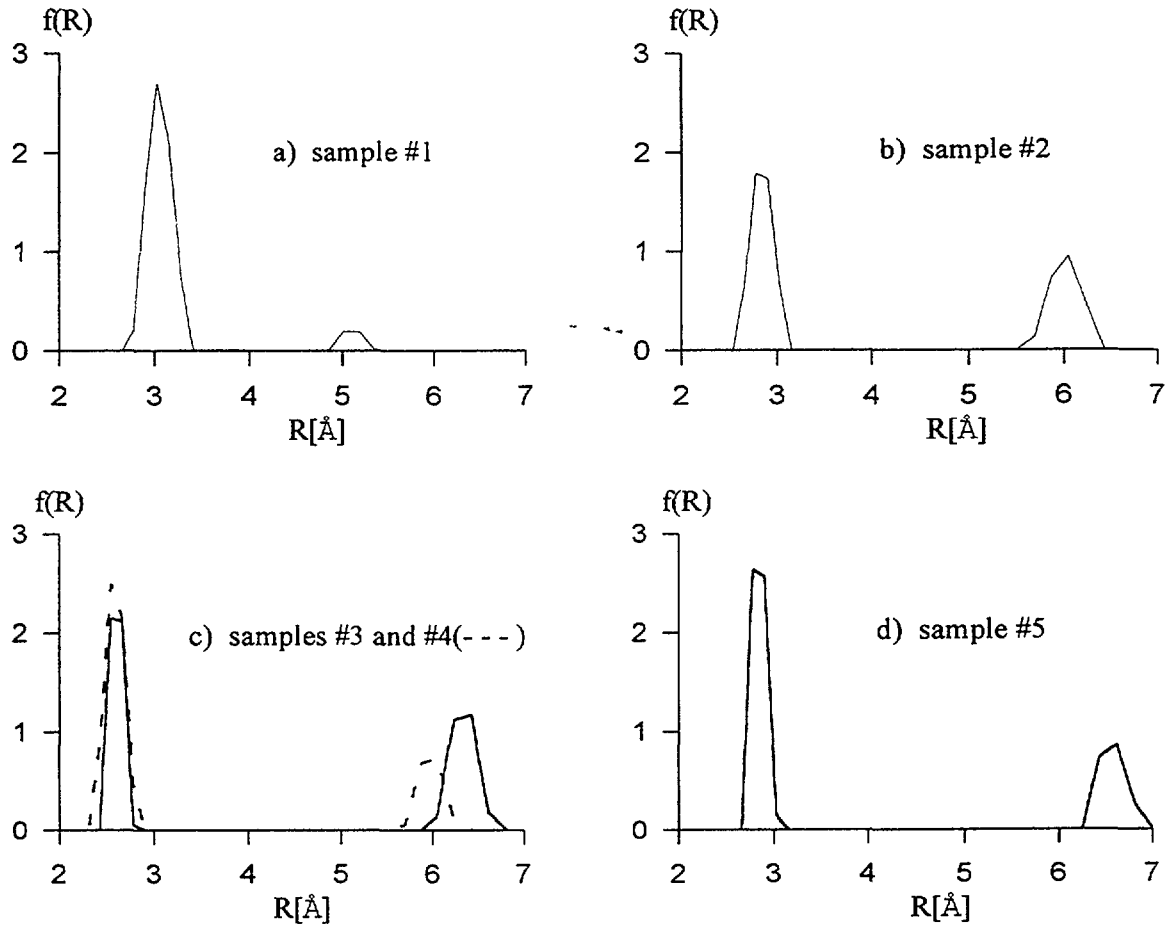

FIG. 2. Radius PDFs

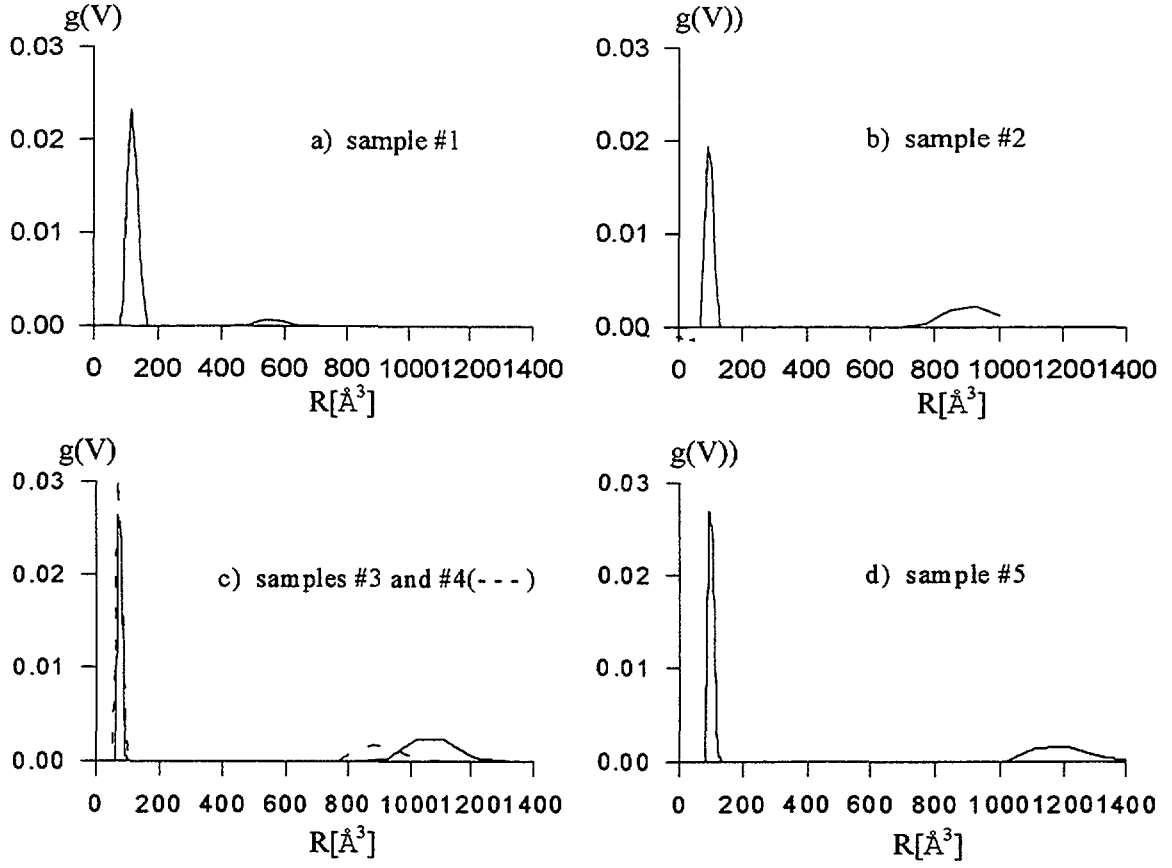

FIG. 3. Volume PDFs

Keeping in mind that the annealing of the samples at 850°C leads to (i) desorbtion of hydroxyls and (ii) decreasing of the pore size, from fig.2c and 3c one could conclude that (i) it seems that the water is located mainly in the smaller holes as the distributions of hole radius around 2.6 Å and corresponding volume for sample #4 are wider than for sample #3 and (ii) the main effect of the water in holes is to diminish their sizes.

3.3. Doppler broadening of annihilation line

The S parameter as a function of W parameter is presented in fig.4 As it can be seen, only the points corresponding to samples #1, #2 and #3 lie on the same straight line. So, only these samples have the same defect structure (see section 2.4). The experimental point for sample #5 lies near by the straight line whereas that for sample #4 is situated far away.

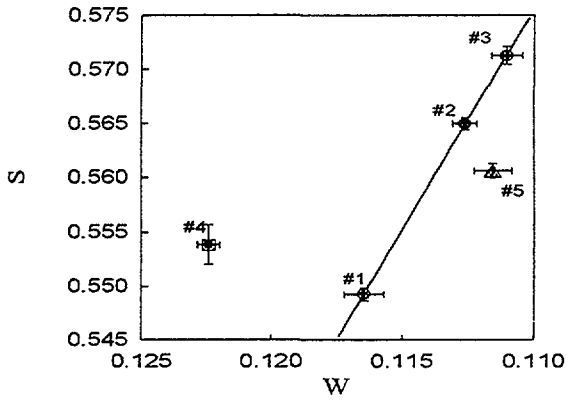

FIG. 4. Valence annihilation parameter S as a function of core parameter W

Taking into account data in table I, one can conclude that the defect structure seen by positrons is determined mainly by the heat-treatment of material. The molar content of TiO_2 has the minor effect on defect structure. The most "ideal" (the lowest concentration of defects) of the samples heat-treated at 120°C is sample #1 (the small value of R and small value of ethanol/alkoxides molar ratio). The concentration of defects is the highest in the sample #3 (large value of R).

The results from the study of Doppler broadening of the annihilation γ-line confirm the established fact [15] that the structure of the system $xTiO_2(1\text{-}x)SiO_2$ is determinated from the heat treatment, the molar ratios H_2O/alkoxides and ethanol/alkoxides.

Acknowledgments

This work is partially supported by International Atomic Energy Agency under Contract No.7567/R1/RB and Contract No.

We thank Dr. Provencher for sending users manual and Prof. Gregory for sending CONTIN (PALS-2) computer code

References

[1] L. Yang and G. You, J. Non-Cryst. Solids 100 (1988) 309.
[2].L.M.M.Salvado and J.M.F.Navarro, J.Matter Sci.Lett. 9(1990)173
[3].R.Ramani, P.Ramachandra, J.S.G.Ravichandram, G.Ramagopal, S.Gopal, C.Ranganathaiah, Appl.Phys. A60(1995)481
[4].H.Leidheiser Jr.,C.Szeles, A.Vertes, Nucl.Inst.Meth. A255(1987)606
[5].S.Y.Chuang and S.J.Tao, J.Chem.Phys.54(1971)4902
[6].R.Gregory, J.Appl.Phys.70 (1991)4665
[7].G.H.Dai, Q.Deng, J.Liu, H.Shi, C.M.Huang and Y.C.Jean, J. Phys.IV, Coll.C4, suppl. J.Physique II, 3(1993)233
[8].C.L.Wang and S.J.Wang, Phys.Rev.B51(1995)8810
[9].Y.C.Jean, Microchem.J.42(1990)72
[10] P.Kirkegaard et al., Comp.Phys.Comm. 23(1981)307
[11].S.V.Provencher, Comp.Phys.Comm.27(1982)229
[12].R.B.Gregory, in "Positron and positronium chemistry", ed.Y.C.Jean (World Scientific, Singapore), 1990, p.136
[13]..Gregory and .Zhu, Nucl.Instr.Meth.Phys.Res.A290(1990)172
[14].L.Liszkay, C.Corbel, L.Baroux, M.Bayhan, A.W.Brinkman and S.Tatarenko, Appl.Phys.Lett. 64(1994)1380
[15].F.Margaca, Report of the first RCM of Co-ordinated Research Programme on "Advanced Ceramic Materials Characterization using thermal neutrons",1994
[16].H.Nakanishi, S.J.Wang, and Y.C.Jean, in "Positron Annihilation studies of fluids", S.C.Sharma, ed.,World Scientific, Singapore, 1988,p.292
[17].Y.C.Jean, Mat.Sci.Forum, vols 175-178(1995)59

STUDY OF THE OXYGEN AND SUBSTRATE BIAS EFFECTS ON THE DEFECT STRUCTURE OF REACTIVE SPUTTER-DEPOSITED SnO_X FILMS

M. MISHEVA
Faculty of Physics, University of Sofia,
Sofia

N. NANCHEVA, P. DOCHEVA, P. HADJIISKA
Department of Physics, Technical University,
Rousse

N. DJOURELOV
Faculty of Physics, University of Sofia,
Sofia

D. ELENKOV
Institute of Nuclear Research and Nuclear Energy,
Sofia

Bulgaria

Abstract

The effects of oxygen and substrate bias on the defect structure of reactive sputter-deposited SnOx films were investigated. Samples were analysed using transmission electron microscopy (TEM), transmission electron diffraction (TED), X-ray diffraction (XRD) and positron annihilation spectroscopy (PAS). The oxygen played an important role in the film growth and surface morphology. TEM, TED and XRD showed that increasing of the oxygen partial pressure leads to the formation of films with different crystal phases. The void sizes also depended on oxygen partial pressure. The positron lifetimes and their relative intensities depended on the void concentration, the partial annealing of the vacancies and oxidation of SnO to SnOx. This investigation also showed that the mechanical strength of the films obtained at negative substrate bias is higher and the concentration of vacancy defects is smaller, than in the films prepared without substrate bias.

1. Introduction

In the recent years the research interest to SnO_X thin films has been renewed due to their industrial applications [1-7]. Specific uses have been found in liquid crystal displays, heated car windscreens, as a tool of ensuring mechanical reaction stability of glass bottles, transparent heat reflectors in sodium or incandescent lamps and as high quality optical elements [2]. Especially SnO_2 films are of great technological interest as transparent electrodes and as heat-reflecting filters, since in SnO_2 there is a high energy gap (3.6 eV) and it may possess high carrier concentrations [4,6].

The properties of deposited films are influenced by many factors which favour specific microstructures. Some of the most important factors affecting the microstructure of sputtered films are: kind and temperature of the substrate, rate of deposition of the condensing atoms, pressure of the working gas, substrate surface roughness, substrate bias and bombardment of the surface by ions or electrons. The changes in the film properties depend on the conditions of annealing, especially temperature range, time period and gaseous atmosphere (air, oxygen,

argon, vacuum, hydrogen). So, the properties of the films depend strongly on the preparation mode of and could vary considerably depending on the specific character of the technique used [7].

The present study is meant to contribute to the effect of oxygen and substrate bias on the defect structure of sputter deposited SnO_X films. The study was carried out using transmission electron microscopy (TEM), transmission electron diffraction (TED), X-ray diffraction and positron annihilation spectroscopy (PAS). Using PAS is provoked by the presence of point defects. Several studies have supposed that dislocations and vacancies play a major role in determination of the thin films properties (see, for example, refs. 8-13).

2. Experimental

2.1 Samples

The SnO_X films with thickness, d, of 1 μm, were deposited on tin plates of diameter 20 mm by d.c. reactive magnetron sputtering in argon-oxygen atmosphere at different oxygen partial pressures. The film thickness and deposition rate, v_d, have been measured during the deposition using a quartz oscillator MIKI FFM. The substrate temperature was not controlled during the deposition, but it was permanently <100 °C. The total pressure was kept constant ($P_{total}=8x10^{-3}$ mbar). Two kind of films were obtained-without substrate bias and at bias of -120 V. The source material was 99.99% pure tin. The samples were left to cool at room temperature after deposition before being removed from the vacuum system. Table I summarizes the deposition parameters of the samples studied. The last column in the Table I electric current was kept constant (I = 0.3 A). The films have been devided into four sets according to partial oxygen pressure.

TABLE I. DEPOSITION PARAMETERS OF THE SAMPLES STUDIED

	Sample	Bias [a] (V)	d [b] (μm)	P_{O2} x10^{-4} [c] (mbar)	O_2 [d] (mol %)	v_dx10^{-4} [e] (μm/s)	N, [f] (W)	Class [g]
Set I								
	1	0	1	5.0	6.2	18.0	90	A
	1*	-120	1	5.0	6.2	18.0		B
Set II								
	2	0	1	8.0	10.0	6.5	84	A
	2*	-120	1	8.0	10.0	6.5		B
Set III								
	3	0	1	11.0	13.7	0.7	75	A
	3*	-120	1	11.0	13.7	0.7		B
Set IV								
	4	0	1	14.0	17.5	0.4	78	A
	4*	-120	1	14.0	17.5	0.4		B

a) Substrate bias in volts
b) Sample thickness in microns
c) Oxygen partial pressure during deposition
d) Oxygen concentration
e) Deposition rate
f) Target sputtering power
g) Sample classification using the A/B scheme described in the text

2.2 X-ray, TEM and TED measurements

X-ray diffraction studies were performed using a URD6 (DDR) difractometer with monochromatic CuK_α radiation. The TED patterns were obtained by electron microscope ÝMB 100 Ë at accelerating voltage of 75 kV. The films for these measurements had been deposited on <100> oriented single KCl crystals and were detached from the substrate by dissolving KCl substrate in distilled water.

2.3. Positron annihilation

For positron lifetime measurements, two identical samples were used. $^{22}NaCl$ radioactive source, sealed between two thin (0.723 mg/cm^2) kapton foils, was sandwiched by the samples. The positron lifetime spectrometer used is based on a fast-fast type coincidence circuit and provides 260 ps time resolution (FWHM). The activity of the source was (13±1) μ Ci. About $1.2x10^6$ counts were collected for each spectrum. The samples were measured at least four times. The spectra have been analyzed by Positronfit Extended Program. The lifetime spectra were corrected for source lifetime components by the computer program LAYER, based on the Monte Carlo method [15, 16]. To get the net effect of the positron annihilation in the films, two types of lifetime measurements were done for positron incidences from the film side and from the substrate side of the samples ("face-to-face" and "back-to-back" case correspondingly).

In the back-to-back case only one positron lifetime is needed to fit the spectra. This lifetime, τ_3 , was kept constant in the face-to-face spectra processing with 3 lifetimes. To minimized the scattering of the results the ratio $(I_1+I_2)/I_3$ was fixed to the value obtained by LAYER for the fraction of positrons annihilating in the SnO_x films. All the samples were measured as-obtained except for the sample #1 (class A) which was measured twice, the second time after low temperature annealing.

In addition to the positron lifetime we have also measured the Doppler broadening of the 511 keV annihilation γ-line using a high purity germanium detector of energy resolution 1.17 keV FWHM at 514 keV gamma line of ^{85}Sr. Each spectrum, containing more than 10^6 counts was collected for 10^4s. Eight spectra have been recorded for each pair of samples.

The annihilation gamma line was characterized by the usual shape S and W parameters. The S parameter is defined as a ratio of the counts from the annihilation line central region ($0<|\Delta E_\gamma|<0.933$ keV) and the total counts number N_{tot} in the line. The W parameter is the ratio of the counts in the annihilation line (2.33 keV$<|\Delta E_\gamma|<$7.31 keV) wings and N_{tot}. S(W) parameter for the face-to-face case can be written as [17]

$$S = f\,S_{film} + (1-f)\,S_{sub}$$
$$W = f\,W_{film} + (1-f)\,W_{sub}$$

where f is the fraction of positrons annihilating in the film and $S_{film}(W_{film})$ and $S_{sub}(W_{sub})$ are characteristics of the film and the substrate respectively. As the film thickness is the same for all samples (f=const) we have not separated the S_{film} (W_{film}) from S(W). All conclusions based on S(W) values are valid for $S_{film}(W_{film})$ as well. By checking linearity of the S parameter versus the W parameter Liszkay et al [12] introduce a method for analysing data which directly show that the same vacancy defect could be present in all the films.

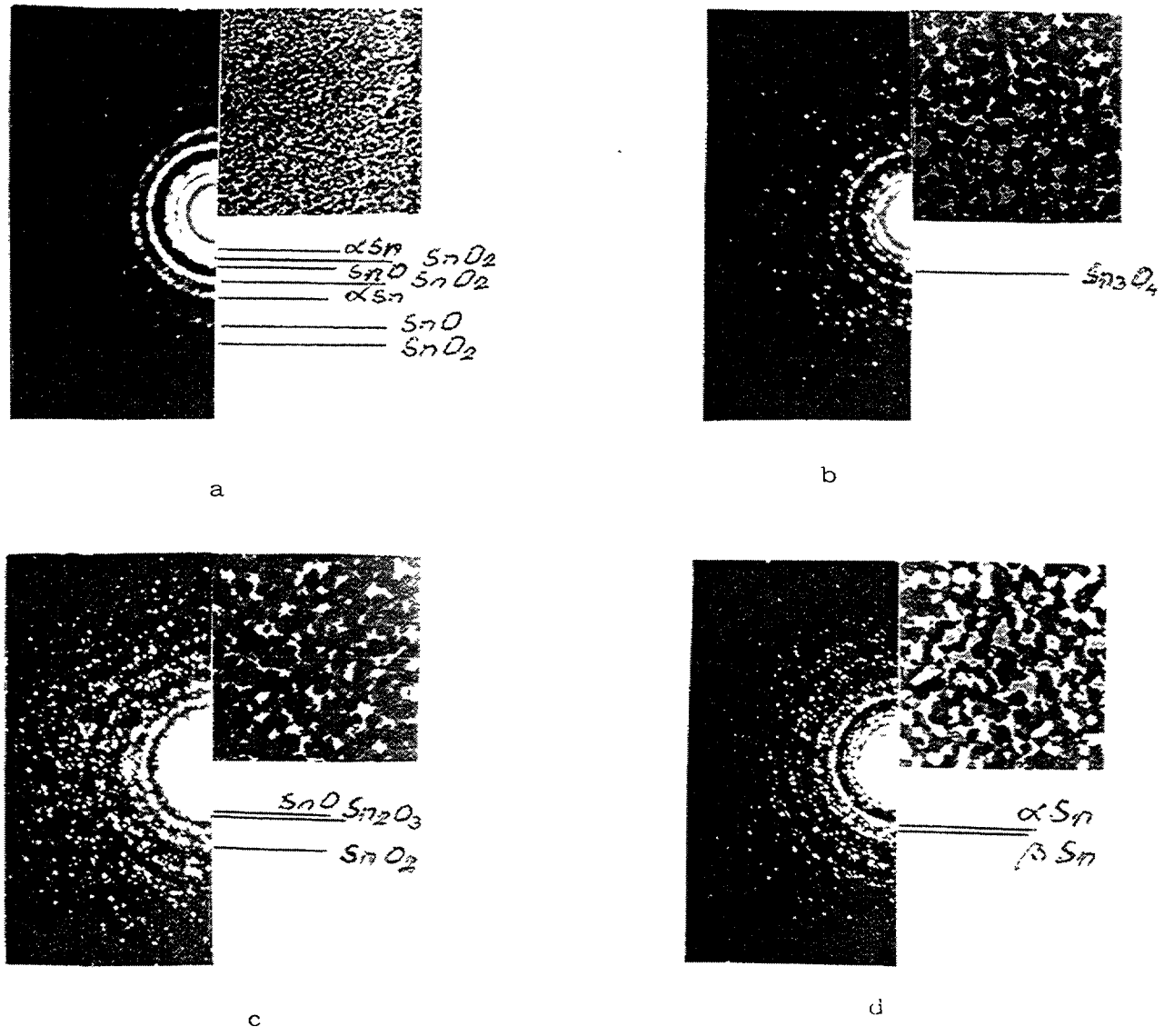

FIG. 1. TEM micrograps (magnification, x30000) and TED patterns of samples 1, 2, 3 and 4.

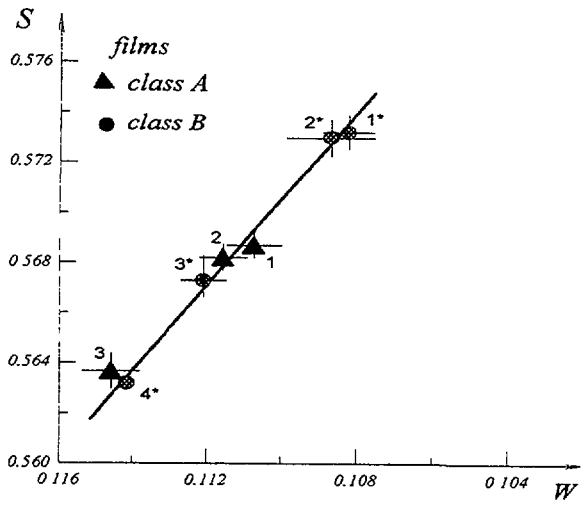

FIG. 2 Annihilation parameter S as a function of annihilation parameter, W, in vacuum d.c.magnetron sputtering thin SnO_x films

3. Results and discussion

Tin oxide films are usually composed of a mixture of different phases. The dominant phase depends sensibly on the deposition and/or annealing conditions. When the substrate is amorphous, the magnetron d.c. reactive sputtering technique usually leads to amorphous highly defective tin oxide films with α-Sn precipitates [6]. Variations in the substrate temperature T_S change the film structure from amorphous to crystalline [5]. The formation of SnO can be prevented by introducing oxygen during deposition. In our TEM studies the substrates have been <100> oriented single KCl crystals and SnO_X layers were polycrystalline.

3.1 TEM, TED and X-ray diffraction studies

i) Figure 1 a-d show TEM micrographs of films, deposited at different partial oxygen pressures. It is evident that oxygen plays an important role in the film growth as it was shown in [18]. The film surfaces, deposited at $P_{O2} = 5x10^{-4}$ mbar (Figure 1- a) indicate a very small-sized polycrystalline structure and a smooth surface. The surface morphology of film, deposited at $P_{O2} = 8x10^{-4}$ mbar (Figure 2- b) differs considerably from that one of the first type of films. They are homogeneous too, but the grain size is larger. TEM micrographs of films, deposited at $P_{O2} = 1.4x10^{-3}$ mbar shows a coarse grain structure (Figure 1-d).

In Figure 1 a-d the selected area of electron diffraction patterns are presented too.The major α-Sn, SnO and SnO_2 reflections have been identified. Diffraction data provide evidence for the presence of SnO_2 even at low oxygen concentration (6.2 mol % O_2). The Sn_2O_4 phase appears at partial oxygen pressure of $P_{O2} = 1.1x10^{-3}$ mbar (10 mol % O_2). The Sn_2O_3 phase is present in the films, obtained at $P_{O2} = 1.4x10^{-3}$ mbar (17.5 mol % O_2), while the β-Sn - phase appears only in sample 3 (13.7 % O_2).

The results from TEM and TED clearly show that increasing of the oxygen partial pressure leads to formation* of films of different grain size and a mixture of different phases. In the viewpoint of the rate of deposition, the high v_d leads to formation of small - sized structure, which is in accordance with other results.

ii) In general, X-ray diffraction studies do not allow to characterize structurally the films, because of their small thickness.

3.2. Positron annihilation lifetime (PAL) results

The PAL data for all of the samples studied are listed in Table II. For comparison, the characteristic lifetimes in Sn and SnO_2 are shown as well. In the "back-to-back" experiment only one lifetime component was found - $\tau = 204.0$ ps for samples class A and $\tau = 196$ ps for samples of class B. These values are close to the results for bulk lifetime in Sn [19,20]. In the "face-to-face" case three distinct lifetime components are necessary to fit the spectra with τ_3 fixed to the "back-to-back" value.

Only the lifetimes and their relative intensities, I_1 and I_2, for positron annihilation in the films are presented in the table.

The longer lifetime τ_2=1200-2000 ps is characteristic for pick-off annihilation of orthopositronium (o-Ps) the bound triplet state of electron and positron. As o-Ps can be formed only in comparatively large free volume holes [22] our results enable us to affirm that such large voids exist both in the films and in the interfaces between the films and their substrates and in both simultaneously.

The first lifetime τ_1=320-380 ps is considerably longer than the positron lifetime in the bulk of SnO_2 τ_b =220 ps (the results for sample 3, class A will be discussed below). Such long lifetimes are characteristic for annihilation of positrons trapped in mono- and divacancies. So,

TABLE II. PAS DATA FOR THE SAMPLES STUDIED ($\bar{\tau} = \sum_{i=1}^{N} \tau_i I_i$ IS MEAN POSITRON LIFETIME IN THE CORRESPONDING FILMS)

Sample	class	τ_1, ps	I_1, %	τ_2, ps	I_2, %	$\bar{\tau}$, ps
1	A	378(4)	84.89(4)	1960(39)	15.14(4)	617(8)
2	A	322(3)	90.55(2)	1792(55)	9.45(2))	460(6)
3	A	247(1)	94.87(4)	1197(67)	5.13(4)	296(4)
4	A	345(5)	92.86(9)	1432(162)	7.14(9)	423(14)
1*	B	319(5)	84.89(4)	1164(263)	15.11(4)	447(40)
2*	B	360(1)	97.52(2)	1346(295)	2.48(2)	409(8)
3*	B	365(5)	98.02(4)	1541(231)	1.98(4)	388(8)
4*	B	372(2)	97.59(2)	1857(288)	2.41(2)	408(8)
1 annealed for 75 min at t=130°C in air		218(5)	89(1)	1090(46)	11(1)	248(2)

Sn bulk	vacancy	
τ = 201 ps [19]	τ = 242 ps [19]	
199 ps [20]		
SnO_2		
τ_1 = 195 ± 10 ps	I_1 = 78.9 ± 6.3%	[21]
τ_2 = 463 ± 14 ps	I_2 = 21.2 ± 1.1%	

it could be considered that τ_1 is a mixture of at least three lifetimes - one due to free annihilation in the bulk of the films, second - due to annihilation of positrons trapped in mono- or divacancies and the third, of 125 ps, due to self annihilation of para-positronium (p-Ps the bound singlet state).

From the results shown in the table the following conclusions, concerning the quality of the films, could be made:

1. In both classes of the samples, the increase of the partial oxygen pressure leads to decrease of the concentration of the large voids (I_2 decrease). This decrease of the void concentration is accompanied by decrease of the void sizes (τ_2 decrease) in the samples of class A. This behaviour of the voids can be connected with the film grain sizes (Figure 1). Only sample #4 (class A) drops out from the above mention systematic. It is interesting to note that this film is the only one deposited after restoring the same experimental conditions in the vacuum chamber after opening. This is indicator for the well known sensitivity of the film structure relative to the strictly required experimental conditions of their preparation.

2. The void sizes in the samples of class B increase with the increase of the partial oxygen pressure (τ_2 increases).

3. The contribution of trapped positron annihilation in τ_1 decreases in the samples of class A (τ_1 decrease) with increasing of the P_{O2}.

4. Taking into account the relatively large contribution (about 5%) of p-Ps annihilation in τ_1 for sample #1*, class B, which caused a considerable decreasing of τ_1 it can be consider

that the kind of vacancies able to trapped positrons in all samples of class B is the same (τ_1 is almost independent of P_{O2}).

5. The small value of τ_1 for sample #3, class A, the most probably is connected with the presence of β-Sn phase in the film (see section 3.1).

6. The changes of lifetimes and their relative intensities after annealing of sample #1, class A, (see table 2) can be explained by the decreasing of void concentration, the partial annealing of the vacancies and oxidation of the SnO to SnO_2. The last statement is based on the proximity of τ_1 to the value of bulk lifetime of positrons annihilating in SnO_2. Of course, the value of τ_1 remained larger than that required from the trapping model [23]. This is due to incomplete annealing of the vacancies in the film.

3.3. Doppler broadening of annihilation line

The S-parameter as a function of the W-parameter is shown in Figure 2 As can be seen all experimental points fit well to straight line of slope R=1.7±0.1. According to [12] if the measured (S_{film}, W_{film}) values in the different films lie on the same straight line on the (S, W) plane, the types of the defects in the samples are similar.

Our results show that the mechanical strength of the films obtained at negative substrate bias is higher, the adhesion of films to substrates is higher and the concentration of vacancy defect smaller than in films prepared without substrate bias. This is due to ion bombardment of the films during their deposition.

Acknowledgements

This work has been supported in part by International Atomic Energy Agency, Vienna, under contract number 7567/R1/RB and NFSR Bulgaria, under contract number F486.

References

1. E. Leja, T. Pisarkiewicz and A. Kolodziej, Thin Solid Films, 67, p. 45 (1980)
2. H. De Waal and F. Simonis, Thin Solid Films, 77, p. 253 (1981)
3. P. Grosse and F. J.Schmitte, Thin Solid Films, 90, p. 309 (1982)
4. J. Geurts, S. Rau, W. Richter and F. J. Schmitte, Thin Solid Films, 121, p. 217 (1984)
5. D. Das and R.Banerjee, Thin Solid Films, 147, p. 321 (1987)
6. F.C.Stedile, B.A.S.De Barros,Jr., C. V. Barres Leite, F. L. Freire, Jr., I. J. R. Baumvol and W. H. Schreiner, Thin Solid Films, 170, p. 285 (1989)
7. L.I. Popova, M. G. Michailov and V.K.Georgiev, Thin Solid Films, 186, p.107 (1990)
8. R.L. Frost, A.B.Dewald, M.Zaluzec, J.M.Rigsbee, B.Nielsen and K.G.Lynn, J. Vac. Sci. Technol., A8, 4, p.3210 (1990)
9. C.Lopez Gil, M.F.Ferreira Margues, A.P. de Lima, M.T.Vieira and A.Cavaleire, Materials Science Forum, vols. 105-110, p.1137 (1992)
10. J.P.Schaffer, A.J.Perry and Brunner, J.Vac.Sci.Technol., A10, 1, p.193 (1992)
11. J. Brunner, A.J.Perry, J.P.Schaffer and W.D.Sproul, Materials Science Forum, vols.105-110, p.913 (1992)
12. A.Liszkay, C.Corbel, L.Baroux, P.Hautojarvi, M.Bayhan, A.W.Brinkman and S.Tatarenko, Appl.Phys.Lett.64, 11, p.1380 (1994)
13. N.Nancheva, P.Docheva, N.Feschiev, M.Misheva and N.Djourelov, Scripta Metallurgica et Materialia, vol.33, 4, p.575 (1995)

14. P.I.Docheva, PhD Thesis, Technical University, Russe (1991)
15. R.B.Gregory and W.Su, Nucl.Instr.Meth. in Phys. Res., B62, p.1 (1991)
16. R.B.Gregory and W.Su, Mat.Sci.Forum, vols.105-110, p.1875 (1992)
17. K.Saarinen, P.Hautojarvi, J.Keinonen, E.Rauhala, J.Raisanen and C.Corbel, Phys. Rev.B43, 4249 (1991)
18. K.Suzuki and M.Mizuhashi, Thin Solid Films, 97, 119 (1982)
19. K.P.Gopinathan, World Scientific Publ. Co. Pte. Ltd. Singapore, p. 527 (1985)
20. M.A.Monge and J. del Rio, J. Phys.: Cond. Matter, 6, p. 2643 (1994)
21. M.Bertolaccini, A.Bisi, S.Gambarini and C.Zappa, J.Phys.C: Solid State Phys., vol.4, 734 (1971)
22. H.E.Schaefer, R.Wurschum, R.Birringer and H.Gleiter, Phys.Rev.B38,14, 9545 (1988)
23. A.Vehanen, P.Hatojarvy, J.Johansson, J.Jli-Haupala and P.Moser, Phys.Rev. B(1982)762

LATTICE DYNAMICS OF CUBIC Cs_2NaLnX_6 AND $CsNaLn_{1-x}Ln'_xX_6$ ELPASOLITES

R. ACEVEDO, V. POBLETE, R. ALZAMORA, R. VENEGAS,
G. NAVARRO, C. HENRIQUEZ
University of Santiago,
Santiago, Chile

Abstract

Crystal lattice dynamics of stoichiometric Cs_2NaLnX_6 and nonstoichiometric $CsNaLn_{1-x}Ln'_xX_6$, $0.01 \leq x \leq 0.10$, Ln and Ln′ are trivalent positive lanthanide ions and X is chlorine or bromine, were studied. Phonon dispersion relations were computed for similar compound, Cs_2UBr_6, and vibronic absorption spectra with reduced number of required input parameters are considered on the basis of proposed model.

Aims

Many different attepts to rationalize the spectral intensities in pure and doped crystals containing lanthanide ions, having essentially octahedral sites, have been undertaken in recent years.

Elpasolites, of the general stoichiometric structural form Cs_2NaLnX_6 and non-stoichiometric $CsNaLn_{1-x}Ln'_xX_6$, where $0.01 \leq x \leq 0.10$, Ln and Ln' are trivalent positive lanthanide ions, and X is chlorine or bromine, are of both scientific and technological interest, due to their luminiscence properties. Studies of these compounds are particularly complex, due to the complexity of the spectroscopic bands and possible transitions modes (radiative, nono radiative, thermal assisted, etc.). They involve:

1. Synthesis and structural characterization of these elapsolites [1], implying X-ray diffraction and (Bragg) neutron diffraction. Single crystal synthesis is controlled by XRF and TR-XRF, etc.
2. Spectroscopic characterization of elpasolites. This stage implies IR spectroscopy, FT-IR, Luminescence and two photon Absorption Spectroscopy.
3. Theoretical studies of spectra, an intrinsically complex stage, because of the complex nature of the emission absorption processes involved. This studies will address the following subjects:

a) Pure (stoichiometric) crystal lattice dynamics.
b) Force Field simulation, to include crystal lattice short range interactions.
c) Computation of the phonon dispersion relations and of the form of vibronic spectra.

Neutron inelastic, scattering data, from diffuse scattering experiments (could be made at our laboratory) and cocherent inelastic experiments (only in collaboration with foreign laboratories) on stoichiometric and non stoichiometric compounds.
Studies of the role of vacancies and structure of non stoichiometric doped elpsolites. Non stoichiometric compounds are of particular relevance to available experimental facilities at NCLR. Vacancies will certainly have a role in controlling dynamics and electronic excitation processes.

Previous work

Crystal dynamics on non doped crystal lattices. For these purposes, short and long range interactions have to be considered explicitely.

For long range interactions, the Ewald method will be used. This method is based on the introduction of a gaussian distribution for positive and negative charge, which leads to lattice interactions with a potential energy in the reciprocial space $\Phi^{(G)}$ and - $\Phi^{(G)}$, such that the Coulomb potential takes the general form:

$$\text{EWALD:} \quad \Phi^{(C)} = \Phi^{(G)} + \left[\Phi^{(C)} - \Phi^{(G)}\right] = \Phi^{(C)} + \Phi^{(H)} \qquad (1)$$

Assuming this expression, the long range Coulomb contribution to the dynamic matrix given by:

$$g_N g_M e^2 C_{\alpha\beta}\left(\begin{smallmatrix}\vec{k}\\ NM\end{smallmatrix}\right) = \sum_{l'} \Phi^{(C)}_{\alpha\beta}\left(\begin{smallmatrix}ll'\\ NM\end{smallmatrix}\right) e^{i\vec{k}\cdot\vec{r}_{NM}} \qquad (2)$$

$\alpha, \beta = X, Y, Z$

may be decomposed into two series, one running over the direct space (N^H related to the potential $\Phi^{(H)}$ above) and other one running over the reciprocial space (N^G related to the potential $\Phi^{(G)}$ above). In equation 2, q_N reffers to the *n*-th atom's charge in the *l*-th unit cell, k is wave vector and α=X,Y,Z. In the most of the published works the gaussian half width n in eq. 2 is commonly chosen to insure simultaneous convergence on both, reciprocal and direct spaces. This mathematical criteria may lead to a different number of gaussians in the reciprocial space compared to the number of those in the direct space. This fact is of primary importance, because it may introduce a charge desequilibrium in the lattice, otherwise it is neutral. We [2] have developed a convergency test, requiring the gaussian half width to be adjusted, so that crystal charge desequilibrium is precluded. A computation algorithm has been devised to naturally force the lattice charge neutrality, being it of enough generality and flexibility to be used for computations on stoichiometric and non-stoichiometric elpasolites, such as those presented above [2, 3].

Crystal lattice short range interactions. Another sizeable problem consists on the simulation of a force field, as a means to introduce the short range interactions in the crystal lattice. For this purpose, we have developed a mixed Urey-Bradley force field and valence force field (UBFF-GVFF). This formalism allows us to introduce a variety of interactions, between directly and indirectly interacting nuclei, belonging to different unit cells and different coordination spheres on the reference unit.

On the same line, we have progressed on the understanding of the spectroscopical assignation for k=0. Here, the potential, related to internal vibrations and to their interactions, is considered under the fundamental assumption of no time phase difference between unit cells. The method of compatibility tables requires the knowledge of the site and space symmetry group and number of molecules per unit cell. Identifying the point group at which the molecules or ions belong, their vibrational behavior in the crystal can be determined, relating the point group symmetries with those of the site symmetry group occupied by such molecule or ion.

Cs_2UBr_6 - $Fm3m\text{-}O_h^5$

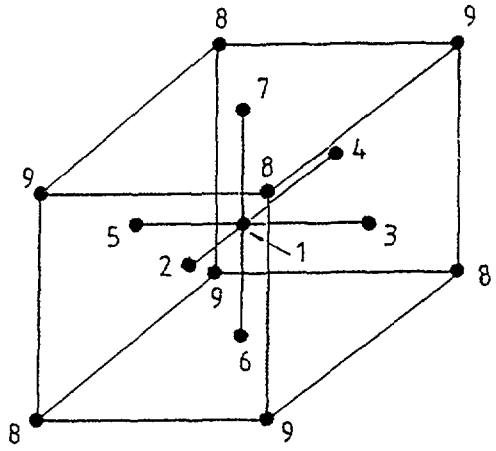

- $UBr_6^{2-}\cdot Cs_2^{+}$

- $Ca^{2+}\cdot F_2^{-}$

1: U

2 - 7: Ba

8,9: Cs

1^{st} $BZ\text{-}O_h^5$

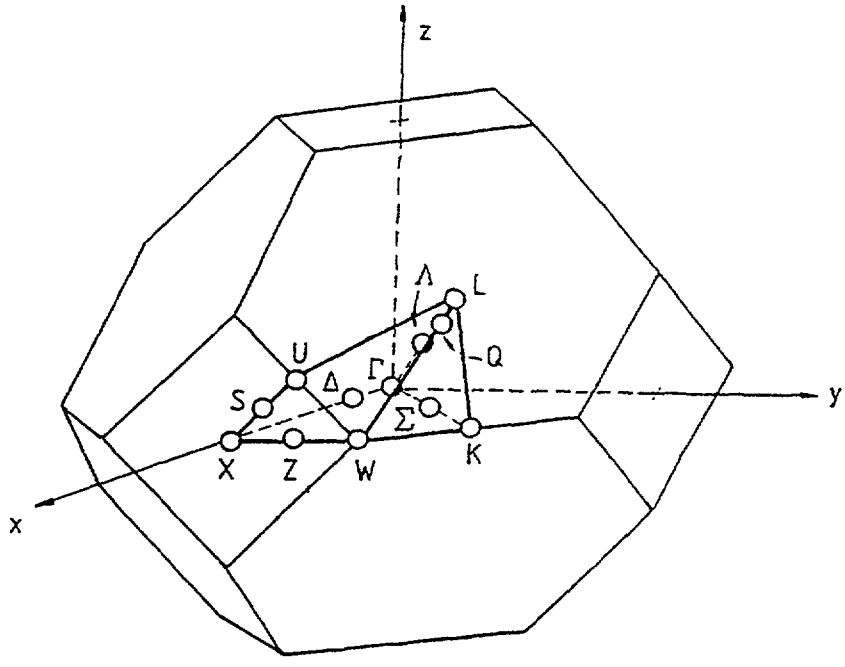

FIG. 1. Structures of the O_h^5 *crystals.*

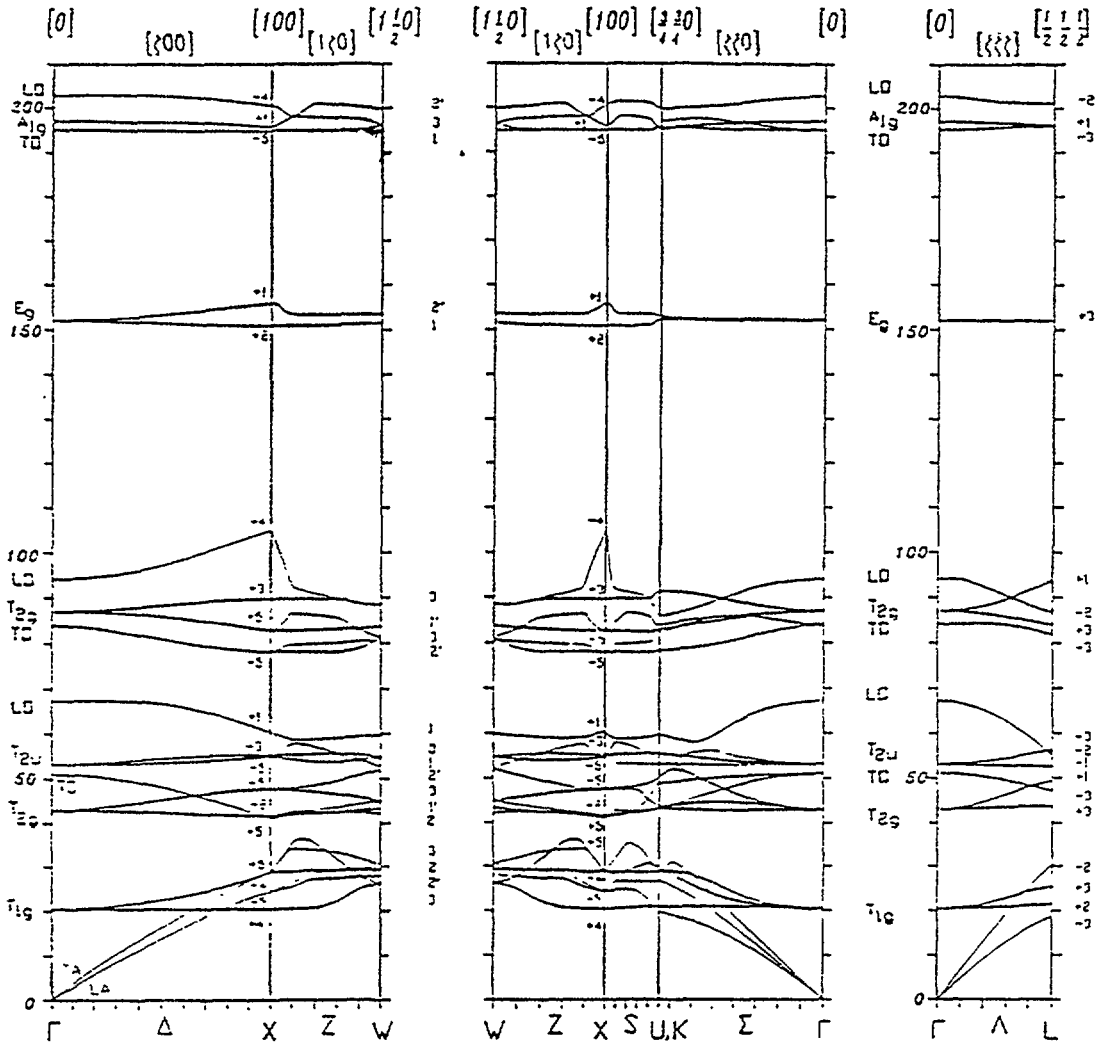

FIG. 2. Phonon dispersion relations for Cs_2UBr_6 [3].

In the case of stoichiometric elapsolites of the type Cs_2NaLnX_6, determination of the symmetry species at which different ions belong, and consequently their IR and/or Raman activity, is immidiate. In our case, the identification is as indicated.

Phonon dispersion relations and vibronic absorption spectra. Phonon dispersion relations have been computed (2) for similar compounds (Cs_2UBr_6) as well as vibronic absorption spectra, with a reduced number of required input parameters, and higher quality on the comparisson of predicted and experimental results (Figures 1 and 2). Analysis of neutron scattering data will be fundamental as a further test for our model computations.

References

[1] R. Acevedo, V. Poblete; Synthesis and X-ray powder diffraction study of the alpasolite Cs_2NaCeC_{16}", Powder Diffraction 10 (2) June 1995.

[2] E. Cortés; "Vibronic Coupling and spectral intensities of the Cs_2ZrBr_6:UBr_{62}- and crystal dynamics for the Cs_2UBr_6", Ph.D. Thesis, University of Chile, Chemistry Department

[3] B. Acevedo, E. Cortés, V. Poblete and P. A. Tanner; "Lattice Dynamics and phonon dispersion curves for the system Cs_2UBr_6: a symmetrized force field", in print.

TIME PULSE PROFILES ON A NEW DATA ACQUISITION SYSTEM FOR NEUTRON TIME OF FLIGHT DIFFRACTOMETER

R. VENEGAS, L. BAEZA, G. NAVARRO
Comision Chilena de Energia Nuclear,
Centro Nuclear de La Reina,
Santiago, Chile

XA9949660

Abstract

A new differential acquisition system was built for a neutron diffuse scattering instrument. We analyze the time, space and velocity behavior of neutron pulse profiles, which can be obtained in a neutron diffuse scattering system of this nature, consisting of a black disc slit chopper and a circular detector bank, in order to design accurate scattering data analyzing methods. Computed direct pulse time spectra and measured spectra show statisfactory agreement.

1. Introduction

Diffuse scattering of neutrons by solid samples using wavelengths longer than Bragg scattering may be used as a tool for examining long range ordering, or defect structure. Whether Bragg scattering is a main tool for a description of the average unit cell of the crystal, the analysis of diffuse (incoherent) scattering is useful to obtain information concerning departures from this average structure, and in special case, for the analysis of inelastic scattering cross sections on solid systems. Many studies using incoherent elastic scattering and inelastic scattering of neutrons on solid and liquid systems have been performed on neutron spectrometers based on simultaneous analysis of neutron velocity and scattering angle, having a similar design to the instrument we discuss here. The neutron beam for this spectrometer is provided by a 5 MW MTR light water reactor at the La Reina Nuclear Center labaratories. Beam flux from this type of reactor is low, and the data acquistion system must be very efficient to collect most of the information in short operating runs.

Two problems associated to this kind of instruments are 1) the need of sufficient counting statistics to have a reasonable signal/noise ratio and b) the eventual mixing of elastic and inelastic scattering. While the first problem can be reduced by an appropriate design and optimisation of the data collection system to obtain the best performance when using a given of sufficiently low energy, the instrument may serve the purpose of inelastic scattering experiments. By the contrary, when the inelastic transitions occur outside the instrument range of Q values available for observation, a situation that is not uncommon, the instrument allows the observation of elastic scattering.

Here, after a brief reminder of the instrument details, we describe an optimised data acquisition unit which was built with the purpose of a simultaneous time differential analysis on every angular position available, in order to obtain the maximum possible data collection capability during operation time. Besides, a stopping motor computer controlled sample changer has been built, to allow the accurate (better than 0.05 mm error in position responsability) change of a minimum of 4 samples, required for calibration during each measurement run. Differential time profile has been measured for $\theta = 0^o$. The agreement between computed and observed time profile for $\theta = 0^o$ shows that the instrument is reliable for the study of differential neutron scattering cross sections.

2. The "Glopper" diffuse scattering time of flight apparatus

Figure 1 shows the schematic presentation of the diffuse scattering instrument at CEN-LA Reina. This consists of a polycrystalline Bi-Be filter, followed by a Fermi type "parallel beam-axis" chopper, sample changer and holder, two U fission chamber monitors and a radial detector bank.

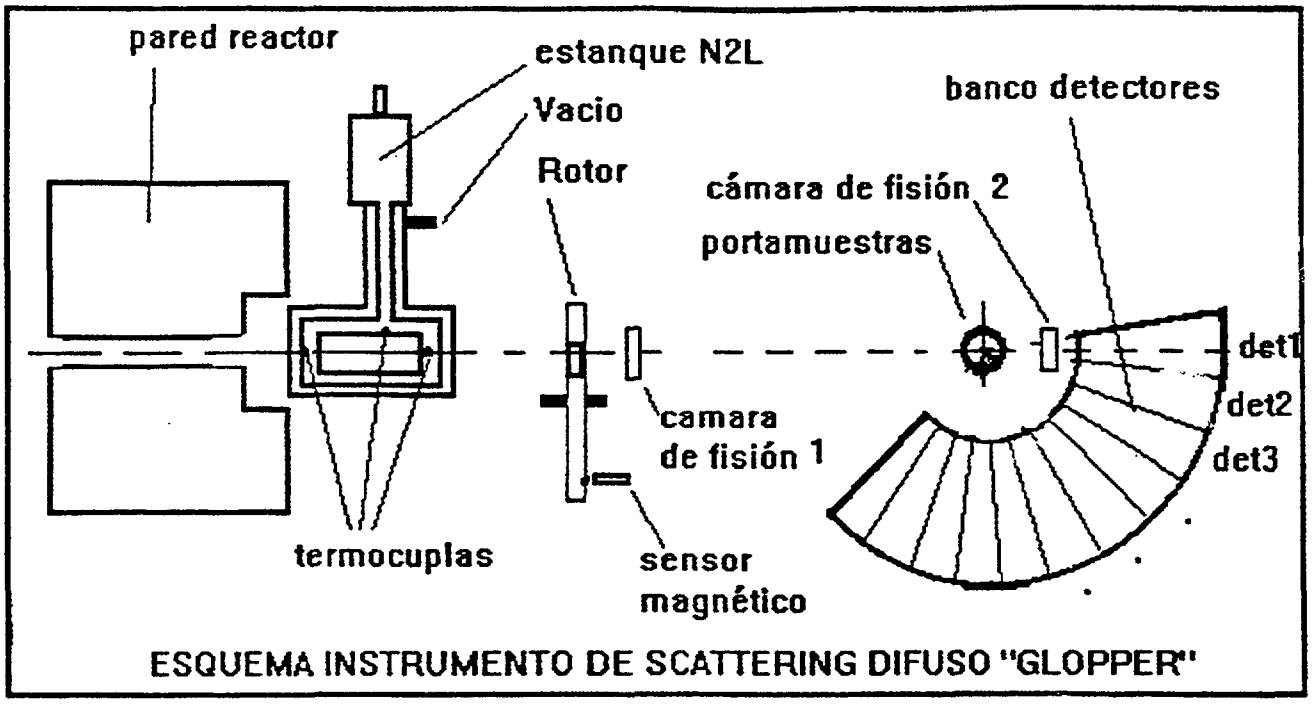

FIG. 1. Shematic presentation of the diffuse scattering instrument "GLOPPER" at the CEN-La Reina (Chile)

The Be filter removes neutron wavelengths with $\lambda \leq 3.99$ Å (removing neutron energies above 5 MeV, or velocities above 1 m/μSec) and the Bi filters decreases the γ ray contents. The filter is cooled at liquid nitrogen temperature to avoid neutron intensity reduction inside the crystal due to inelastic scattering. The chopper is a thermal neutron absorber rotor disc fitted inside of an aluminium casing with six regularly spaced 2cm x 2cm square apertures oppening near the disc border, to pulse the beam. The disc rotates at a nominal speed of 3000 RPM, and a pulse repetition time of 1.67 mSec at a distance of 1.6 m from the chopper disc (Figure 2). A coil pick up generates magnetic trigger signal from the passage of a steel pivot placed at an accurate distance from each rotor window. The time of flight detector bank consists on a multiple He detector assembly, each detector mounted vertically, placed inside of a shielding case and spaced regularly on a circle sector of 1 m radius. Two monitoring fission chambers are placed, one after the chopper tube aperture and one at the front position on the detector bank, to monitor the beam before and after air/sample scattering.

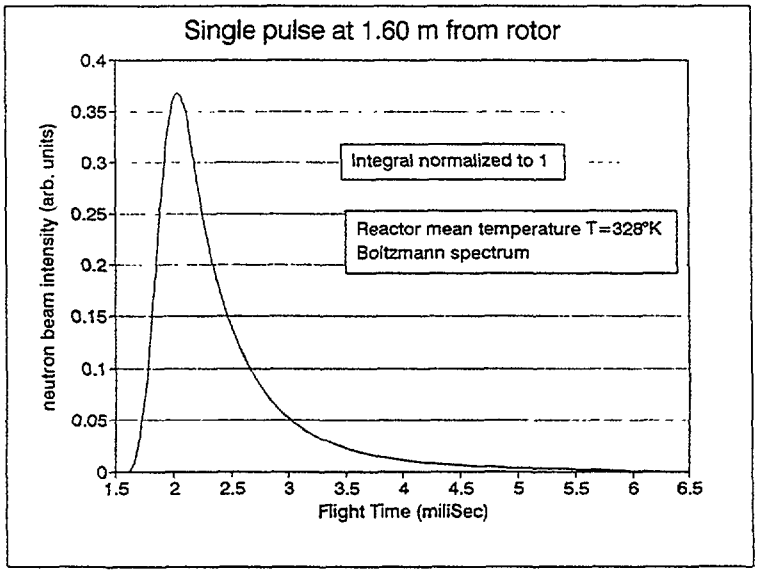

FIG. 2. Single pulse at 1.60 m from rotor

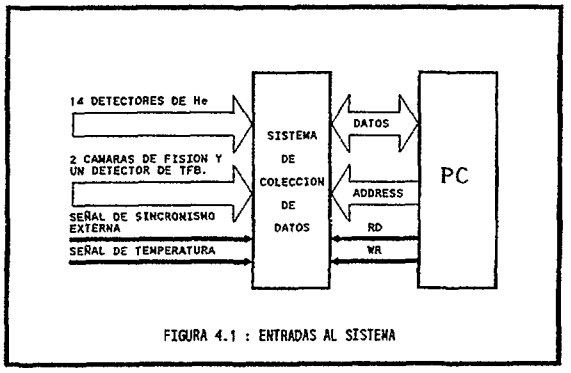

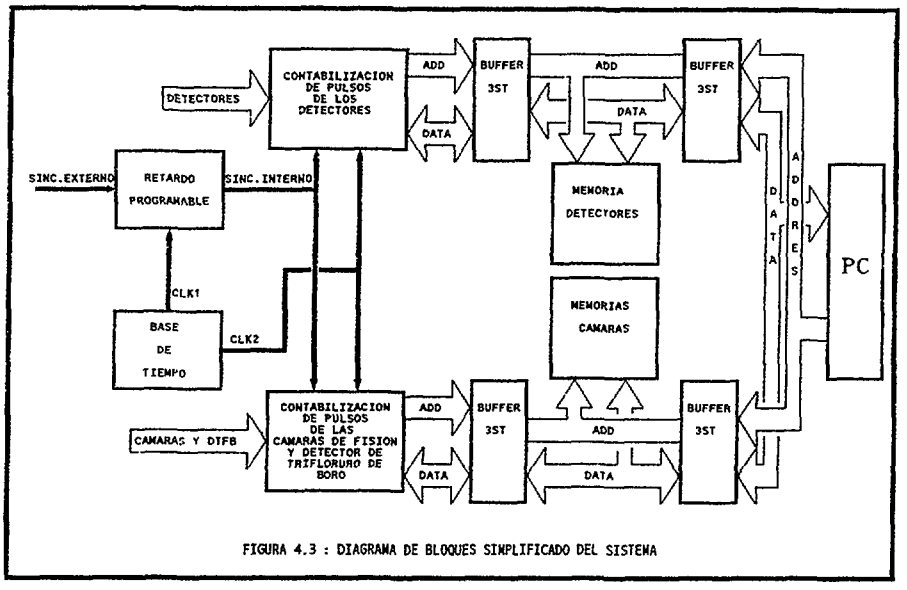

FIG. 3. Schematic diagrams of data acquisition for neutron time of flight diffractometer.

2. 1. Time of flight data analyzing system

The designed time of flight analysis system essentially consists of a mixer-router with two address generators and a memory increment unit: the time channel address generator (higher address bits) provides the detector identifying capability. The memory increment unit increments by one the contents of a memory address built from the timing and detector channel information.

The address generator was designed to start a time measurement sweep after each trigger under program control in increments of 1μSec up to 2.56 mSec. In order to substract and adjust the sum of the pulse flight time offset due to the distance of the window to the position detector. Software selectable dwell times are 5, 10 and 20 μSec for a total of 128 time channels for each detector. This scheme allows the analysis of 0.64 , 1.28 and 2.56 mSec time span.

Counting data rates are sufficiently low (from 0.1 to 10 counts per second) to insure negligible probability of detection event collision. However, two independent analyzing units were built in, one for the off axis detectors and another for the on-axis detectors, in order to avoid data contemption between low frequency counting detectors at the off axis positions and the higher frequency data rates observed at on-axis detectors (fission chambers and front channel detector). This avoids competition between relatively different counting rate channels requesting acces to a single memory addressing and increment unit, which would lead to an indesirable variation in the relative counting ratios on the off axis counters.

The analyzer is packaged in a single circuit board and communicates with a PC Compatible via I/O ports and standard AT-Bus for operation, control and memory data transfers. The operation is transparent for the computer, and communications are based on a master-slave protocol. A detailed block diagrams (Figure 3) are available on request.

3.Neutron Pulse Profiles

We consider here a square section beam tube and a square slit window openning, cut out near the border of the neutron absorbing chopper disc. Distances are measured from the origin at the rotor position towards the sample and the detector bank. The chopper turns at constant angular velocity ω. Under these assumptions, the neutron flux at distance $d = 0$ must have a triangular time profile, as depicted in Figure 1. We call τ_p the total opening time of the window. Obviously, τ_p depends on the chopper disc angular velocity, the window width l_w and the radius of the window center position:

$$\tau_p = \frac{l_w}{\omega r} \tag{1}$$

The neutron pulse time profile at $d = 0$ is resulting from the continuous superposition of neutron group pulses of different velocities, because of the polychromatic nature of the filtered reactor beam. At this position, the velocity spectrum will obviously be the same as the incoming spectra.

At every instant, each velocity pulse component must have a triangular time and space intensity profile $n_v(x,t)$, given by the expression:

$$n_v(x,t) = S_v T_v(x,t) = S_v T(x-vt) \tag{2}$$

where S_v is the beam flux of neutrons with velocity v and $T_v(x,t)$ is a triangular profile function, normalized to $T_v(x,t) = 1$ at its maximum.

3. 1. Velocity spectra

In principle, this function could be obtained from a time of flight experiment as we discuss below. This spectrum function must be normalized, so that

$$K\int_{v_{min}}^{v_{max}} S(v)dv = 1 \tag{3}$$

where K is the normalization constant; hence, the normalized $S(v)$ function is $S(v) = \frac{1}{K}S(v)$. For a rough thermal neutron spectra description, assumming neutrons in equilibrium with a moderator at temperature T, $S'(v)$ can be approximated by the maxwellian distribution:

$$S'(v)dv = \frac{4}{\sqrt{\pi}}\frac{v^3}{(\frac{2kT}{m})^{3/2}}e^{-\frac{v^2}{(\frac{2kT}{m})}}dv$$

where k is the Boltzman constant and m is the neutron mass.

3. 2. Monochromatic intensity profile

The normalized triangular profile function for the neutron pulse of velocity v, can be written as:

$$T_v(x,t) = 2(\frac{x}{vT_p} - \frac{t}{T_p} - 1)\left(h(x - vt - vT_p) - h(x - vt - \frac{3}{2}vT_p)\right)$$

$$-2(\frac{x}{vT_p} - \frac{t}{T_p} - 2)\left(h(x - vt - \frac{3}{2}vT_p) - h(x - vt - 2vT_p)\right) \tag{4}$$

where $h(x)$ is the Heaviside step function, and $T_v(x,t)$ is written in terms of the monochromatic neutron group velocity v and the window aperture time τ_p. This pulse is placed behind the chopper window at t=0.

The monochromatic pulse intensity profile can not change its form during its travel towards the sample (however, some scattering may occur during its travel, which we will neglect now, but has to be taken into account for instrument calibration). If the interaction with the sample is only elastic, it will diffuse changing only its wavevector direction, so that the triangular intensity form will also be conserved after elastic diffuse scattering. As a result, the redially scattered pulse changes only its intensity as a function of the diffusion direction.

The profile function shown in eq. 4 is normalized in the sense that its maximum value will be 1; note also that $T_v(x,t) = 0$ only within the space interval $[v(t_0\text{-}T), vt_0]$ for every instant t_0 and position x_0. This function allows then the representation of the monochromatic triangular pulse profile for every instant t after the window openning and for every distance d measured from the chopper position. The time width of the pulse is allways T_p and its space width is vT_p.

3. 3. Pulse Intensity Profiles

The time intensity profile of the neutron pulse at a certain distance may be obtained by superposition of the individual velocity components. In general, the number of neutrons at distance x and instant t will be characterized with where v_{max} and v_{min} are the maximum and minimum velocities contained in the polychromatic pulse. That for computation purposes, we can suppose finite (v_{max} corresponds to the filter cut-off velocity at minimum wavelength and v_{min} is given by resonable lower limit, considering the probability per unit time).

The time profile at a definite position x may be described by:

$$N_x(t) = \int_{v_{min}}^{v_{max}} n_v(x,t)dv = \int_{v_{min}}^{v_{max}} S(v)T_v(x,t)dv = \int_{v_{min}}^{v_{max}} S(v)T(x-vt)dv \qquad (5)$$

as well as the space profile at some instant t:

$$N_t(x) = \int_{v_{min}}^{v_{max}} n_v(x,t)dv = \int_{v_{min}}^{v_{max}} S(v)T_v(x,t)dv = \int_{v_{min}}^{v_{max}} S(v)T(x-vt)dv \qquad (6)$$

The instantaneous spectrum, *i. e.* the instantaneous distribution of neutron intensities as a function of velocity at a given distance before diffusion at the sample, is given by $N(x,t) = S_vT(x\text{-}vt)$, where the contributing velocity groups at any time $\frac{x}{v_{max}} \geq t \geq \frac{x}{v_{min}} - T_p$ are those with velocities in the range $\left[\frac{x}{t-T_p}, \frac{x}{t+T_p}\right]$.

Figure 2 shows the time pulse profile computed for a 1.60 m distance, using expression 5 considering a maxwellian velocity spectrum. This spectrum is resulting from the convolution integral of the monochromatic time intensity profile with the reactor spectra.

The monochromatic intensity profile depends only on the window chopper time behavior and on the group velocity, and it go back, by deconvolution numerical methods, from $N_x(t)$ to the originating velocity intensity distribution $S(v)$.

4. Results

Figure 4 shows the time pulse intensity profile obtained by time analyzing the neutron pulse intensity at the "glopper" front channel (on-axis) position. Pulses are superimposed due to a time analysis span which is longer than the pulse period (5.12 miliSec). These time spectra were obtained with a null time delay between trigger signal and the analyzer start. The start signal then is not compensated for the flight time delay neither by the geometric relation between the pick up coil and the real window position, but this is unimportant for a detailed experiment where we want a maximum amplification of the time region of interest. The qualitative agreement between computed and observed spectra is clear (Figure 5).

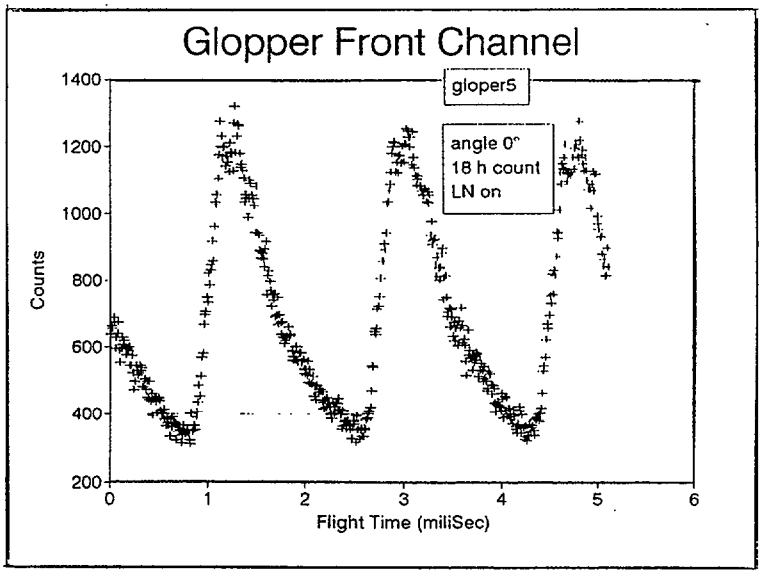

FIG. 4. Time profile intensity at the "Glopper" front channel position.

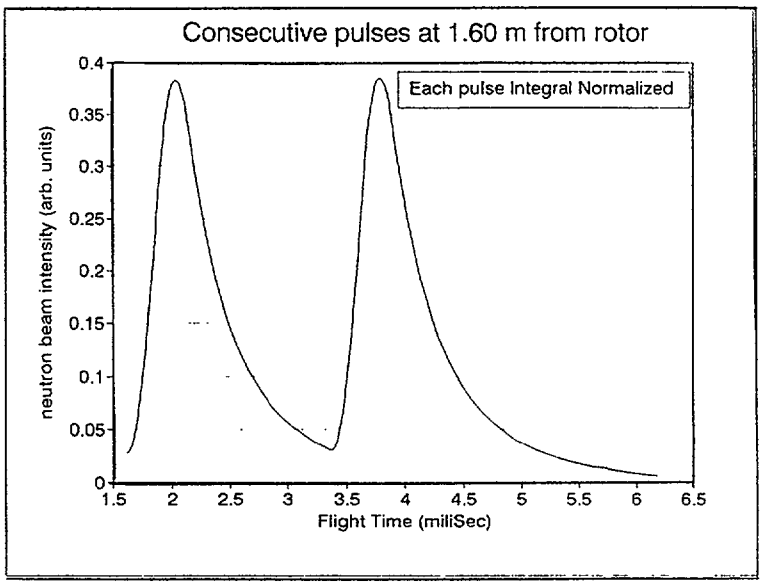

FIG. 5. Consecutive pulses at 1.60 m from rotor.

5. Conclusions

The main aspects of the repair and modifications of the scattering instrument are concluded. A new aquisition system has been built for this instrument, allowing higher time slicing during the acquisition than that which was available in the ancient version, and offering a full detector bank simultaneous measurement. A new window detector assembly is also considered, with the purpose of offering longer pulse repetition periods; an examination of the pulse shapes (slope at the low velocity tail) show that there are sufficient low energy neutron counts to profit from an expanded time analysis.

NUCLEAR TECHNIQUES IN THE DEVELOPMENT OF ADVANCED CERAMIC TECHNOLOGIES

J.D. AXE
Brookhaven National Laboratory,
Upton, New York,
United States of America

A.W. HEWAT
Institut Laue-Langevin,
Grenoble, France

J. MAIER
Max Planck Institut für Festkörperforschung,
Stuttgart, Germany

F.M.A. MARGAÇA
Instituto Technologico e Nuclear,
Departamento de Fisica,
Sacavém, Portugal

H. RAUCH
Atominstitut der Österreichischen Universitäten,
Vienna, Austria

Abstract

The importance of research, development and application of advanced materials is well understood by all developed and most developing countries. Amongst advanced materials, ceramics play a prominent role due to their specific chemical and physical properties. According to performance and importance, advanced ceramics can be classified as structural ceramics (mechanical function) and the so-called functional ceramics. In the latter class of materials, special electrical, chemical, thermal, magnetic and optical properties are of interest. The most valauble materials are multifunctional, for example, when structural ceramics combine beneficial mechanical properties with thermal and chemical sensitivity. Multifunctionality is characteristic of many composite materials (organic/inorganic composite). Additionally, properties of material can be changed by reducing its dimension (thin films, nanocrystalline ceramics). Nuclear techniques, found important applications in research and development of advanced ceramics. The use of neutron techniques has increased dramatically in recent years due to the development of advanced neutron sources, instrumentation and improved data analysis. Typical neutron techniques are neutron diffraction, neutron radiography, small angle neutron scattering and very small angle neutron scattering. Neutrons can penetrate deeply into most materials thus sampling their bulk properties. In determination of the crystal structure of HTSC, $YBa_2Cu_2O_7$, XRD located the heavy metal atoms, but failed in finding many of the oxygen atoms, while the neutron diffraction located all atoms equally well in the crystal structure. Neutron diffraction is also unique for the determination of the magnetic structure of materials since the neutrons themselves have a magnetic moment. Application of small angle neutron scattering for the determination of the size of hydrocarbon aggregates within the zeolite channels is illustrated.

1. Introduction

The shift from traditional to high technology-based industries depends on the development of advanced materials. Better functional materials have their impact not only on economic, but also on environmental issues. Products made from high durability materials have a longer life cycle, producing less waste and effecting lower overall energy invenstment.

Similar advantages are gained when using miniaturised systems. Engines made from materials resistant to high temperatures, assure better efficiency of burning, thereby decreasing both fuel output and gas formation. Parasitic heat production will decrease and efficiency increase when electricity can be transferred by superconductors etc.

The importance of development and application of advanced materials is well understood by all developed and most developming countries. The U.S.A. for instance is doubling its expenditure on materials research in the next year. The development as well as the reliable and efficient processing of new materials rely strongly on their characterization.

Many physical, chemical and optical methods are in use, the selection of the technique being dependent on the kind of information to be obtained and on the available equipment. Nuclear methods, and more specifically neutron diffraction and scattering, has proved very fruitful in investigation structural properties of complex materials. The performance of advanced ceramics is dependent on their structural, chemical and electronic configuration. High temperature superconductors for example exhibit wide compositional fluctuations and oxygen disorder effects as a result of aging, method of fabrication and other conditions; these changes, that affect their electrical properties, can be observed by neutron techniques. Apart from superconductor research, the variety of materials studies by neutron diffraction and scattering is equally impressive, inclunding zeolites, fast ionic conductors, permanent magnets, materials with defects, materials undergoing phase transitions, residual stress analysis, ordering and phase separation in alloys and multilayer structures.

Beams of electromagnetic radiation, electrons or other charged particles, which are used as probes, interact primarily with electrons and are therefore confied to the surface. Neutrons can penetrate deeply into most materials thus sampling their bulk properties. As a probe of materials, neutron scattering suffers from a number of limitations: it is expensive, non-portable, cannot be obtained by other means. However, the use of neutron techniques has increased dramatically in recent years due to the develompment of advanced neutron sources, instrumentation, and improved data analysis. For example, the discovery of $YBa_2Cu_3O_7$ was quickly followed by several X-ray determinations of the crystal structure; however, because of twinning problems and relatively weak oxygen stoichiometry and location, X-rays were unable to establish accurately the oxygen stoichiometry and location. This knowledge, which is vital to a proper understanding of this material, cames only as a result of neutron powder diffraction studies.

Material scientists and technologists are finding that the great penetration depth, nondestructive nature of neutrons, their ability to probe materials not only under ambient conditions but also at high and low temperatures and pressures, are also making them indispensable in characterizing real materials using small angle scattering (SANS) techniques. Grain boundary cavitation, whereby small voids develop and accumulate at the grain boundaries of materials subjected to deformation at elevated temperatures, is an important and poorly understood damage mechanism in real high temperature materials. The type of information needed to understand this phenomenon includes the number of densities of the voids and their size distribution. Transformation toughened zirconia represents another example where this kind of knowledge is essential. Another use of neutron scattering in the study of real materials is the measurement of bulk residual stress. Other methods commonly employed, e. g., strain gauges or ultrasonics, are either destructive or strongly affected by texture in the sample. Yet the ability to reliably measure the distribution of internal stress is vital to the safe and effective design of parts made from composite ceramics or metals.

2. Advanced Ceramic Materials: An Overview

Amongst advanced materials, ceramics play a more and more important role due to their specific properties but also in many cases due to availability, low costs and environmental compatibility. According to performance and importance, advanced ceramics can be classified according to their properties, as structural ceramics (mechanical function), and the so-called functional ceramics (Figure 1). In the latter class of materials, special electrical, chemical thermal, magnetic and optical properties are of interest. These materials are expected to become more and more significant as components of intelligent systems composed of sensors (information, cf "senses"), actuators (movement, cf. "legs and hands"), batteries (power, cf. "metabolism") and computers (cf. "brain") (Figure 2). In the field of electroceramics (electric function), high Tc superconductors (e.g. $YBa_2Cu_3O_{6+x}$) play a prominent role in view of many applications such as high performance magnets (Figure 3). Of high potential are ionic conductors such as oxygen, proton, sodium and lithium conductors (e.g. ZrO_2 (Y_2O_3), $SrCeO_3$ (Yb_2O_3), β-Al_2O_3 (Na_2O), LiI:γ-Al_2O_3). They can be used as solid electrolytes for batteries, fuel cells, chemical sensors and electrochemical pumps (Figure 4). Ceramic semiconductors such as $BaTiO_3$, $SrTiO_3$, SnO_2 , TiO_2 , $PbZrO_3$ are used for example as capacitor materials, chemical sensors and actuators (Figure 5). Mixed conducting materials combine both ionic and electronic conductivity, and thus enable neutral components to permeate through, or dissolve or remove them. This is of relevance for advanced electrodes and electrochemical filters e. g. $La_{0.5}Sr_{0.5}CeO_{3+x}(TiS_2)$, for catalysts ($CeO_2$), and for chemical storage of $H_2(NbH_x)$ or $Li(TiS_2)$ as a cathode in Li-batteries. In the latter case accompanying colour changes can be used in electrochromic devices (smart windows) WO_3Li_x) (Figure 6).

Besides the chemical functions mentioned so far, catalytic properties of ceramic surfaces (external or internal) are also significant (e. g. zeolites or γ-Al_2O_3). Thermal functions are important for appropriate substrate materials, such as AlN or diamond (films) exhibiting

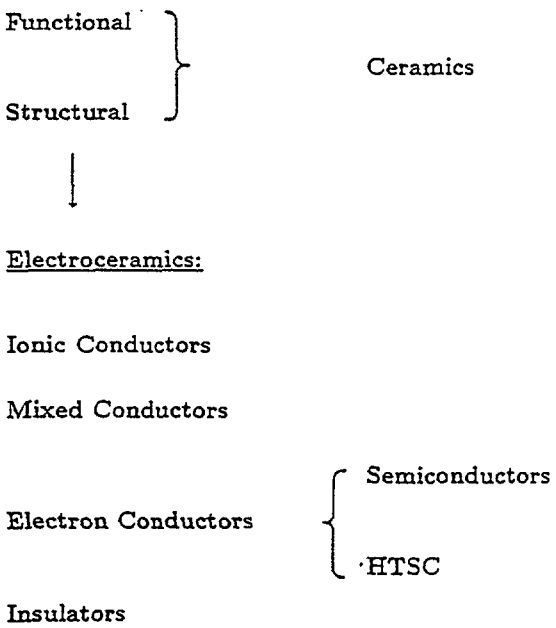

FIG.1. Advanced ceramic materials

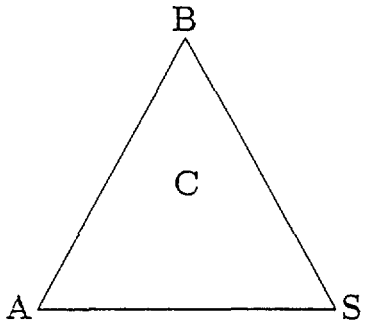

A: Actuator ("arms", "legs")

S: Sensor ("senses")

B: Battery ("metabolism")

C: Computer ("brain")

FIG. 2. Intelligent materials

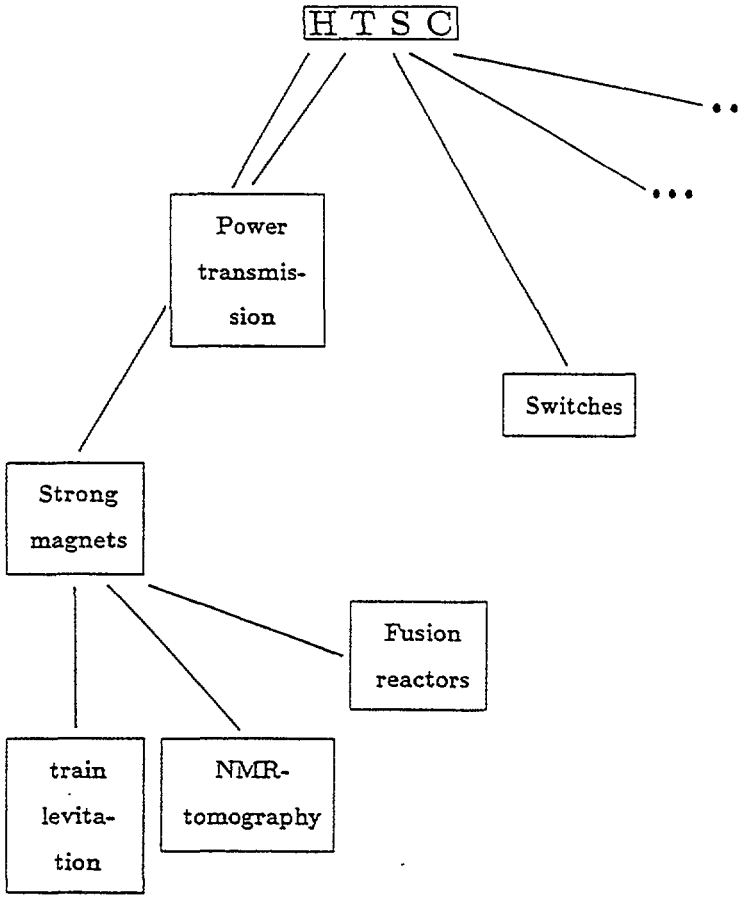

FIG. 3. Possible applications of HTSC.

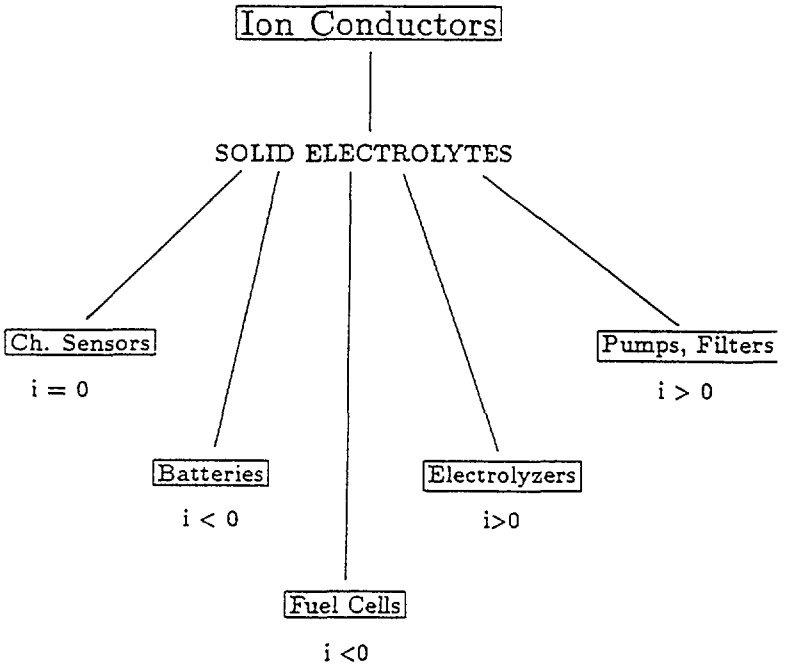

FIG. 4. Possible applications of ion conductors.

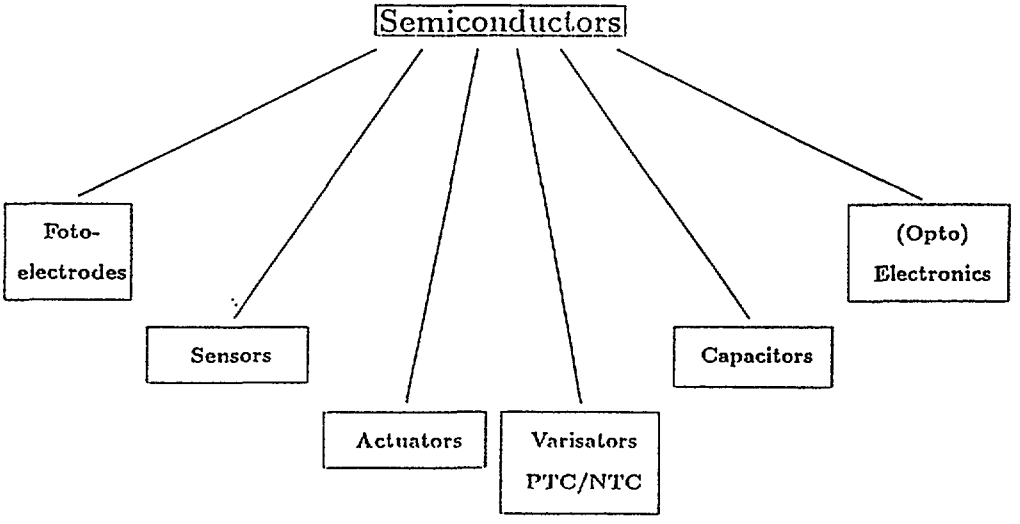

FIG. 5. Possible applications of ceramic superconductors

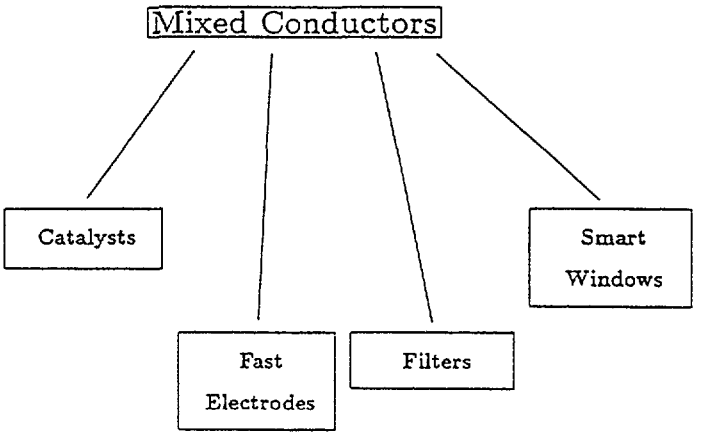

FIG. 6. Possible applications of mixed conductors

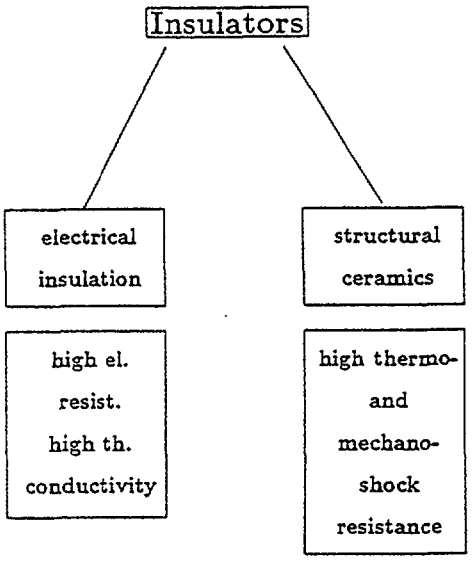

FIG. 7. Possible applications of insulating materials

high thermal conductivity but being nevertheless electrical insulators. Figure 7 indicates important applications of insulating materials. Glass ceramics are examples of composite materials with low (and tunable) thermal expansion. Besides these functions, specific magnetic properties, e.g. ferrites or optical, e. g. laser materials, are also met in ceramic materials. Of course most important materials are multifunctional, e. g. structural ceramics combine beneficial mechanical properties with thermal and chemical resistivity. Multifunctionality can also be achieved by composite materials (e. g. organic/inorganic). Additionaly, properties can be chaned by reducing sample dimensions (thin films, nano-crystalline ceramics (mesoscopic effects).

The main tasks of materials science can be classified as follows:
1) search for new materials
2) understanding and characterization of given materials
3) modification of given materials

Since recommendations will mainly refer to the last two points, the main classes of problems with respect to existing materials may refer to

a) understanding of the kinetics
b) understanding of the structure including the defect structure
c) understanding of the interfacial behavior (outer and inner surfaces, grain boundaries)
d) thermodynamics and kinetics of interactions with neighbouring phases
e) understanding of the interaction of the material with external forces (electrical, magnetic, stress etc. effects) as a function of controlling parameters such as temperature, O_2 partial pressure etc.

Due to the specific weaknesses and strengths of neutron methods the following more specific problems have been selected to be appropriate for neutron investigation:

i) Detection of Impurities in Ceramics-Hydrogenous Impurities in Oxides

This has become a major problem in materials science and is especially important for materials such as Yb-doped $SrCeO_3$, where oxygen vacancies due to the Yb-incorporation provide the possibility for H_2O incorporation and make the material a most prominent proton conductor. (A second problem is detection of oxygen in AlN, where O drastically reduces the thermal conductivity).

ii)Defect-structure

For understanding the properties of functional ceramics, an understanding of the defect structure is especially necessary. With neutron methods the normally low defect concentrations cannot be investigated. A lot of important materials, however, are heavily doped or may exhibit substantial frozen-in intrinsic disorder. Examples are Y_2O_3 doped ZrO_2 a most important ion conductor (solid electrolyte in electrochemical O_2 sensors, or in high temperature fuel cells) where high Y-concentrations (typically 10 %) are present, Yb doped $SrCeO_3$ as mentioned above, Sr doped $LaCoO_3$ used as an advanced anode in high temperature fuel cells; as well as Sr-doped La_2CuO_4 or oxygen and cation disorder in $YBa_2Cu_3O_{6+x}$). In all these cases the influence of small defect concentrations is sufficiently well understood but the effect of the large defect concentration (typically 10 % and more) is still an open and very relevant problem with respect to the properties.

iii) Mesoscopic Effects

In general trend in materials science to reduce the dimensions of the samples, be it by producing thin films or be it by producing ceramics of very fine grain size, gives rise to the question of the dependence of properties and especially of structural changes upon size reduction. Consequences may be changes of transport properties in ionic conductors (e.g. β-Al_2O_3) or the transition temperature in high Tc superconductors.

iv) Interfaces

An overwhelming number of materials problems are connected with interfacial problems (e. g. grain bounderies and interfaces reducing critical currents in superconductors, enhancing or decreasing overall conduction in ionic conductors). With neutrons, however, only materials with high interfacial densities as in zeolites (catalysis), γ-Al_2O_3 (catalysis, composite electrolytes) and nano-nano composites can be studied.

v) Mechanical Failure

The occurrence of stress effects especially in view of cracking of the material is of crucial significance for structural ceramics (cracking is often induced by macroscopic inclusions), e. g. used as engine parts or turbines where high (thermo-) mechanical demands have to be fulfilled. In the same way e. g. the sodium conductor, β-$Al_2O_3(Na_2O)$, used as a solid electrolyte in high performance Na/S cells (electrovechicles) shows a tendency to crack at 300 °C in contact with liquid sodium on one side, and with liquid sulfur on the other side, after a certain number of de- and reloading cycles.

vi (Ideal) Structure

Although the (ideal) structure of most advanced materials has been clarified, studies of this type are nevertheless important to elucidate the average local structure in non-crystalline systems such as glasses or gels. This is particularly true for characterizing multiphase mixtures (e. g. during the preparation) porous materials or composite materials in general.

vii) Kinetics

The above points essentially refer to static experiments. A field which has not been tackled so much but which is of substantial interest for understanding and optimizing materials in view of preparation, modification and also durability (aging effects!) is the investigation of transistent phenomena. Examples would be preparation and kinetic stability of high Tc superconductors which are thermodinamically unstable under real conditions.

viii) Materials Modification by Neutrons

A completely different neutron application from using them as a tool of characterization, is their use in the preparation or modification of a given material. Successfull examples are the increase of the critical current density in HTSC materials ($YBa_2Cu_3O_{6+x}$) due to flux pinning by the introduction of defects, and P-doping of Si by inducing nuclear reactions.

3. Neutron Scattering in Materials Science

As a tool for the charcterization of materials thermal neutrons offer several well-known but unique advantages over other common probes such as protons, electrons or X-rays. Carrying no electrical charge, they are weakly interacting and therfore deeply penetrating. Because of their low energy they are non-destructive. Their low energy also makes them ideal for inelastic scattering studies-extremely important for the detailed fundamental understanding of all classes of materials. However, inelastic scattering cross-sections are invariably very low and such studies are best left to high flux reactor facilities. By contrast in neutron transmission and elastic scattering experiments a substantial fraction of the incident neutron flux is actually measured, and these studies can be successfully carried out at reactors with very modest fluxes. Furthermore-and this is a key point-several of these techniques are particularly powerful in attacking the important ceramic materials problems discussed below on a level likely to lead to practical progress which can be rapidly passed on to the technological sector.

Generally, the techniques that we feel are particularly well-suited to modest research reactor facilities fall into three broad catagories depending upon the magnitude of the angle, Q_S , by which the neutron beam is refracted or scattered-

1) $Q_S = 0$, neutron transmission or radiography which reveal microscopic features (e.g. cracks) of charcteristic size 1μ = 10-3 cm.
2) .001 -<Q_S-<1o, small angle neutron scattering (SANS) which probe homogeneity (e.g., granularity, pores) of mesoscopic dimensions, 100 Å - 1μ.
3) Q_S-> 10°, powder diffraction which explores structure on the interatomic length scale (10 Å - 1 Å).

Note that the length scale examined is inverse to the scattering angle. Each of these techniques require different instrumentation which will be briefly described later, but in each case the instrumentation is (a) comparatively simple, robust and inexpensive and (b) requires a minimum degree of sophistication to operate. Both of these characteristics are important for developing countries.

It must be clearly understood that thermal neutron techniques are not a sufficiently broad base upon which to build a successful program of advanced ceramic materials characterization. Other traditional methods (electrical, optical, electron microscopy, x-ray scattering, etc.) are also indispensable tools which can and must be used as appropriate. But, as we hope to make clear, the development of home-grown neutron capabilities of the type discussed here would be a substantial benefit to any well-conceived program in ceramic synthesis and processing. Furthermore, such facilities already exist, at least at a rudimentary level, in many developing countries or could be developed at existing low flux reactors at minimal incremental cost. (Suitable reactors exist in many countries.). Of course, such facilities, once developed, are useful in the context of other industrially significant, materials studies (metals, polymers, etc.).

4. Neutron Materials Science Techniques at Small Reactors

Neutrons are a very capable tool for investigating new advanced materials and modifying their properties by irradiation to produce defects. At small and medium flux reactors it is necessary to choose problems appropriate to the manpower and beam hole resources. Often simple techniques can be used to investgate properties of new materials which are of basic technological interest - for example, formation of cracks, aging effects, fatigue effects and structural changes. Neutron radiography, neutron small angle and very small angle scattering are examples of suitably simple techniques.

Neutron Radiograpy

This is one of the most typical application of small reactors and is a first step for materials orianted neutron work. Neutron radiography can be devoted to applied as well as to more fundamental research. One can investigate metalurgical problems such as the diffusion of hydrogen in various ceramic materials, and changes in atomic diffusion and exchange rates for hydrogen at the surface with different atmospheric conditions. For example, one can study the distribution and aggregation of 3He produced by the decay of tritium in such ceramics. Extreme internal strains and the formation of bubbles with very high He-pressure occur, and contribute to the embrittlement of such materials. This can be a limitting factor in future fusion devices. Long term investigations can deal with the aging process and with the increasing embrittlement stage of the materials. Sensitivities for hydrogen detection to the order of 1 %, for oxygen to the order of 3 %, and for metallic composites to 5 % are feasible. A typical radiography installation is shown in Figure 8.

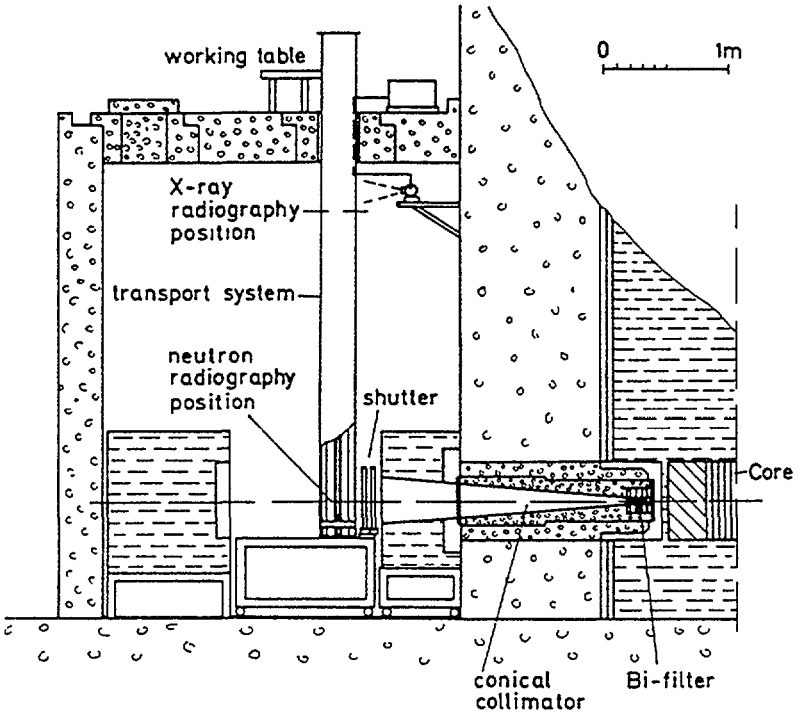

FIG. 8. An installation for neutron radiography at the Vienna University reactor.

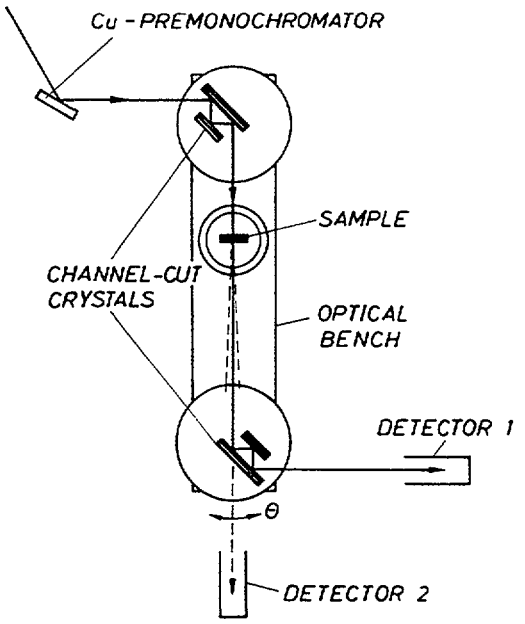

FIG. 9. The perfect crystal small angle scattering camera at the Vienna University reactor

Neutron Small Angle Scattering

We recommended the use of the perfect crystal small angle scattering camera because it is especially sensitive to large inhomogeneities and ckracs, which are serious problems related to the performance of new ceramic materials. This kind of small angle camera (Figure 9) is based on the non-dispersive arrangement of two perfect crystals, and operates with thermal neutrons, avoiding the need for a cold neutron source. Such an instrument is equipped with monolithic channel crystals increasing the angular resolution, which is of the order of several seconds of arc - i.e. two orders of magnitude better than for standard small angle scattering instruments. Because the resolution is decoupled from the divergence of the incident beam, a rather divergent beam can be used, providing sufficient intensity at small and medium flux reactors. Due to the compactness of this kind of camera, real time experiments can be performed to investigate aging and fatigue effects. The formation of precipitates or other inhomogeneities can be investigated. Even the forward transmitted intensity contains valuable information of the bulk properties of the sample. Cracks and other inhomogeneities with spatial dimension in the order of 1mm can be detected very easily. Measurements at different temperatures, different surrounding atmospheres and different strain conditions can help to develop these new materials in a form applicable for routine use. In future such materials will also be used in filament form. In such cases this kind of very small angle scattering can contribute substantially to testing such materials before industrial use.

Ceramics Irradiation

Semiconductor and superconducting properties can be effectively influenced by neutron irradiation. In many cases the critical current, which for presently available HTC-superconductors is a weak point, can be increased by more than one order of magnitude. Several kinds of neutron irradiation at different temperatures can produce different pinning centres causing various changes in the superconducting properties, which can be stable as well as unstable. Such investigations can help in the basic understanding of ceramic superconductors, but are also of importance for increasing their performance.

5. The Microstructure of Ceramics Investigated by SANS

Ceramics are currently made from a wide variety of raw materials, and come in a wide variety of forms, which range from glasses to conglomerates of small crystals and combinations of the two. The consequence of such diversity of forms and compositions is the wide range of their applications.

Ceramics are complex materials. A material that is a mixture of two or more component substances, my consist of two or more phases - homogeneous, physically distinct and mechanically separable portions. Under ideal conditions the phases are in equilibrium. However, in practice the material is manipulated under non ideal conditions. When a material is heated, worked and cooled, it may pass through various nonequilibrium states. Indeed, it has been primarily by the processing of materials far from equilibrium that a range of truly new structures have been obtained, exhibiting new properties and performing in new vays. It is common knowledge that the coupling of a materials bulk properties to its microscopic structure is essential to drive advances in the development of new materials and new processing technology. Namely, information is required on relations among structure, properties and performance and how those mutual interactions are affected by processing.

In all their applications ceramics are valuable for their ability to withstand heat and chemical attack. These properties stem directly from the strong bonds (ionic and covalent) which hold their constituent atoms together but, on the other hand, this also leads to brittleness. Indeed,

ceramic materials under load have a propensity to crack and break instead of to deform. They are thus particularly sensitive to the presence of imperfections in the microstructure that migt serve as starting points for cracks. Ceramics can be made more crack-resistant if such defects as voids or chemical impurities segregated between the materials grains, could be eliminated.
A ceramics microstructure on a scale of the order of 100 Å can be investigated by conventional Small Angle Neutron Scattering (SANS) techniques, using a neutron beam produced at a medium flux reactor. Basically it requires a well collimated beam of roughly monochromatic neutrons around the transmitted beam axis. The restriction to small angles eliminates "Bragg" scattering from individual atoms, which occurs at larger angles. Thus, as far as the SANS technique is concerned, the material presents itself as a continuum with a certain average scattering power for neutrons. SANS occurs whenever there are significant changes from this average value in the material due, for example, to voids or precipitates in the matrix. Material homogenity, on the 100 A scale, can therefore be examined by SANS [1, 2].
Microstructure modifications caused by thermal, mechanical and other specific treatments can be detected by comparing SANS spectra measured before and after treatment [3, 4]. The stability of the microstructure can be checked as a function of time. For example, aging effects can be followed by SANS measurements at different times. This is particularly relevant for technologically important materials, which are used in a "metastable" state [5]. Microstructure dependence on the processing parameters can be investigated by performing systematic SANS measurements as each parameter is changed. Ultimately, the optimum processing conditions can be found. This is also an important aspect since the microstructure of ceramic samples obtained, for example from oxide powders by sintering, strongly depends upon such parameters as the powders grain size, applied pressure, temperature and sintering time [6].
SANS intensities, adequately treated and analysed, can provide quantitative information on the volume fraction, average size and even shape of inhomogeneities present in the matrix and responsible for the scattering. To this end, experimental results should be compared with the predictions of analytical and/or numerical models [7]. It should be noted that, for most technical materials, this type of information can only be obtained using neutrons. As for any neutron method, SANS provides information (on the material's microstructure) averaged over the whole volume sampled by the beam (a few cm^3); it is a non-destructive technique which means that a given piece of material can be examined repeatedly at different times and/or under different conditions; it does not require any special preparation of the sample, unlike transmission electron microscopy (TEM), for example. For these and other reasons, conventional SANS instruments are currently the neutron scattering facilities subject to the heaviest demand by materials scientists and engineers all over the world. It is fortunate that such an instrument can be a useful tool for materials R&D even when installed at low flux reactor [8]. The reason for this is that only rough monochromatization is required for the incident beam, so that a relatively large slice of the thermal neutron spectrum can be used. It has therfore been considered one of the first-choice instruments for low flux reactors [9]. The small angular spread of the incident beam, which is required in order for small scattering angles to be measured, is the main factor reducing the neutron intensity at the sample. Recently, however, it has been shown that the intensity can be substantially increased if the instrument is large enough to use the full neutron source area [10]. Several SANS instrument designs have been described in the literature [7]. Under certain circumstances it is advisable to opt for a SANS facility that uses a collimation assembly without movable guide segments [11]. Its implementation is simpler and less expensive than that of an instrument using quides in the collimation path [12], and this can be a valuable asset when it comes to the implementation of a performing instrument at a lower flux reactor.
A SANS instrument can be partially constructed locally but there are a few parts that, because of their intrinsic complexity, should be purchased-the mechanical velocity selector for rough

monochromatization, and the position sensitive detector for neutron detection and angular positioning. The remaining components are the beam-plug and shutter, the collimator with a set of diaphragms, the sample chamber, and the detector chamber, which can all be constructed at a normally equipped mechanical workshop. Some basic vacuum equipment will be needed since the whole beam line should be in rough vacuum, to avoid neutron intensity losses due to air scattering. Microstructure investigation by SANS, including data analysis at different levels of complexity, as well adapted to the training requirements of both undergraduate and graduate students engaged in the preparation of thesis to obtain a University degree. Cooperation between research group using small reactors with similar capabilities in different countries should be promoted. The same applies to the collaboration between groups that do complementary work by investigating different properties of the same material. Finally, groups that work at low flux reactors should have access to neutron scattering instruments at higher flux reactors whenever necessary to complement measurements carried out at their home facilities, and to perform more detailed studies of particularly interesting (or samples).

References

[1] F. Larche, M. Roth and J. Zarzycki, "Small-Angle Neutron Scattering Study of Glasses Containing Chemical and Magnetic Inhomogeneities", in Proceed. of Symposium "Physics and Chemistry of Glasses", Ed. P. Gaskell, Taylor & Francis Ltd., London 1977.

[2] H. Franz, M. Müller-Stach, G. Wallner, J. Peisl, W. Petry and U. Herr, "Small-Angle Scattering from Nanocrystalline Solids", Proc. of VIII Int. Meet. on Small Angle Scattering, J. Appl. Cryst. 24 (1991)

[3] R. A. Page, J. Lankford and S. Spooner, "Nucleation and Early-stage Growth of Creep Cavities in Hot-pressed Silicon Carbide", Acta Metall. 32(1984)1275.

[4] R. A. Page, J. Lankford and K. S. Chan, "Creep Cavitation in Liquid-Phase-Sintered Alumina, "J. Amer. Ceram. Soc. 70(1987)137.

[5] A. J. Allen and L. D. Howe "Time-resolved Phenomena in Cements, Clays and Porous Rocks", Proceed. of VIII Int. Meet. On Small-Angle Scattering, J. Appl. Cryst. 24(1991)

[6] K. A. Hardman-Rhyne, K. G. Frase and N. F. Berk "Applications of Multiple Small-Angle Neutron Scattering to Studies of Ceramic Processing", Physica B, 136B(1986)223.

[7] G. Kostorz "Small-Angle Scattering and its Applications to Materials Science" in Treatise on Materials Science and Technology, Vol. 15, Ed. G. Kostorz, Academic Press, New York, 1979.

[8] C. P. Galotto, P. Pizzi, H. Walther, V. Angelastro, N. Cerullo and G. Cherubini, "A Cold Neutron Small-Angle Scattering Device for Technological Applications", Nucl. Instrum.&Meth. 134(1976) 369.

[9] T. Springer "Use of a Medium or Low Flux Reactor and its "Background Laboratories" in IAEA Advisory Group Meeting on the "Use of Research Reactors in Basic Research in Developming Countries", Sacavem, Portugal 12-15 Sept. 1983.

[10] F. M. A. Margaça, A. N. Falcäo, J. F. Salgado and F. G. Carvalho, "Solving of a SANS Instrument Optimization", J. Appl. Cryst. (1991).

[11] F. M. A. Margaça, A. N. Falcäo, J. F. Salgado and F. G. Carvalho, "Optimization of a SANS Spectrometer using a Fixed Collimation", J. Appl. Cryst. (1991)

[12] F. M. A. Margaça, A. N. Falcäo, A. D. Sequeira and J. F. Salgado, "Optical Effects in Neutron Guide Tubes Produced by Collimation", J. Appl. Cryst. (1991).

6. Characterization of Materials by Neutron Diffraction

Defects and Structure of Materials

One of the most basic measurements of a material that can be performed with neutrons is to determine its crystalline structure. Of course, X-rays are normally used for this purpose, but neutrons have unique adventages. For example, classical X-ray diffraction requires the growth of a small single crystal of the material. In some cases this is not possible, or perhaps undesirable since crystal growth is a "purification" process that may change the properties of the material. Neutron powder diffraction provides a method of obtaining the crystal structure from the ceramic material itself, without the need for growing a single crystal. This powder method using Rietveld refinement is less successful with X-rays because then scattering is from very small volumes of sample, and the "texture" of these small samples introduces important systematic errors. The much greater penetrating power of neutrons means that large samples can be used, eliminating most systematic errors. As well, X-rays are scattered mainly by heavy atoms, while neutrons are scattered equally well by oxygen, nitrogen and other light atomic constituents of ceramics. Finally the penetrating power of neutrons means that samples can more easily be examined under extremes of temperature and pressure, when their structure often changes. The structure of the 90 K superconductor $YBa_2Cu_2O_7$ is perhaps the most well known example of the success of neutrons compared to X-rays, but is typical of many of the structural problems that must be tackled for ceramics. The most concerted efforts at X-ray analysis have ever performed were of course applied to this material as soon as it was discovered, yet the structure was not understood until neutron measurements were made. Figure 10a shows the structure obtained with X-rays, in this case at Bell Labs [1], but typical of the results obtained at other large laboratories. Figure 10b shows the apparently quite different structure obtained by neutrons, in the case at ILL Grenoble [2] but typical of results obtained at other neutron centres. The X-ray structure located the heavy metal atoms, but failed to find many of the oxygen atoms, while the neutron structure located all atoms equally well. This was particularly important in the case of the ceramic oxide superconductors, because the oxidation state of these materials drastically changes their superconducting properties.

Magnetic Structures-Hard Permanent Magnets

Neutron diffraction is of course unique for the determination of the magnetic structure of materials, since the neutrons themselves have a magnetic moment.
In the early 1980's a Nd-Fe-B alloy was found to have remarkably good magnetic properties up to 585 K, with an energy product up to 360 J/m^3. Since these new materials are also cheaper than rare-earth-cobalt magnets such as $SmCo_5$, they are of interest for many applications. Initially, even the chemical formula of this new phase, $Nd_2Fe_{14}B$, was not known until the crystal and magnetic structures were established [3]. The Nd and B atoms were found to occupy layers (Figure 11), separated by Fe-layers. The strong anisotropic magnetic properties of these materials up to room temperature and above, due to the rare earth ions, and the relatively large proportions of common iron compared to an expensive rare earth element, make these materials particulary attractive.

Interfaces and Catalysis e.g. Zeolites

The active surface of a catalyst makes up a large part of its volume, so neutron scattering from the bulk material can provide information about the catalytic interface. For example, zeolites are important for hydrocarbon production, as molecular sieves, etc.. They consist of a silicate skeleton containing channels of various sizes that can accommodate

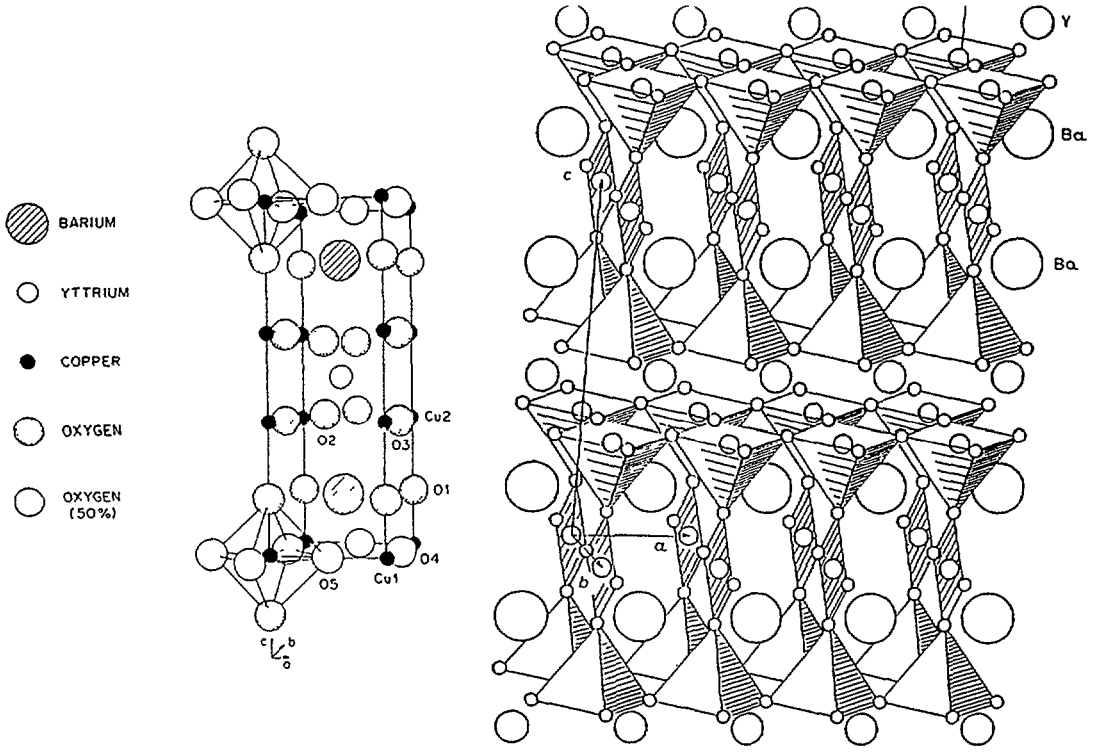

FIG 10. The structure of the 90 K superconductor $YBa_2Cu_3O_7$ as obtained by a) X-rays [1] and b) neutrons [2].

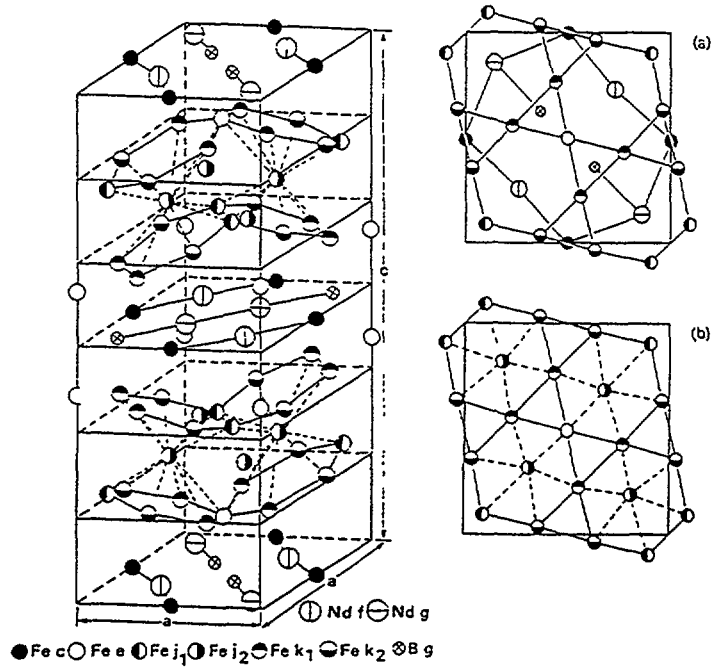

FIG. 11 Tetragonal layer structure of the hard permanent magnet $Nd_2Fe_{14}B$ obtained by neutron powder diffraction: notice that the (Nd,B)-layers are separated by layers of Fe, the inexpensive major constituent of the material. These Fe-layers are shown more clearly in projections (a) and (b) [3].

different hydrocarbon molecules; it is important to understand how these molecules interact with the zeolite interface and with each other. The basic zeolite structure can of course be obtained with X-rays, but neutrons are much better for seeing the light atoms of the hydrocarbon. Hydrogen itself has a large negative scattering length, and even greater contrast can be obtained by comparison with deuterated materials, since the deuterium hydrogen isotope has a large positive scattering length. The experiment is simply to collect the neutron diffraction pattern from a powdered sample of anhydrous zeolite, and to compare it with the pattern from the same sample containing hydrocarbon. The difference between the two can be used to construct a "Fourier" map of the location of the hydrocarbon in the channels. In this way one can identify which atoms of the hydrocarbon interact with which atoms in the zeolite channels. Figure 12a shows a simple example of such a difference Fourier map, showing benzene in sodium Y-zeolite [4]. In Figure 12b this information has been used to show schematically how the benzene molecules pack into the zeolites channels. Since these channels

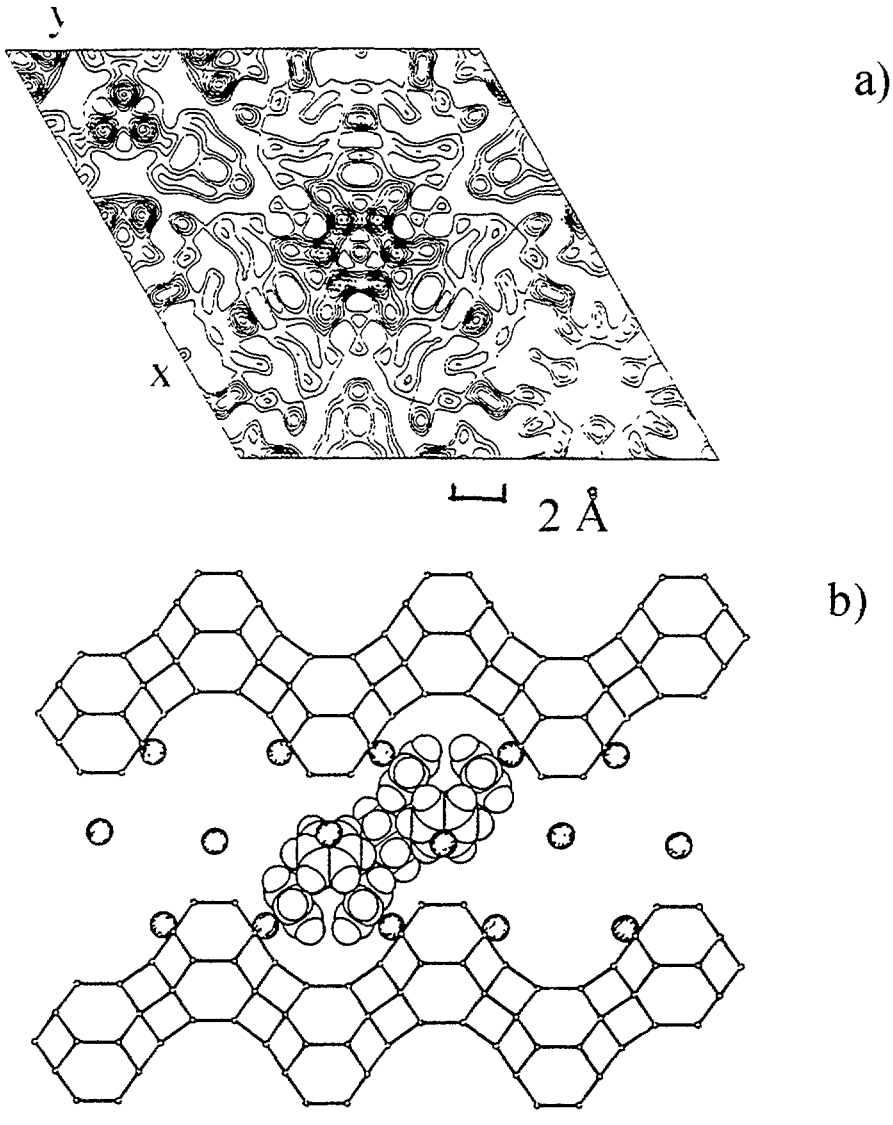

FIG. 12. a) A Fourier difference map showing the location of a benzene molecule in Y-zeolite
b) Small angle neutron scattering showed that the benzene molecules clump together in the zeolite channels

and molecules are of a size that can be investigated by neutron small angle scattering, a further simple experiment can be performed. Neutron small angle scattering patterns are collected, again for the anhydrous and the loaded zeolite. In this case, the difference gives a direct measure of the size of hydrocarbon aggregates within the zeolite channels. For benzene in sodium Y-zeolite it was found that the molecules are not uniformly dispresed, but clump together in small groups. This information is of interest for understanding how the zeolite may catalyse interactions between the hydrocarbon molecules.

Chemical Kinetics

Because neutrons are highly penetrating, it is possible to study physical and chemical reactions in large volumes in real time. For example, when $YBa_2Cu_3O_7$ is heated, it loses oxygen and its superconductivity as it transform to $YBa_2Cu_3O_6$. These structural changes can be monitored directly because of the changes on the neutron diffraction pattern [5] and the strong neutron scattering power of oxygen: with X-rays, scattering is instead dominated by the heavy metals. It is possible to study the effect of oxydising and reducing atmospheres, of quenching from different temperatures, and of aging the resulting material at room temperature. Another example is provided by hydration of Portland cement (a mixture of calcium silicates and aluminates), resulting in solidification. Christensen et al. [6] used neutron diffraction to investigate the reactions between water and the constituent oxides of cement. They showed that the hardening process for Ca_3SiO_5 consists of three stages: initialisation, induction and reaction. During the first stage there is a rapid dissolution of Ca_3SiO_5. The induction period may be due to the formation of a protective layer surrounding the grains until it too is dissolved. Precipitation of $Ca(OH)_2$, the only crystalline product, marks the beginning of the final reaction stage, where all dissolved silicon goes into producing an amorphous gel, with a neutron diffraction pattern quite different from the crystalline phase. Since both hydrogen and oxygen scattering neutrons strongly, the detection of water is relatively easy. Chemical reactions which proceed through hydrated (or hydroxylated) precursors are then ideal for study by neutron diffraction. For example, Figure 13 illustrates the thermal dehydration of $Fe_2F_{5.2}H_2O$ [7]. At low temperature (160 °C) the high background level is due to incoherent scattering from water : as the temperature is increased, the decrease in water content can be measured directly from the decrease in the background, which is accompanied by the transformation of the peaks due to crystalline $F_2F_{5.2}H_2O$ into the different set of peaks due to the anhydrous product. Other examples of chemical reactions then can be followed with kinetic neutron diffraction including solid state reactions where the reactants are strongly mixed and pressed, and then heated while observing the changes on the neutron diffraction pattern. Crystallisation processes can be easily observed with kinetic neutron diffraction. For example when a quasi-crystalline material such as the quenched Al-Mn alloy $Al_{85}SiMn_{14}$ is heated to 630 K it transforms into orthorhombic Al_6Mn with the silicon producing an α-AlMnSi phase at 710 K. Amorphous materials and quasi-crystals have recently excited interests because of their unique electronic and other properties. Kinetic neutron diffraction can help us understand the relations between amorphous and crystalline phases. For example, when $Al_{65}Cu_{20}Fe_{15}$ is cooled from the melt at 1235 K to the solid at 1040 K, neutron diffraction showed that the amorphous phase is not produced directly, but rather via intermediate Al-Fe phases which finally dissolve in the remaining Cu-rich liquid. Complex phase diagrams can be mapped out.

Stress and Texture

The mechanical properties of materials are in part determined by internal stresses and "texture" i. e. the preferred orientation of the constituent crystallites. Neutrons are

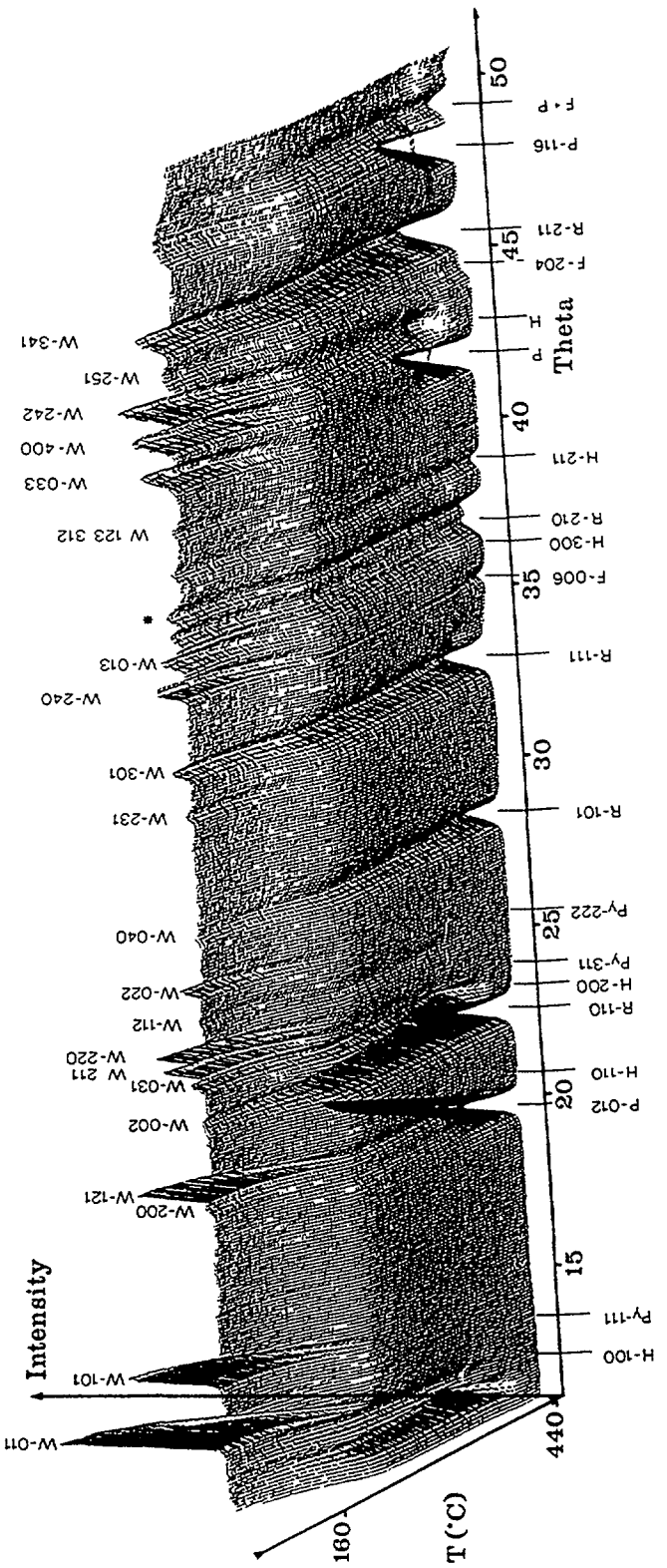

FIG 13 The thermal dehydration of $Fe_2F_5.2H_2O$ studied by kinetic neutron diffraction, with powder patterns collected at many different temperatures Note the high background due to scattering from water at low temperature, and the disappearance of some lines and the appearance of others with the crystalline phase change

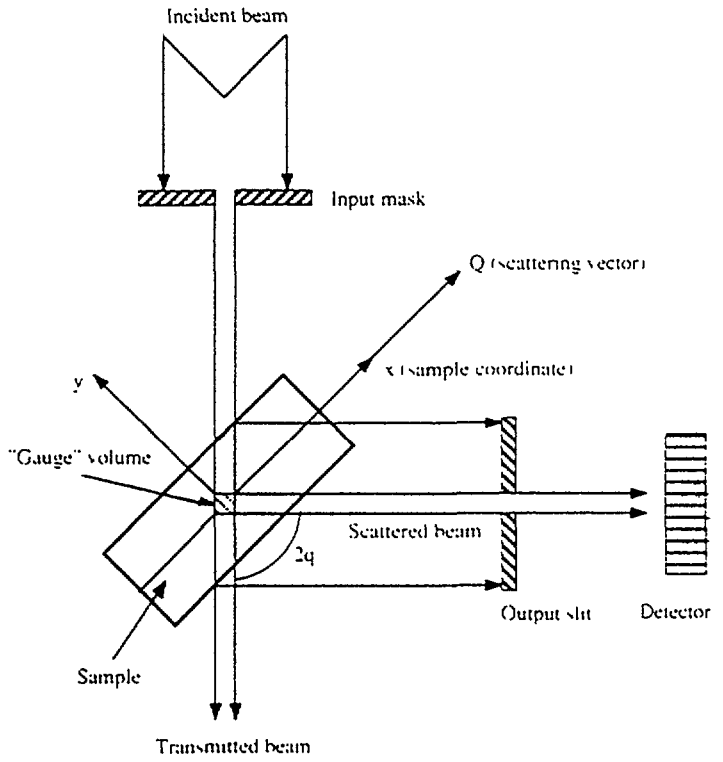

FIG. 14. Simple neutron scattering geometry used to study stresses in materials by measuring small shifts in the positions of the diffraction lines (10). Neutrons see inside the bulk material, while X-rays see only the stresses at the surfaces, which may be quite different

particularly suited to the study of such problems because they can penetrate large objects, while X-rays are scattered mainly by surface. For example, alumina can be strengthened by sintering Al_2O_3 powder with SiC fibres at high temperature. When cooled to room temperature, strong internal stresses are induced in the resulting composite because of differences in thermal contraction of the two materials [8]. Clearly, the mechanical properties also depend on the relative orientation of the SiC fibres (texture). It is important to understand the physical reasons that make this material one of the most successful ceramic-ceramic composites. A second well known example of the use of internal stress to toughen materials is provided by partially stabilised zirconia. The zirconia is toughened zirconia ceramics can exist as cubic, tetragonal, orthorhombic and monoclinic phases. The martensitic tetragonal-monoclinic transformation is accompanied by a volume increase of almost 5 %, and induces strong stresses in the resulting composite material which depend on the relative volume fractions of the different phases. Neutrons cannot only probe the internal stress in the bulk material, but also measure with precision the amounts of the different phases [9]. X-rays are also used to measure the relative phase abundance, but only on the surfaces, and phase transformation on surfaces, which can be altered by grinding for example, may not be typical at the bulk material. These different experiments, to measure internal stress, "texture" and phase abundance can be performed on the same simple neutron diffraction equipment. Figure 14 shows a collimated beam at monochromatic neutrons incident on a large ceramic sample. Simply by measuring the diffraction pattern, the relative abundance of the different phases can be determined from the relative intensities of the peaks characteristic of these phases. If the sample is heated in situ, changes in the relative abundance of the different phases can be monitored. If the orientation of the sample is changed, the intensities of some of the peaks also change when the crystallites are aligned in preffered directions. Such "texture" can then be

investigated by measuring the intensity of a few peaks for a variety of sample orientations. Finally, the changes in internal stress can be monitored by measuring small changes in a peak positions, which reflect changes in the crystal lattice dimensions due to stress. The material then acts as its own strain gauge. This method has been applied with great commercial success to look at stresses in oil pipe-line welds, railway lines [10] etc.

References

[1] Siegrist, T., Sunshine, S., Murphy, D. W., Cava, R. J., and Zahurak, S. M., Phys. Rev. B35 (1987) 7137.

[2] Capponi, J. J., Chaillout, C., Hewat, A. W., Lejay, P., Marezio, M., N. Nguyen., Raveau, B., Soubeyroux, J. L., Tholence, J. L., and Tournier, R., Europhys. Lett. 3(1987)1301.

[3] Givord, D., Li, H. S., Moreau, J. M., and Perrier de la Bathie, R., Solid State Comm., 5(1984)857

Herbst, J. F., Croat, J. J. and Yelon, W. B., J. Appl. Phys. 57 (1985) 4086.

[4] Fitch, A. N., Jobic, H. and Renouprez, A., J. Phys. Chem. 90 (1985) 1311.

[5] Rodriguez, J., Bassas, J., Obradors, X., Vallet, M., Calbet, J., Anne, M. and Pannetier J. Physica C 153-5 (1988) 1671.

[6] Christensen, A. N., Fjellvag, H. and Lehmann, M. S., Acta Chem. Scand A39(1985)593.

[7] Laligant, Y., Ferey, G. and Pannetier, J., Chemica Scripta 28 (1988) 101.

[8] Torné, Carlos, N., Bertinetti, Maria, A. and MacEwen Stuart, R., J. Am. Ceram. Soc. 73 (1990) 3428.

[9] Howard, C. J. and Hill, R. J., J. Materials Sci. 26 (1991) 127.

[10] Webster, P. J., Neutron News 2 (1991) 19 and Steel Times 218 (1990) 321.

THERMAL NEUTRON INDUCED Gd-POINT DEFECTS IN $Ba_2Cu_3O_{7-\delta}$ CERAMICS

G. BRANDSTÄTTER, M.C. FRISCHHERZ, H.W. WEBER
Atominstitut der Österreichischen Universitäten,
Vienna, Austria

A. PETROV
Nuclear Research Center,
Salaspils, Latvia

Abstract

The main purpose of this work is to study the role of point defects for flux pinning in high temperature superconductors. In order to do so, two ceramic samples of superconducting Gd $a_2Cu_3O_{7-\delta}$, one containing ^{153}Gd (σ=61000 b) and one ^{160}Gd (σ=0.77 b) were irradiated in the thermal column of the TRIGA reactor in Vienna. Both samples were subjected to thermal neutron fluences of $7 \cdot 10^{17}$, $7 \cdot 10^{18}$, $7 \cdot 10^{19}$, $2.66 \cdot 10^{20}$, and $4.77 \cdot 10^{20}$ m^{-2}. After each irradiation step the superconducting transition temperature T_c was measured and the critical current densities J_c were calculated from magnetization loops using a simple Bean model. We find that T_c remains unchanged in both samples within experimental uncertainity. J_c does not increase in ^{160}Gd-123, whereas it shows first signs of an enhancement in ^{155}Gd-123 after the last irradiation step. At 10 K and at 0.3 T the enhancement factor is about 1.5.

1. Introduction

The effects of fast neutron irradiation on high temperature superconductors have been intensively studied in both polycristalline and single crystalline materials [1,2]. The most imortant result of these investigations is the strong enhancement of the critical current density J_c [3] and the shift of the irreversibility line to much higher fields and temperatures, especially in two dimensional materials [4]. The oxide superconductors are quite resistant to fast neutron irradiation and lose their superconducting properties only at fluences of about $10^{23}m^{-2}$ (E>0.1 MeV) [5].

The effects of thermal neutron irradiation have not been studied so far. Two groups [6,7] report on such experiments, but they always used a mixed spectrum containing thermal neutrons (E<0.5 eV) and fast neutrons (E>0.1 MeV). Both papers summarize the changes of structural and superconductive parameters in Gd-123 after "thermal neutron" irradiation. However, those data are not quite correct, since the effects of the fast neutrons, which are also present in the spectrum, are not accounted for. To date, no irradiations oı high temperature superconductors by a pure thermal neutron spectrum have been reported on, although important information on the influence of point defects on flux pinning could be revealed, if isotopes with suitable thermal neutron cross sections are chosen.

The thermal column of the TRIGA reactor in Vienna has a very well thermalized neutron beam with a Cd-ratio of about 500, but only a low flux density (7.5 1013 $m^{-2}s^{-1}$). The irradiation experiment was carried out on two polycristalline Gd-123 ceramics, one containing ^{160}Gd and one ^{155}Gd. The samples were sequentally irradiated and the superconductive material parameters were assessed before and after each irradiation step.

2. Experimental

$^{153}GdBa_2Cu_3O_{7-\delta}$ and $^{160}GdBa_2Cu_3O_{7-\delta}$ ceramic superconductors were prepared and ground into powder with an average grain size of 30 μm. The ^{155} Gd-123 and ^{160}Gd-123 powders were then throughly mixed with quartz powder, which is nonmagnetic and has a low cross section for thermal neutrons. The resulting mixtures (14.5 mg ^{160}Gd-123 powder + 260 mg quartz powder and 15.5 mg ^{155}Gd-123 + 260 mg quartz powder) were put into aluminium cylinders with an outer diameter of 3 mm and a length of 25 mm. The dilution of the superconducting powder is necessary to get a mean free path for the thermal neutrons, which is comparable to the sample size.

The samples were put into a plastic tube and irradiated at room temperature in the thermal column of the TRIGA reactor in Vienna. In contrast to fast neutrons, which form defect cascades, the effect of thermal neutrons is very moderate. Each thermal neutron produces a Gd-recoil with a recoil energy of about 180 eV in the sample containing ^{155}Gd (σ=61000 barns) resulting (according to TRIM calculations) on average in 2.7 point defects per Gd-recoil and one in the sample containing ^{160}Gd (σ=0.77 barns). Thus, a lot of randomly distributed Frenkel pair defects are created, from which an unknown number will recombine immedeately. The rest may act as point pinning centers for flux lines. If we use the cross-section for ^{155}Gd and the above TRIM result for the number of defects created per Gd-recoil, the total number of defects amounts to $4.6 \cdot 10^{25}$ m^{-3} at our highest neutron fluence of $4.77 \cdot 10^{20}$ m^{-2}. The crystalline lattice remains largely undistributed. The samples were sequentially subjected to thermal neutron fluences of $7 \cdot 10^{17}$, $7 \cdot 10^{18}$, $7 \cdot 10^{19}$, $2.66 \cdot 10^{20}$, and $4.77 \cdot 10^{20}$ m^{-2}.

The investigations were carried out in a low field (LF) as well as in a high field (HF) SQUID magnetometer. The cylinders were fixed with a thread on the sample rod. T_c was measured in the LF-SQUID in a field of 1.1 mT. Hysteresis loops were measured in the HF-SQUID in fields up to 8T at 10 K, 20 K, 40 K, 60 K, 77 K, and 85 K. From these hysteresis loops the crytical current density J_c was calculated using a simple Bean model.

The transition temperature T_c

The transition temperature was obtained by fitting the field cooled curve near T_c to an exponential law. The transition temperature as a function of fluence are shown for both samples in Figure 1. We find that within experimental accurency the transition temperature remains unchanged.

Critical Current Density

J_c was calculated from the hysteresis loops using the expression $J_c = 3\Delta m/\mu_0 Vd$, where V is the superconducting sample volume, d is the grain diameter, and $\Delta m = m(H\uparrow) - m(H\downarrow)$. $H\uparrow$ denotes increasing. $H\downarrow$ denotes decreasing applied fields. The diamagnetic moment is obscured by strong paramagnetic moments from the Gd-atoms, which shift and rotate the hysteresis loops.

Assuming that this paramagnetic contribution is independent of weather the applied field is increased or decreased. Δm for the J_c-calculation follows from $m(H\uparrow) - m(H\downarrow)$. Taking into accont that m can be measured with a relative error of 1%, that the mass m is weighed with an accuracy of ±1 mg, and that the grain diameter is accurate within at least ±2μm, we get a relative error of about 15 % for the critical current density. For both samples J_c is strongly

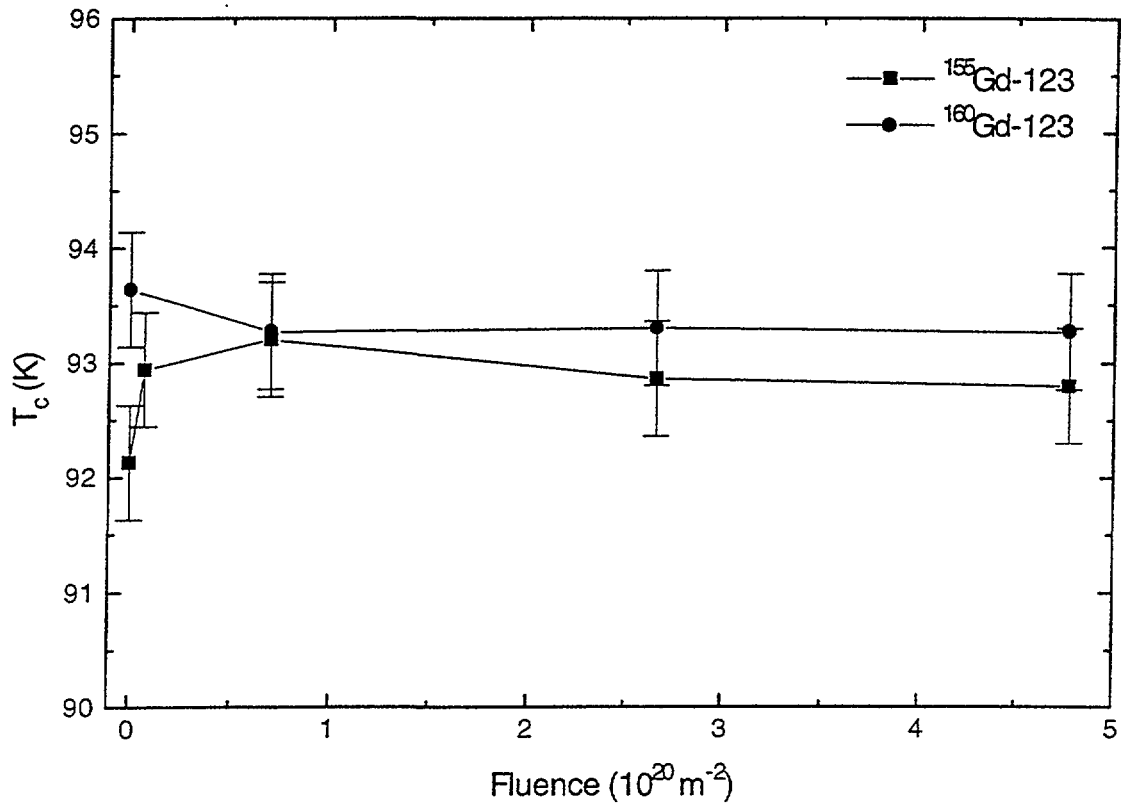

Fig. 1. T_c as a function of fluence for ^{155}Gd-123 and ^{160}Gd-123

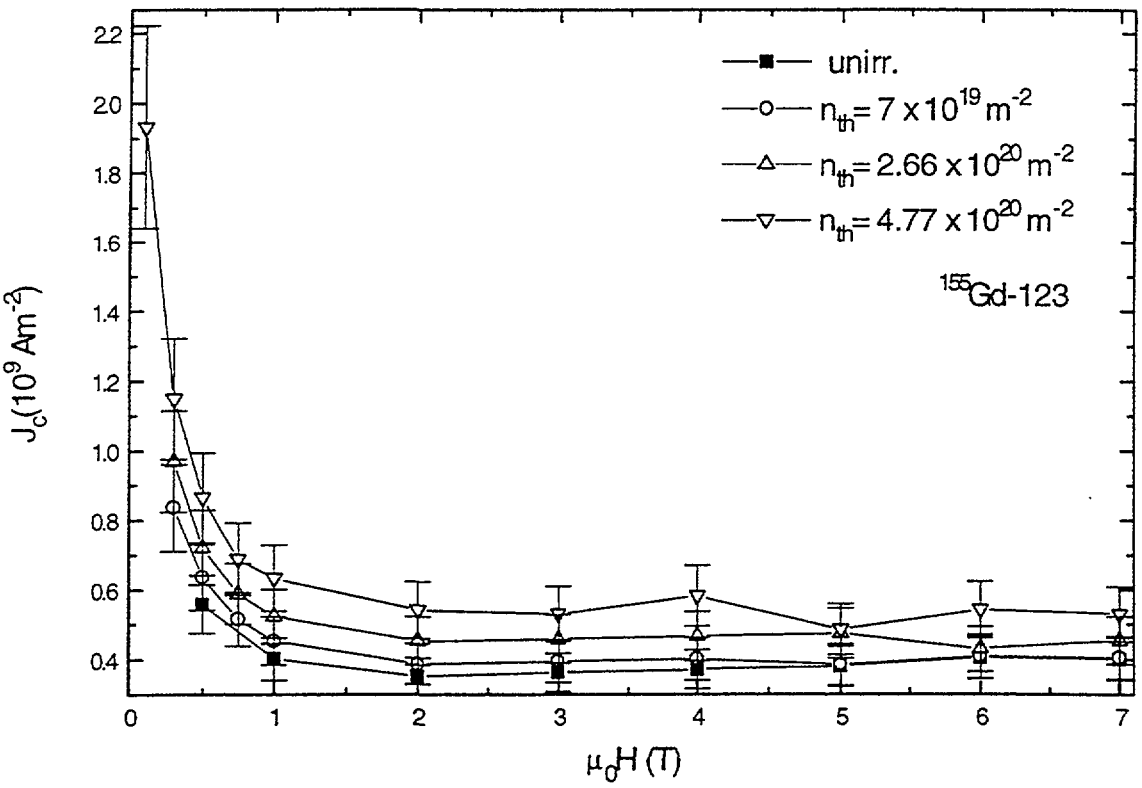

Fig. 2. J_c at 20 K in ^{155}Gd-123

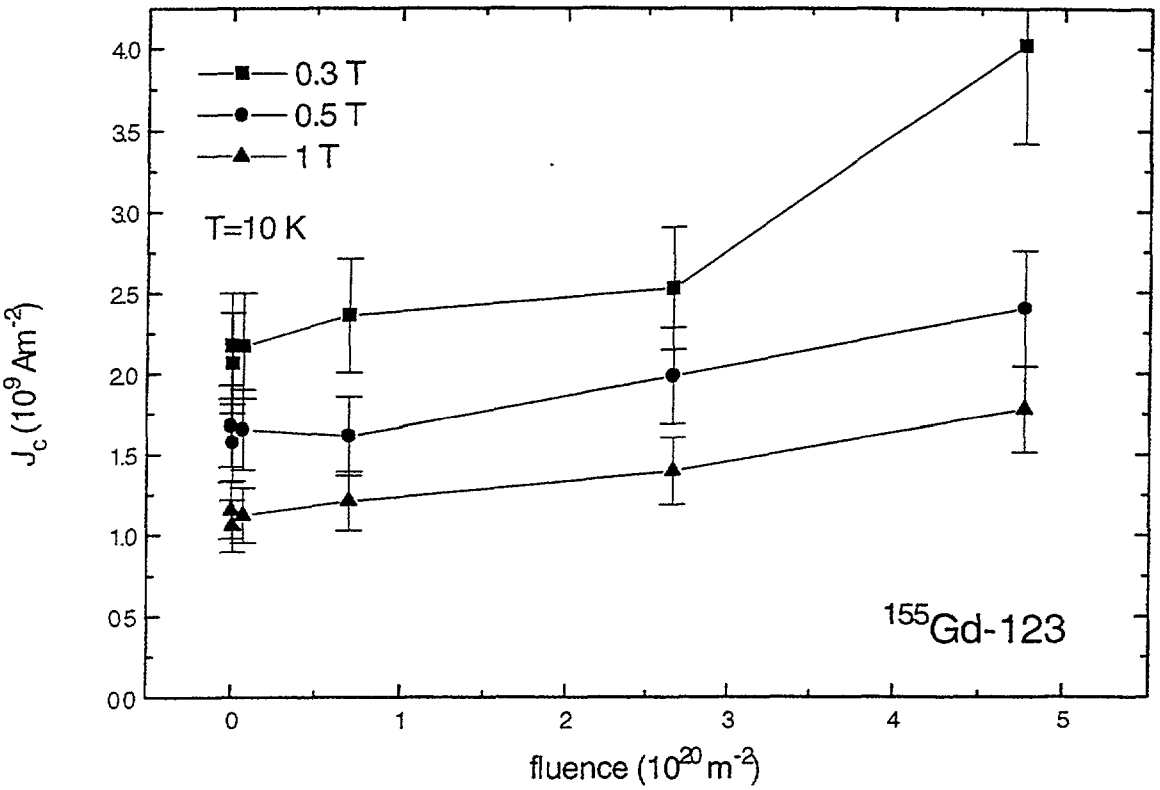

Fig 3 J_c as a function of fluence at 10 K for different magnetic fields in ^{155}Gd-123.

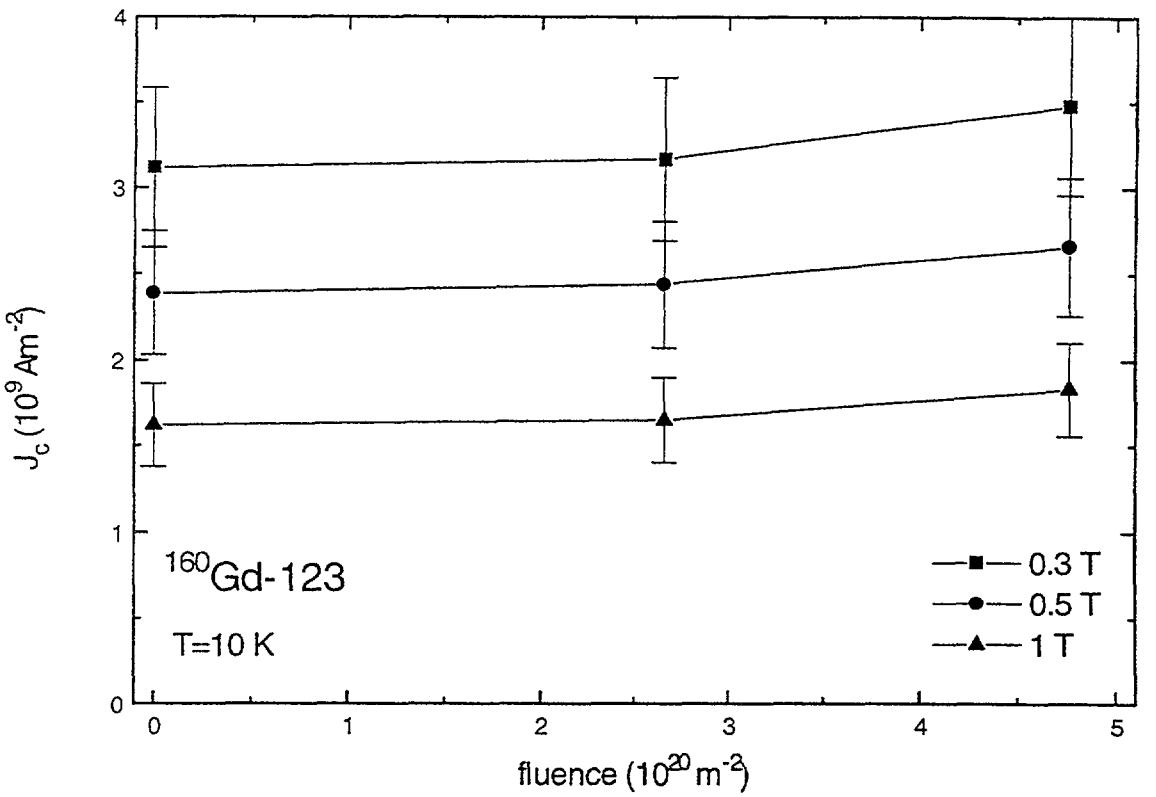

Fig. 4. J_c as a function of fluence at 10 K for different magnetic fields in ^{160}Gd-123.

field and temperature dependent. Significant J_c values exist only at low temperatures and below 2 T, *e. g.* unirradiated ^{155}Gd-123 $J_c = 1.2 \cdot 10^9$ Am^{-2} and in unirradiated ^{160}Gd-123 $J_c = 1.6 \cdot 10^9$ Am^{-2} at 10 K and 1 T. no change in J_c was observed in the ^{155}Gd-123 sample after the first three irradiation steps. The differences in Jc at 20 K and at a certain field are smaller than the experimental error (see Figure 2). Even after the fourth irradiation step no change can be observed within experimental uncertainity. After subjecting the sample to a fluence of $4.77 \cdot 10^{20}$ m^{-2} first changes, especially at low applied fields (below 1 T) are found. J_c at 10 K and at 0.3 T is enhanced by a factor of about 1.5 (see Figure 3). At higher temperatures the changes are moderate and the differences are within experimental uncertainity. In the ^{160}Gd-123 sample J_c remains unchanged after all irradiation steps at all temperatures (see Figure 4).

Conclusions

In summary we find that T_c of both samples is not changed within experimental uncertainty after all irradiation steps. At low temperatures and small fields J_c is slightly enhanced in the ^{155}Gd-123 sample, whereas J_c remains unchanged in ^{160}Gd-123 at all temperatures. This confirms that the contribution of point defects to flux pinning in high temperature superconductors is rather moderate. A further irradiation step to a fluence of about $7 \cdot 10^{20}$ m^{-2} is currently under way.

References

[1] A. Wisniewski, G. Brandstatter, C. Czurda, H. W. Weber, A. Morawski, T. Lada, Physica C **220** (1994) 181

[2] H. P. Wiesinger, F. M. Saurzopf, H. W. Weber, H. Gerstenberg, G. W. Carbtree, Europhysics. Lett. **20** (1992) 541

[3] F. M. Sauerzopf, H. P. Wiesinger, H. W. Weber, Phys. Rev. B **51** (1995) 6002

[4] G. Brandstatter, F. M. Sauerzopf, H. W. Weber, A. Aghaei, E. Schwarzmann, Physica C **235-240** (1994) 2797

[5] M. C. Frischherz, M. A. Kirk, J. Farmer, L. R. Greenwood, H. W. Weber, Physica C **232** (1994) 309

[6] K. E. Sickafus, J. O. Willis, P. J. Kung, W. B. Wilson, D. M. Parkin, M. P. Maley, F W. Clinard Jr., C. J. Salgado, R. P. Dye, K. M. Hubbard, Phys. Rev. B **46** (1992) 11862

[7] M. M. Brezgunov, S. V. Belogurov, A. E. Petrov, A. N. Karpov, I. V. Kudrenitskis, V. N. Kovalev, E. N. Kurkin, A. A. Makletsov, Yu. G. Morozov, M. D. Nersesyan, Superconductivity **3** (1990) 843

FAST NEUTRON INDUCED FLUX PINNING IN Tl-BASED HIGH-T_c SINGLE CRYSTALS AND THIN FILMS, HIGHLY TEXTURED TAPES AND MELT-TEXTURED BULK 123-SUPERCONDUCTORS

G. BRANDSTÄTTER*, G. SAMADI HOSSEINALLI*, Q.Y. HU**, C. KERN*, F.M. SAUERZOPF*, G.W. SCHULZ*, W. STRAIF*, X. YANG*, H.W. WEBER*

*Atominstitut der Österreichischen Universitäten, Vienna, Austria

**Centre for Superconducting and Electronic Materials, University of Wollongong, Wollongong, NSW, Australia

Abstract

Various compounds (Tl-2223, Tl-1223, Tl-2212) as well as material forms (single crystals, thin films, ceramics, tapes) of Tl-based high temperature superconductors were investigated by magnetic and transport techniques. Tl-2223 has a very "low lying" irreversibility line (H||c) and negligible critical current densities J_c at 77 K. However, the irreversibility line shifts to higher fields and temperatures and J_c is strongly enhanced, even at 77 K, after fast neutron irradiation. In contrast, the related Tl-1223 compound has a much steeper irreversibility line (H||c) similar to that of Y-123. J_c is significant up to 77 K, even in the unirradiated state, and can be largely improved by neutron irradiation. Transport measurements made on Tl-1223 tapes still show much lower critical current densities. Tl-2212 and Tl2223 thin films have J_c's at 77 K, which are comparable to those of Tl-1223 single crystals. Transport measurements on highly textured Bi-2223 tapes as well as flux profile measurements on Nd-123 bulk superconductors confirm the beneficial effects of neutron induced defects (collision cascades) for flux pinning.

1. Introduction

In contrast to classical technical superconductors such as Nb_3Sn, most of the high temperature superconductors show a very wide range in their (H,T)-phase diagram, which is charaterized by a reversible state. Although this opens up the possibility of determining essential mixed state parameters such as the penetration depth of the upper critical field, which is of interest for a fundamental understanding of superconductivity in these materials, many attempts have been made to increase the irreversible state, which is usually very small and separated from the reversible regime by the so called irreversibility line. Only in the irreversible state currents can be carried without dissipation. For applications of superconductors critical current densities $J_c<5\ 10^8\ Am^{-2}$ in fields of at least 2 T are required, but this has not yet been reached in practical materials at liquid nitrogen temperature. Although there is a variety of superconductors with $T_c<100$ K, they all have one common problem: vortices are only weakly pinned because of the two-dimensional (2D) charcater of these materials and the high temperatures they are used at.

Flux pinning can be improved by subjecting the material to fast neutron irradiation leading to a tremendous increase of J_c and a shift of the irrevesibility line to higher fields and temperatures [e. g. 1]. We will show that this is also the case in Tl-based superconductors. Furthermore, results on one member of the large family of Tl-cuprates, i. e. the one with the 1223 structure with only one Tl-layer in between the Cu-O-layers, will be discussed. Its high irreversibility line, comparable to that found in Y-123 or even higher, and the high J_c-values render this material a candidate for future applications. In this paper, studies of the irreversibility line and Jc on Tl-1223 (ceramic and single crystal) and on Tl-2223 single crystals, in both cases prior

to and following neutron irradiation, are presented. They are compared to transport critical current densities measured on Tl-2212 and Tl-2223 thin films and on Tl-1223 tapes. Furthermore, we will briefly discuss enhancements of transport J_c's in highly textured Bi-2223 tapes [2] and of critical current densities in bulk Nd-123 [3] superconductors.

2. Experimental

Single crystals with the nominal composition Tl-1223 were examined by SQUID-magnetometry. For a detailed description of the growth of these compounds, see [4, 5, 6]. The crystals are small plateletes with dimensions 1030·430·65 μm^3 (Tl-2223) and 380·350·108 μm^3 (Tl-1223), respectively. They were mounted onto small U-shaped aluminium sample holders, which fit into an aluminium rod and allow a reproducible and accurate orientation with respect to the field. Hysteresis loops were measured in an 8T-SQUID magnetometer up to an applied field of 8 T; zero-field-cooled (ZFC) and field cooled (FC) measurements were carried out both in the 8 T- and in a 1 T-SQUID magnetometer with H||c. The superconducting transition temperature was measured in an applied field of 1.1 mT with H||ab. The Tl-2223 single crystal was subjected to fast neutron irradiation (E<0.1 MeV) to fluences of $2 \cdot 10^{21}$ m^{-2}, $4 \cdot 10^{21}$ m^{-2}, $8 \cdot 10^{-21}$ m^{-2}, and $16\ 10^{21}$ m^{-2}, for the Tl-1223 single crystal only the first three irradiation steps are available at present.

(TlPb)$Sr_2Ca_2Cu_3O_9$-ceramics were prepared as described e. g. in [7]. From the resulting pellet a cubic piece (2·2.5·1.84 mm^3) was cut and examined by SQUID magnetometry. The average grain size determined from SEM photographs is 4.2 μm.

Measurements of the transport critical current densities were made on Tl-2223 [8] and Tl-2212 [9] thin films as well as on Tl-1223 and Bi-2223 [10] tapes. The epitaxial thin films were deposited onto single crystalline $LaAlO_3$ substrates and patterned to bridge dimensions of 15-28 mm width, 400-6000 mm length, and thicknesses between 150 nm (Tl-2212) and up to 1550 nm (Tl-2223). Large contact pads (~0.5 mm^2) were covered with silver layers. Indium was used as a buffer between the silver contact pins and the film, which resulted in sufficiently low contact resistances. J_c was defined by an electric field criterion of 10 mV/cm. A rotating device allowed us to vary the orientation of the films with respect to the field direction ($\upsilon=0°$: H||ab), but the current was always kept prependicular to the c-axis.

The silver sheated tapes were fabricated by the "powder in tube" (PIT) technique. They were glued onto a small copper plate. This plate is isolated with a thin ceramic layer and has four contact pads for the transport measurements. The sample can be measured in fields up to 6 T at temperatures between 2 K and 150 K. The orientation of the tape in the magnetic field can be varied by rotating the sample holder, keeping the field and current perpendicular to each other. 0° corresponds again to H||ab and 90° to H||c. The angular resolution is better than 1°. The critical current was determined using a standard four probe DC technique and a criterion of 1 mV/cm.

Finally, the bulk 123-superconductors were investigated by the flux profile technique [11] and by ac susceptibility in an 18 T magnet system. The sample were cut into cubes of about 3·3·3 mm^3 with their edges being parallel to the main crystallographic directions.

All the irradiations were made in the central irradiation facility of the TRIGA Mark-II reactor in Vienna, whose flux density distribution has been established accurately [12]. At full reactor power, the flux density of fast neutrons amounts to $7.6 \cdot 10^{16}$ $m^{-2}s^{-1}$ (E>0.1 MeV). The sample temperature during irradiation is not well known, but estimated to be < 50 °C. During irradiation, the samples were kept under He atmosphere in a sealed quartz cylinder, which was inserted into an open aluminium container.

3. Transition Temperature

T_c was measured on all single crystals in the unirradiated state as well as after each irradiation step. Tl-2223 has the highest T_c (121.5 K), which decreases continuously with irradiation (120.5 K, 118 K, 117.3 K 113.5 K). T_c as a function of fluence shows a small plateau at the lowest fluence [13], but generally a linear decrease with a slope of -4.8 K per 10^{22} neutrons/m^2. This decrease is more pronounced than in Y-123 [14]. Tc should reach 0 K at a fluence of 3 10^{23} neutrons/m^2, which is almost three times higher than for Y-123, because of its higher T_c (15). The Tl-1223 single crystal has a much lower T_c of 107 K, which is even lower than values found by other groups for this material [6]. Only the bulk sample and the Tl-1223 tape show transition temperatures similar to published data (114 K and 117 K, respectively). The decrease of Tc with neutron fluence in the Tl-1223 single crystal is almost linear (107 K (unirradiated), 105.2 K (2 1021 m^{-2}), 104.7 K (4 1021 m^{-2}), and 101.7 K (8 10^{21} m^{-2})) with a slope of -6.37 K per 1022 neutrons/m^2, which represents a much stronger decrease than in Tl-2223. Furthermore, the small plateau at the lowest fluences is not found. T_c of the films was found from resistivity measurements (I = 1 μA) to be 111 K (Tl-2223), about 10 K below that of the single crystal, and 107.5 K for the Tl-2212 film. The transition temperatures of the Bi-2223 tape and of the Nd-123 sample are in agreement with published results.

4. Critical current densities J_c of the Tl-superconductors

The critical current densities J_c of the single crystals were calculated as a function of the local induction B using an anisotropic Bean model, which takes demagnetization effects into account [16]. A simple bean model was employed for the determination of the intragrain critical current densities as a function of the applied field for the polycrystalline bulk sample. The grains were assumed to be infinite cylinders. A direct comparasion between J_c of the single crystals and the bulk sample is possible, since the difference between B and moH is very small. Figure 1 shows J_c for the Tl-2223 and Tl-1223 single crystals at 10 K for Hllc. J_c of Tl-2223 is strongly temperature and field dependent and disappears above 40 K. Tl-1223 shows fishtails, which are already pronounced at 10 K and keep J_c nearly constant (about $2.3 \cdot 10^{10}$ Am^{-2}) over a wide local induction range at 10 K, at least up to 8 T. Compared to Tl-2223, the temperature dependence of Jc is not so strong, it drops below 109 Am^{-2} only above 60 K and is still significant (about $2 \cdot 10^8$ Am^{-2}) at 0.5 T and 77 K. The polycrystalline Tl-1223 sample does not show a fishtail effect. J_c is higher than in the single crystals and higher than in Y-123 (~10^{10} Am^{-2}), namely 10^{11} Am^{-2} at 5K and $5\text{-}12 \cdot 10^9$ Am^{-2} at 40 K. Even at 93 K hysteresis loops were found, which correspond to a critical current density of $2.7 \cdot 10^8$ Am^{-2} at 0.5 T.

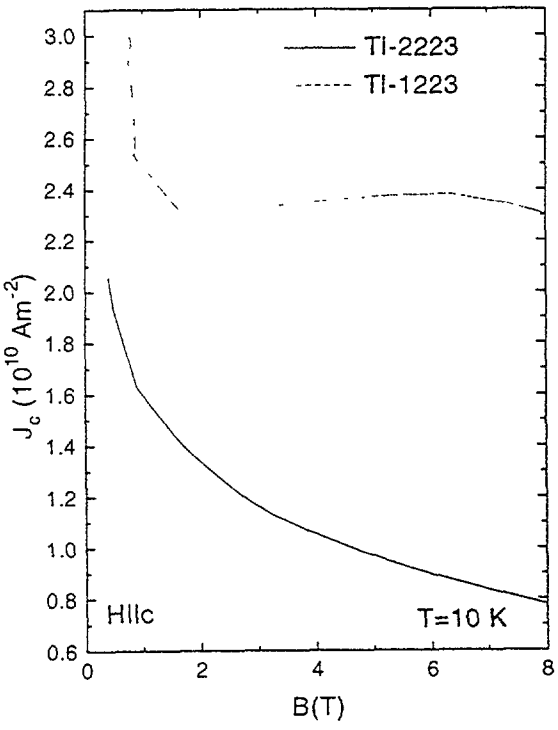

Fig. 1. Comparasion of J_c at 10 K in Tl-2223 and Tl-1223 single crystals.

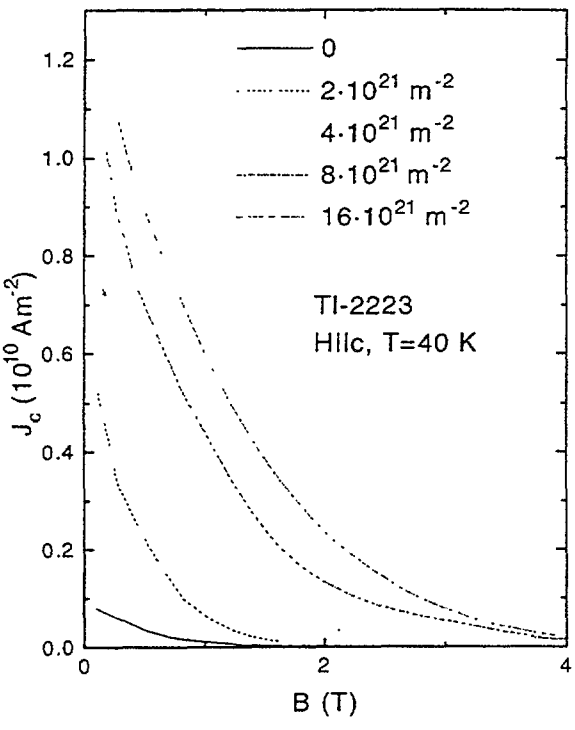

Fig. 2. J_c in a Tl-2223 single crystal irradiated to different fluences.

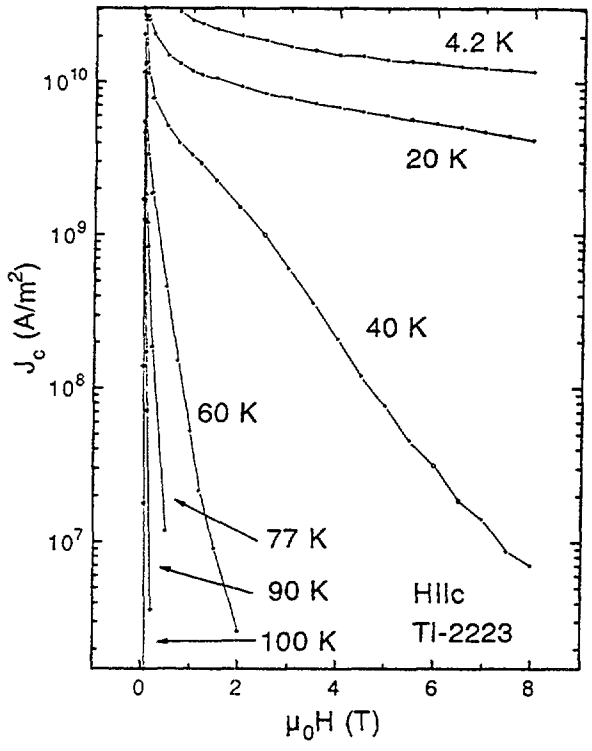

Fig. 3. J_c of a Tl-2223 film.

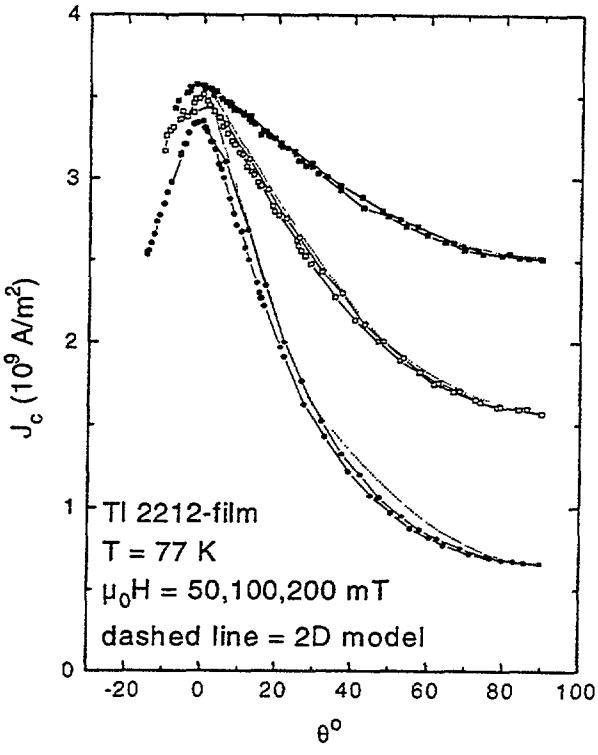

Fig. 4. J_c anisotropy in Tl-2212.

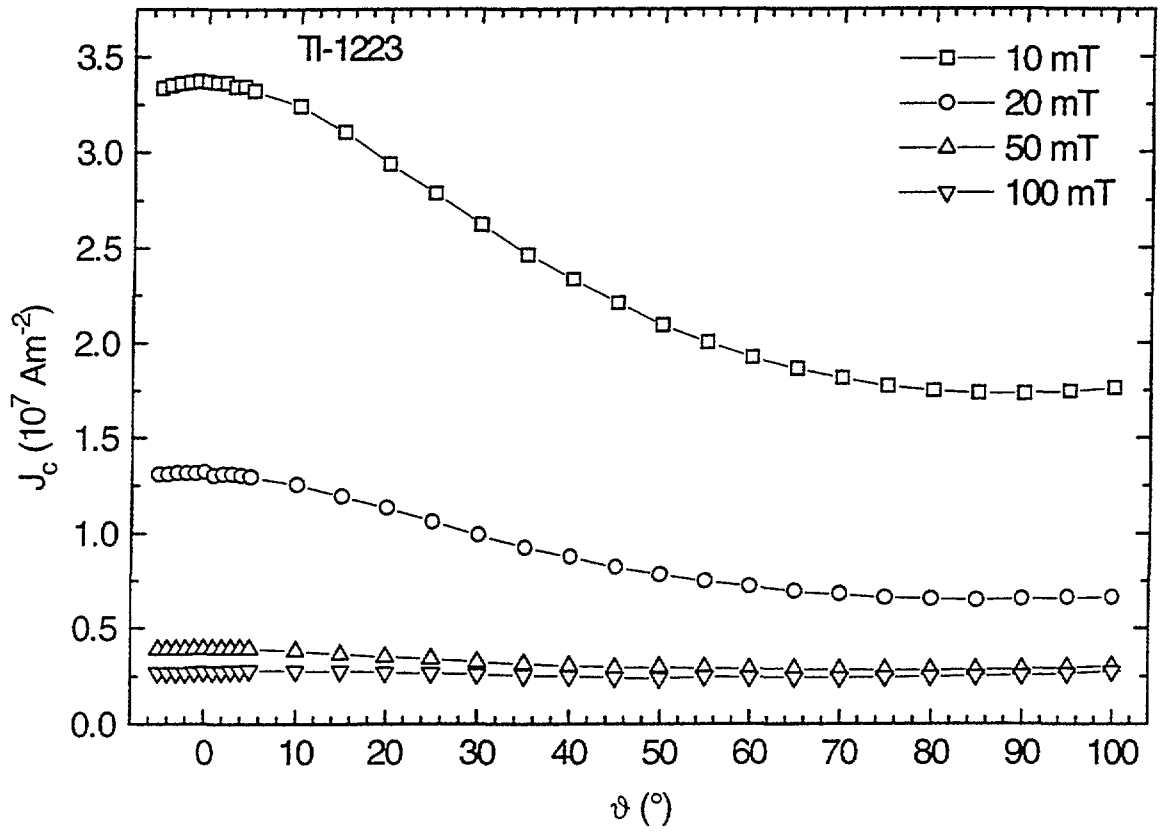

Fig 5 J_c anisotropy in a Tl-1223 tape at 77 K.

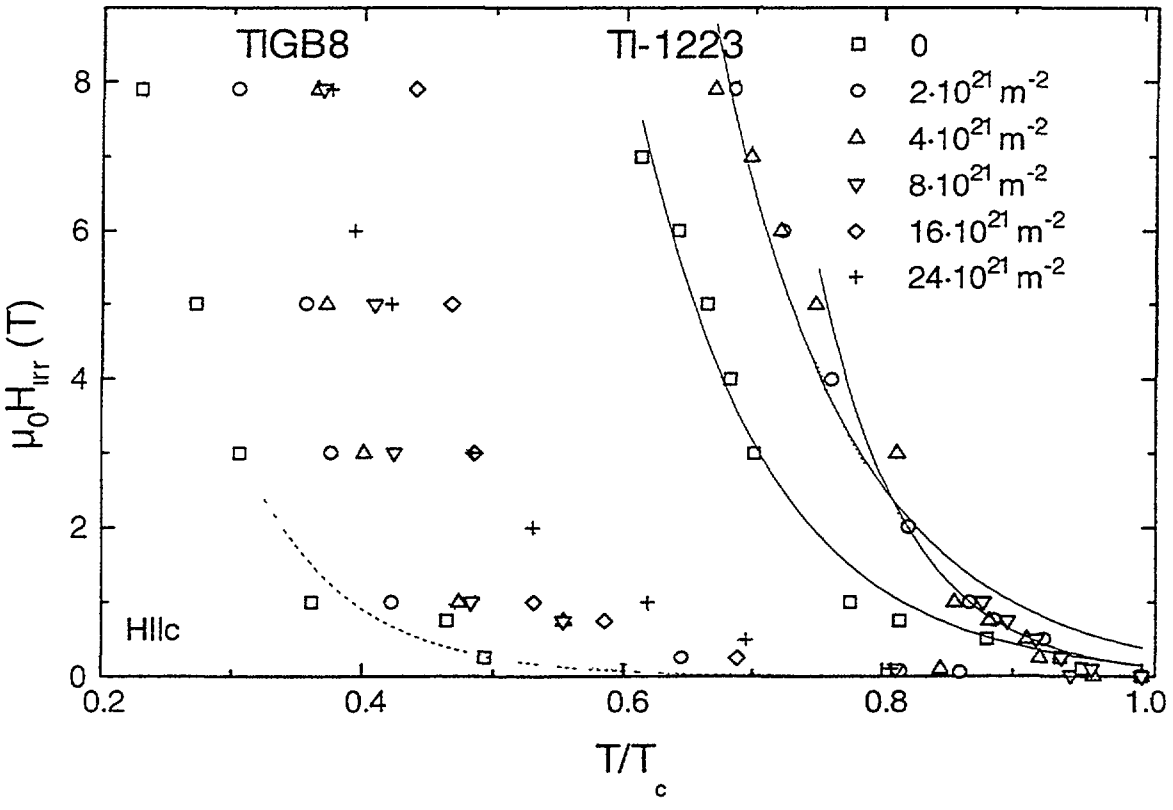

Fig 6 Irreversibility lines of Tl-2223 and Tl-1223 single crystals.

The best Tl-2223 single crystal was subjected to fast neutron irradiation to cumulative fluences up to 16 10^{21} m^{-2}. The J_c-values increase systematically after each irradiation step. At 1 T and 5 K, J_c changed from about $2.7 \cdot 10^{10}$ Am^{-2} to $5\text{-}6 \cdot 10^{10}$ Am^{-2} after the last irradiation step. At 40 K and 1 T the increase is much more pronounced, from $1 \cdot 10^8$ Am^{-2} to $6.1 \cdot 10^9$ Am^{-2} corresponding to an enhancement factor of 61 (Figure 2). At 77 K, critical current densities above $5 \cdot 10^7$ Am^{-2} are observed for B>0.3 T. After the last irradiation step J_c is of the same order of magnitude of small inductions as for Tl-1223 in the unirradiated state.

Neutron irradiation of the Tl-1223 single crystal led to similar results. The fishtails disappeared after the first irradiation step, leading to a strong enhancement at low and high inductions, respectively. J_c at 77 K and at 0.5 T increased from $2.19 \cdot 10^8$ Am^{-2} (unirradiated) to $1.4 \cdot 10^9$ Am^{-2} ($2 \cdot 10^{21}$ m^{-2}), $1.9 \cdot 10^9$ m^{-2} ($4 \cdot 10^{21}$ m^{-2}), and finally to $2.14 \cdot 10^9$ Am^{-2} after the last irradiation step, i.e. by one order of magnitude. A similar behaviour is found at lower temperatures. At 40 K and 1T J_c increased from $3.23 \cdot 10^9$ Am^{-2} (unirradiated) to $2.5 \cdot 10^{10}$ Am^{-2} ($8 \cdot 10^{21}$ m^{-2}) corresponding to an enhancement factor of 7.7. Even at 93 K J_c-values up to $3 \cdot 10^8$ Am^{-2} are found below 0.2 T after the last irradiation step. At this temperature J_c was zero before irradiation.

Transport critical current densities as a function of the applied field at several temperatures are shown in Figure 3 for a Tl-2223 film. The J_c-values are of the same order of magnitude as in the Tl-2223 single crystal, i.e. $\sim 8 \cdot 10^9$ Am^{-2} (Tl-2223) and $\sim 5 \cdot 10^9$ Am^{-2} (Tl-2212) at 4 T and 20 K. Rotation measurements performed on the Tl-2212 and Tl-2223 films, reveal 2D behaviour [17] (Figure 4), even up to transition temperature. The anisotropy is higher in the Tl-2223 films than in Tl-2212, and the critical current density is much more field dependent.

For the Tl-1223 tape the field dependence of the transort critical current density with the magnetic field applied parallel and prependicular to the tape surface, was measured at 77K and 4.2 K up to 3T. The zero field value of the crytical current density J_c is $1.9 \cdot 10^8$ A/m^2 at 4.2 K and it is 8.4 10^7 A/m^2 at 77 K. However, J_c still drops very rapidly in magnetic fields, and disappears at about 0.2 T at both temperatures. Rotation measurements in fixed magnetic fields were made at the same temperature (Figure 5). The flat behaviour near 0° shows that the sample is poorly textured. Applying a 2D-model to the rotation measurements, the misalignment angle of the grains inside the tape can be obtained [18]. It is found to be approximately 16°, i.e. more than twice as high as in Bi-2223 tapes (cf. Below).

5. Irreveribility lines

For the single crystals and the bulk sample the irreversibility lines were determined using a method based upon the distortion of the SQUID response curve. For a detailed description of this technique see [19, 20]. Results for $\mu_o H_{i\pi}$ as a function of the reduced temperature $t=T/T_c$ are plotted in Figure 6. The reversible regime of Tl-2223 is very large and extends almost down to $t \approx 0.5$, leading to a very small initial slope of the irreversibility line. A rapid increase occurs below $t \approx 0.3$. Although Tl-1223 is more three dimensional, like for example Y-123, the shape of the irreversibility line is more related to that of the Tl-2223 compound. The form of the irreversibility line can be described by an exponential law $\mu_o H_{i\pi}(t)=b \cdot \exp(-at)$ with fit parameters a and b.

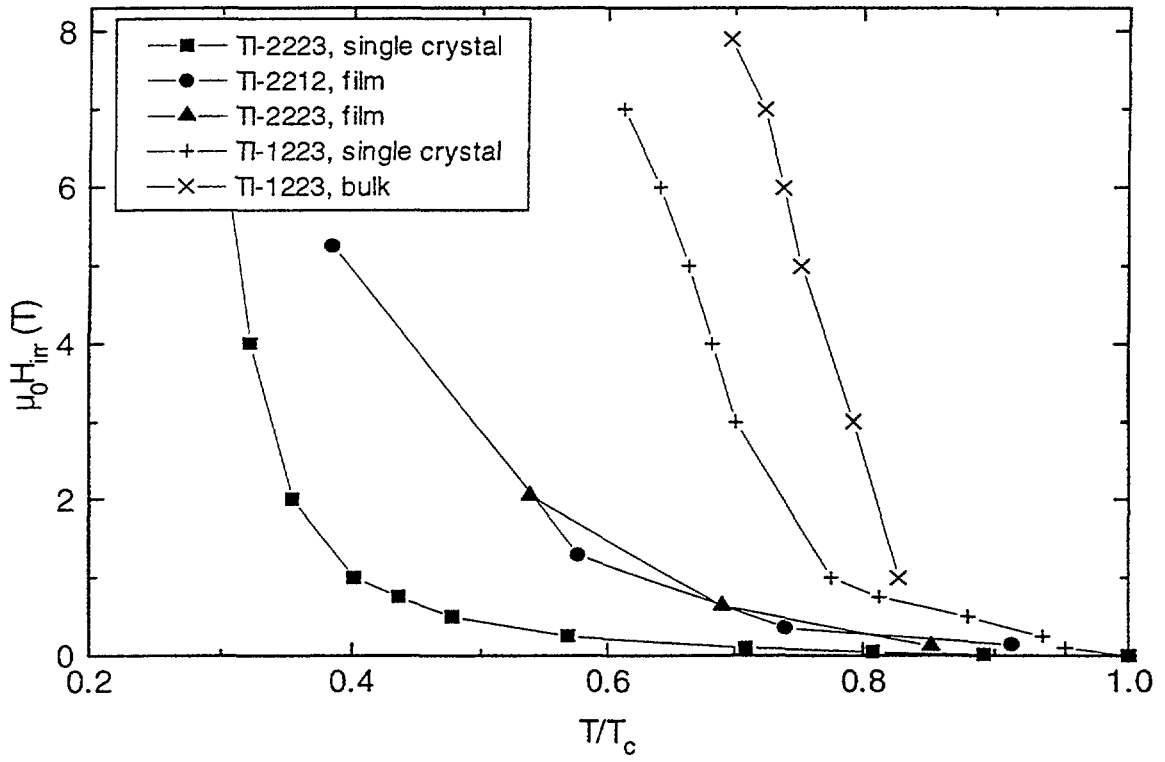

Fig. 7. Comparison of irreversibility lines in single crystals and thin films.

After each irradiation step the irreversibility line of the Tl-2223 single crystal (Hllc) shifts to higher fields and temperatures. Between the last two irradiation steps there is almost no change indicating that $16 \cdot 10^{21}$ m^{-2} is probably the highest fluence the material can sustain without major degradation of superconductivity. Compared to the irreversibility line of Tl-1223 in the unirradiated state, they are still much lower and folow again an exponential law.

Neutron irradiation of the Tl-1223 single crystal has led to the following results (Hllc). After the first irradiation step ($2 \cdot 10^{21}$ m^{-2}) the irreversibility line is shifted to higher fields and temperatures. After the second and third step ($8 \cdot 10^{21}$ m^{-2}) no further changes are observed within experimental uncertainity. Thus, the increase of the irreversible regime is much more moderate than in Tl-2223. However, since J_c is still enhanced and the decrease of T_c is not dramatic after the third irradiation step, a further moderate shift of the irreversibility line may be expected after subjecting the sample to a fluence of $16 \cdot 10^{21}$ m^2.

Using a criterion of $4 \cdot 10^6$ A/m^2, the irreversibility points at high temperatures were also calculated from the I-V characteristics of the Tl-based films. This criterion is somewhat larger than that used for SQUID measurements (~10^6 Am^{-2}). The irreversibility lines for the Tl-2212 and Tl-2223 films show the same shape as found for the single crystals. However, the rapid increase occurs already at about t=0.5, which is slightly higher than for the Tl-2223 single crystals, but still far below Tl-1223 (see Figure 7).

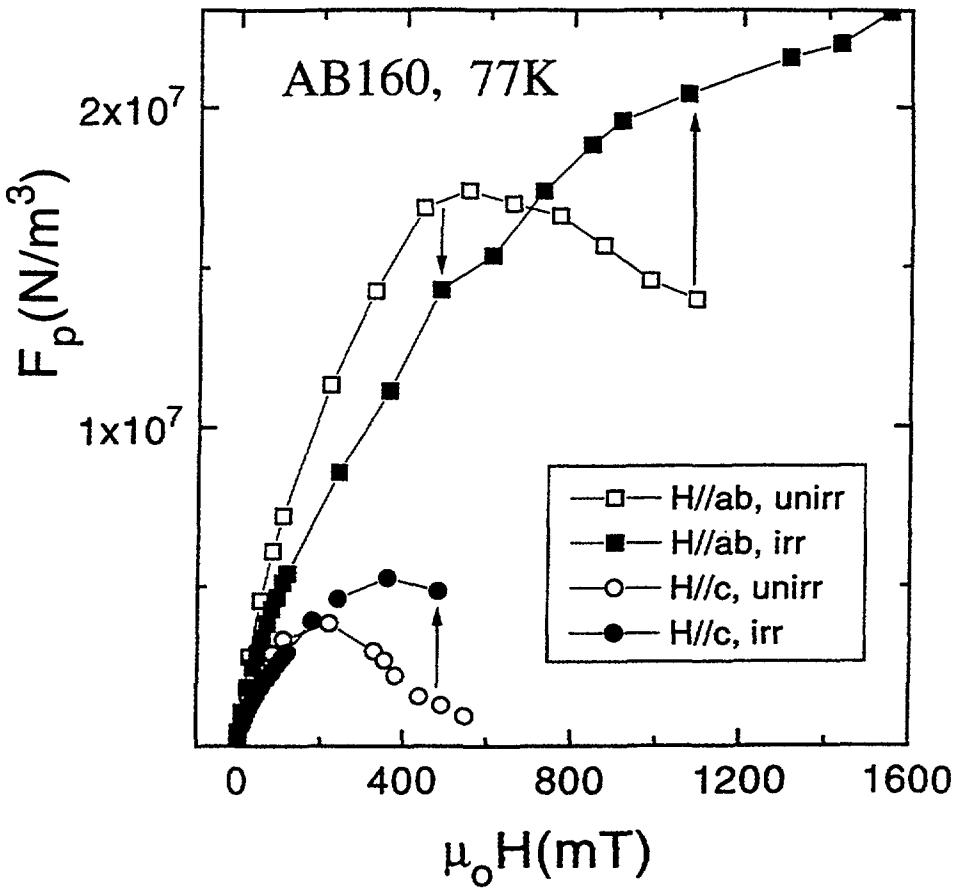

Fig. 8. Volume pinning forces vs applied field prior to and following fast neutron irradiation.

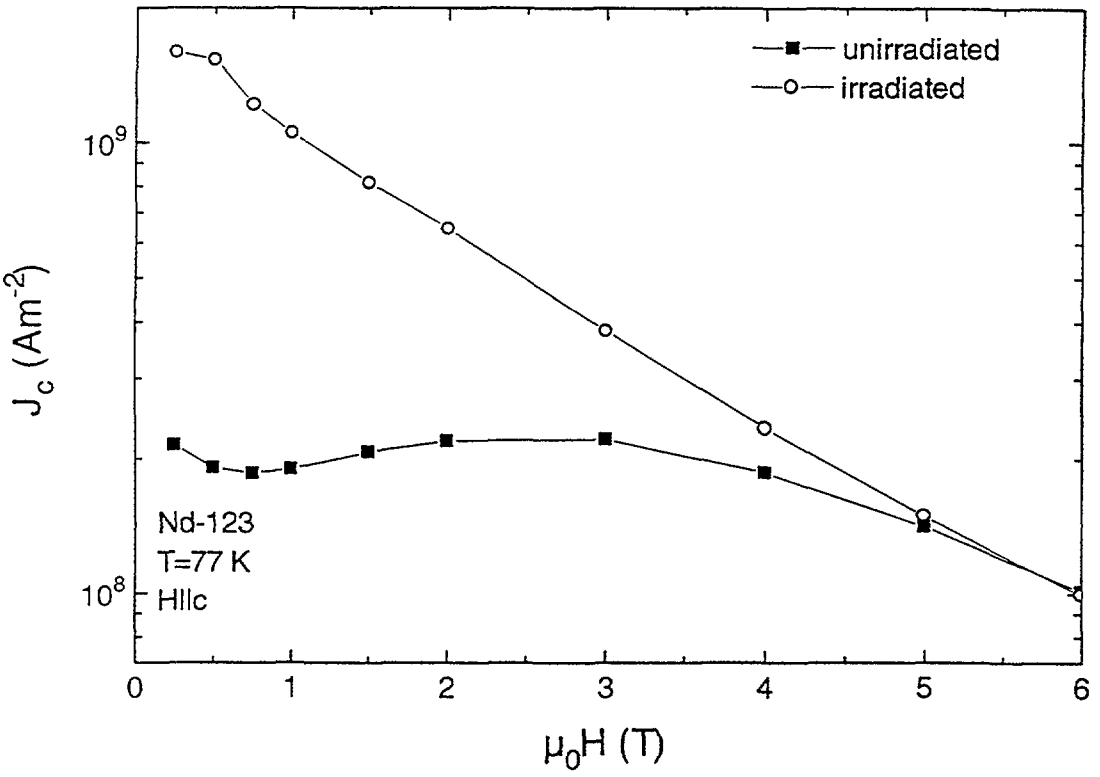

Fig. 9. J_c at 77 K in Nd-123 before and after irradiation.

6. Radiation Effects on Bi-2223 tapes

Since all of the measurements discussed so far, are based on the magnetic response of the sample and further evaluation in terms of some models, a direct transport measurements of J_c following irradiation seemed to be of considerable interest. The corresponding experiment was done on a well textured Bi-2223 tape prepared by the powder in tube technique. After characterization in the unirradiated state, the tape was irradiated to a fluence of $4 \cdot 10^{21}$ m^{-2} (E>0.1 MeV). Because of the high level of radioactivity induced in the silver sheath, a waiting time of four months was needed prior to the experiment. Typical results for the volume pinning forces at 77 K are shown in Figure 8. We note that both for Hllc and for Hlla,b, the critical current densities decrease at low magnetic fields, but then significantly increase beyond the levels in the unirradiated state. The initial degradation in the low field regime is ascribed to radiation-induced damage of the weak link structure, which has been generally observed in transport experiments on irradiated ceramics. However, once the weak link dominated field regime is surpassed, the experimental data clearly show, that flux pinning of pancake and/or Josephson vortices is obviously improved by the defects introduced by fast neutron irradiation. This holds for both major orientations of the tape surface with respect to the magnetic field. Furthermore, from a complete measurement of the angular dependence of J_c we find, that J_c still scales with the c-component of the magnetic field, i. e. that the superconductor is still in a optimization studies of this material, because it demonstrates the necessity of not only improving the grain alignment within the tapes, but also of enhancing the flux pinning capability within individual grains.

7. Critical Current Densities of Nd-123 Bulk Superconductors

Considerable progress has recently been achieved by synthesizing Nd-123 bulk materials under reduced oxygen atmosphere [3]. This leads to an enhancement of T_c by approximately 2 K compared to the standard Y-123 phase. Furthermore, a strong "fishtail" feature is introduced into the material (Figure 9), which keeps the critical current density at a relatively high level up to magnetic fields of about 5 T, in marked contrast to melt textured Y-123, where this field is close to the irreversibility point at 77 K. In fact, the irreversibility field (Hllc) reaches 9 T in Nd-123 at the boiling point of liquid nitrogen. Neutron irradiation of such a compound to a relatively low fluence ($2 \cdot 10^{21}$ m^{-2}) has led to rather spectacular results as shown in Figure 9. Because of the radiation-induced defects, the fishtail behavior is completely removed and the critical current density pushed up by a factor of ~10 to approximately $2 \cdot 10^{9}$ Am^{-2} for $H \rightarrow 0$. In present considerations for applications of these bulk materials, such data for J_c and $\mu_0 H_{irr}$ indeed push the frontiers for their application potential quite far ahead. Further work on the subject is currently under way.

SUMMARY

Various compounds as well as material forms of Tl-based high temperature superconductors were investigated. The critical current densities of Tl-2223 can be strongly enhanced and the irreversibility lines shifted to high temperatures and fields to fast neutron irradiation. However, the J_c values found in the related Tl-1223 compound and the position of its irreversibility line cannot be reached. Neutron irradiation of Tl-12223 single crystals has led to an irreversibility line, which exceeds that of Y-123 at 77 K. J_c in the presently available Tl-tapes is still very small and strongly field dependent, thus indicating weak link limitations

for the current transport. Tl-2212 and Tl-2223 films show critical current densities which are of the same order of magnitude as those for single crystals 2D behaviour is found up to the transition temperature. Attempts to improve their flux pinning capability by neutron and heavy ion irradiation are currently under way. With regard to textured materials, such as Bi-2223 tapes or Nd-123 bulk superconductors, the successful defect modification by neutron-induced collision cascades demonstrates a high potential for material optimization programs by suitable metallurgical defects.

ACKNOWLEDGEMENTS

We wish to gratefully acknowledge the cooperation of several groups, who provided us with samples as follows: F. Ladenberger and E. Schwarzmann, Universitat Gottingen; M. Manzel, Institut fur Physikalische Hochtechnologie, Jena; S. L. Yan, Nankai University, Tianjin; W. Y. Liang, IRC in Superconductivity, Cambridge; R. Galdyshevskii and R. Flukiger, Universite de Geneve; H. W. Neumuller, Siemens AG, Erlangen; and M. Murakami, ISTEC, Tokyo, We thank S. Proyer, E. Stangl and D. Bäuerle (Universität Linz) for patterning the thin films, and P. Wiede and K. Mereiter (TU Wien) for structural characterization of some Tl-based single crystals and ceramics.

References

[1] H. P. Wiesinger, F. M. Sauerzopf, H. W. Weber, H. Gerstenberg, G. W. Crabtree, Europhys. Lett. **20** (1992) 541.

[2] Q. Y. Hu, H. W. Weber, F. M. Sauerzopf, G. W. Schulz, R. M. Schalk, H. W. Neumuller, S. X. Dou, Appl. Phys. Lett. **65** (1994) 3008.

[3]S. I. Yoo, N. Sakai, H. Takaichi, T. Higuchi, M. Murakami, Appl. Phys. Lett. **65** (1994) 633.

[4] G. Brandstätter, F. M: Sauerzopf, H. W. Weber, W. Mexner, H. C. Freyhardt, A. Aghaei, F. Ladenberger, E. Schwarzmann, in "Applied Superconductivity", ed. By H. C. Freyhardt, DGM Informationsges. Verlag, 1993, 109.

[5] K. Winzer, Annalen der Physik **1** (1994) 479.

[6] K. Aihara, T. Doi, A. Soeta, S. Takeuchi, T. Yuasa, M. S. Eido, T. Kamo, S. Matsuda, Cryogenics **32** (1992) 936.

[7] W. Mexner, S. Heede, K. Heinemann, H. C. Freyhardt, B. Ullmann, F. Ladenberger, E. Schwarzmann, in "Critical Currents in Superconductors", ed. By H. W. Weber, World Scientific, Singapore, 1994, pp. 513-516.

[8] S. Huber, M. Manzel, H. Bruchlos, S. Hensen, and G. Muller, Physica C **244** (1995) 337.

[9] S. L. Yan, L. Fang, Q. X. Song, J. Yan, Y. P. Zhu, J. H. Chen, S. B. Zhang, Appl. Phys. Lett. **63** (1993) 1845.

[10] Q. Y. Hu, H. W. Weber, S. X. Dou, H. K. Liu, H. W. Neumuller, J. Alloys Comp. **195** (1993) 515.

[11] R. W. Rollins, H. Kupfer, W. Gey, J. Appl. Phys. **45** (1974) 5392.

[12] H. W. Weber, H. Bock, E. Unfried, L. R. Greenwood, J. Nuc. Mat. **137** (1986) 236.

[13] G. Brandstätter, F. M. Sauerzopf, H. W. Weber, A. Aghaei, E. Schwarzmann, Physica C **235-240** (1994) 2797.

[14] F. M. Sauerzopf, H. P. Wiesinger, H. W. Weber, G. W. Crabtree, Phys. Rev. B **51** (1995) 6002.

[15] M. C. Frischherz, M. A. Kirk, J. Farmer, L. R. Greenwood, H. W. Weber, Physica C **232** (1994) 309.
[16] H. P. Wiesinger, F. M. Sauerzopf, H. W. Weber, Physica C **203** (1992) 121.
[17] G. Samadi Hosseinali, R. M. Schalk, H. W. Weber, A. Ponninger, S. Proyer, P. Schwab, Physica B **194-196** (1994) 2357.
[18] Q. Y. Hu, R. M. Schalk, H. W. Weber, H. K. Liu, R. K. Wang, C. Czurda, S. X. Dou, J. Appl. Phys. **78** (1995) 1123.
[19] M. Suenaga, D. O. Welch, R. Budhani, Supercond. Sci. Technol. **5** (1992) 3.
[20] F. M. Sauerzopf, H. P. Wiesinger, H. W. Weber, G. W. Grabtree, Advances in Cryog. Engineering **38** (1992) 901.

NEUTRON DIFFRACTION BY THE FLUX LINE LATTICE IN $YBa_2Cu_3O_{7-\delta}$ SINGLE CRYSTALS

G. BRANDSTÄTTER, H.W. WEBER
Atominstitut der Österreichischen Universitäten,
Vienna, Austria

T. CHATTOPADHYAY, R. CUBITT, H. FISHER
Institut Laue-Langevin,
Grenoble, France

M. WILEY
School of Physics and Space Research,
University of Birmingham,
Birmingham, United Kingdom

G.A. EMEL'CHENKO
Institute of Solid State Physics,
Cernogolovka, Russian Federation

Abstract

Neutron diffraction was used to image the mixed state in a large superconducting $YBa_2Cu_3O_{7-\delta}$ single crystal. Flux line lattice structures were observed in fields up to 2 T at various temperatures from 2.4 to 80 K. The integrated intensity of one reflection was calculated as a function of temperature for three different fields. The results are discussed in terms of BCS theory.

1. Introduction

A periodic array of magnetic fields scatters neutrons elastically since it interacts with the magnetic moments of the neutrons. Thus, neutron diffraction is an excellent tool for probing Abrikosov's prediction of a vortex lattice in type II superconductors. Experiments carried out on low temperature superconductors such as Nb almost thirty years ago confirmed the existence and the bulk character of a single crystalline hexagonal flux line lattice [1]. However, although large single crystals of Nb were available, such experiments were very tricky. The lattice parameter depends upon the magnetic induction B and varies between a few hundred nm's at low inductions and only a few nm's at high inductions. As a matter of fact, the corresponding Bragg angles are only of the order of a few minutes or even seconds. Therefore, cold neutron sources providing neutron beams with longer wave lengths, l-1 nm, and detectors allowing long neutron flight paths are necessary.
Experiments on high temperature superconductors are much more difficult due to the lack of large high quality crystals and because they scatter only weakly. The penetration depth of these compounds is very large, which leads to a very small intensity I, because I is proportional to λ^{-4}. Diffraction patterns are, therefore, only visible after background substractions and are usually of low intensity, even after counting times of several hours.

2. Experimental

The quality of a large $YBa_2Cu_3O_{7-\delta}$ single crystal (10·7·2 mm^3, 0.9 g) was characterized by X-ray and neutron diffraction at NIST in 1994 and checked for its twin structure by polarized light microscopy. The sample is of a high crystalline quality with the exception of a small spot in one corner and contains a dense twinning pattern. T_c is estimated to be about 92 K according to measurements of the transition temperature on a smaller companion crystal.

The neutron scattering experiments were carried out at the small angle neutron scattering facility V4 at HMI in Berlin. The crystal was mounted onto an aluminum sample holder and inserted into a cryostat with a horizontal magnet. The crystallographic c-axis was oriented paralel to both the magnetic field and the incoming monochromatic neutron beam. The neutron wave length λ_n was set to 0.8 nm. The counting time for each point was 20 minutes (1994) and 1 hour (1995), respectively. The scattered neutrons were registrated by 32·32 cm^2 detector set at 4 to 7.2 m behind the sample. The unscattered beam was intercepted by a beam stop. The diffracted intensity in the mixed state was obtained after cooling through T_c in a certain field and after subtracting the background recorded above T_c at the same filed. Diffraction patterns as a function of temperature were measured in fields of 0.8 T, 1 T, and 2 T.

3. Results and Discussion

The diffraction pattern at 5K and 0.8 T is plotted in Figure 1, which shows a fourfold symmetry instead of a hexagonal one. This has already been reported in earlier publications [2] and is attributed to the twin structure of the crystal, since the flux lines are pinned by twinn planes. The two lower spots are of higher intensity than the upper ones, because the cryostat was tilted to satisfy the Bragg condition.

The rocking curve was taken in a field of 1 T at 6 K. It has a FWHM of 0.55(6) degrees, which is similar to previously observed values[2, 3]. They vary from sample to sample due to differing twin morphologies. The integrated intensity I as a function of temperature at different fixed fields was obtained from the diffraction patterns. It is of fundamental interest since I(T) is related to the penetration depth $\lambda(T)$ and thus can reveal the pairing mechanism of the superconducting state. For high K superconductors the form factor for certain reflections (hk) is given by [4, 5]

$$F_{hk} = \frac{1}{1+(q_{hk}\lambda)^2} \qquad (1)$$

with the reciprocial lattice vector $q_{hk} = 2\pi/d_{hk}$, $d_{hk} = \Phi_0/B$ (lattice spacing for a square lattice), and the penetration depth λ. The integrated intensity, e. g. for the (10) reflection, is then given by

$$R_{10}\frac{I_{10}}{\Phi_n} = d_{10}\lambda_n^2\left(\frac{\gamma}{4}\right)^2 V\frac{B^2}{\Phi_0^2}|F_{10}|^2 \qquad (2)$$

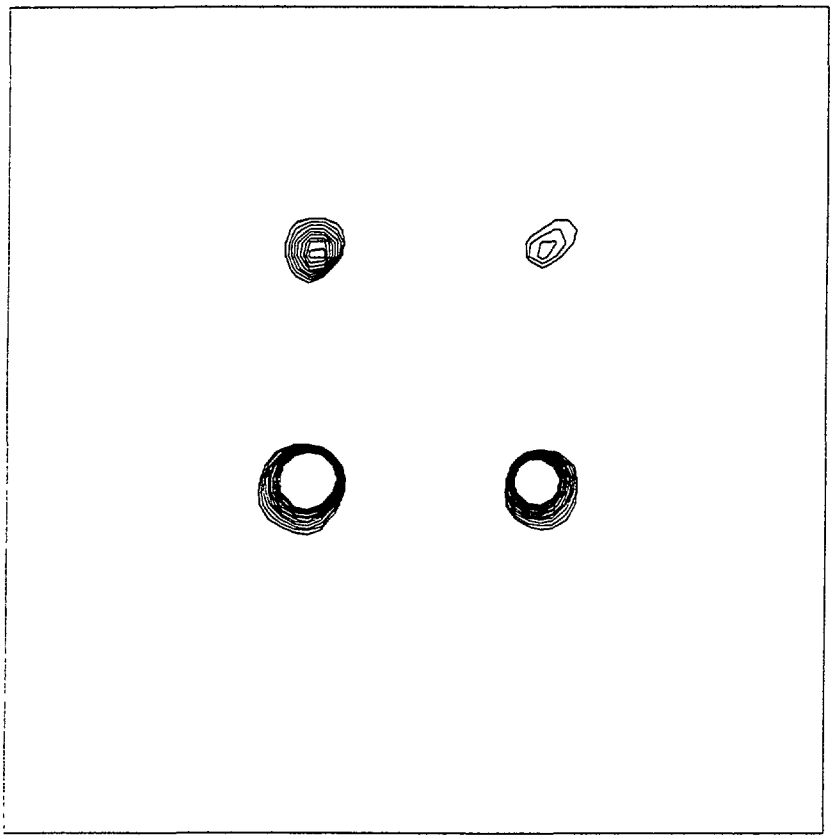

Fig. 1. Diffraction pattern of the flux line lattice in $YBa_2Cu_3O_{7-\delta}$

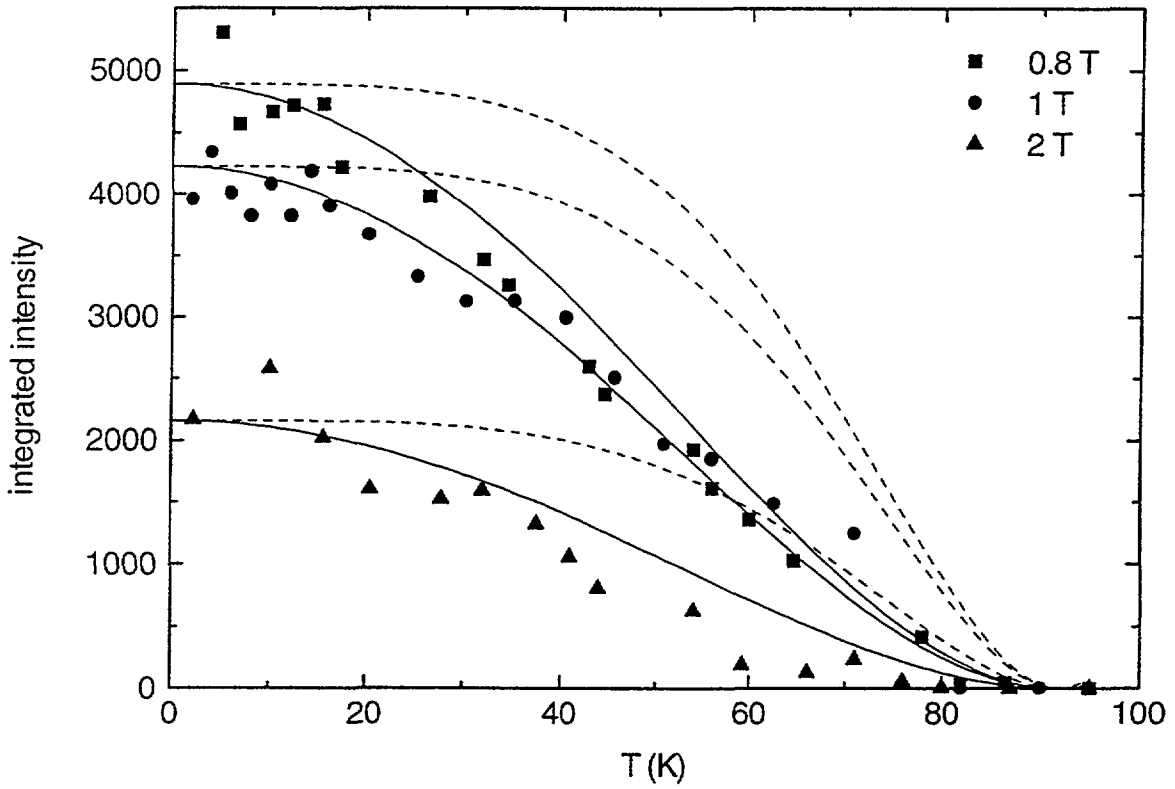

Fig. 2. I(T)-curves at different fields. Solid lines are calculated from BCS-theory, dashed lines from the two-fluid model.

where γ=-1.9131 (ratio of the magnetic moment of the neutron to μ_K), ϕ_n is the neutron fluence, λ_n the neutron wave length, and V is the volume of the sample hit by the neutrons. Therefore, I(T) displays the temperature dependence of the penetration depth. In the case of s-wave pairing, normalized λ(T)-data are tabulated in reference [6]. A fit to these data results in

$$\lambda_{ab}(T) = \frac{\lambda_0}{\sqrt{1 - t^2}} \qquad (3)$$

with $t=T/T_c$. λ_0 is the penetration depth at 0 K. Inserting Equ. (1) and (3) into Equ. (2) we get

$$R_{10}(T) = \frac{I_0}{\left(1 + \frac{\Lambda}{1 - t^2}\right)^2} \qquad (4)$$

with $I_0=\lambda_n^2(\gamma/4)^2V\cdot(B/\phi_0)^{3/2}$ and $\Lambda=4\pi^2\lambda_0^2B/\phi_0$. The neutron fluence ϕ_n was calculated from transmission experiments: $\phi_n = 1.36 \cdot 10^{13}$ m^{-2} for 4 m collimation, and $\phi_n = 1.28 \cdot 10^{13}$ m^{-2} for 8 m collimation. Figure 2 shows the experimental results $I_{10}(T)$ at different fields normalized to a standard monitor count of $1\cdot10^8$ corresponding to a counting time of 100 minutes. The solid lines are obtained from $I_{10}(T)=\phi_n R_{10}(T)$ with $R_{10}(T)$ from Equ. (4). The dashed lines represent $I_{10}(T)$ calculated with the two fluid model for λ(T) as done in many previous publications. The agreement between experiment and results obtained from the BCS-theory is excellent. However, the calculation fails for Bi-2212, which seems to indicate that the pairing mechanism is quite different from that in Y-123. Since $I_0\phi_n$ is known, it is possible to derive λ_0. We get $\lambda_0\approx205$ nm for B=0.8 T and 1 T, and $\lambda_0\approx227$ nm for B=2 T. This difference comes mainly from ϕ_n, which is not accurately known just behind the sample. λ_0 of Y-123 samples with oxygen content. Thus, as I_0, I(0), and λ_0 are all linked, high λ_0-values may only be due to the inaccurately known neutron fluence.

4. Conclusions

Neutron scattering experiments provide us with fundamental information on the pairing mechanism in high Tc superconductors. Although BCS-theory provides a good description of the experimental data, the actual piring state cannot yet be deduced within experimental uncertainty [8].

Acknowledgement

Valuable discussion with Dr. Wiedenmann (HMI) as well as with Dr. F. M. Sauerzopf and Prof. H. Kaiser (Atominstitut) are gratefully acknowledged.

References

[1] H. W. Weber and O. Hittmair, Atomkernenergie **25** (1975) 234.

[2] M. Yethiraj, H. A. Mook, G. D. Wignall, R. Cubitt, E. M. Forgan, D. M. Paul, and T. Armstrong, Phys. Rev. Lett. **70** (1993) 857.

[3] R. Cubitt et al. Physica **B 180&181** (1992) 377.

[4] J. Schelten, H. Ullmaier, and W. Schmatz, Phys. Stat. Sol. **B48** (1972) 619.

[5] H. W. Weber, J. Schelten, and G. Lippmann, J. Low Temp. Phys. **16** (1974) 367.

[6] B. Muhlschlegel, Z. Physik **155** (1959) 313.

[7] P. Zimmermann, H. Keller, S. L. Lee, I. M. Savic, M. Warden, D. Zech, R. Cubitt, E. M. Porgan, E. Kaldis, J. Karpinski, C. Kruger, Phys. Rev. **B 52** (1995) 541.

[8] G. Brandstätter and H. W. Weber, work in progress

STRUCTURE OF MINERAL GELS

I.M. MIRANDA SALVADO
Dep. Eng. Ceramica e Vidro,
University of Aveiro,
Aveiro, Portugal

F.M.A. MARGAÇA
Dep. Fisica, ITN,
Sacavém, Portugal

J. TEIXEIRA
CEA Centre d'Etudes Nucleaires de Saclay,
Gif-sur-Yvette, France

Abstract

Small Angle Neutron Scattering (SANS) measurements have been performed to investigate the nanoscale structure of materials of the systems $x TiO_2$-$(1-x)SiO_2$ and $x ZrO_2$-$(1-x)SiO_2$ with $x \leq 10$ mol % at different processing stages. The materials were prepared by sol-gel using the alkoxides method, in strong acidic conditions. Samples were studied as xerogels heat-treated at 120 and 850 °C and as wet gels at gel point and after aging. All samples showed identical microstructure at gel point, extended linear chains ~10 nm long. The aged gel has a mass fractal structure with fractal dimension of 1.7 – 1.9. The 120 °C heat-treated xerogels show homogeneous oxide regions with mass fractal structure. For the 850 °C heat-treated xerogel the oxide regions average size has reduced and it has densified as compared to 120 °C heat-treated sample.

1. Introduction

Materials of the systems xMO_2-$(1-x)SiO_2$ with x in mol % can be prepared by the alkoxide method [1] in which silicon and metalic alkoxides, $Si(OR)_4$ and $M(OR)_4$, respectively, undergo hydrolysis and polymerization via condensation reactions with elimination of H_2O and alcohol ROH. The properties of the final material strongly depend on the processing conditions namely, composition and concentration of reagents, water content, pH, temperature and heat treatment [2]. The motivation for sol-gel processing is primarily the potentially higher purity and homogeneity and the lower processing temperatures of the materials compared with traditional glass melting or ceramic powder methods.

Small Angle Scattering of Neutrons (SANS) and X-ray proved to be well suited techniques to investigate, on a nanometer scale, the microstructure of the material at the different stages of the sol-gel processing. Silica gels have been the object of intense research [2]. However, systematic studies in multicomponent gels are still very few.

SANS measurements have been carried out in gels of the systems $x TiO_2$-$(1-x)SiO_2$, and $x ZrO_2$-$(1-x)SiO_2$ with $x \leq 10$ mol %. The samples were all prepared in strong acid conditions (pH~1) and with the stoichiometric water/alkoxides molar ratio, R=4. The study focused on the variation of composition M, concentration of precursors x, aging and heat treatment of samples. The present work reports the most important SANS results obtained from fresh gels (just gelified, aged gels and xerogels heat treated at 120 °C and 850 °C.

2. Experimental

Tetraethylorthosilicate, titanium isopropoxide and zirconium propoxide were used as starting chemicals to prepare gels with x = 0, 2, 4, 6 and 10 mol % in TiO_2 and ZrO_2 in strong acidic conditions. The procedure followed in the gel preparation is described elsewhere [3, 4]. The solutions obtained were put in sealed quartz cells of 1mm thickness, at 60 °C until gelation occured. The wet gels (solutions in which flow was not visually observed) were measured by SANS after 0, 2, 4 and 6 hours at 60 °C. For the preparation of xerogels, the solutions obtained were left in Petri dishes covered with plastic foil at 60 °C for gelation. After a period of 15 days at 60 °C the gels were heat-treated at 120 °C for 48 h, and then heat-treated for 5.5 h at 850 °C. The heating rate to 850 °C was equal to 60 °C h^{-1}.

Neutron scattering measurements were performed using the PAXE instrument at the Léon-Brillouin Laboratory. A monochromatic beam of neutrons of a given wavelenght λ, with $\Delta\lambda/\lambda \sim 10$ % was collimated by diaphragms of apertures of 1.0 and 0.7 cm diameter at source and sample, respectively, separeted by distance L. The detector, position sensitive with 64 x 64 cm^3 active area and 1 cm^2 pixel area, was positioned at a distance L from the sample. Different experimental settings were used, i. e., different values of λ and L, in order to change the range of the scattering vector modulus, Q, given by $Q = 2\pi\theta/\lambda$, where θ is scattering angle.

SANS measurements were carried out in wet gels, both fresh (just gelified) and aged, keeping the sample temperature $\leq$ 8 °C, and in xerogels after heat-treatment at 120 °C and 850 °C (550 °C in the case of x = 0) with the sample at room temperature. Scattered intensities have been corrected for detector efficiency and normalized for sample thickness, transmission and incident beam flux. They have also been calibrated by the use of the incoherent scattering of 1 mm thick light water. In case of xerogels, the constant contribution to be scattered intensity has been substracted taking its approximate value as that of the average intensity at the larger Q values measured (0.41 $Å^{-1}$). Some data from wet gels were collected at different experiments at which the Q range extended only up to 0.22 $Å^{-1}$. In this case, data have been corrected for the incoherent scattering from the estimated total number of protons per unit volume in the sample.

3. Data analysis

Gels are, in general, difficult samples to deal with in what concerns interpretation of the scattering data as the chemistry involved is quite complex. Sols consist of growing units which might be hydrolized and/or polymerized in various degrees. Likewise, the products of these reactions (H_2O and alcohols) can be present in various concentration values. As a consequence the actual composition of the solvent is unknown, except that it consists mainly of water and alcohol. Similarly, the oxide network composition varies from the fresh gel to the heat treated xerogel. The contrast in wet gels (fresh or aged) originates from the rather different scattering length densities of the solvent dominated by the hydrogen of water and alcohols and that of the oxide network. In heat treated xerogels the contrast is between the oxide network and pores. The scattering law for an homogeneous solution (at Q^{-1} scale) of N particles (or pores) with volume V and scattering density ρ in an homogeneous solvent or matrix with scattering length density ρ_0 is given by

$$I(Q) = \phi \left| F\left(\vec{Q}\right) \right|^2 S(Q) \qquad (1)$$

where ϕ is the density of particles in the sampled volume, $F\left(\vec{Q}\right)$ is the particle form factor and $S\left(\vec{Q}\right)$ the structure factor. The particles are considered identical and centrosymmetric. $S\left(\vec{Q}\right)$ accounts for the spatial distribution of pores or particles in the matrix or solvent if thermal density or/and concentration fluctations are neglegible, which in most cases exist at a very small scale and give only a Q-independent contribution at small angles. If the interactions among particles are weak and there are relatively few particles in the sampled volume (dilute system), the structure factor will be that of a perfect gas: S(Q) = 1, for all Q. However, the more common situation is that where short range order is observed and the structure factor is similar to that of a simple liquid [5]. This usually manifests itself by the presence of a broad peak in the scattering law. As for particle form factor, it has a straightforward expression for simple geometrical shapes. Assuming complete desorientation of the particles it is, for spheres of radius r:

$$\left|F\left(\vec{Q}\right)\right|^2 = V^2K^2\frac{\left[3\sin(Qr)-Qr\cos(Qr)\right]^2}{(Qr)^3} \qquad (2)$$

$K=\rho-\rho_0$ being the scattering contrast, whereas for thin cylinders of length L and radius h ($h<<L$) it becomes:

$$\left|F\left(\vec{Q}\right)\right|^2 = V^2K^2\frac{\pi}{QL}\exp\left(-Q^2h^2/4\right) \qquad (3)$$

However, the low Q asymptotic behaviour of the particle form factor is independent of the particle's shape and is given by the Guinier approximation as:

$$\left|F\left(\vec{Q}\right)\right|^2 = V^2K^2\exp\left(-Q^2R_G^2/3\right) \qquad \text{for } QR_G<1 \qquad (4)$$

where R_G is the radius of gyration of the particle given by:

$$R_G = \sqrt{3/5}\,r \qquad \text{for spheres of radius r and} \qquad (5)$$

$$R_G = h/\sqrt{2} + L/\sqrt{12} \cong L'/\sqrt{12} \qquad \text{for thin cylinders with } L>>h. \qquad (6)$$

SANS data from wet gels, both fresh and aged are analysed as resulting from a system of growing particles in a solvent whereas xerogels appear as porous materials.

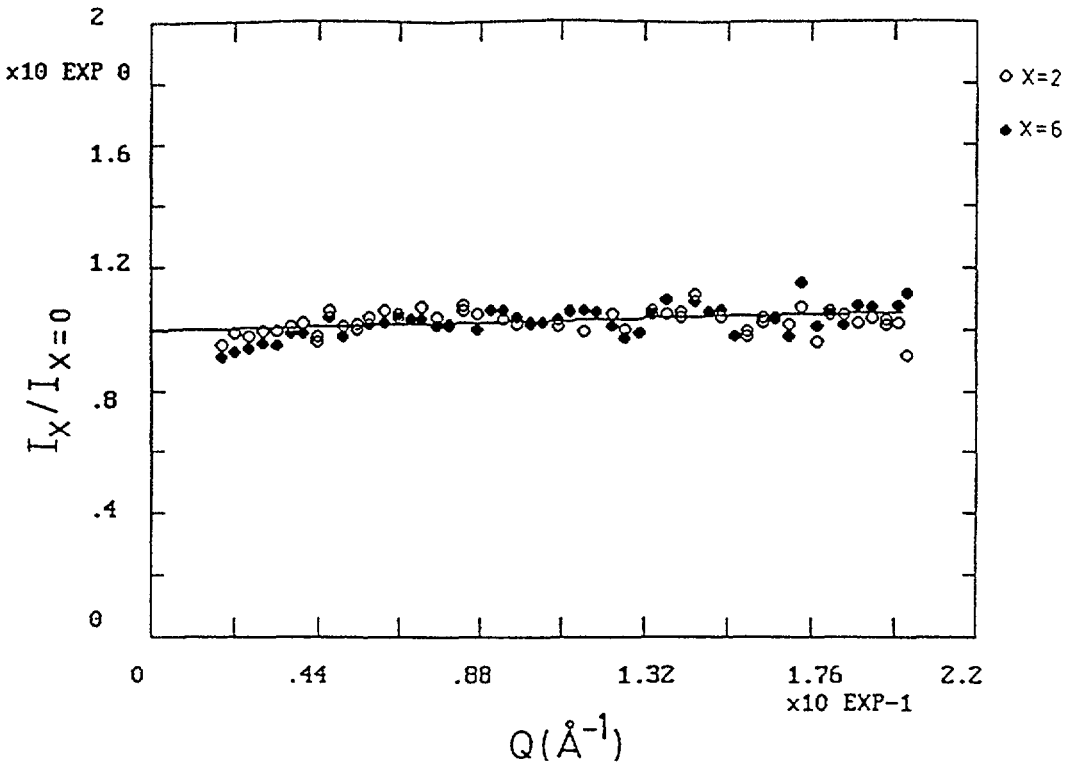

FIG. 1. Ratio of I(Q) obtained from x=2 and 6 mol % fresh $xZrO_2$-(1-x)SiO_2 gels each divided by I(Q) from x=0.

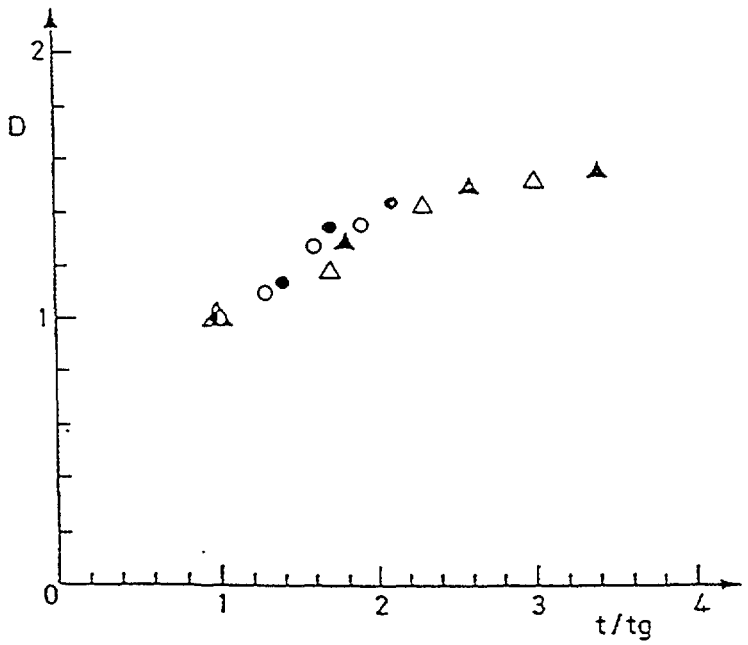

FIG. 2. Variation of the slope D in the log-log plot of I(Q) as a function of the ratio of the aging tome, t, to the gelling time, tg, for x = 0 (o), 2 (•), 4 (Δ) and 6 (▽) mol % of TiO_2.

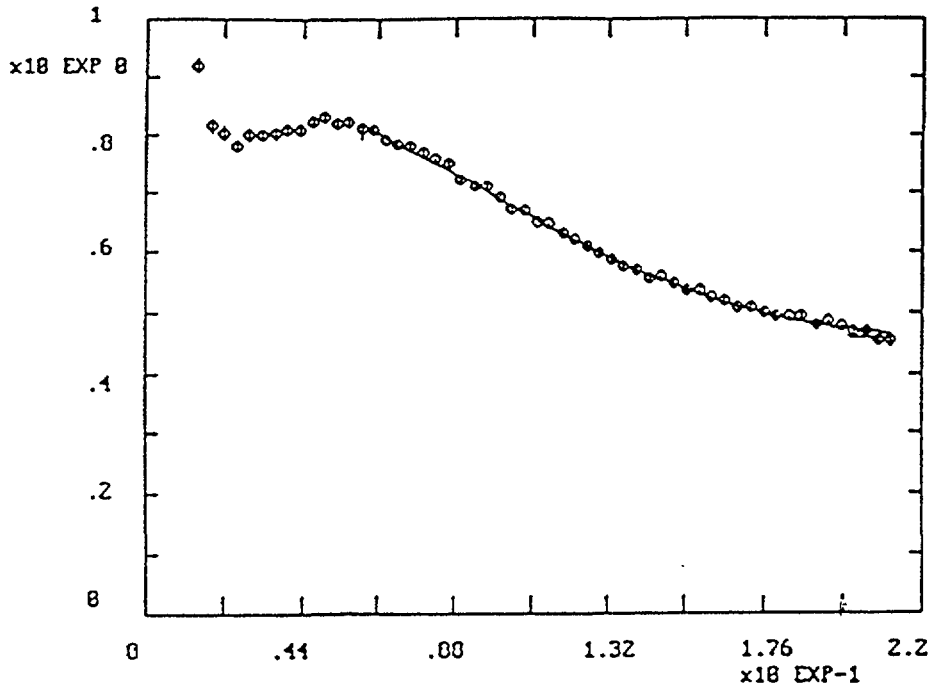

FIG. 3. I(Q) for 2 mol % TiO_2 xerogel heat-treated at 120 ^oC with fitting of a sphere from factor.

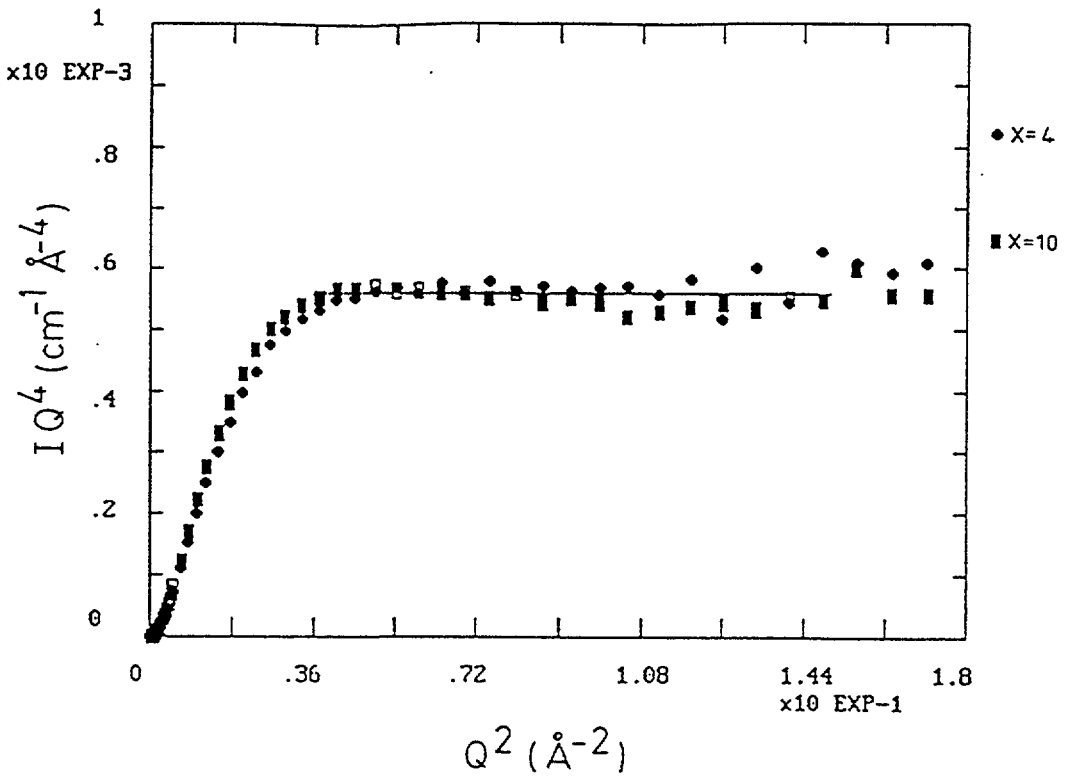

FIG. 4. I(Q) in a plot of Q^4I vs Q^2, for 850 ^oC heat-treated xerogels, with x=4 and 10 mol % ZrO_2.

4. Results and discussion

4. 1. Fresh gels

Samples at gel point, called fresh gels, originate a scattered intensity I(Q) which is a monotonously decreasing function, typical of a solution of non-interacting elongated objects. All fresh gels produce identical I(Q), within the experimental error (~10%), for all measured x values and for both TiO_2 and ZrO_2 systems. Figure 1 shows the result of the division of I(Q) for x=2 and 6 mol % fresh gels by I(Q) obtained from x=0 fresh gel, in the $x ZrO_2$-(1-x)SiO_2 system. A fairly approximate constant equal to 1 is found.

Thus, the nanostructure at gel point is independent of the amount of TiO_2 or ZrO_2 present in SiO_2, at least for x<10 mol %, as seen by SANS. The authors found for the scattering object, a gyration radius of 3 nm and cylindrical shape, the cylinder length being of the order of 10 nm [3, 6] from equations (3) and (6).

Later, SANS measurements were extended to higher Q values to obtain information on the cylinder radius. It was found to be of the order of the interatomic distance in condensed matter [7]. The picture which emerges from the set of results obtained so far is that, at the gel point, the scattering object is an extended linear polymer chain, ca. 10 nm long, whose longitudinal network should extended as

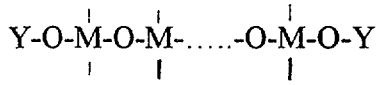

whereas, in the radial direction the oxide network is simply M-O-Y, with M=Si, Ti or Zr and Y=H or some ethyl group R. Other authors [2] have concluded that SiO_2 in acidic solutions forms linear polymers but apparently only in strong acidic solutions are these extended.

4. 2. Aged Gels

The authors first studied the aging of gels of the system $x TiO_2$-(1-x)SiO_2 [6]. It was found that the extended chains grow with aging loosing the cylindrical shape. The growth was observed to be consistent with the cluster-cluster diffusion limited aggregation model. Such model generates random or disordered systems characterized by self-similarity in real space within a characteristic length scale, often refered as, mass fractal systems, with a fractal dimension of around 1.7. Since, such a dimension between 1 and 2 indicates a loosely connected network, as branches on the tree, the above model generates an open ramified object. In this model [8] particles are placed on a lattice and allowed to move by random motion. Each time clusters approach within one lattice constant, they stick permanently and then move as a unit. The larger units then also stick on contact with other clusters. The aging of gels of the system $x TiO_2$-(1-x)SiO_2 led to a fractal dimension of ~1.7 [6] as can be observed in Figure 2. For the aged gels of the $x ZrO_2$-(1-x)SiO_2 system a slightly larger value, ca. 1.9, was obtained [7].

4. 3. Xerogels heat-treated at 120 °C

The scattering intensity from xerogels dried at 120 °C of the system $x TiO_2$-(1-x)SiO_2 with x < 6 mol % presents [3] a broad peak as well as significant scattering at lower Q, which increases with the TiO_2 content. The peak position is seen to move to lower Q with x. Beyond the peak position, I(Q) has been fitted with a sphere from factor (eq. 2), as shown in figure 3. The best fit was achieved for a diameter of 3.6 nm, for x=2 mol % xerogel. Such a sphere can be associated with pores in agreement with the results reported in [3]. The peak in I(Q) can be attributed to the presence of homogeneous regions with average diameter

$2\pi/Q_{peak}$. This equals 13 nm for the x=2 mol % sample. Given the relative sizes, the pore might be located in the meeting point of three or four oxide spheroids. SANS results from $x ZrO_2$-(1-x)SiO_2 xerogels with x<10 mol % show a broad peak at Q=0.04 $Å^{-1}$ in I(Q), for all ZrO_2 contents. Therefore, the average diameter of the oxide regions in this system is ~ 16 nm. Furthermore the internal structure of these regions was studied and found to have mass fractal nature, with a fractal dimensions < 2. This means that the homogeneous oxide region is, in fact, an open ramified network.

4. 4. Xerogels heat-treated at 850 °C

In the $x TiO_2$(1-x)SiO_2 xerogels with x<10 mol %, heat-treated at 850 °C, the scattered intensity shows a broad peak which has moved to higher Q value, as compared to the 120 °C heat-treated sample. It is Q~0.05 $Å^{-1}$ in the case of x = 2 mol %. Beyond the peak position, I(Q) has been fitted with a sphere form factor. A good fit was obtained for 3 nm diameter, for the 2 mol % sample.

In the $x ZrO_2$(1-x)SiO_2 system with $x \leq 10$ mol % xerogels produced scattered intensities with broad peaks centered at Q~0.05 $Å^{-1}$, corresponding to an average oxide region diameter of 12.5 nm. The internal structure of the oxide region was studied and found to be that of a dense particle with smooth surface, as shown in Figure 4.

5. Conclusions

For both systems, at the gel point, cylindrical clusters or extended linear polymer chains, about 10 nm long were found; these grow with aging time showing mass fractal behaviour; the growth is consistent with the cluster-cluster difussion limited aggregation model. At this stage the only apparent difference is slightly larger fractal dimention of the $x ZrO_2$-(1-x)SiO_2 aged gel 1.9, compared to 1.7 for that of $x TiO_2$-(1-x)SiO_2.

Xerogels heat-treated at 120 °C show homogeneous oxide regions with diameter of about 10-16 nm and pores with average diameter of 3-4 nm. In the $x TiO_2$-(1-x)SiO_2 xerogel these values increase with TiO_2 content, whereas in the $x ZrO_2$-(1-x)SiO_2 system they are independent on the ZrO_2 content. Xerogels heat-treated at 850 °C show similar microstructure within each system but with reduced size of both oxide region and pore as compared to the 120 °C heat-treated sample. At the same time, the low density (open ramifield) oxide regions of the 120 °C heat-treated xerogel gave rise to dense (hard core) oxide particles in the 850 °C heat-treated xerogels.

References

[1] Miranda Salvado, I. M., and Fernandez Navarro, J. M., J. Matter. Sci. Lett. 9(1990)173.

[2] Hench, L. L., and West, J. K., Chem. Rev. 90(1990)33.

[3] Miranda Salvado, I. M., Margaca, F. M. A., and Teixeira, J., J. Non-Cryst. Sol. 163 (1993) 115.

[4] Miranda Salvado, I. M., and Fernandez Navarro, J. M., Proc. XVI. Int. Congress on Glass, Bol. Soc. Esp. Ceram. e Vid., 31c(1992)251.

[5] Teixeira J., in "Structure and Dynamics of Strongly Interacting Colloids and Supramolecular Aggregates in Solution", Edited by Chen, S-H., et al., (Kluwer Academic Pub., 1992) p.635.

[6] Miranda Salvado, I. M., Margaca, F.M.A., and Teixeira, J., J. Sol-Gel Sci. and Techn. 2(1994)289.
[7] Margaca, F. M. A., Miranda Salvado, I. M., and Teixeira, J., J. Non-Cryst. Solids (1995) in press.
[8] Schaefer, D. W., and Keefer, K. D., in "Better Ceramics Through Chemistry II", Vol. 73 Edited by Brinker, C. J., Ulrich, D. R., and Clark, D. E. (north-Holland Amsterdam 1986), p. 277.

STUDY ON FUNCTIONAL HEAT-RESISTANT CERAMICS SiC USING SMALL ANGLE NEUTRON SCATTERING

LI JIZHOU, YANG JILIAN, KANG JIAN, YE CHUNTANG
China Institute of Atomic Energy,
Beijing, China

Y. ITO, S. IMAI
Institute for Solid State Physics,
University of Tokyo,
Tokyo, Japan

Abstract

The mechanical properties of functional heat-resistant silicon carbide SiC ceramics are significantly influenced by the concentration and dimensions of pores. 3 SiC samples with different densities were sintered with different kind and amount of additives (such as Al_2O_3, B_4C and C) using different sintering conditions of the Department of Material Science and Engineering at the University of Science and Technology in Beijing. Small angle neutron scattering measurements for 3 SiC samples were carried out at C1-2 SANS instrument of the University of Tokyo in Japan Atomic Energy Research Institute. The neutron data with 8 and 16 m of secondary flight path and 10 and 7 Å of neutron wave length respectively have been obtained. After deducation of background measurement and transmission correction, both neutron data were linked up with each other. The cubic patterns of 3 neutron data with Q range from 0.0028 - 0.05 $Å^{-1}$ are almost with axial symetry. It shows that the shape of pores, whose dimensions are relative to the Q range, is almost spherical. For spherical particles (or pores) we can obtain an expression of size distribution directly, using Mellin Transform (J. Appl. Phys. 45, 1974, 46.). According to our calculating program for the expression, the size distribution of pores for 3 samples were obtained. The average size (~190 Å) of pores for hot-pressed SiC sample with more density is smaller than others (~210 Å). It seems to be the reason why the density of hot-pressed SiC sample is higher than no-hot-pressed sample.

1. Introduction

The functional heat-resistant ceramic, silicon carbide, SiC, is a highly feasible material for high temeprature engineering applications [1]. Nowdays, hot-pressure sintering SiC has been widely used for the parts material of heat engines. It can resist the temperature as high as its decomposition temperature (2300 °C), the high temperature strength decrease only a little, and the thermal expansion coefficient is very small.

For hot-pressure sintering SiC, the effects of additives (B_4C and C [2], as well as Al_2O_3 [3] and other processing parametrs on the sintering behaviour and mechanical properties were studied. The results can be summarized as follows:

1. Boron carbide, carbon or aluminium oxide are jointly necessary as additives for obtaining hot-pressed SiC of high density. The lower limit of B_4C, C or Al_2O_3 addition required to give high density is about 0.5 % .
2. The strength of hot-pressed SiC is about 500 MPa which remains almost unchanged from room temperature up to 1400 °C and is nearly irrelevant to carbon content up to 3 %.
3. The samples of SiC containing 1 % B_4C and 3 % C hot-pressed at 2050 °C for 45 minutes under pressure of 40 MPa possesses the following properties: density 3.17 g/cm^3, bending

strength at room temperature 480 MPa, coefficient of thermal expansion 4.6 x 10^{-6}/°C, hardness HRA 93.5.

4. Comparing with the sample of density 3.17 g/cm^3, there are a lot of pores inside the SiC crystallites and the crystal boundary for other sample (such as density 3.00 g/cm^3, at 2000 °C).

In this paper, the size, shape and distribution of pores in SiC samples, which were sintered with different kind and amount of additives as well as different sintering conditions, are studied using SANS (small angle neutron scattering) technique.

2. Sample preparation

The silicon carbide SiC samples with different kind and amount of additives (such as Al_2O_3, B_4C and C) were prepared by the Department of Material Science and Engineering of University of Science and Technology (Beijing). The prepared samples for the experiments with SANS are as follows:

sample	size(mm)	additives	sintering conditions	density
No. 1 SiC	∅11.5x2.6	Al_2O_3, B_4C, C	hot-pressed	2.97 g/cm^3
No. 2 SiC	∅10.0x5.7	Al_2O_3 , B_4C, C	no hot-pressed	2.63 g/cm^3
No. 3 SiC	∅10.0x5.7	Al_2O_3 , Boric acid, C	no hot-pressed	2.60 g/cm^3

All samples were sintered using pure alpha-SiC powder (~3μ) as main component, and using Al_2O_3 powder (325-mesh) as one of additives (3 wt %). Boron carbide, B_4C, (325-mesh, 1 wt %) and carbon, C, (1 wt %) were used as other additives for both samples No. 1 and No. 2. For sample No. 3, the additive of boron was in the form of boric acid. At first, mixtures of SiC and additives were formed into sheets by cold-pressing. Then the sheets were sintered at temperature 1950 °C to 2000 °C for 1 hour. Hot pressing was conducted at 0.3 MPa only for sample No. 1.

3. Chinese SANS Spectrometer

A samall angle neutron scattering spectrometer has been designed and manufactured. The SANS spectrometer was installed at the end of neutron guide tube using cold neutron beams coming from the Heavy Water Research Reactor of the China Institute of Atomic Energy.

The main technical specifications are the follows:

Monochromator	Mechanical Selector
Incident neutron wavelength	3 - 10 Å
Incident beam wavelength resolution	$\Delta\lambda / \lambda \sim 16$ %
Source to sample distance	5 m
Sample to detector distance	2 - 4.2 m
Q range	$0.01 < Q(Å^{-1}) < 0.1$ (for λ=6 Å)
Maximum flux for sample position	64x64 elements 2D position sensitive detector
Detector	with each element of 1x1 cm in size

Unfortunately, the 2D position sensitive detector was unworkable because one of anode wires was broken. Up to now, we can only use an assembly detector consisting of 15 pieces of He^3 counter to do SANS experiments. The sample size to be needed is a cuboid of 5x5x30 mm.

So, this SANS spectrometer was not suited for the SANS experiments of round SiC sample. The SANS experiments for the SiC samples were performed at C1-2 SANS instrument, which belongs to the Institute for Solid State Physics (ISSP) at the University of Tokyo, located at the JRR-3 reactor of Japan Atomic Energy Research Institute (JAERI).

4. Japanese C1-2 SANS Instrument

In the Guide Hall of JRR-3 reactor of JAERI, there are three guide tubes (C1, C2 and C3) of cold neutron and two tubes (T1 and T2) of thermal neutron. 15 neutron scattering instruments are installed at 5 tubes respectively. The C1-2 SANS instrument with a two-dimensional position sensitive detector is located at the end of C1 tube.

The 2D position sensitive detector with multidetector of 128x128 elements of 5x5 mm^2 cross section can be moved automatically in a vaccum tube to change the secondary flight path from 1m to 16 m. The Q range is $5x10^{-4}$ - 2.5 $Å^{-1}$. The neutron wavelength λ can be changed from 4 to 10 Å according to the preset of Velocity Selector, and $\Delta\lambda/\lambda$ = 8 - 30 %. The maximum of beam size is 20(H) x 50(V) mm^2. 30 samples can be measured in the meantime one by one.

5. SANS measurements for SiC samples

SANS measurements for 3 SiC ceramic samples with different additives (such as Al_2O_3, B_4C and C) and different sintering conditions were carried out at C1-2 SANS instrument. The neutron data for SiC samples No. 1, No. 2 and No. 3 with 8 and 16 m of distance between sample and detector as well as 10 and 7 Å of neutron wavelength have been obtained.

Measuring condition

No.	Wavelength λ(Å)	Preset of velocity selector (/rpm)	Secondary flight path (m)
1	10	12500	8
2	7	18000	16

Neutron transmissivity measurement

Sample	for 10 Å (12500/rpm)	for 7 Å (18000)/rpm)
No. 1	42.2 %	55.8 %
No. 2	96.5 %	97.8 %
No. 3	96.2 %	97.4 %

According to the results of transmissivity, we can know that the amount of boron contained within sample No. 1 is more than that contained within sample No. 2 and No. 3.

6. SANS curves from SiC samples

The scattered neutrons were collected at a position sensitive detector covering a relatively large range of the scattering angle Q. For example, the cubic pattern for sample No. 2 collected at a 2D position sensitive detector with 128x128 elements is shown in Figure 1. You can see that the neutron data are almost with axial symmetry. The shape of pores, whose dimensions are relative to the Q range, is almost spherical.

Both neutron data of experiment 1 (with 8 m of distance between sample and detector and 10 Å of neutron wavelength) and experiment 2 (with 16 m and 7 Å) were linked up with each other for 3 samples. The Q range is from 0.0028 to 0.05 $Å^{-1}$. The comparasions of SANS curves of I(Q) for 3 samples are shown in Figure 2. Both curves for samples No. 2 and No. 3 are almost similar, but different from the curve for sample No.1. A log plot of $I(Q^2)$ for sample No. 1 is presented in Figures 3 and 4 for No. 2 and Figure 5 for No. 3.

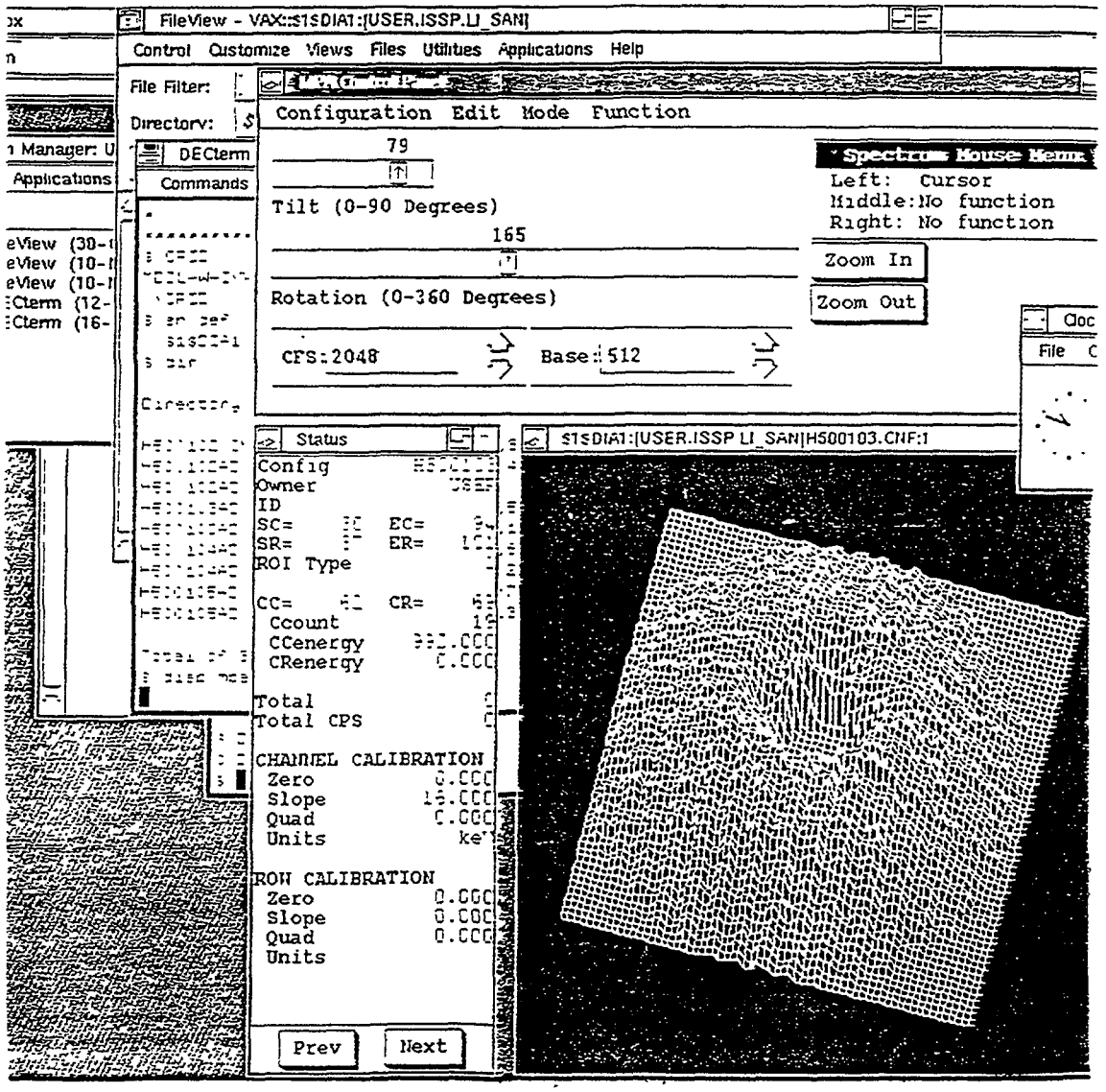

FIG. 1. The cubic pattern for sample No. 2 collected at a 2D position sensitive detector with 128x128 elements.

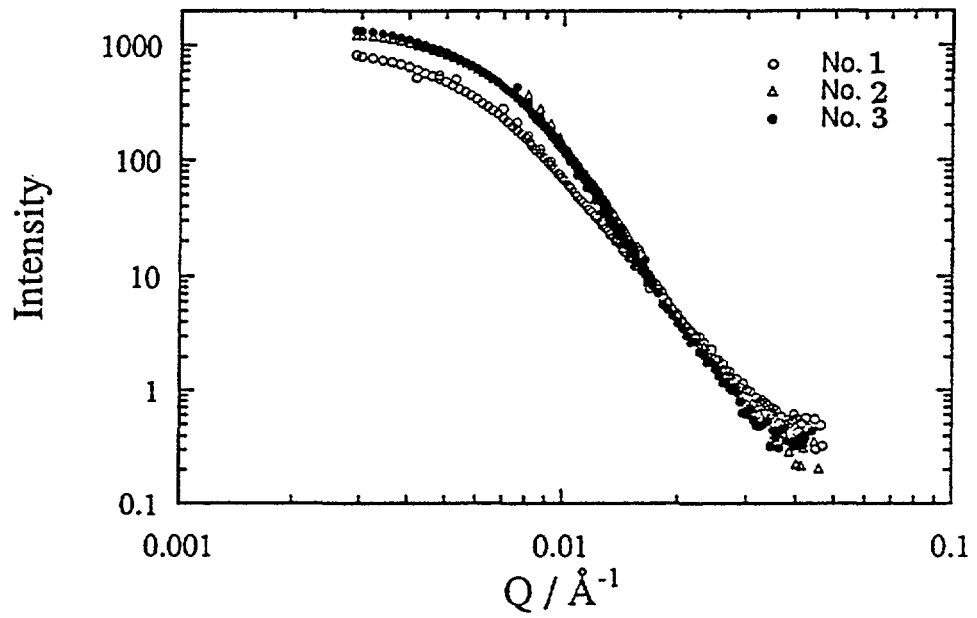

FIG. 2. The comparison of SANS of I(Q) from SiC sample No. 1. And No. 2. And No. 3.

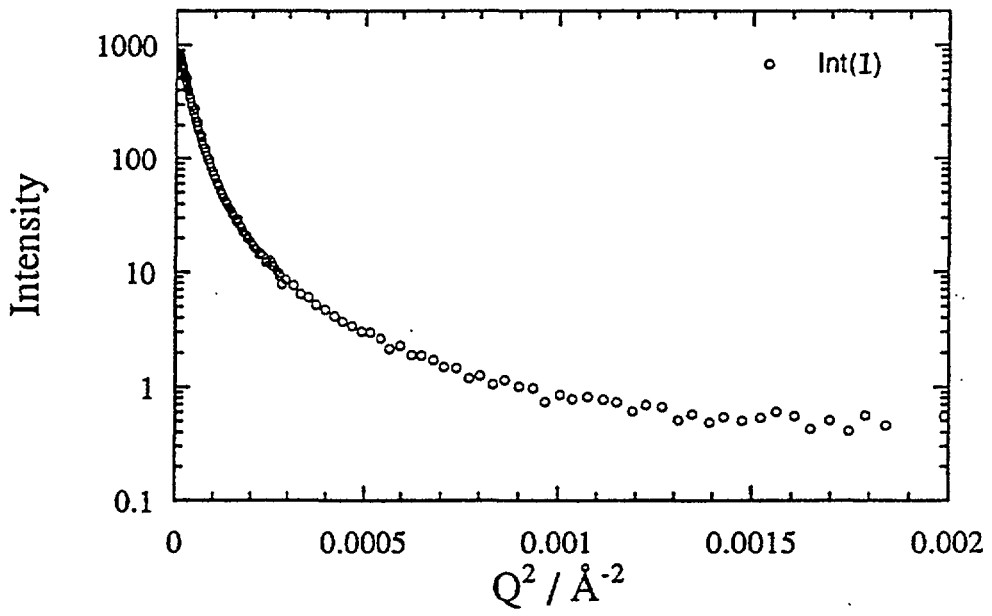

FIG. 3. A log plot of I(Q2) for sample No.1.

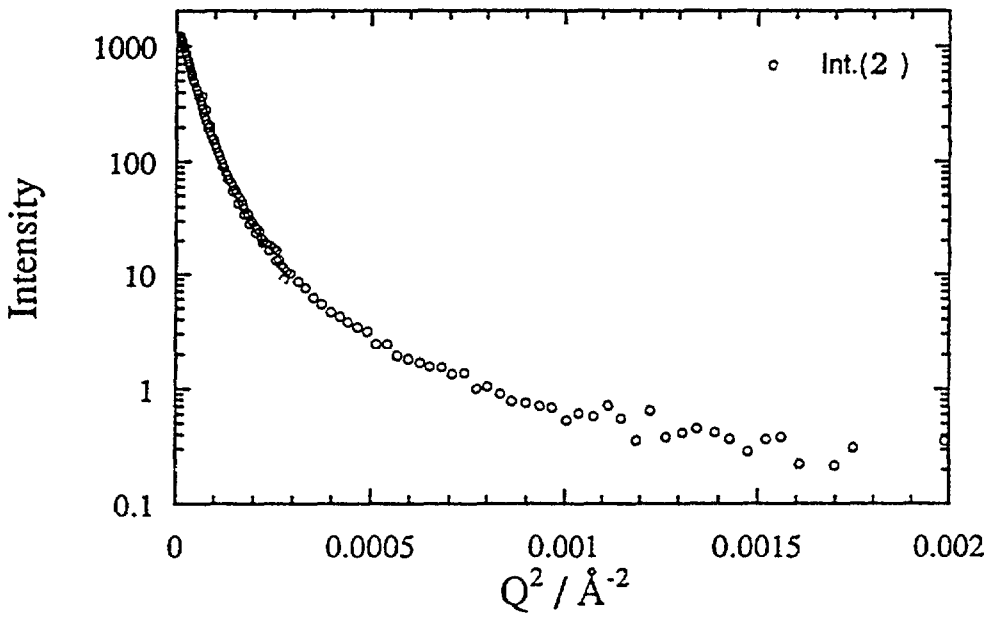

FIG. 4. A log plot of I(Q2) for sample No.2.

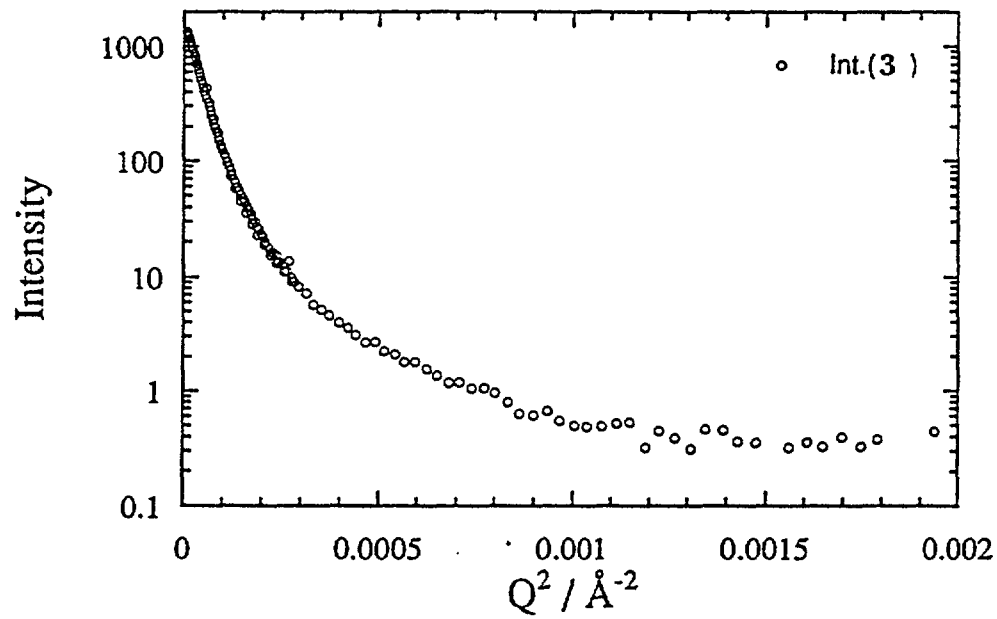

FIG. 5. A log plot of I(Q2) for sample No. 3.

7. The size distributions of pores for 3 SiC samples

One of the most frequent applications of SANS concerns the problem of scattering from polydispersions of particles (or pores) whose shape is known in principle. The tangent method and the Mellin transform are available to treat this problem which give information on the size distribution $D_N(R)$ of these particles (or pores). [4].

The tangent method assumes that the particle (or pore) distribution $D_N(R)$ can be divided into a number of groups with equal dimensions R_{gi}. The scattering curve, plotted as log I versus Q^2, can then be decomposed into single straight lines whose single slopes become $1/3\ R_{gi}^2$. The relative group concentrations are easily obtained. According to the log plot of $I(Q^2)$ Figures 3, 4 and 5, the average values of size distribution of pores for samples No. 1, No.2 and No. 3 are 193.0, 225.9 and 229.6 Å respectively, using tangent method.

The Mellin transform allows , where the measured scattering cross-section is due to scattering from spherical particles (or pores), to express the size distribution directly as [5]

$$D_N(R) = \frac{1}{3}\int_0^\infty Q^3 I(Q)\zeta(QR)dQ \qquad (1)$$

$$\xi(QR) = (QR)^{-1/2}\left[2-(QR)^2\right]J_{3/2}(2QR) - \frac{3}{2}(QR)J_{1/2}(2QR) \qquad (2)$$

in which $J_{3/2}$, $J_{1/2}$ are Bessell function

$$J_{3/2}(x) = \sqrt{\frac{2}{\pi x}}\left(\frac{\sin x - x\cos x}{x}\right) \qquad (3)$$

$$J_{1/2}(x) = \sqrt{\frac{2}{\pi x}}\sin x \qquad (4)$$

To analyze the data easily, we can break the integral of Eq. (1) into two parts:

$$D_N(R) = \frac{1}{3}\left[\int_0^\eta Q^3 I(Q)\xi(QR)dQ + \int_\eta^\infty Q^3 I(Q)\xi(QR)dQ\right] \qquad (5)$$

SANS data can only be taken to a finite value of Q in any case, so that the integral must be cut off at some point. For large Q, I(Q) must be proportional to Q^{-4}. Thus, if the η value is large enough, the second integral in Eq. (5) is negligible. The first integral may easily be evaluted on a computer for each R value of interest and $D_N(R)$ may then be obtained directly from the data.

The fitting results of pore radius distribution using the Mellin transform for SANS data of SiC sample No. 1 in Figure 2 are listed in Table I, in which the I_o is the experimental result and the I_c is the calculated result after fitting. The last value R_{av} is the average value of

TABLE I. THE FITTING RESULTS OF PORE RADIUS DISTRIBUTION FOR SANS DATA OF SiC SAMPLE NO. 1 IN FIGURE 2.

Q(Å)	I_c	I_o	I_c-I_o
0.00290	796.9638	793.6973	3.2665
0.00300	781.3136	770.9866	10.3270
0.00320	749.4456	747.8893	1.5563
0.00340	716.9941	717.0227	-0.0286
0.00360	684.1642	689.7667	-5.6025
0.00380	651.1555	660.9107	-9.7552
0.00400	618.1599	622.3973	-4.2375
0.00420	585.3600	584.1573	1.2027
0.00440	552.9279	546.3133	6.6146
0.00460	521.0233	520.5240	0.4993
0.00480	489.7922	491.2720	-1.4798
0.00500	459.3669	457.9133	1.4535
0.00520	429.8645	429.6293	0.2352
0.00540	401.3868	399.5360	1.8508
0.00560	374.0202	376.9440	-2.9238
0.00580	347.8354	351.5480	-3.7126
0.00600	322.8877	326.8800	-3.9923
0.00620	299.2175	298.5133	0.7042
0.00640	276.8511	280.8733	-4.0222
0.00660	255.8010	258.9227	-3.1217
0.00680	236.0670	241.9000	-5.8330
0.00700	217.6373	223.8013	-6.1641
0.00720	200.4895	207.5627	-7.0732
0.00740	184.5917	189.9413	-5.3497
0.00760	169.9036	175.9733	-6.0697
0.00780	156.3783	163.3333	-6.9551
0.00800	143.9625	150.3107	-6.3482
0.00820	132.5989	140.2947	-7.6957
0.00830	127.2927	129.5400	-2.2473
0.00850	117.3920	118.2733	-0.8814
0.00870	108.3867	111.2027	-2.8159
0.00890	100.2121	102.3973	-2.1852
0.00910	92.8031	93.4773	-0.6742
0.00930	86.0960	87.9173	-1.8214
0.00950	80.0284	81.3120	-1.2836
0.00970	74.5403	74.5747	-0.0344
0.00990	69.5746	68.9013	0.6733
0.01010	65.0771	64.6667	0.4105
0.01030	60.9974	59.6533	1.3441
0.01050	57.2887	55.5853	1.7033
0.01070	53.9078	51.1907	2.7171
0.01090	50.8157	48.0187	2.7970
0.01110	47.9772	44.3213	3.6558
0.01130	45.3606	42.0067	3.3540
0.01150	42.9383	40.1120	2.8263

TABLE I. (cont.)

0.01170	40.6857	36.6760	4.0097
0.01190	38.5816	35.2293	3.3522
0.01210	36.6077	33.2347	3.3730
0.01230	34.7485	30.9053	3.8432
0.01250	32.9908	29.4267	3.5641
0.01270	31.3237	29.4280	1.8957
0.01290	29.7380	25.6187	4.1194
0.01310	28.2263	24.3067	3.9197
0.01320	27.4963	22.8480	4.6483
0.01350	25.4016	21.6040	3.7976
0.01360	24.7335	20.0973	4.6362
0.01380	23.4397	19.5000	3.9397
0.01400	22.2002	18.9000	3.3002
0.01420	21.0127	18.3000	2.7127
0.01440	19.8751	17.7000	2.1751
0.01460	18.7857	17.1000	1.6857
0.01480	17.7430	16.5000	1.2430
0.01500	16.7459	15.9000	0.8459
0.01520	15.7930	15.3000	0.4930
0.01540	14.8832	14.7000	0.1832
0.01560	14.0154	14.1000	-0.0846
0.01580	13.1885	13.5000	-0.3115
0.01600	12.4014	12.9000	-0.4986
0.01620	11.6532	12.3000	-0.6468
0.01640	10.9427	11.7000	-0.7573
0.01660	10.2690	11.1000	-0.8310
0.01680	9.6310	10.5000	-0.8690
0.01730	8.1863	9.0000	-0.8137
0.01770	7.1772	8.0000	-0.8228
0.01800	6.5012	7.0000	-0.4988
0.01880	5.0113	6.0000	-0.9887
0.01950	4.0415	5.0000	-0.9585
0.02050	3.0932	4.0000	-0.9068
0.02210	2.2624	3.0000	-0.7376
0.02450	1.5369	2.0000	-0.4631
0.03050	0.6702	1.0000	-0.3298
0.03150	0.5852	0.9000	-0.3148

RESIDUAL= 1.5932398E-02

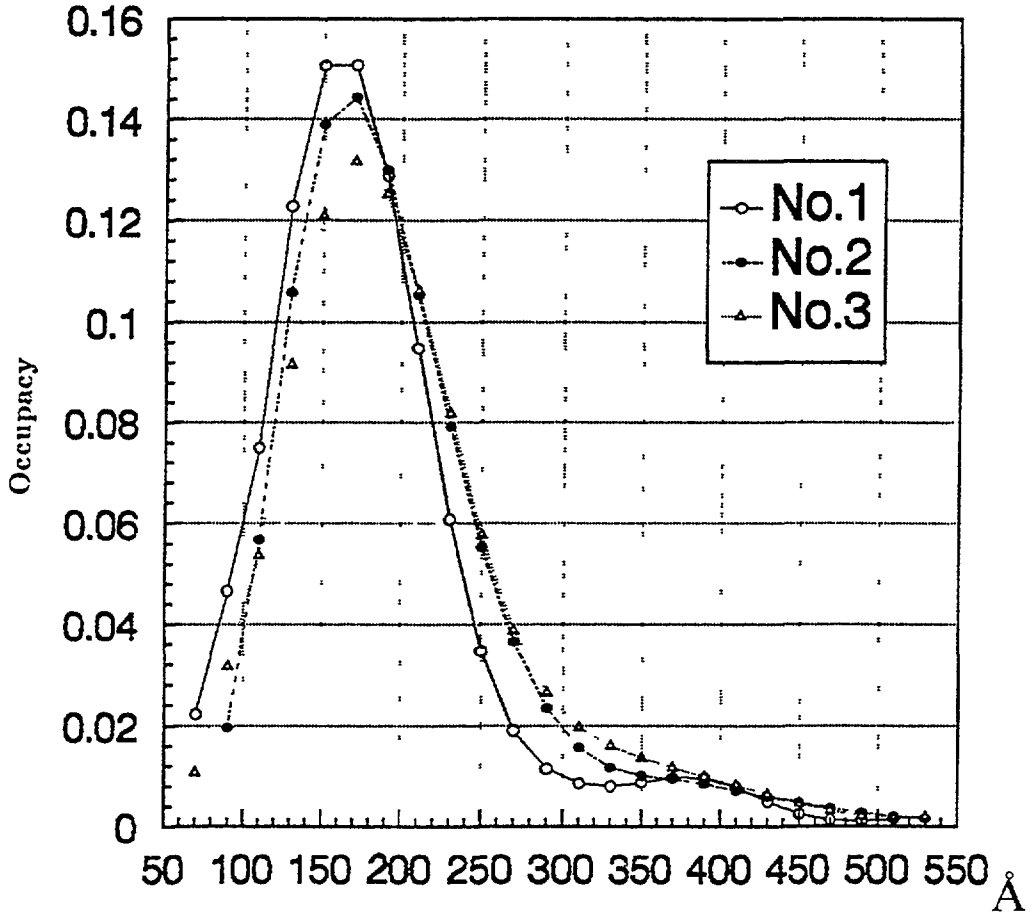

FIG 6 A comparision of fitting results of pore radius distributions using Mellin transform for 3 SiC samples.

pore radius distribution. The comparasion of fitting results of pore distribution using the Mellin transform for SiC samples No.1, No. 2 and No. 3 is shown in Figure 6. The comparasion of the average value of pore radius distribution for 3SiC samples using the tangent method and Mellin transform, respectively, is listed in Table II. The results using both methods are nearly similar. Since the results using tangent method are more dependent on the dividing of groups of equal dimensions, so the results using Mellin transform are more reliable.

8. Results and conclusion

The mechanical properties of ceramics are significantly influenced by the concentration and dimensions of pores or inclusions In hot-pressed and reaction-bonded SiC the microvoid dimensions are usually in the range between 10^2 and 10^5 Å This large extension of scattering center dimensions give rise to the superposition of multiple neutron refraction from large voids and the usual diffraction phenomena for small voids

For the sample No. 1, in hot pressed the pressure was only 0.3 MPa, which was much less than the pressure of 40 MPa for obtaining a sample of SiC with density 3.17 g/cm^3 (99 % theoretical density), so its density is only 2.97 g/cm^3. For other 2 samples without hot-pressing, the densities are 2.63 and 2.60 g/cm^3 , respectively. There are a lot of pores inside the SiC crystallites and the crystal boundary for these SiC samples. The results of pore

The fitting parameters of sample No.1
-0.0002, 82, 25

R(Å)	Occupancies
70.0000	0.02221562
90.0000	0.04656984
110.0000	0.07490792
130.0000	0.12275511
150.0000	0.15072471
170.0000	0.15080015
190.0000	0.12869455
210.0000	0.09472879
230.0000	0.06073831
250.0000	0.03465295
270.0000	0.01896505
290.0000	0.01142729
310.0000	0.00853996
330.0000	0.00798384
350.0000	0.00867966
370.0000	0.00964975
390.0000	0.00959276
410.0000	0.00776541
430.0000	0.00493481
450.0000	0.00253562
470.0000	0.00128855
490.0000	0.00118546
510.0000	0.00145006
530.0000	0.00153931
550.0000	0.00149582
570.0000	0.00158524

R_{av} = 191.2547

TABLE II. THE AVERAGE VALUES (Å) OF PORE RADIUS DISTRIBUTIONS FOR 3 SiC SAMPLES USING TANGENT METHOD AND MELLIN TRANSFORM

Sample	Tangent method	Mellin transform
No. 1	193.0	191.3
No. 2	221.6	210.4
No.3	225.9	214.5

radius distribution for 3 SiC samples are shown in Figure 6. Table II show that the average value Rav of pore radius distributions for sample No. 1 is smaller than others (~10%).

In addition, for sample No. 1, No. 2 and No. 3 the dispersions of pore radius distributions are about 160 Å, 170 Å and 178 Å respectively (see the FWHM of peaks of pore radius distribution curves in Figure 6). From the curve of sample No. 1 in Figure 6, besides the group of pores with R_{av} ~190 Å, there is other group of pores, whose R_{av} is about 370 Å.

With smaller pore size and dispersion seems to be the reason why the density of hot-pressed SiC sample is higher than that of no-hot-pressed samples, and the additive of boron in the form of boric acid is not suitable in SiC sintering comparing with the born carbide B_4C.

References

[1] Shi Ke-shun, "Development of High Temperature Ceramic Composites", J. Chinese Ceramic Soc., 21 (1993) 77.
[2] Jiang Dong-liang et al., "Studies on Hot-pressed Silicon Carbide", J. Chinese Silicate Soc., 9 (1981) 133.
[3] F. F. Lange, J. Mat. Sci., 10 (1975) 314.
[4] H. Walther and P. Pizzi, "Small Angle Neutron Scattering for Nondestructive testing", RESEARCH TECHNIQUES IN NONDESTRUCTIVE TESTING Volume IV Edited by R. S. Sharpe, 1980, London, Academic Pr., p. 341-391.
[5] H. A. Mook, "Neutron Small-Angle Scattering Investigation of Voids in Irradiated materials" J. Appl. Phys., 45 (1974) 43.

PARTICIPANTS IN THE CO-ORDINATED RESEARCH PROJECT

Jizhou, Li	China Institute of Atomic Energy Dept. of Nuclear Physics Beijing, China
Venegas, R	Comisión Chilena de Energia Nuclear Departomento de Fisica Santiago, Chile
Weber, H.W.	Atominstitut der Österreichischen Universitäten Schüttelstrasse Vienna, Austria
Petrov, A.	Latvian Academy of Sciences, Institute of Physics Salaspils, Latvia
Margaça, F. M. A.	Instituto Technologico e Nuclear Depart. de Fisica, Estrada Nacional Sacavém, Portugal
Misheva, M.	Faculty of Physics, University of Sofia Sofia, Bulgaria
Ramos Parente, C. B. R.	Instituto de Pesquisas Energéticas e Nucleares Comissao Nacional de Energia Nuclear Sao Paolo, Brazil
Pollak, H.	University of the Witwatersrand, Chemistry & Physics Department Johannesburg, South Africa
Musiç, S.	Rudjer Bošković Institute, Dept. of Technology, Nuclear Energy & Radiation Protection Zagreb, Croatia